DEVELOPMENT OF AROMATIC POLYESTERS FOR HIGH PERFORMANCE APPLICATIONS AND USE OF INTERCHAIN TRANSESTERIFICATION REACTIONS AS A SOLID-STATE FABRICATION TOOL

BY

JACOB LEE MEYER

THESIS

Submitted in partial fulfillment of the requirements
for the degree of Master of Science in Materials Science and Engineering
in the Graduate College of the
University of Illinois at Urbana-Champaign, 2015

Urbana, Illinois

Adviser:

Professor James Economy

ABSTRACT

Deposition and cure of aromatic thermosetting copolyester (ATSP) oligomers is explored across several potential schemes: plasma spray, solvent-borne, and as an electrostatic powder coating. It is generally found that all methods are potentially viable as low friction, low wear coatings but that ATSP as an electrostatic powder coating is the simplest and highest performing deposition mechanism in terms of wear rate and provides the highest glass transition temperatures in an electrostatically-deposited polymeric powder coating known in literature or commercially. Low production of wear debris coupled with stable and high mechanical property films transferred to the tribopair counterface (as seen via energy-dispersive X-ray spectroscopy) lends evidence that during tribological experiments that produce contact temperatures of up to 320°C that interchain transesterifications (ITR - a class of solid state chemical reactions available to aromatic polyesters) are responsible in part for low wear rates via ATSP reincorporating its own wear debris and development of a stable transfer film. Additionally, it is found that a mixed liquid crystalline/amorphous oligomer set will phase segregate and produce surface texture corresponding to the phase segregated ordered region. This surface texture and the high glass transition temperature of ATSP enables the in-situ formation of micro-reservoirs of lubricant during lubricated tribotesting.

Micromechanical experiments were used to assess the contribution of cohesive wear to ATSP resins as well as several neat polymer and commercially deposited

coatings. In instrumented scratch experiments ramped up to 80mN in applied force with a 4.3 μm conispherical indenter tip, it is found that ATSP exhibits a uniquely high tendency towards what is termed “elastic recovery” wherein the scratched region of the coating surface recovers most of the deformed depth during retrace experiments. As well, the wear mode of amorphous ATSP coatings maintains this performance at applied loads significantly in excess of any other observed coating. It is hypothesized that the crosslinked structure and potential for the aromatic polyester chains to deform via crankshaft motion about the ester bond may be responsible for this interesting mechanical feature.

Vacuum assisted resin transfer molding is demonstrated as a potential fabrication technique for continuous fiber ATSP composites. The potential for ATSP to be the first weldable thermoset material is also explored. Fully cured laminae of ATSP/carbon fiber are fused into a single workpiece via solid-state interchain transesterification reactions. Resin-dominated mechanical properties of the composite such as interlaminar shear strength and the Mode I fracture toughness of the composite at the bondline adhered via ITR. Results indicate interlaminar properties beyond that of traditional epoxy and polyimide resins. Additionally, cryogenic thermal cycling experiments are used to assess the composite’s resistance to microcracking which indicates excellent resistance to microcracking as well as potential repair schemes for ATSP composites. Single fiber fragmentation testing was used to determine the interfacial shear strength of the fiber/matrix bond. The high strength here and observation via scanning electron microscopy of all fibers

entirely coated in resin suggest that cracking in ATSP composites predominantly occurs within the resin phase. The lack of low energy surfaces at fiber/matrix interface to propagate suggests a rationale to the high Mode I fracture toughness observed for ATSP composites.

Mechanical and thermal performance of ATSP foams and fully dense structures recycled from the foams via interchain transesterification reactions are described. Tribological results of the fully dense structures when filled with PTFE lubricating additives suggest application as a low-friction and low wear material. Several novel additive fabrication schemes and a process to weld aromatic polyester composites are also suggested as future areas of research.

To My Wife Amanda and My Son Oliver

TABLE OF CONTENTS

CHAPTER 1

INTRODUCTION & BACKGROUND

1.1 Background

Aromatic polyesters, polyamides, and polyimides are established classes of polymers generally incorporating an aromatic structure as the basis of their mesogenic units. These semi-rigid structures have seen a broad range of commercialization, with their greatest commercial success as polymeric fibers such as most notably the lyotropic LCP poly(p-phenylene terephthalamide) (PPTA), which is marketed as Kevlar and Twaron [1,2]. The thermotropic copolymer of 4-hydroxybenzoic acid (HBA) and 2,6-hydroxynaphthoic acid (HNA) is also marketed under the trade name Vectran [1,2]. Aromatic polyesters are sold for molding purposes notably include the copolymer of terephthalic acid, biphenol, and p-hydroxybenzoic acid known as Xydar and Vectran also marketed as Vectra[1]. The related homopolymer of HBA, commercially known as Ekonol, was the first to enter the commercial sphere after the original discovery and development work at Carborundum Corporation by Economy and co-workers of the solution/suspension phenyl ester route [3].

The high mechanical properties of these materials are seen to arise from their orientational self-ordering [1,38] and high rigidity of their constituent units. Examining one of the prototypical and most common constituent of aromatic polyesters, poly(HBA) as shown in Figure 1, the phenylene units are prevented from rotating and conformational freedom is only available through crankshaft motion about the ester bond [38].

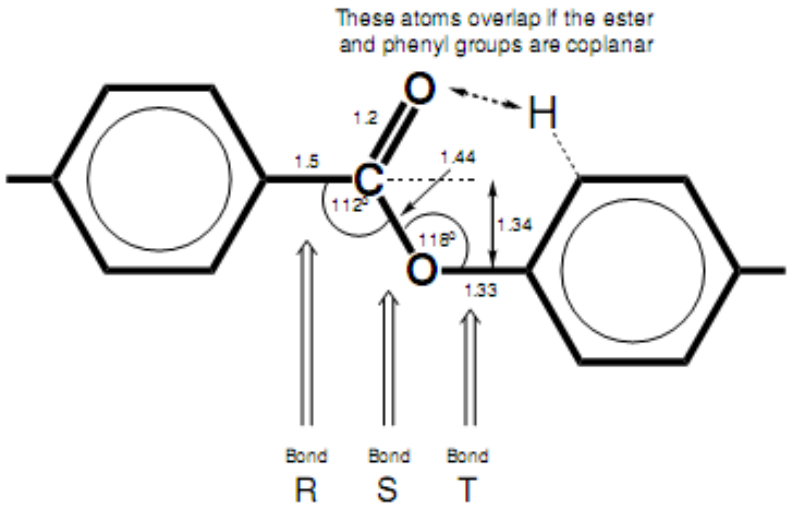

Fig. 1.1: Schematic of poly(HBA) repeat unit with bond angles and lengths expressed. From [37].

In addition to their robust mechanical properties [1-5], aromatic polyesters are also known to have excellent chemical resistance [4], high heat deflection temperatures and flame resistance[9,42], and hydrolytic stability [7]. These features make them attractive as matrices in high performance composites. To date though, no all-aromatic polyester is known to have been successfully marketed as a matrix for continuous fiber reinforced composites, in spite of the lack of a generally accepted polymeric matrix material for service temperatures above 135°C [41].

1.2 Aromatic Polyesters

Aromatic polyesters represent some of the earliest reports on polymeric materials, with Klepl reporting on residue he called p-oxybenzid during his synthesis of the dimer and trimer of HBA in 1883 [43]. Fischer later confirmed the synthesis of the dimer and trimer in 1909 [44]. Work on aromatic polyesters laid dormant until Gilkey and Caldwell reported on the polymerization of p-acetoxybenzoic acid and m-acetoxybenzoic acid [45]. They erroneously concluded the polymer of HBA as unstable due to their melt polymerization producing the phenyl ester of p-

hydroxybenzoic acid by an acid catalyzed condensation of the phenolic hydroxyls or acetoxy units [46]. Economy first successfully produced the homopolymer of HBA (PHBA) in 1963 by use of a phenyl ester to cap the carboxylic acid and use of a heat exchange medium to control the reaction temperature [3]. The highly crystalline product was thermally stable in air at 350°C and was by 1970 commercialized for use in thermal spray and high energy rate forging [2].

This was soon followed by the development of the copolymer of PHBA and biphenol terephthalate (BPT) which by 1971 was commercialized as Ekkcel [1]. It was observed early in the work that the 2:1 ratio of PHBA:BPT yielded an injection moldable grade that melted at 408°C while the 1:2 ratio copolymer yielded a compression moldable grade.

The 3:2 copolyester of p-hydroxybenzoate and ethylene terephthalate was commercialized by Eastman-Kodak in the mid-1970s, though it was withdrawn soon thereafter due to poor thermal stability. The 3:7 copolyester of HNA and PHBA, sold as Vectra and Vectran as mentioned above, was commercialized in 1980 by Celanese. This copolymer has seen utilization in both moldable products and as fibers, however its low glass transition temperature of 150°C and degradation during annealing [51] has limited its further deployment.

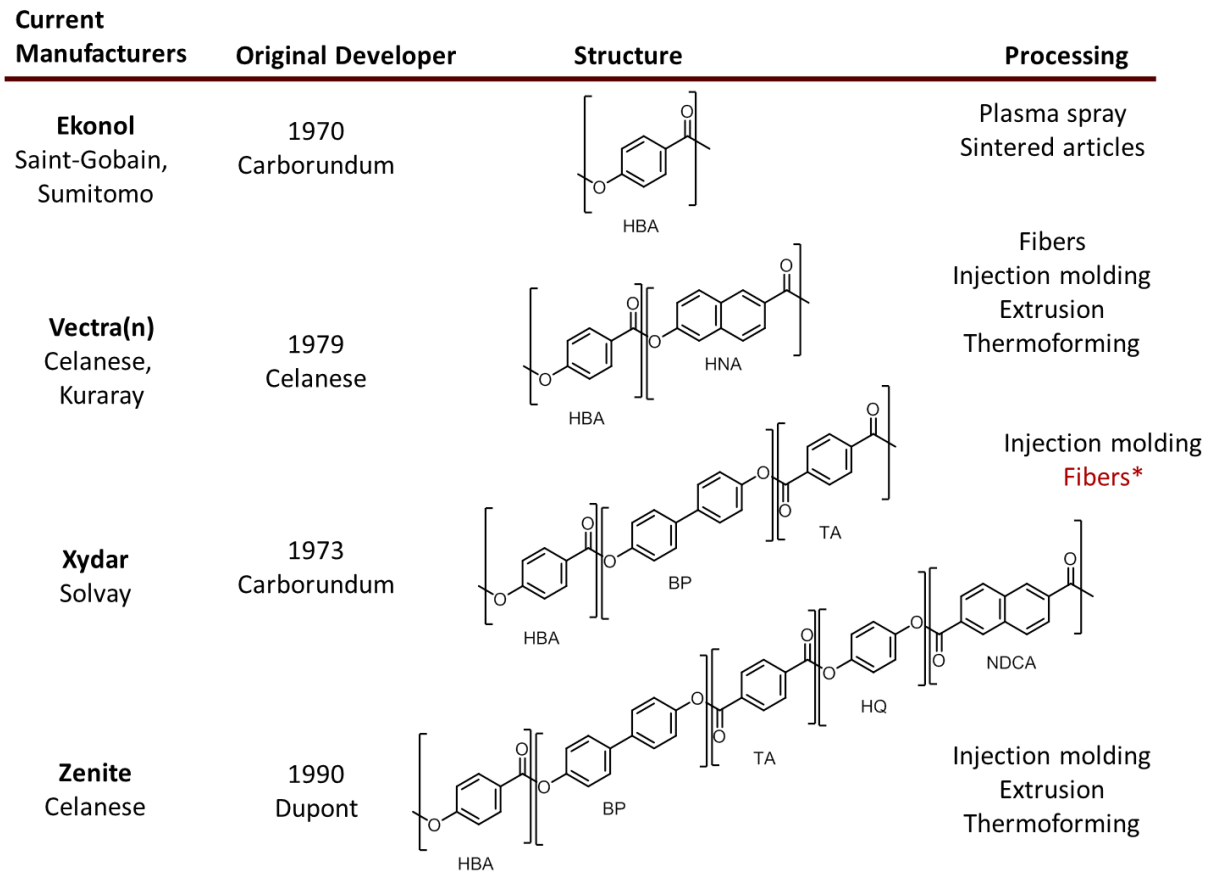

Fig. 1.2. Structures of previously commercialized aromatic polyesters.

1.3 Aromatic Thermosetting Polyester (ATSP)

Aromatic thermosetting polyesters (ATSPs) are a relatively new family of thermosetting polyesters made from low cost monomeric precursors. Commercially available monomers (HBA, trimesic acid, hydroquinone, and isophthalic acid) with phenyl hydroxyl-capped monomers acetylated to acetoxy form via acetic anhydride with sulfuric acid catalyst. The acetoxy and carboxylic acid capped aromatic monomers undergo melt condensation reactions at 100-270°C, depending on the molecular weight of the desired oligomeric system, to yield either acetoxy-

terminated or carboxylic acid-terminated melts [4]. The oligomers are blended then cured at 250-330°C to yield ATSP (Figure 2).

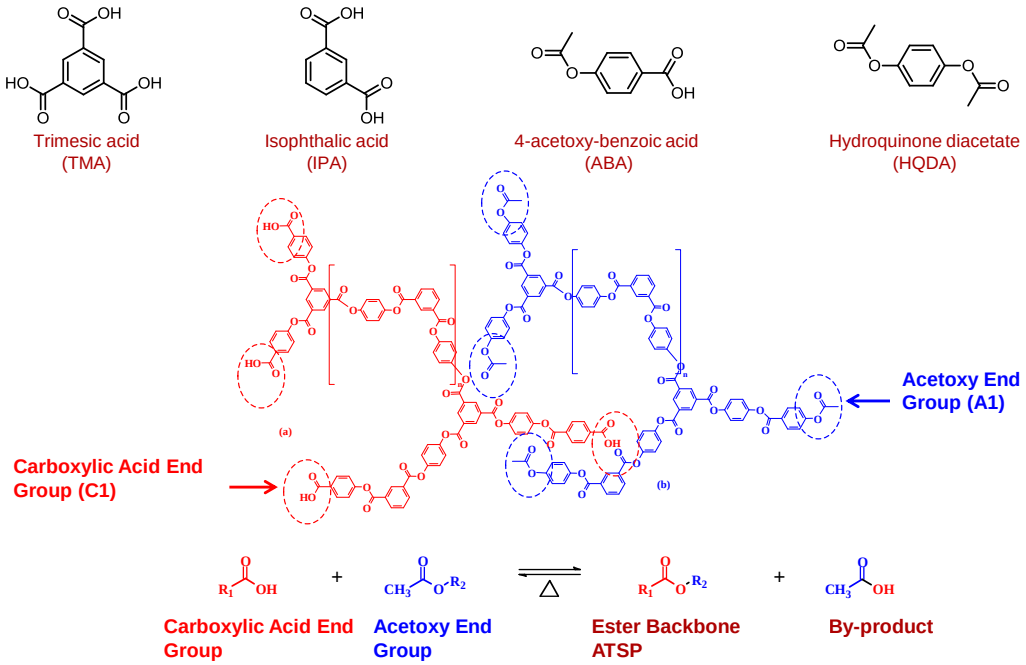

Fig. 1.3: Proposed structure of ATSP. From [51]

A number of oligomeric systems with varying functionality and molecular weight have been developed and characterized. The oligomers can be tailored to be liquid crystalline by adjusting the molar ratio, thus providing unique advantages compared to conventional polymers. In addition, the number of functional groups can be modified to affect the crosslink density. Varying the molecular weight adjusts the mechanical properties of the neat resin and composite. Table 1 shows some of the typical oligomeric compounds that have been synthesized along with their softening points.

Table 1.1: Properties of ATSP oligomers. From [4].

Oligomers marked with * exhibit liquid crystallinity in melt

oligo-mer	molar feed ratio of monomer					MW_{av} (g/mol)	function-ality	softening point (°C)
	TM	TAB	ABA	IPA	HQDA			
C-1	2		6	3	4	1934	4	172
C-2*	1		6	4	4	1890	3	143
C-3	2		4	2	3	1454	4	189
C-4	2		5	1	2	1334	4	188
C-5*	1		5	2	2	1290	3	161
C-6	2		3	1	2	1094	4	162
C-7	2		3		1	854	4	148
C-8	1		3	1	1	810	3	136
A-1	2		2	2	7	1750	4	128
A-2*	1		5	2	5	1692	3	130
A-3*	1		5	1	4	1452	3	160
A-4		2	4	2	1	1270	4	128
A-5		2	2	2	1	1030	4	107
A-6		2	3	1		910	4	105
A-7		1	2	1	1	732	3	81

ATSP can be produced in either amorphous or liquid crystalline formulations by selection of appropriate monomer feed ratio to select crosslink density. Oligomers which do not display birefringence individually in their melt form amorphous polymers when cured while those that do display birefringence produce polymers which are birefringent after full curing [7,8]. Birefringent oligomers have similar molecular weights as isotropic oligomers but with a lower feed ratio of the crosslinker (TMA) which results in a longer chain length between crosslinks, as shown in Table 2.2. Figure 1.4 displays the difference in birefringence between amorphous and liquid crystalline fully cured ATSP.

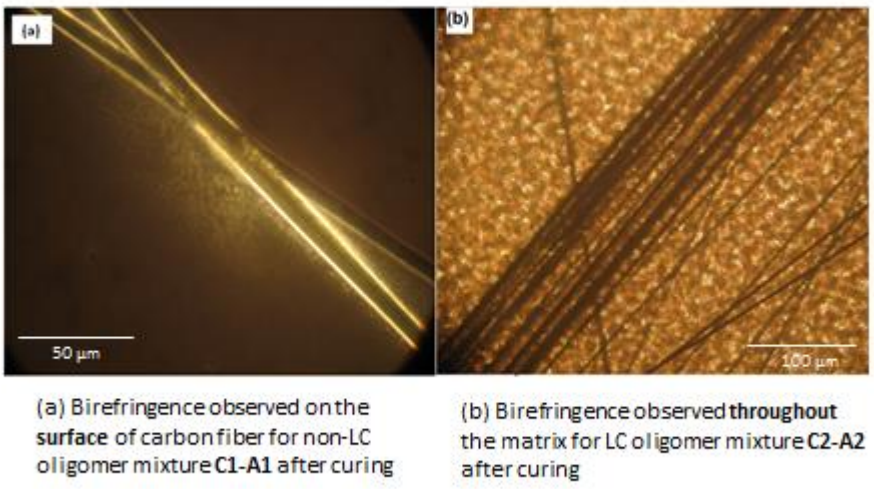

Fig. 1.4: Observation of birefringence of ATSP fiber/resin compositions via cross-polarized light microscopy. From [51].

1.4 ATSP Physical Properties

As described above, ATSP is a high temperature resin that has unique properties [1-5,7,9]. Prior experiments demonstrate ATSP has better thermal stability and low moisture pickup compared to epoxies, with properties equivalent to those of best performing thermoset polyimides [12-15] and can be repaired more easily than either [21]. ATSP is stable in air at 350 C and in nitrogen at 425 C [4,20] whereas most thermally stable epoxies decompose at 170-190 C in air or nitrogen. The moisture pickup of the resin is relatively low (0.3 wt%, as compared to 2.3% for epoxy and 2.6% for polyimides) [12-15], increasing the potential durability against physical ageing. ATSP also shows outstanding flame [42] and ablative character [9] which may be of utility in the design of high performance aerospace structures. In these experiments, ATSP composites formed a stable char and evidenced no

interlaminar delamination after exposure to oxyacetylene torch events while Parkar et al [9] demonstrated its potential suitability as a heat shield material for both Earth and Mars re-entry via COIL-type laser ablation experiments at marker flux rates.

The liquid crystallinity of the matrix [36] and the tendency of the aromatic polyester repeat unit to be oriented [37-40, 49] is hypothesized to aid in reducing thermally induced interfacial stresses when used as matrix for carbon fiber composites [12,18,36,50-51] via local matching of the coefficient of thermal expansion around the carbon fiber. It has been observed that birefringence (and thereby implying orientational order) in the resin is preserved in regions immediately surrounding carbon fibers [17,50] even in temperature regimes where the resin would normally be in an amorpous state. An example of this is illustrated in Fig. 1.4 wherein a normally amorphous C1A1 resin shows induced birefringence surrounding a carbon fiber. Further, the order parameter in LCPs surrounding carbon fibers are enhanced to approximately that of the substrate carbon fiber [55] and was found to be independent of fabrication approaches. Preliminary experiments [51] for coefficient of thermal expansion in ATSP/C composites demonstrated a reduced transverse coefficient of thermal expansion and a significantly reduced difference between transverse and longitudinal as compared to epoxy/C composites of comparable resin CTE, identical fiber and weave type, and volume fraction of resin. Such an effect could be anticipated to be of utility in

cryogenic or high temperature applications where thermal cycling was encountered such as in reusable composite cryogenic fuel storage tanks.

Table 1.2. Summarized ATSP (C1/A1) Physical Properties [7,10,11,42,47]

Properties	ATSP
Density (g/cm3)	1.35
Glass Transition (°C)	240-310
Moisture Pickup (%)	0.3
Thermal Stability (°C)	425 (In Nitrogen) 350 (In Air)
Heat Capacity (J/g°C)	1.44 (at 25°C)
Thermal conductivity (W/m·K)	0.1
CTE (1/K)	$40x\ 10^{-6}$
Dielectric constant	3.0
Dielectric breakdown strength (V/µm)	384

1.5 Interchain Transesterification Reactions

One of the most salient feature of this system is an ability to form adhesive bonds even after being cured. The ester crosslinks impart to the resinthe ability to undergo interchain transesterication reactions (ITR) [14]. Interchain transesterication reactions (ITR) are unique to polymers with ester linkages and have been found to aid in the formation of bonds between molecular chains [5, 10, 21]. This can be exploited to obtain adhesive bonds between polymers with ester linkages. Surface reactions can occur at high temperatures to form strong chemical bonds.

Interchain trans reactions, of which ITR is a constituent member, have several distinctive features. Firstly is that the functional groups present before and after the reaction are identical [56]. Trans reactions (also known as chemical interchange reactions or exchange reactions [96]) are not unique to polyesters and are, in fact, conceptually plausible in any condensation polymer, though only a few have been identified. Other interchange reactions so far identified include those those among polyamides between amide and amine functional groups and between amide groups [57]. Interchange reactions have been identified among siloxanes in the presence of strong base or sulfuric acid [57-58]. Interchange reactions in polysulfides are known to occur via 1) between thiol and disulfide bonds, 2) adjacent disulfides, and 3) between inorganic and organic disulfides, which produces mercaptan [57,59]. These have been proposed as a stress-relief mechanism in vulcanized rubbers under strain at elevated temperatures [60].

Exchange reactions within the polyester backbone can be classed into three types: The first type is an exchange reaction between a hydroxyl end group with a neighboring ester that is termed an alcoholysis reaction [56] and is completely reversible at every step. This proceeds by nucleophilic addition of the hydroxyl to a carbonyl group of an ester linkage. This induces a positive charge to the hydroxyl oxygen and a negative charge to the carbonyl oxygen. The intermediate structure expels an alchohol via electron transfer from the negatively-charged oxygen which captures a proton from the original hydroxyl. The final result is that exchange occurs at the carbon-oxygen single bond in the original ester [62]. Flory previously

demonstrated that presence of an acid catalyst enabled ready reaction of copolymers in excess decamethyle glycol and adipic acid, which produced hydroxyl terminated polymers. This was determined by inferring a decrease in molecular weight to the copolymer by observing a viscosity decrease with decamethylene glycol monomer addition to the high MW polymer melt. This type exchange reaction in polyesters is commercially exploited for the synthesis of polyethylene terephthalate from ethylene glycol and terephthalic acid[61].

Figure 1.5 and the lower diagram in Figure 1.6 demonstrates the second type of exchange reaction observed for polyesters: acidolysis. This reactions proceeds by nucleophic addition in a similar manner described for alcoholysis above wherein an acyl oxygen on a carboxylic acid adds to a carbonyl of a backbone ester. Again, the tetrahedral intermediate of the original polyester acyl oxygen eliminates an ester linkage formed between the original ester oxygen and the carbonyl of the original carboxylic acid. This also produces a new carboxylic acid [62]. An example of use this class of reaction is the reaction of PET with with 4-acetoxybenzoic acid (4-ABA) to produce a copolymer [64]. It was assumed in this study that only acidolysis proceeded, however that may not be a valid assumption due to the possibility that the third class of ester exchange reactions occurred between the acetoxy unit of the 4-ABA and the ester backbone units of the high MW PET.

Ester-ester exchange, known as esterolysis, is the third mechanism for ITR in polyesters. An example reaction for aromatic polyesters is show in the upper portion of Figure 1.6. Rather than the nucleophilic pathways for alcoholysis and

acidolysis, this exchange reaction is thought to proceed by what is termed an associative reaction mechanism [66-67]. Two carbonyls of adjacent ester bonds experience formation of an association complex and the acyl groups of the original esters are switched. While Flory and others [57,68,69] have suggested that evidence indicates that esterolysis proceeds very slowly, contradictory evidence exists [67,70,71] for exchange of PET and bisphenol-A diacetates. These were determined both through NMR and viscosity changes.

Although three reactions have been shown to exist, obviously they cannot all have the same rate constant. Complications in determining the rate constant for each mechanism arise from difficulties in separating the rates of ITR from condensation esterifications as well as isolating the individual reaction contributions (alcoholysis, acidolysis, and esterolysis). Flory inferred that rates of alcoholysis and esterification were approximately the same for similar conditions and without the addition of an external catalyst for polymers of adipic acid and decamethylene glycol. Esterification rates were determined by mixing equimolar quantities of decamethylene glycol and adipic acid and monitoring the change in viscosity. Alcoholysis rates meanwhile were determined by measuring the viscosity change upon addition of decamethylene glycol to decamethylene adipate polymers. He found that acidolysis rates were approximately an order lower than for alcoholysis [68]. Hamb [70] and Tijsma [67,71] however estimated that esterolysis was significantly faster than acidolysis and of the same order as alcoholysis.

Later technological advances aided in the determination of transesterification rates within a polymer. Kugler [73] determined that alcoholysis and esterolysis were responsible for decrease in length of deuterated and protonated segments via small angle neutron scatter (SANS) with no associated change in viscosity which indicates a randomization process. These experiments further suggest this follows an Arrhenius process as the decrease in the segment length was as a function of both temperature and time [73]. Arrighi observed a similar result via SANS study of dimethylbenzalazine copolyesters [74] and suggested that ITR functioned to produce the most probable MW distribution of the polymer (broadening polydispersity index, PDI) while leaving the number average molecular weight M_N unchanged. This randomization is a natural consequence of the property of ITR to leave the count of functional groups unchanged. MacDonald et al [113] used SANS against a partially deuterated wholly aromatic polyester of high molecular weight to determine an activation energy of of 157 kJ mol^{-1}.

Economy and Schneggenburger [53,54,75] demonstrated via ^{13}C NMR that a mixture of 4-hydroxybenzoic (HBA) and 2,6-hydroxynapthoic acid (HNA) powders homopolymers would undergo extremely rapid randomization via ITR (within 10 seconds at 450°C) to produce a HBA/HNA copolymer. This had drastic physical effects on the sample: the melting point of the copolymer was drastically lower than either of the homopolymers. The HNA/HBA diad sequences were obvious via the ^{13}C NMR spectra. From the NMR data and physical observations a reaction rate of 10000 transesterifications per molecule per minute – a tremendously fast rate.

These observations enabled subsequent studies to demonstrate the ability to alter average molecular weight and distribution via blends of high MW polymers [76-77] and showed the potentional for localized post-processing of polyesters [78-79]. Frich and Economy demonstrated that a crosslinked and fully cured network polymer (ATSP) coated onto an aluminum alloy substrate and then bonded at 330°C to a counterpart coated substrate demonstrated excellent cohesion. A lap shear strength of up to 20 MPa was demonstrated, comparable to commercially available epoxy adhesives of similar of bondline thickness. Furthermore, it was observed that the failure mechanism of the lap shear coupons was entirely adhesive at the aluminum/ATSP bondline rather than at the ATSP/ATSP bondline. This suggested high strength for this joining mechanism. An associated neutron reflectivity study by Frich and Economy [10] an interdiffusion distance of 30 nm across a bondline of two ATSP thin films adhered via ITR in a similar manner as above, an order lower than that predicted by Kramer as necessary for adhesion in the case of strictly physical diffusion of rigid chains across an interface [143]. As these were previously fully cured films, a strictly physical diffusion was not a viable mechanism. Frich and Economy also demonstrated via ^{1}H NMR that deuterated oligomers of ATSP undergo exchange with protonated counterpart oligomers [48]. This body of work demonstrated that the ITR mechanism was a chemical process and that it can be used to fuse two adjacent surfaces at the bondline in a solid-state. This suggested of utility for manufacturing, bonding, and repair of thermosetting polyester composites (ATSP/C). Lopez et al. have shown that cured lamina can be

bonded together using ITR [5]. Thick consolidated sections of ATSP are obtained by bonding single laminae under heat and pressure. It was also demonstrated that ATSP films could be bonded in the solid-state to polyimide films of commercial Kapton [102,103]. This suggests an enabling fabrication technique for microelectronic and micromechanical devices which may require an all-solid state process. Interesting as well is that the experiments indicated a diffuse boundary layer between the Kapton and ATSP films [103]. A precise identification of an exchange process versus a physical process was not produced in that study, but the potential of an imide-ester exchange reaction remains a viable hypothesis from that experiment. This also opens the possibility that an aromatic imide-ester copolymer as in Xu [106] could undergo ITR.

Huang and Economy use ITR as a solid-state bonding process for thin films deposited on copper foils [104]. Huang [107] and Zhang [19,20] demonstrated that a fine powder of ATSP could be consolidated via ITR at 330°C and under applied pressure and that this evidenced a relatively high glass transition temperature as well as excellent tribological properties when a high concentration of PTFE [19,20] was added as a lubricating filler though a relatively poor oxidative stability profile was obtained due to limitations of the ATSP powder synthetic route chosen in that study. Recent studies by Calleja [96] and Capelot [112] used ester units bound within monomeric species that were cured using an epoxide functional group. Exchange reactions were then used to produce a chemically contiguous networks that could be dynamically deformed. These studies as well demonstrated that

catalysts used in commercial small molecule syntheses employing transesterifications were pertinent to solid-state ITR in that they increased the observed rate of exchange reactions.

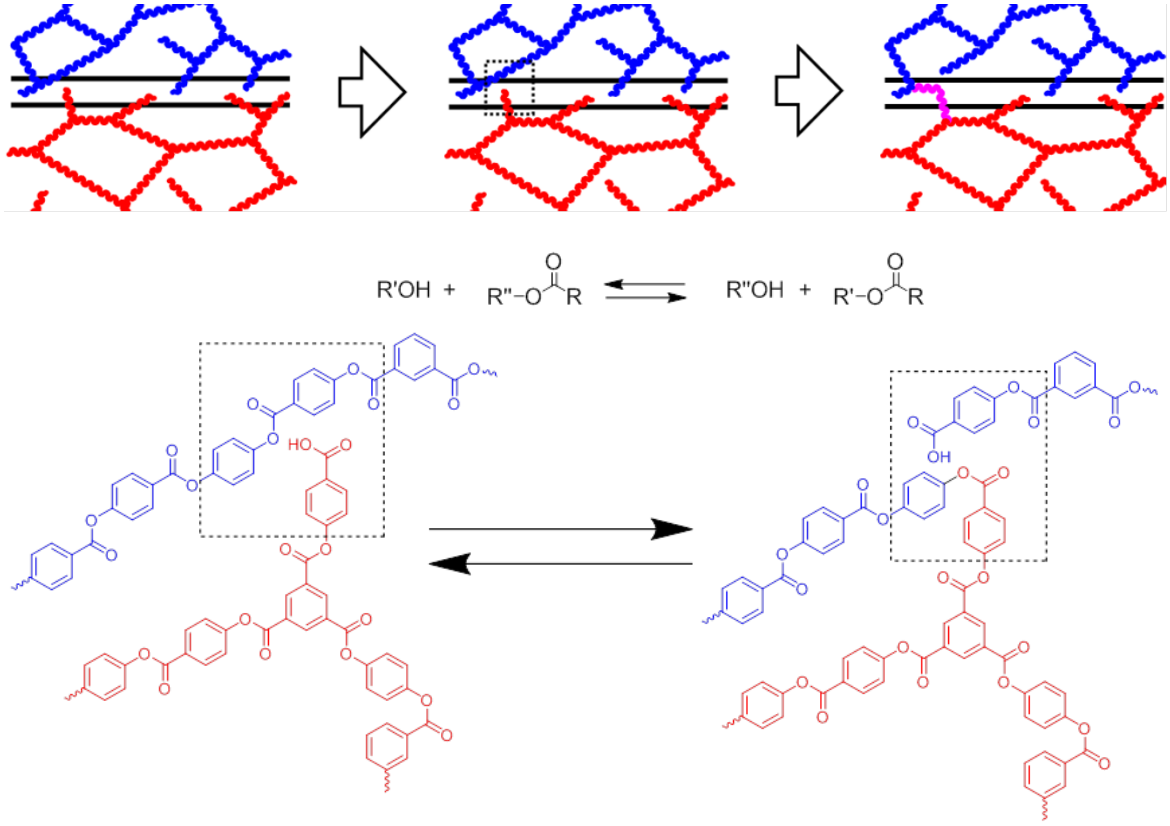

Fig. 1.5. Example chemical reaction at surface between carboxylic acid and ester unit via acidolysis. An example reaction for surface-surface bonding of crosslinked aromatic polyesters.

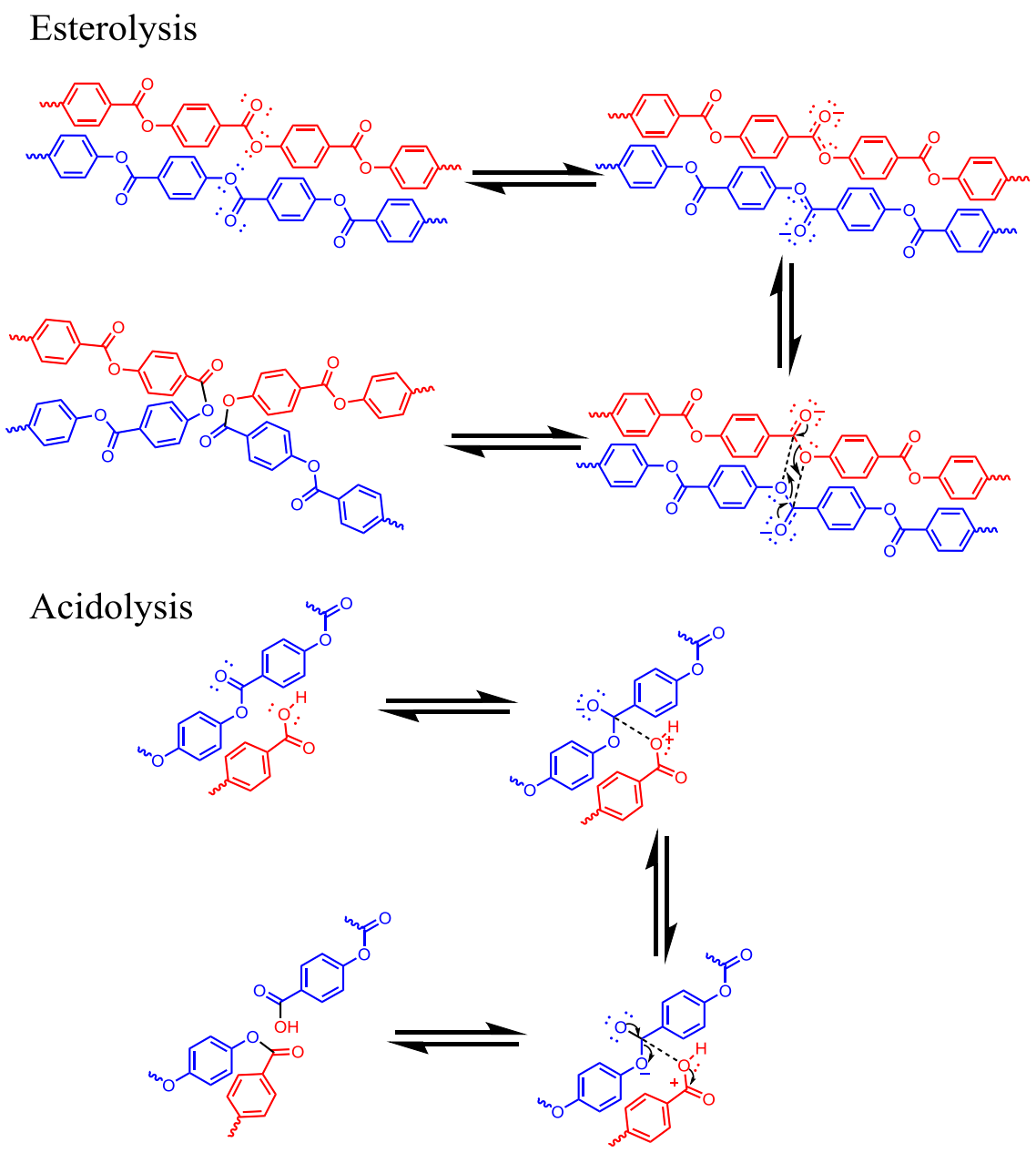

Fig. 1.6. Proposed interchain transesesterification reaction mechanisms in aromatic polyesters for esterolysis and acidolysis.

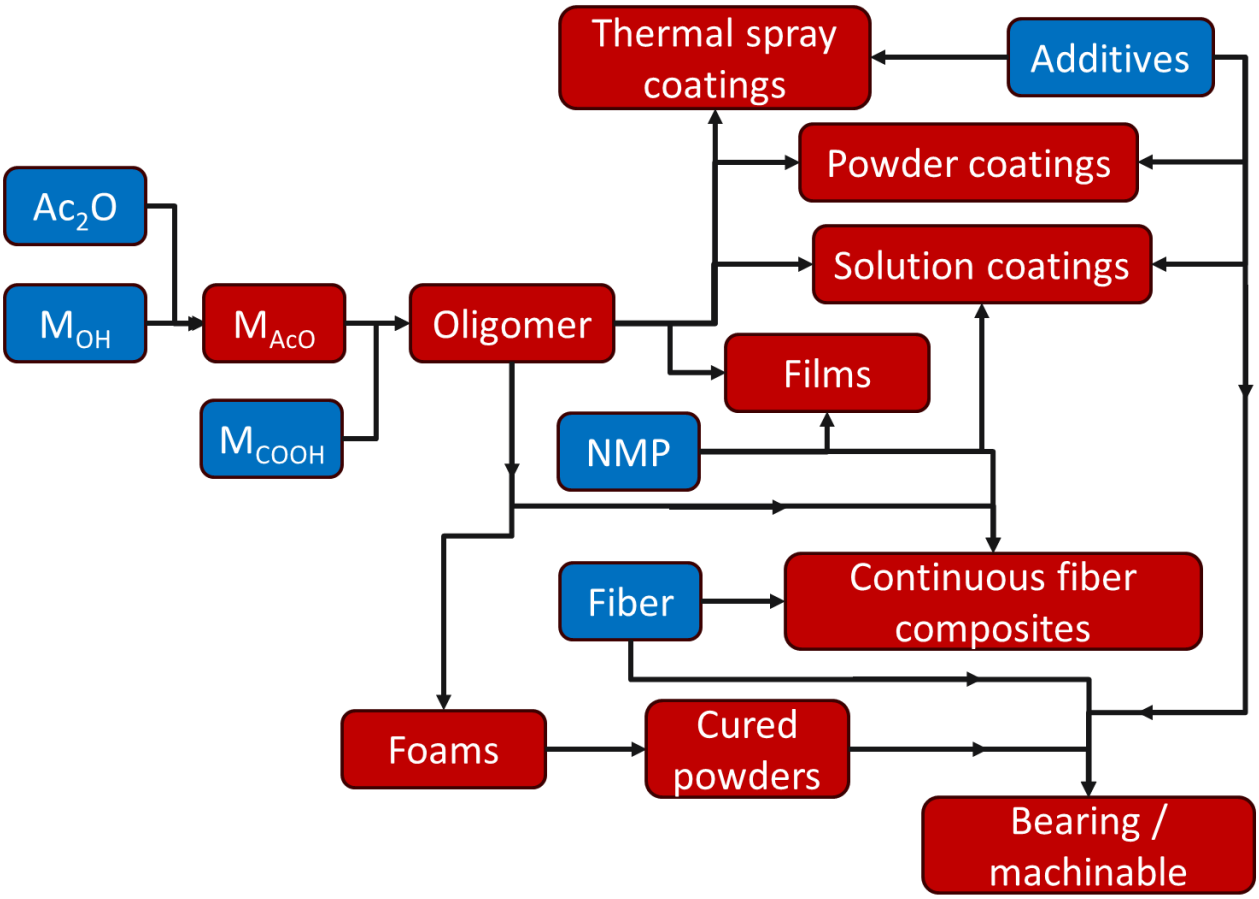

Fig. 1.7. Overall process schematic for fabrication of ATSP structures. Blue indicates input materials, red indicates output materials.

With these available mechanisms and several pathways that will be demonstrated in this document, we put forth the following overall process schema for fabrication of ATSP structures (Figure 1.7). A mechanistic diagram for ITR is show in Figure 1.6.

Chapter 2 will discuss oligomer synthesis and network parameters of several cured structures. Chapter 3 will describe the coating deposition methods and macro-tribological characterization of ATSP coatings and covers evidence for a self-healing effect for ATSP coatings under aggressive and high temperature tribological

coatings via the ITR mechanism. Chapter 4 will cover micromechanical characterization of ATSP coatings and elucidates at the micro-scale some observed features of ATSP . Chapter 5 reports on progress towards out-of-autoclave synthesis of continuous fiber ATSP composites and advanced characterization of laminates produced via ITR. Chapter 6 will discuss high specific strength and stiffness ATSP foams and their recyclability into fully dense articles with high mechanical and tribological performance and aw well proposes several fabrication techniques using ITR.

CHAPTER 2

OLIGOMER SYNTHESIS

2.1: Oligomer Synthesis

Oligomer synthesis followed a process derived from Economy and Frich [47] with some modifications as described for new ATSP oligomers below.

Monomers were acquired from Alfa-Aesar at 99% grades excepting: biphenol, which was acquired from Akron Polymer Systems at 99% grade; perfluorosebacic acid, which was acquired from ExFluor Research Corporation at 95% grade; and acetic anhydride, which was acquired from Sigma-Aldrich at 99.5% grade.

To increase the glass transition temperature of the resin, the hydroquinone, which is the ATSP component most thermally sensitive [2,114,115] (primarily by reactions yielding phenoxy species and ketene), was replaced by biphenyl units that are more thermally stable (see Figure 2.1) and have lower vapor pressures at elevated temperature thereby reducing losses from ITR at exposed surfaces. Hydroquinone diacetate was replaced with biphenol diacetate in carboxylic acid- and acetoxy-capped oligomers to increase the oxidative stability of oligomers. Acetoxybenzoic acid (ABA) and biphenol diacetate (BPDA) were prepared by acetylation of p-hydroxybenzoic acid and dihydroxybiphenyl, respectively. The designated CB oligomers were synthesized by melt-condensation of TMA, ABA, IPA and BPDA (molar ratio 1:3:2:2 respectively) at 260°C in the reactor. AB oligomers were

synthesized similarly with TMA, ABA and BPDA taken in the molar ratio 1:3:3. CB and AB oligomers were then mixed and cured to make CBAB cured powders.

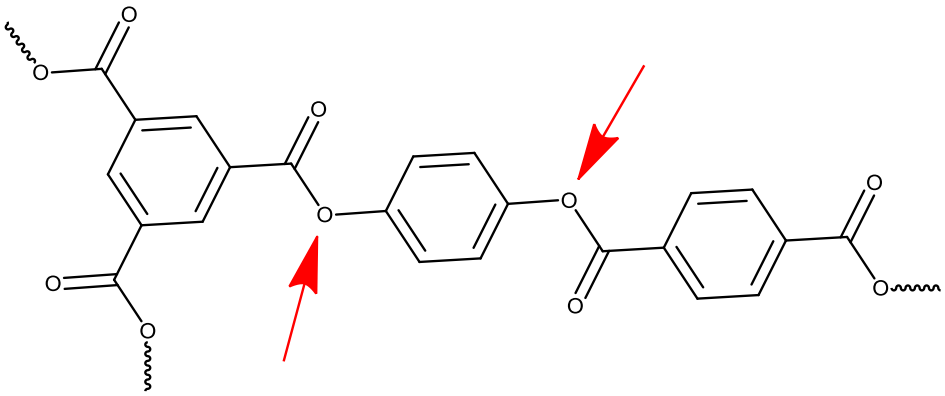

Fig. 2.1. ATSP backbone locations off hydroquinone monomer most sensitive to side reactions.

Biphenol diacetate (hereinafter BPDA) was synthesized by acetylation of biphenol (hereinafter BP) analogously to the synthesis of 4-acetoxybenzoic acid. In this case, 500 g of BP was mechanically stirred in 850 mL of acetic anhydride (molar ratio of about 2.7:8.9) in a cylindrical vessel in an ice-water bath at 10°C at which point 2-3 drops of sulfuric acid was added to catalyze the acetylation reaction. The solution temperature immediately increased to 80-85°C due to the exothermic reaction. After allowing the solution to cool to room temperature, BPDA was precipitated out with distilled water. BPDA was then filtered, washed with copious volumes of distilled water and dried in a convection oven at 70 °C for 48 hours. The reaction yield was above 95% as determined by integration of ^{1}H (proton) nuclear magnetic resonance (NMR) spectra following methodology from Guo [99].

To produce carboxylic acid end-capped oligomer CB, 129.4 g TMA, 333 g BPDA, 204.7 g IPA, and 332.9 g ABA were mixed in a 2 L cylindrical reactor flask. The flask was equipped with a three-neck head connected to an inlet inert gas, a screw-type impeller driven by an overhead mechanical stirrer, a J-type thermocouple, and an Allihn-type condenser with a 3-way valve to offer a toggle between reflux and distillation modes. The reactor was continuously purged with argon while emplaced within a Glas-Col aluminum-housed electric heating mantle operated via temperature controller with the thermocouple operating as feedback. The reactor was heated to260 °C for 30 min to obtain a low-viscosity melt during which stirring was maintained at 300 revolutions per minute (rpm) and which evidenced a substantial acetic acid by-product which was refluxed during this stage. After refluxing for 30 minutes, the condenser was toggle to distillation mode and acetic acid condensation by-product was collected in an Erlenmeyer flask and the mass of the acetic acid was continuously monitored by digital weighing balance which indicated the extent of reaction. The reaction was stopped with 220 mL of acetic acid collected (theoretical 258 mL). Reaction yield of the CB oligomer was about 696 g (approximately 94 %). The CB oligomer product, a viscous melt, was ground into a fine powder. Average molecular weight of oligomer product was determined following from Guo by ratio of integrated proton NMR spectra between ester and carboxylic acid end group protons and was within 1% of theoretical molecular weight. Theoretical molecular weight is determined by subtraction of the number of moles of acetoxy functional groups in the reactor feed mass multiplied by the mass of acetic acid from the molecular weight of the feed monomers times their monomer

ratio within the feed mass. The CB oligomer product, a viscous melt at 260 °C and a brittle solid at 23 °C, was ground into a fine powder. An example structure is shown in Figure 2.2

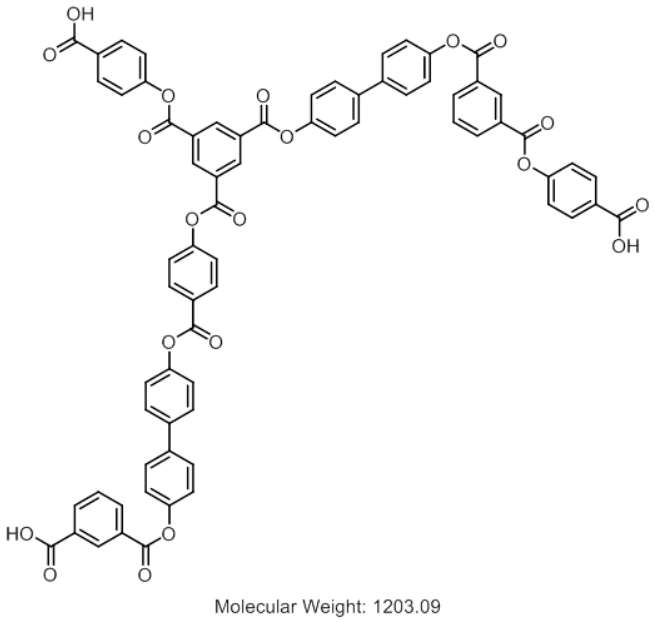

Fig. 2.2. Example structure of CB oligomer.

For the carboxylic acid end-capped oligomer CB2, 86.8 g TMA, 205.9 g IPA, 372.2 g ABA, and 335.1 g BPDA were used with the same procedure as above for CB oligomer. 215 mL of acetic acid was collected after 3 hours at 260 °C (theoretical 272.9 mL) and reaction yield of the AB oligomer was 690.8 g (approximately 95 %). Average molecular weight of oligomer product was likewise as for oligomer CB determined to be within 1% of theoretical molecular weight. The CB2 oligomer product, a viscous melt at 260°C and a brittle solid at 23°C, was ground into a fine powder. An example structure is shown in Figure 2.3.

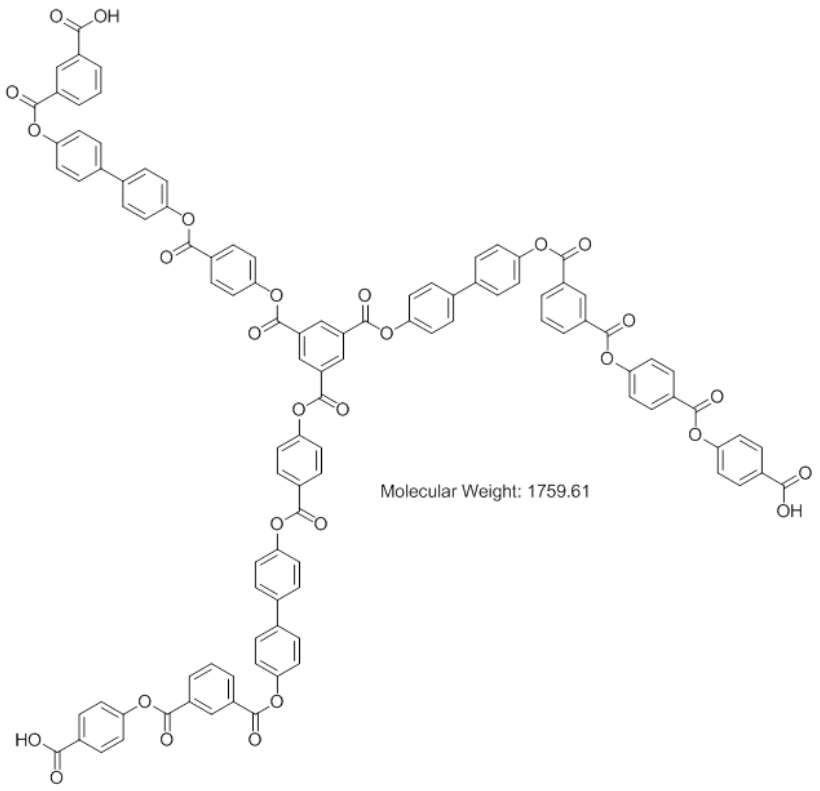

Fig. 2.3. Example structure of CB2 oligomer.

For the acetoxy end-capped oligomer AB, 134.6 g TMA, 346.1 g ABA, and 519.3 g BPDA were used with the same procedure as above. 195 mL of acetic acid was collected after 3 hours at 260 °C (theoretical 230 mL) and reaction yield of the AB oligomer was about 731 g (approximately 95 %). Average molecular weight of oligomer product was determined by ratio of integrated proton NMR spectra between ester and acetoxy end group protons and was within 1% of theoretical molecular weight. Theoretical molecular weight is determined by subtraction of the number of moles of carboxylic acid functional groups in the reactor feed mass multiplied by the mass of acetic acid from the molecular weight of the feed monomers times their monomer ratio within the feed mass. The AB oligomer

product, a viscous melt at 260 °C and a brittle solid at 23 °C, was ground into a fine powder. An example structure is shown in Figure 2.4.

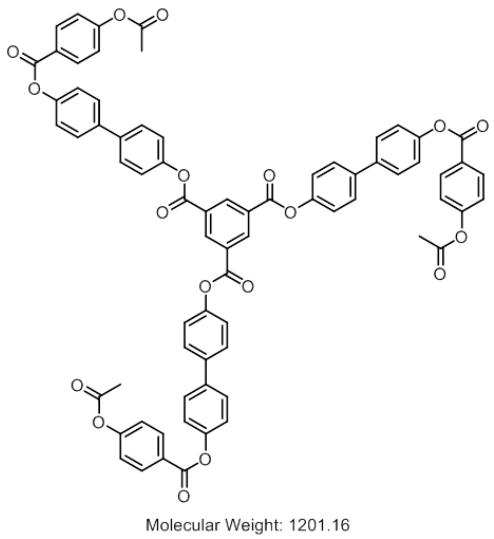

Fig. 2.4. Example structure of AB oligomer.

For the acetoxy acid end-capped oligomer AB2, 89.1 g TMA, 70.4 g IPA, 382.0 g ABA, and 458.5 g BPDA were used with the same procedure as above for CB oligomer. 203.7 mL of acetic acid was collected after 3 hours at 260 °C (theoretical 254.6 mL) and reaction yield of the AB oligomer was 715.7 g (approximately 96 %). Average molecular weight of oligomer product was likewise as for oligomer AB determined to be within 1% of theoretical molecular weight. The AB2 oligomer product, a viscous melt at 260°C and a brittle solid at 23°C, was ground into a fine powder. An example structure is shown in Figure 2.5.

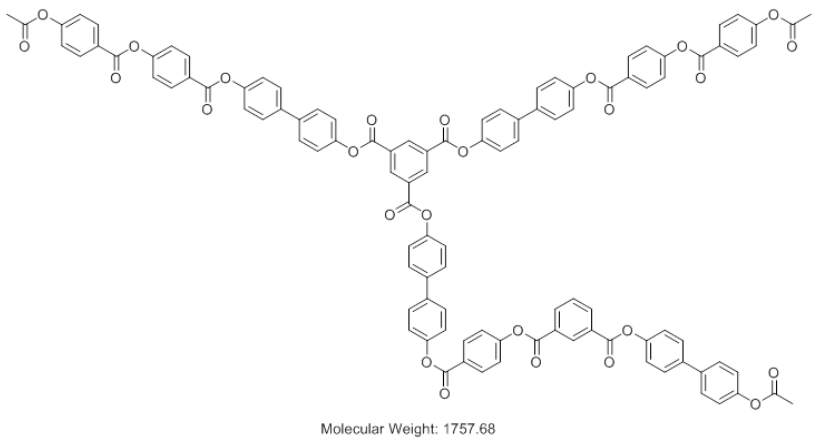

Fig. 2.5. Example structure of AB2 oligomer.

PTFE was demonstrated to be a potent lubricating agent, enabling low wear and COF when blended with ATSP at low weight percent, therefore we tailored the ATSP polymer backbone to incorporate fluorinated ethylene units. For this purpose, perfluorosebacic Acid (PFSA) was used. A1F, C1F, A2F and C2F, which are analogous to amorphous oligomers A1 and C1 and liquid crystalline oligomers A2 and C2, respectively, with a small concentration of PFSA (5% weight) were made.

To produce carboxylic acid end-capped fluorinated oligomer C1F, 37.9 g TMA, 12.5 g PFSA, 40.6 g IPA, 97.3 g ABA, and 70.0 g HQDA were mixed in a 500 mL spherical reactor flask and a reaction procedure analogous to that of CB oligomer was conducted. The flask was equipped with a three-neck head connected to an inlet inert gas, a screw-type impeller driven by an overhead mechanical stirrer, a J-type thermocouple, and an Allihn-type condenser valve to offer a toggle between reflux and distillation modes. The reactor was continuously purged with argon while emplaced within a Glas-Col aluminum-housed electric heating mantle operated via temperature controller with the thermocouple operating as feedback. The reactor

was heated to 260 °C for 15 min to obtain a low-viscosity melt during which stirring was maintained at 300 revolutions per minute (rpm) and which evidenced a substantial acetic acid by-product which was refluxed during this stage. After refluxing for 15 minutes, the condenser was toggle to distillation mode and acetic acid condensation by-product was collected in a 100 mL graduated cylinder and the mass of the acetic acid was continuously monitored by observation of volume, which indicated the extent of reaction. The reaction was stopped with 64 mL of acetic acid collected (theoretical 75.7 mL). Reaction yield of the C1F oligomer was 178.9g (approximately 98 %). The C1F oligomer product, a viscous melt at 260 °C and a brittle solid at 23 °C, was ground into a fine powder. An example of PFSA incorporation into the backbone is shown in Figure 2.6.

For the carboxylic acid end-capped perfluorinated oligomer C2F, 19.2 g TMA, 56.5 g IPA, 98.9 g ABA, 71.1 g HQDA, and 12.5 g PFSA were used with the same procedure as above. 65 mL of acetic acid was collected at 260 °C (theoretical 76.9 mL) and reaction yield of the C2F oligomer was about 178.7 g (approximately 98%). The C2F oligomer product, a viscous melt at 260 °C and a brittle opaque solid at 23 °C, was ground into a fine powder.

For the acetoxy end-capped perfluorinated oligomer A1F, 42.5 g TMA, 29.4 g IPA, 36.5 g ABA, 137.5 g HQDA, and 12.5 g PFSA were used with the same procedure as above. 61.5 mL of acetic acid was collected at 260 °C (theoretical 72.8 mL).

For the acetoxy end-capped fluorinated oligomer A2F, 21.8 g TMA, 30.2 g IPA, 93.3 g ABA, 100.6 g HQDA, and 12.5 g PFSA were used with the same procedure as above. 63 mL of acetic acid was collected at 260 °C (theoretical 74.2 mL).

Reactor vessel configurations used for ATSP oligomerizations is shown in Figure 2.7.

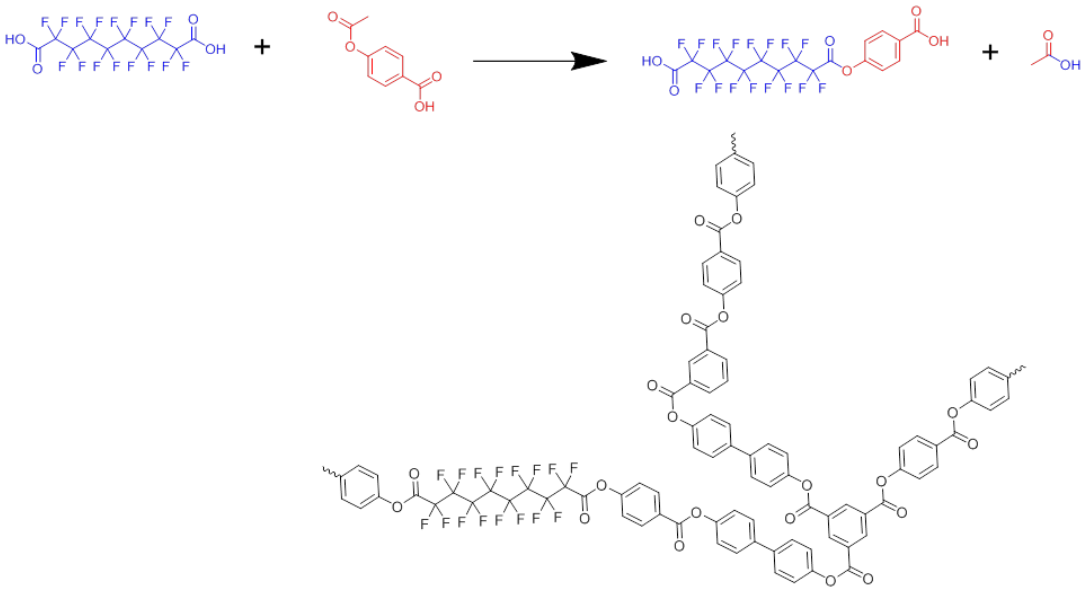

Fig. 2.6. Backbone incorporation and example reaction between aromatic constituent and PFSA.

Fig. **2.7** (Left) 500 mL reactor used for aromatic polyester oligomerizations. (Right) 2000 mL reactor used for aromatic polyester oligomerizations.

2.2: Justification of Oligomer Architecture

Frich, Economy, and subsequent researchers appear to have never explicitly stated their rationale for some features of the architecture of the oligomers seen in Table 5.1.

Table 2.1. Oligomer molar feed ratios, theoretical number average molecular weights, functionality, and softening points as determined by thermomechanical analysis. Highlighted oligomers were used hereafter. From Frich [47]

oligo-mer	molar feed ratio of monomer					MW_{av} (g/mol)	function-ality	softening point (°C)
	TM	TAB	ABA	IPA	HQDA			
C-1	2		6	3	4	1934	4	172
C-2*	1		6	4	4	1890	3	143
C-3	2		4	2	3	1454	4	189
C-4	2		5	1	2	1334	4	188
C-5*	1		5	2	2	1290	3	161
C-6	2		3	1	2	1094	4	162
C-7	2		3		1	854	4	148
C-8	1		3	1	1	810	3	136
A-1	2		2	2	7	1750	4	128
A-2*	1		5	2	5	1692	3	130
A-3*	1		5	1	4	1452	3	160
A-4		2	4	2	1	1270	4	128
A-5		2	2	2	1	1030	4	107
A-6		2	3	1		910	4	105
A-7		1	2	1	1	732	3	81

The mole ratio of functional groups relative to mole ratio of crosslinker necessary to be in place is for a 3-functionality crosslinker (TMA) is defined by functional groups = crosslinker + 2 . Examples are: C1, which would be functional groups = 2 + 2 = 4; C2 functional groups = 1 + 2 = 3; etc. For example, if you sum C1's molar ratio basis count of COOH (2*3+3*2+6*1=18) and the AcO (4*2 + 6*1 = 14) count of as COOH (carboxylic acid) is greater than AcO (acetoxy) by 18 - 14 = 4, that means that the product oligomer will have (on average, since it is a condensation product) four carboxylic acid functional caps. A similar process is used for all non-perfluorinated ATSP oligomers.

The functional group / crosslinker relationship works differently if you use a crosslinker with >3 functionality. For example, [1,1'-biphenyl]-3,3',5,5'-tetracarboxylic acid is a 4-functional carboxylic acid monomer. For a crosslinker with a functionality of 4, the number of functional groups scales as 2*N+2. For an imaginary crosslinker of functionality 5, it would be 3*N+2 and so on. So, the generalizable rule would be where N is the mole ratio of the crosslinker and C is the functionality count of the crosslinker, the number of functional groups (F) needs to be: F = (C-2)*N+2. A final generalization for arbitrary crosslinker functionality and molar ratio is:

$$|AcO - COOH| = F = \sum_{i}^{n} (C_i - 2)N_i + 2$$

2.3: Theoretical Crosslink Density and Branch Configuration

In additional to the functional group equimolar approach ratios used by Frich and all subsequent workers, it is possible to deliberately bias the resin towards content of free AcO and COOH functional groups. Table 2.2 summarizes number average theoretical mass between crosslinks $(M_c)_N$, branch coefficient x_n, functional group ratio COOH/AcO and mass feed ratio for the C1A1 → C2A2 oligomer set.

Table 2.2. Mass feed ratio and resultant structure parameters.

Sample	Oligomer mass feed ratio (C#/A#)	Oligomer molar feed ratio (C#/A#)	COOH / AcO	x_n	$(\bar{M}_c)_N$
ID#					(g)
C1A1	1.105	1.000	1.00	0.1440	834.10
C1A2	1.140	1.000	1.33	0.1051	1142.82
C1A2+	1.243	1.087	1.45	0.1063	1129.92
C1A2-	1.029	0.900	1.20	0.1030	1166.12
C1A2=	0.857	0.750	1.00	0.1010	1189.21
C2A1	1.080	1.000	0.75	0.1100	1117.30
C2A1-	1.224	1.133	0.85	0.1075	1117.30
C2A1=	1.440	1.333	1.00	0.1040	1091.91
C2A1+	1.584	1.467	1.10	0.1020	1177.55
C2A2	1.117	1.000	1.00	0.0718	1672.84

Where x_c equals moles of cross-linked monomeric units divided by moles of monomeric units present and crosslink density is defined by [48]:

$$(\overline{M_c})_n = \overline{M}_u / x_c$$

where *Mu* is the sum of the formula average molecular weights of the oligomers after accounting for cure loss (number of matched carboxylic acid and acetoxy functional groups x mass of acetic acid). COOH/AcO is determined by formula basis of functional groups of oligomer feed.

CHAPTER 3

DEVELOPMENT OF PRACTICAL COATING SCHEMES UTILIZING ATSP

3.1: Background

The higher performance requirements and lighter weights in air-conditioning and refrigeration (ACR) compressors as well as operating condition requirements that have been expanding in terms of higher speed and load has made tribological characteristics of interacting surfaces within the compressor environment play a significant role in the compressor's reliability[86]. Compressor reliability, and generally the interaction of mechanical systems utilizing tribo-pairs, can degrade as components become more worn [86,87]. This can have secondary issues such as spikes in power draw. In order to better resist cascading wear caused by hard third-body wear, an advanced protective coating on the interacting surfaces may be prudent to mitigate this mechanism in addition to the boundary/mixed lubrication that is traditionally employed. [117] Due to favorable tribological performance as well as heavy marketing by private entities owning tradename polymers of this class, resin-bonded polytetrafluoroethylene (PTFE)- and polyetheretherketone (PEEK)-based PTFE-filled polymeric coatings have received interest in ACR compressor applications, as a potential solution to supplement and potentially replace conventional oil lubricants. However, compared to a great amount of research and experiments done so far for bulk of polymers, there is limited literature on the tribological performance of polymeric coatings.

The main advantages of the polymeric-based coatings are their relatively low cost and simple substrate surface conditioning (i.e., no need for expensive surface preparation before coating) as compared to advanced hard coatings (i.e. DLC, [87]). However, commercially available polyamideimide, polyimide and polyetheretherketone-based polymeric coatings still exhibit the following problems:

- their wear rate is still high (compared to hard coatings);
- because they rely heavily on the interaction between the PTFE/PEEK wear debris/solid lubricant and the substrate for surface protection, in the presence of lubricant they may become ineffective;
- the addition of hard particles in these mixtures scratches the counterface, thus creating excessive abrasive wear [117];
- the wear debris likely contains hard particles that can damage downstream machinery via third-body wear;
- the highest glass transition polymeric electrostatic coatings available previous to developments described here are those that based on PEEK [120], which evidences a glass transition of only 143°C [119]

ATSP was investigated by Zhang and Economy [105] as a potential ultra-low wear polymeric coating system that can mitigate the above problems. We can identify some of the properties of ATSP that make it ideal for this application, which includes:

- ATSP is designed to be high-temperature stable, with a glass transition temperature ranging up to 310°C (Figure 5.18)

- Unlike other soft coatings, like PTFE and PEEK, it offers a crosslinked structure that is more stable under aggressive conditions.
- It has a unique ability among high temperature thermoset polymers to react with itself (below thermos-oxidative degradation region) even after curing, undergoing interchain transesterification reactions (ITR). This has been proposed to offer unique functionality during processing and during use - allows reincorporation of wear debris into the coating surface.
- Like the homopolymer p-hydroxybenzoic acid (commercially known as Ekonol®), ATSP coatings show potential for plasma spraying due to the similarity in structure and properties.
- ATSP exhibits very good adhesion to different metal substrates. Copper, titanium, stainless steel and aluminum bonded by ATSP have high lap shear strengths. [11]

The work by Zhang [105] demonstrated excellent performance in some respects, but there were several features missing in regards to using this roll-on scheme (Figure 3.3) to apply ATSP as an effective and relevant tribological coating system.

1. The specific coating methodology (rolling on an oligomeric solution in NMP) has the potential to be very non-uniform
2. It is not amenable to tribo-parts of complex geometry.
3. The ATSP coating itself absent a fluoropolymer lubricating phase evidenced a relatively high coefficient of friction. The fluoropolymer lubricating phase was added by Zhang in the form of a sprinkling of Zonyl onto the cured surface prior to testing. Within state-of-art polymeric coatings, generally the

lubricating phase is bonded within the resin. However, the author's personal knowledge of sample preparation difficulties during that project is that Zhang and her coworkers did not have a specific method for introducing a fluoropolymer lubricating additive phase during preparation

4. All samples were cured under vacuum which makes cure cycles for larger components or large numbers of components a much more difficult production problem. As one of the arguments for use of polymeric tribological coatings is their simplified processing (and thereby lower expense) relative to elastically hard protective coatings.

This chapter details the processing experiments and tribological results that demonstrate that these concerns have been completely overcome. At this point ATSP-based coatings can be scaled to arbitrary levels of production and applied to parts of complex geometry – including those where line of sight to deposition device is not feasible.

Three coating techniques are demonstrated and explored: thermal spray coating, solvent-borne coating, and electrostatic powder coating. Of these electrostatic powder coating is by a wide margin found to be the preferred method and as a method has been claiming market share within extant commercial processes [120] from solvent-borne coatings due to their obvious lack of solvent and therefore ease with which they can meet VOC criteria for both workplace and finished products. Additionally powder coatings lend themselves easily towards producing a uniform coating thickness within the sample by virtue that surfaces already covered with powder screen the electrostatic field that draws powder in the first place: bare metal is more attractive to

the oppositely charged powder than that screened by already existing powder layers. The precipitation polymerization of fully cured ATSP powders was also explored as a pathway towards thermal spray is also reported here. Finally, tribological results of the various fabrication schemes are also summarized.

3.2: Synthesis of Crosslinked ATSP Powder with Controlled Particle Size

Cured Powder Synthesis

Ekonol® has been studied extensively with respect to the appropriate particle size and particle size distribution for plasma spraying. It is well known that the optimum particle size distribution for plasma-sprayed coatings is in the range of 30-100 μm. It was thought that ATSP, due to its similarity in structure and properties to Ekonol®, should exhibit a similar behavior.

To synthesize cured ATSP powders, trimesic acid (TMA), hydroquinone diacetate (HQDA), isophthalic acid (IPA), and 4-acetoxybenzoic acid (ABA) (molar ratio of 4:11:5:8 respectively) was charged into a 3-neck reactor with Therminol-66, which was continuously purged with nitrogen. The monomer mixture was stirred using mechanical stirring during the reaction. The monomers were then refluxed at 270-285 °C for 30 min. The apparatus was switched to acetic acid removal and the temperature increased to 270 °C. The reaction was carried out at this temperature until 90% of the theoretical yield of the by-product (acetic acid) was captured. The temperature was increased to 320-330 °C for the final 5 hrs. The reaction product was then filtered and washed with acetone and then finally purified using Soxhlet extraction with acetone for 24 hours. It was also found possible to instead not advance the yield of the by-product to quite the same degree and allow instead a partially cured structure. The reaction was simply

halted once 75% of theoretical yield of acetic acid was reached. All other steps remained analogous. This partially cured ATSP derived by this route was used for initial thermal spray trials which appear below.

In a 2L reactor with a total monomer concentration of 0.113g/mL and a final reaction time of 5 hours, it was found that particle size could be well-controlled with stir speed as shown in Table 3.1. Powders were filtered through progressively finer meshes and then weighed and the results expressed as a weight percentage (wt%) finer than a given mesh size. Increased stir speed yielded decreased particle size and by this method a yield of over 90% smaller than 105 μm was achieved. A 300 minute hold time at 320-330°C was as well found to be viable to produce the desired particle size distribution.

Table 3.1. Particle size distribution as determined by screening.

stir speed (rpm)	wt% finer than 250um	wt% finer than 210um	wt% finer than 149um	wt% finer than 105um	wt% finer than 74um	wt% finer than 53 um	wt% finer than 37 um
150	99.79	98.45	95.67	78.12	15.03	3.1	0.36
175	99.29	98.34	95.26	83.18	28.2	4.3	0.97
200	99.34	98.71	96.12	84.39	49.88	7.08	0.95
225	99.1	98.48	96.79	87.85	58.23	18.27	1.85
255	99.28	98.61	96.04	90.46	64.17	23.4	8.59

Figure 3.1 shows a photograph of the ATSP powder material and a scanning electron microscopy (SEM) image of the material particulates. Objective for powders for thermal spray coatings is generally assumed to be a globular, rounded morphology.

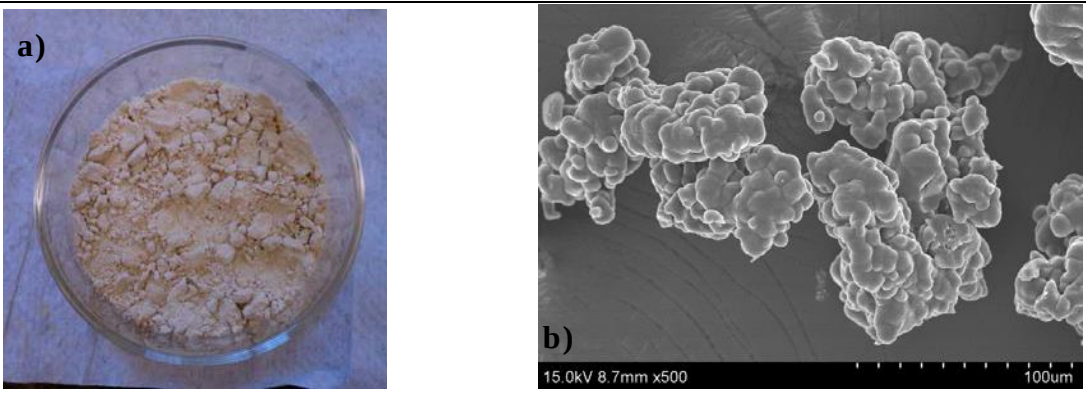

Fig. 3.1. Cured ATSP powder: a) photograph and b) SEM showing individual particulates.

3.3: Preparation of ATSP coatings

Two types of ATSP coatings, typically blended with polymeric or other additives, were prepared on metal substrates using either compression sintering or solvent casting. Additives that were examined include PTFE, polyimide, MoS_2, graphite, and mullite while the metal substrates were aluminum (Al390-T6, air conditioning compressor), cast iron (G2 Durabar, refrigeration compressor), and 304 stainless steel. All coatings were deposited on 1-inch diameter samples for tribological testing using a ball-on-disk configuration. A complete listing of all ATSP coatings fabricated at this initial stage is shown in Table 3.2.

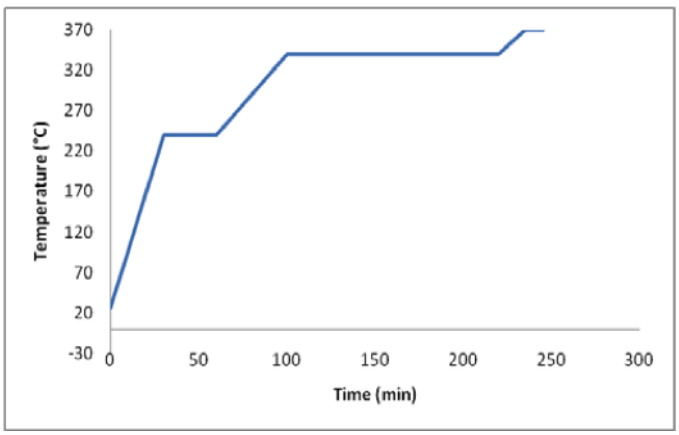

Fig. 3.2. Cure cycle for ATSP blend

Method 1: Compression Sintering

The ATSP powder and appropriate additive were mixed in a mechanical blender to ensure uniform dispersion. These powder mixtures were then sintered on the selected substrates using the cure cycle shown in Figure 3.2. Interchain transesterification reaction (ITR) was utilized to form a uniform cohesive film and, when the additive is a polymer, an adequate interpenetrating network. A pressure of 400 psi was applied at the start of the cycle and the entire cure reaction carried out under nitrogen purge.

Good quality coatings were produced however reproducibility was low. The coating thickness, measured using profilometry is 40-60 microns.

Method 2: Solution Casting

A second method, following from Zhang [105] of applying the blends was also utilized, wherein ATSP oligomers were mixed in 1.1:1 ratio of A1:C1 at 0.5 g/mL in N-methylpyrrolidinone (NMP) so that the resulting solution had a desired consistency for ease of spreading.

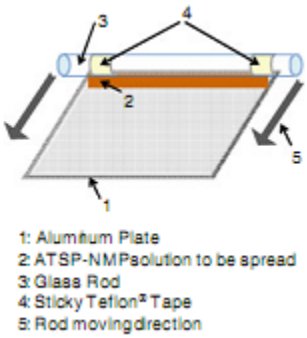

Fig 3.3. Schematic of solution casting procedure [5].

A schematic of the casting process is depicted in Figure 3 Many different permutations were tried including pure ATSP, as well as blends of ATSP with PTFE, graphite, mullite, MoS_2, PI and combinations thereof (Table 3.2).

Table 3.2. Comprehensive list of all ATSP coatings fabricated including date produced, additives incorporated, and type of substrate.

	SUBSTRATE	
Al390-T6	**G2 Durabar**	**304 stainless**
Pure ATSP	Pure ATSP	
5% PTFE	5% PTFE	
5% Gr + 5% PTFE	15% PTFE	
15% Gr + 5%		
		Pure ATSP
		5% and 15% PTFE
Compression		5% and 15% Gr
Solution Cast		5% PTFE + 15% Gr
		5% PTFE + 5% Gr
		15% PTFE + 5% Gr
		15% PTFE +5% Gr
		5% PTFE
	Pure ATSP	Pure ATSP
	5% and 15% mullite	5% and 15% mullite
	5% and 15% PTFE	5% PTFE + 5% mullite
	5% mullite + 5% PTFE	5% PTFE + 15%
	15% mullite +	1% PTFE
	1% PTFE	5% PI
	5% Gr + 5% PTFE	5% PI + 5% PTFE
		15% PI + 5% PTFE
		5%PI+5%mullite+5%P
	5% MoS_2	1% and 5% MoS_2
	5% MoS_2 + 5% PTFE	1% MoS_2 + 1% PTFE
	1% PI + 1% PTFE	5% MoS_2 + 5% PTFE
	5% PI + 5% PTFE	5% PI
		1% PI + 5% PTFE
		5% PI + 5% PTFE

3.4: Tribological Experiments

Since a large number of coatings were made using three different methods, namely (a) compression sintering (CS), (b) solution casting (SC), and (c) thermal spray (TS), we decided to perform controlled ball-on-disk experiments to screen these coatings. Such tests would readily provide coating adherence to the substrate, friction, and wear performance. Three different conditions were used, identified as "mild", "intermediate" and "aggressive" conditions, with the majority of tests performed at the intermediate conditions. Realistic compressor conditions, refer to higher speeds, but typically lower contact pressures as nominal flat (pin) on flat contact are encountered, e.g., in a scroll compressor.

Below is a photograph of the tribometer utilizing a ball-on-disk geometry, located in the tribology laboratory at the UIUC, that was used for all experiments in this subsection (Fig. 3.4). Also, shown is a photograph of a typical disk sample that carries the coating and a chrome steel sphere as the counter surface. A first set of experiments was performed at a sliding speed of 120 mm/s, a normal load of 5 N (corresponding to a contact Hertzian pressure of 75.2 MPa) for 30 min (216 m sliding distance) at ambient laboratory conditions (designated as mild testing conditions). An intermediate case increased the load to 10 N but decreased the sliding speed to 60 mm/s (108 m sliding distance) while a final severe case utilized a normal load of 10N (corresponding to a contact Hertzian pressure of 124.2 MPa)

for 30 min and returned the sliding speed to 120 mm/s.

Fig. 3.4. Photographs of tribology equipment at UIUC along with standard 1-inch diameter sample disk and ¼ inch diameter chrome steel sphere.

The best performing friction and wear data were obtained with the 5% PTFE samples using both cast iron and Al390-T6 substrates. Figure 2 shows a typical result from the Al390-T6 aluminum substrate, exhibiting "zero" wear and very stable coefficient of friction. Similar results were obtained on the G2 cast iron sample as well. The experiments were also repeatable, confirming the excellent performance of these coatings. These results are extremely promising as they show superiority over state-of-the-art commercially available polymeric-based coatings. Case in point a commercially available state-of-the art PTFE/Pyrolidone coating was tested under identical conditions and the results were very similar, namely

stable/similar friction coefficient around 0.2 and mild burnishing-no significant wear. The statement about superiority is that it is expected as shown in earlier data [5] that at higher stress levels, the ATSP coating showed significantly lower wear performance. At the more aggressive wear conditions, our CS coatings tended to flake off, indicating poor adherence to the substrates and not poor tribological performance. Higher percent of PTFE in the coating (15%) showed poorer performance. As seen before, which is somewhat counterintuitive, pure ATSP coatings exhibited high friction coefficient (0.5 and higher), wearing the chrome steel ball and yet showed no wear of the coating.

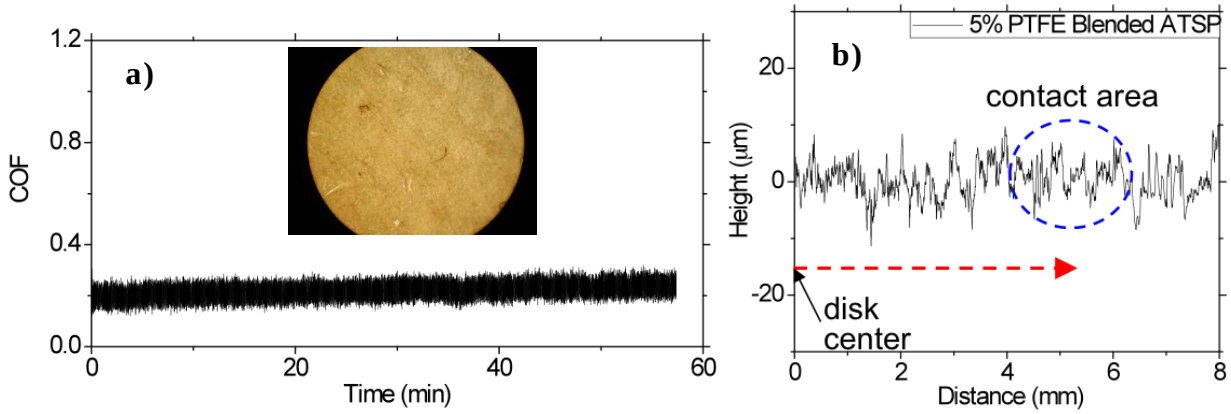

Fig. 3.5. 5% PTFE-blended ATSP compression sintered (CS) onto Al under mild testing conditions. a) Graph showing stable COF over time (inset is picture of sample disk), b) Profilometry of sample after wear test showing no material has been removed compared to baseline.

Solutions of ATSP were cast and overall, they resulted in more uniform coatings and stronger adherence to the substrates since no flaking of the coatings was

observed. The friction coefficient was similar to the compression sintered coatings, with somewhat higher wear rate in the case of 5% PTFE. Under the intermediate testing conditions as described above, the cast iron substrates were initially examined and the coatings of pure ATSP, 1% PTFE, 5% Mullite, 1%PI+1%PTFE, and 5%PI+5%PTFE failed prematurely. However, the best performing coatings were 5% MoS_2 and the 5% PTFE+5% MoS2 with wear rates of ca. 9.2 x 10^{-4} and 4.6 x 10^{-4} mm^3/Nm, respectively. The friction coefficient was steady and the lowest achieved with the 5% MoS2 coating and steady COF of 0.15 while the second best is very close with 5%PTFE+5% MoS_2. Figures 3.8 and 3.9 display the overall results of all wear tests and the corresponding coefficients of friction. In general, the wear rates are very low except when mullite is the only additive, while the presence of any mullite results in a sharp increase of the COF.

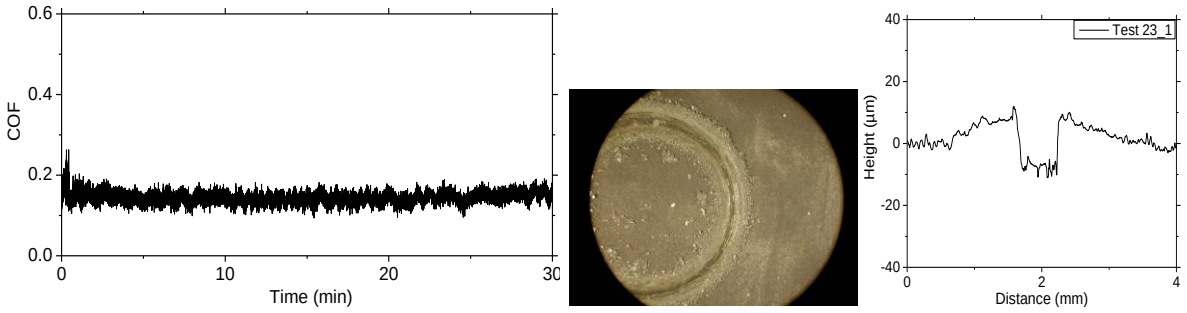

Fig. 3.6. 5% MoS_2-blended ATSP (CS) and tested at 124.2 MPa Hertzian pressure.

In addition, several disks that were coated on 304 stainless steel were tested at the intermediate wear conditions. In general, the wear data was not as high quality as

the cast iron samples and the COF was higher. The reason for the poorer performance of the stainless-steel substrates is that it is well known that cast iron possess good tribological properties and since these coatings are very thin any penetration of the coatings will result in exposure of the substrate. Further investigation as to which substrates are suitable with ATSP, and whether any optimization of the coatings could be done to improve performance with substrates such as stainless steel is needed.

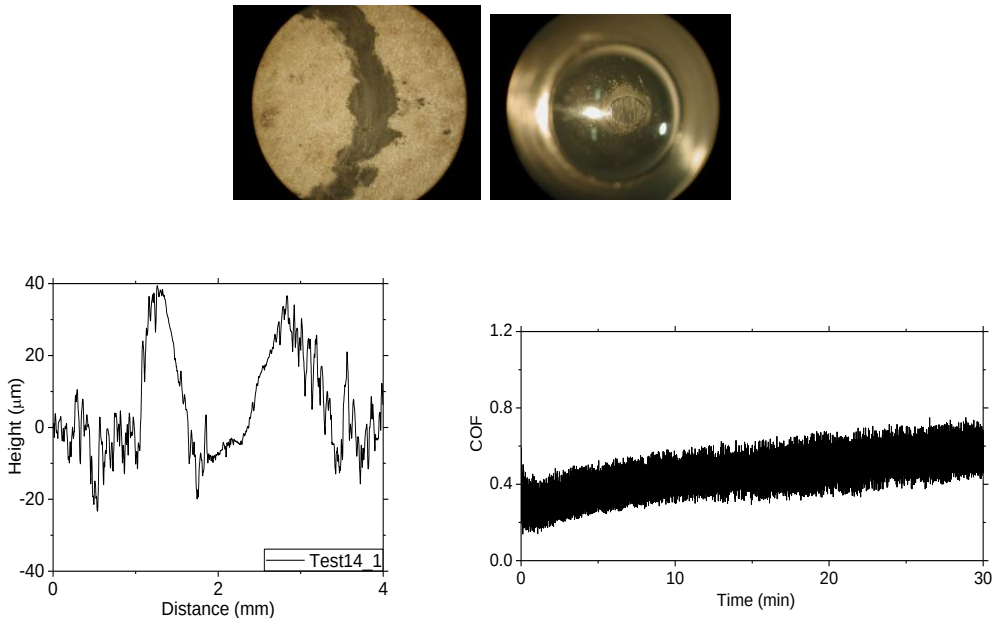

Fig. 3.7. 5% PTFE+5% Mullite blended with ATSP (CS) and tested at 124.2 MPa Hertzian pressure.

A comment is in order in regards to the performance of mullite in the ATSP coatings, which was initially unexpected. The friction coefficient is clearly high (> 0.5), it wears significantly the chrome steel ball and yet there is no measurable wear

of the coating. Instead there is material pile up as shown in Figure 3.7. Such material could be further explored in applications where a higher COF and no wear are required such as clutches and brakes.

3.5: Preliminary Thermal Spray Coatings

The primary objective for this task was to thermal spray ATSP powder onto button coupons for characterization. The goal was to generate fully coalesced coatings that exhibit minimal oxidation/degradation. In addition, key processing parameters were identified for future work that will yield improvements in coating deposition and performance.

This work was carried out with Prof. Sanjay Sampath at the State University of New York at Stony Brook in the Center for Thermal Spray Research (CTSR).

Technical Approach

Two thermal spray techniques were selected and used for deposition trials; namely, combustion spray processing and DC plasma spray processing. The combustion spray process entailed using a Terodyn 3000 gun (Messer Eutectic) to deposit the partially cured ATSP powder on 09/23/11 and the fully cured ATSP powder on 12/21/11-12/23/11. A Sulzer Metco 3MB Plasma torch with a standard 7MC console was used to generate plasma sprayed coatings on 12/22/11.

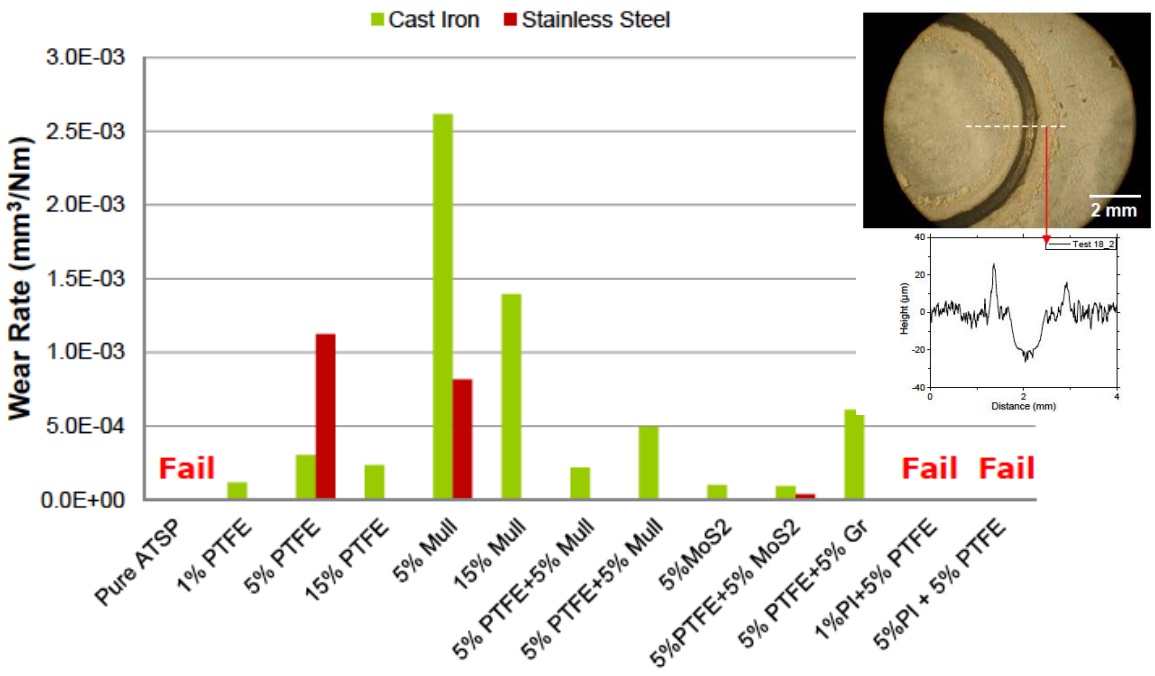

Fig. 3.8. Wear rates at intermediate testing conditions for solution cast ATSP samples. Inset shows a representative disk with a distinctive wear track and the subsequent profilometry graph used to calculate wear rate.

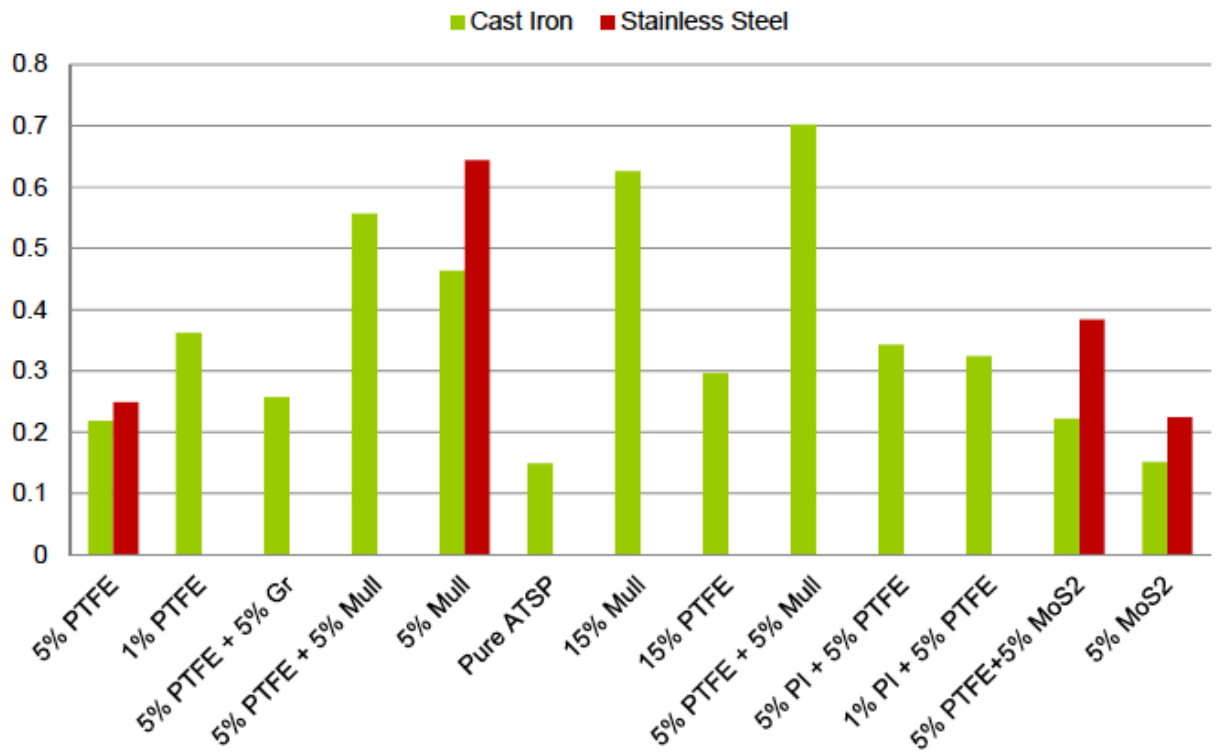

Fig. 3.9. Average COF at intermediate testing conditions for solution cast ATSP samples.

A low temperature nozzle (LT 250) was used with the Terodyn combustion gun based upon prior experience with spraying polymers. A low temperature shroud assembly was also used to cool the flame and provide a spray parameter to control the extent of particle melting. It has been determined that the shroud is integral to prevent polymer degradation in flight and can be used to vary the flame temperature. The Plasma Technique Twin 10 feeder was used to feed the ATSP powder into the oxy/acetylene flame.

A schematic of the combustion spray process is shown below in Fig. 3.8. Oxygen and acetylene are used for combustion. Nitrogen is used as the carrier gas to inject

the powder into the flame. Compressed air is used in the shroud assembly. The spray gun was mounted on a computer controlled, linear x-y traverse system. A robot was not required since only flat coupons were sprayed requiring 2-axis of motion. The traverse speed and standoff distance (distance from nozzle to sample) can be varied systematically.

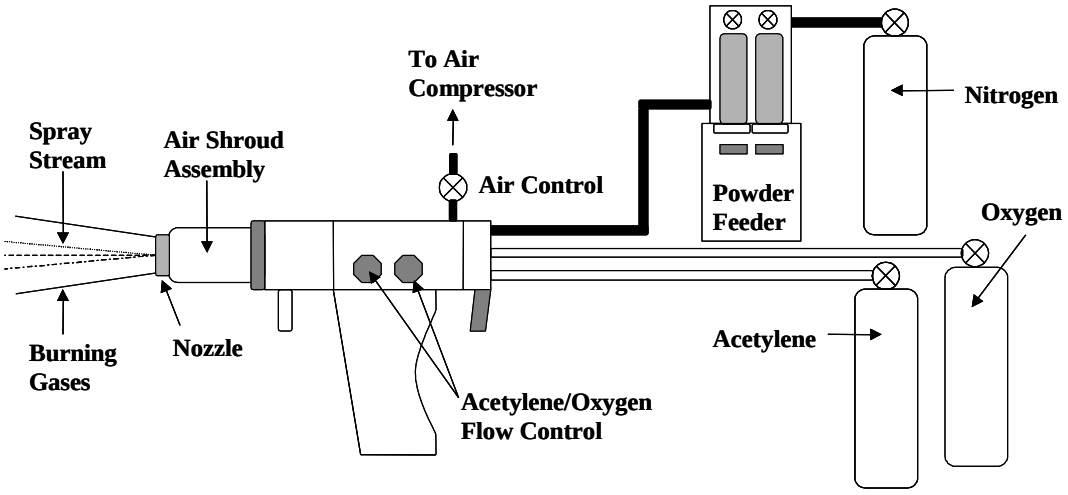

Fig. 3.10. Schematic of Eutectic Terodyn 3000 combustion spray gun.

The ATSP team evaluated the full range of parameters that are typically optimized while carrying out thermal spray studies and down-selected the first order parameters that should be studied in the first series of trials (Figure 11 outlines the first order parameters that were studied).

At the beginning of the trial day, initial studies were carried out to demonstrate that the ATSP powder could melt on a substrate surface. Initial process parameters were determined to be 275 and 325 °C by virtue of available DMA profiles at the time

[20] which suggested a potentially low enough storage modulus at that range [94]. Finally all metal substrates were suitably primed using surface grit blasting with #24 mesh alumina.

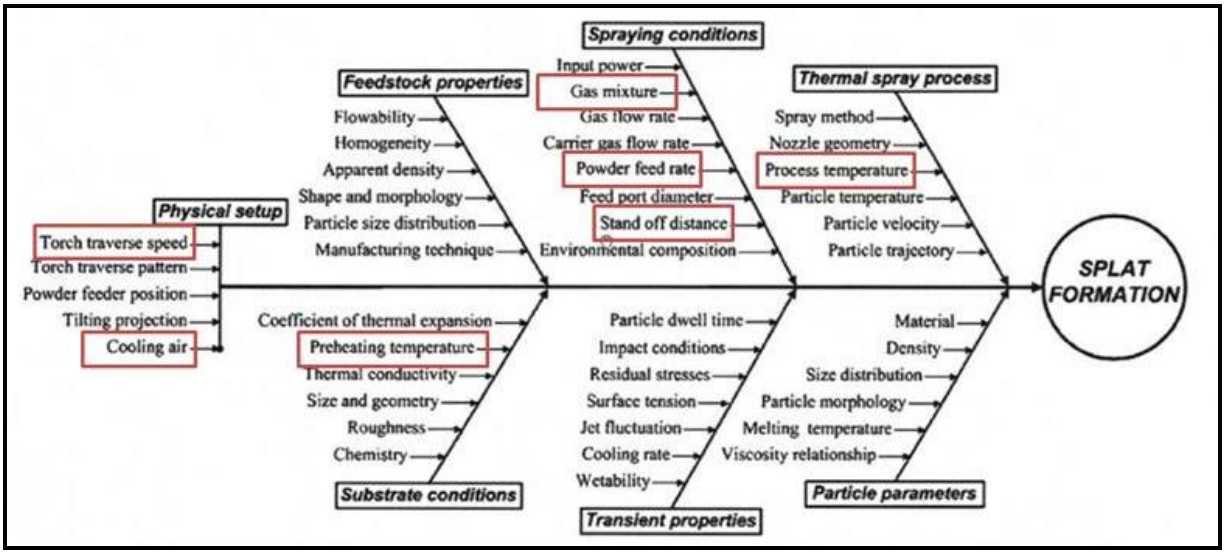

Fig. 3.11. First order parameters (outlined in red) selected to be examined in this study. Original figure from [121].

First Trial: Partially-Cured ATSP Powder

Partially-cured ATSP powder derived by solution polymerization in Therminol 66 was loaded into the Twin 10 feeder hopper and used for combustion spray trials. An initial set of parameters was chosen based on prior experience with depositing liquid crystal polymer powders. The first two samples in Table 3.3 were for the purpose of generating splats. However, very little in-flight melting occurred and the substrate pre-heat temperature was insufficient to promote splatting. Attention was then focused on generating coatings whereby additional passes of the spray torch are needed to heat the polymer during deposition. The following parameters were chosen and then varied as shown in Table 3.3 to influence flame temperature,

particle velocity, and substrate temperature. High carrier flow rates were also used to create high shear upon impact. Temperatures of the deposited coating were recorded using an infrared pyrometer with emissivity set to 0.95.

Spray Distance: 3 inches
Air Back Pressure: 60 psi
Acetylene pressure/flow: 15 psi / 15 FMR
Oxygen pressure/flow 50 psi/13 FMR
Argon Carrier pressure/flow: 4 bar / 10 FMR
Traverse Rate: 100% (2 inches/sec)

Table 3.3. Partially-cured ATSP sample summary (combustion spraying).

Sample Number	**Pre-Heat (°F)**	**Air Shroud (psi)**	**Cycles**	**Powder Wheel RPM %**	**Coating Temp (°F)**	**Thickness (mils)**	**Comment**
0923-**01**	110	60	1	5	NA.	Splats	No splats
0923-**02**	270	60	1	5	NA.	Splats	No splats
0923-**03**	250	60	3	30	450	10	Poor melting
0923-**04**	325	60	2	30	550	7	Some melting
0923-**05**	320	50	2	30	420	6.5	Poor melting
0923-**06**	320	45	2	30	500	6	Poor melting
0923-**07**	450	45	1	30	520	3	150% Traverse Speed. Some Melting
0923-**08**	450	45	3	30	520	7	150% traverse.
0923-**09**	550	45	2	30	600	5.5	Some melting
0923-**10**	550	20	1	30	>600?	2	Degraded
0923-**11**	650	None	1	30	380	1.5	No Flame – Powder Only. Coating is WHITE. Post-heated to 450F, coating turned BLACK
0923-**12**	600	50	2	30	580	5	Some Melting

The partially cured ATSP did not exhibit melt flow behavior like a traditional thermoplastic polymer. Coatings were not completely coalesced although some particle melting was observed under a stereomicroscope. At low temperatures (clear coatings), the ATSP powder does not melt uniformly, leading to a coating that is not fully reacted. The polymer is sensitive to thermal-oxidation as witnessed by the discoloration at coating temperatures above 500F. It was difficult preheating the substrate to temps above 450F and keeping the substrate at that temperature just prior to deposition due to substrate cooling effects. These first order parameters produced a wide variety of results, indicating that they are indeed the critical parameters to optimize, and also providing a processing window to be further refined. Figure 3.12 shows pictures of the 12 substrates after thermal spraying.

Fig. 3.12. Twelve coated substrates produced by varying the first order parameters.

Several of these samples were also tested under the intermediate wear conditions. Overall, they had a very high level of COF (as expected for pure ATSP coatings) and the two samples on stainless steel (0923-3 and -6) wore away quickly and the test had to be stopped prematurely. Sample 0923-11 on cast iron appeared to

perform better Test 30 is shown below: The tribological performance is as expected or better than earlier pure ATSP specimens. An additional qualitative assessment is that the coatings did not peel off by attempts to delaminate via human finger nail, indicating that adhesive strength was

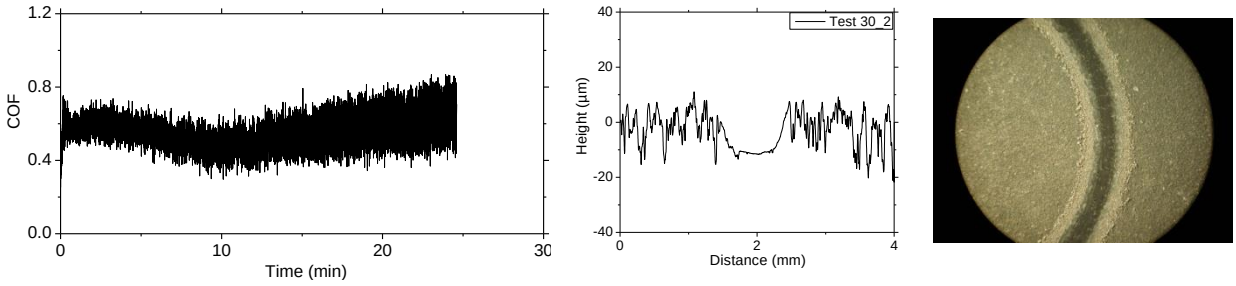

Fig. 3.13. Pure ATSP (TS) on cast iron tested at 124.2 MPa Hertzian pressure.

Second Trial: Fully-Cured ATSP Powder

The fully-cured powder was chosen for the 2nd round of spray trials. The powder was also passed through a ~60 mesh sieve to screen out any large polymer particles. Based on the initial spray trials conducted with the partially cured ATSP powder, a resistive substrate heater was implemented to maintain the high substrate temperature throughout the deposition process. The heater employs a controller based on a Type K TC input as feedback to controls the heater power. It was determined that the maximum heater setpoint was 500 °C (932F). A range of substrate heating temperatures was chosen to determine optimal heating to melt the polymer powder. The following parameters were fixed:

Spray Distance: 3 inches
Air Back Pressure: 45 psi
Acetylene pressure/flow: 15 psi / 15 FMR
Oxygen pressure/flow 50 psi/13 FMR
Argon Carrier pressure/flow: 4 bar / 10 FMR
Traverse Rate: 100% (2 inches/sec)
Powder Wheel RPM rate: 30%

Table 3.4. Fully-cured ATSP sample summary (combustion spraying).

Sample Number	**Heater Setpoint (°F)**	**Button Surface Temperature (°F)**	**Cycles**	**Thickness (mils)**	**Comment**
1222-**01**	none	70	2	17	Unmelted, color = brown
1222-**02**	392	212	2	14	Unmelted, color = brown
1222-**03**	662	302	2	9	Unmelted, color = brown
1222-**04**	932	482	2	5	Some melting, color = brown
1222-**05**	932	572	2	3	Some melting, color = black
1222-**06**	932	572	1*	3	Some melting, color = black

*50% traverse speed

The tribology of these are shown in Figure 3.14 tests 35 (sample 03) test 36 (sample 04), test 37 (sample 07), test 38 (sample (08) and clearly Sample 4 performing the best, as it did not wear the coating, despite the high friction and the ball wear

The fully-cured ATSP powder also did not exhibit traditional melt flow behavior and became dark in color due to thermal oxidation before melting occurred (comparing samples -04 to -05). The coating surface is rougher than coatings made by the partially-cured ATSP powder due to the larger powder size.

Next, a Sulzer Metco 3MB Plasma gun was used to examine the feasibility of depositing fully-cured ATSP polymer powder. A number of settings were used and 2 buttons were generated from the following parameters.

1222-**07:** GH nozzle, #2 powder port, 500 Amps/70 V, 80F Ar Flow, 15F Hydrogen Flow.

6 passes = 1 mil thickness. Coating is black. Very little deposition, most of the powder was not melted and degraded in-flight.

1222-**08:** GH nozzle, #1 powder port down stream injector, 400 Amps/70 V, 80F Ar Flow, 5F Hydrogen Flow.

10 passes = 2 mil thickness. Coating is black. Very little deposition, most of the powder was not melted and degraded in-flight.

The plasma spray trials were not successful in melting the powder and caused extensive oxidation/degradation to the ATSP powder based on the parameters chosen during that experiment. This is thought to be a consequence of the highly crosslinked cured C1A1 structure that prevented melting during thermal spray and therefore appropriate splat formation [93].

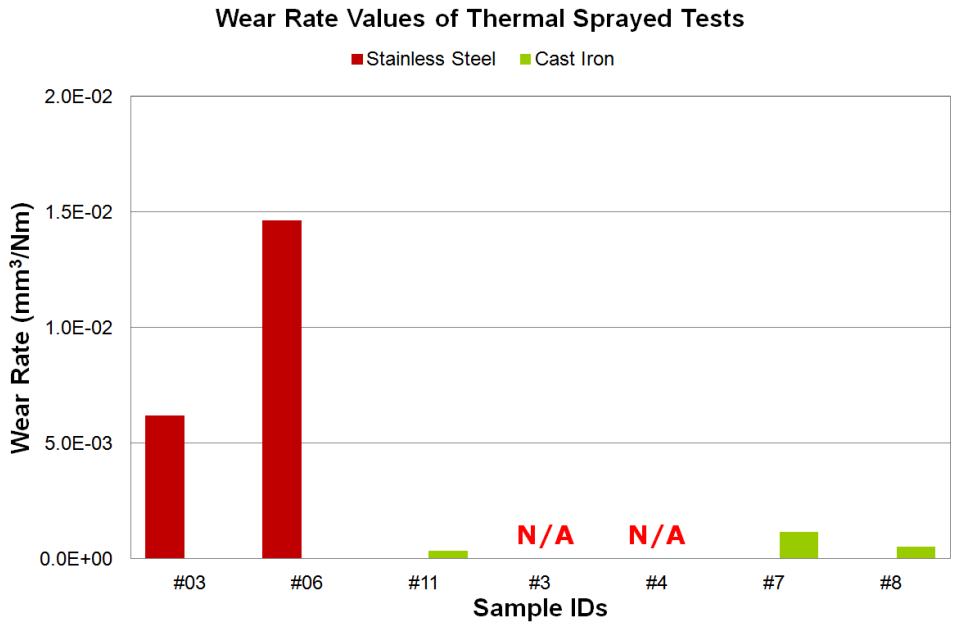

Fig. 3.14. Wear performance of several TS ATSP specimens tested at 124.2 MPa Hertzian pressure.

3.6: ATSP Thermal Spray Coatings Derived By Two-Part Oligomeric Approach

To address the deposition limitations encountered in 3.5 and improve the thermal window between melting point and degradation temperature, an alternative synthetic approach was employed. As ATSP material derived by oligomeric route was discovered during this course of development to have a superior thermogravimetric curve (Figure 3.15) than those intended to be cured powders. Powders of C2A2 and CBAB were partially cured at 230 °C and 260 °C to produce intimate blending and advance molecular weight while retaining greater melt flow during processing. The powders were designated as follows: CBAB-230, CBAB-

260, C2A2-230 and C2A2-260. Target materials were ground and wet sieved into the desired particle size range. Figure 3.15 shows the TGA analysis of the produced ATSP powders.

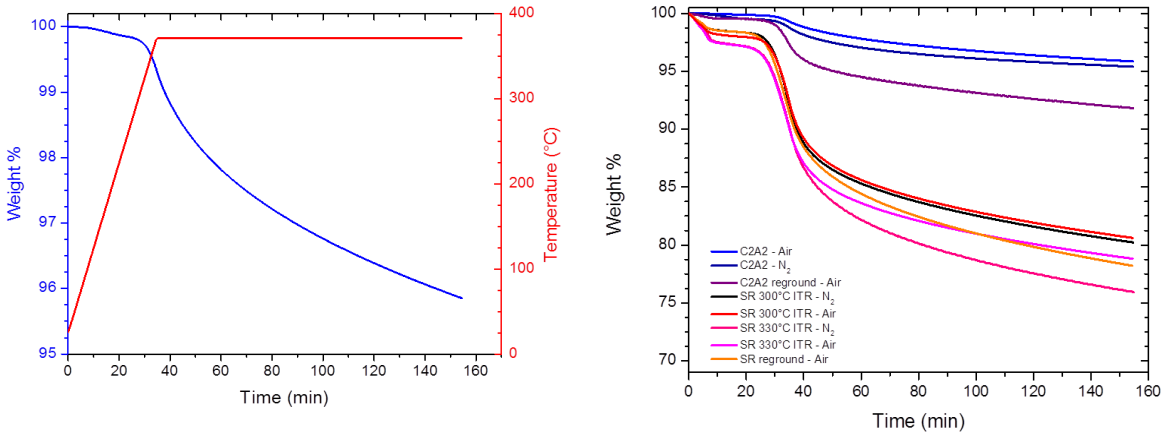

Fig. 3.15. (Top Left) Example thermogravimetric trace with temperature versus time in red and oligomer-derived C2A2 in blue. (Top Right) Comparison of melt oligomerization derived C2A2 with several conditions of cured powder synthesis under both flowing air and N_2 exposed to temperature profile at right. Powders produced via solution-suspension route are designated "SR".

It can readily be observed from Figure 3.15 that powders produced via the route used by Huang [107] and Zhang [19,20] evidence an additional 10-15% weight loss during a 371°C hold experiment.

A Beckman Coulter Particle Size Analyzer was used to measure the powder size distribution for each powder, as summarized in 3.5. The powders were all of similar size distribution and quite flowable and, thus, did not require a flow enhancer to be blended such as cabosil (silica fume).

Table 3.5. Powder size distribution summary.

ATSP Powder Designation	Mean (microns)	d10 (microns)	d90 (microns)
CBAB-230	72	36	110
CBAB-260	71	36	109
C2A2-230	65	29	105
C2A2-260	67	34	102

Mild steel coupons measuring 1”x2”x0.125” were used as substrates in the current study. All coupons were grit-blasted using 60 mesh aluminum oxide grit at 60 psi. Fixturing was set up to enable one coupon to be coated at a time using a magnetic substrate holder.

A Messer-Eutectic Terodyn 3000 gun with LT250 nozzle and low temperature shroud assembly was used to deposit the four polymer powders. It has been determined that the shroud is integral to prevent polymer degradation in flight and can be used to vary the flame temperature. Oxygen and acetylene are used for combustion. Argon was used as the carrier gas to inject the powder into the flame. The spray gun was mounted on a computer controlled, liner x-y traverse system.

An initial set of parameters was chosen based on prior experience with depositing the copolyester powders from 3.4. Both the gun traverse speed and number of spray cycles (sets of passes) was varied to influence coating temperature. Initially the intent was to vary substrate preheat temperature as well but it became evident that the supplied polymers did not require a preheat to induce melt flow. However, a butane torch was used to slightly preheat the samples to 70°C where moisture was

visibly removed from the steel substrate surface and coatings were then deposited once the steel surface measured 35°C. Surface temperatures of the steel and deposited polymer coatings were measured with a simple hand-held infrared pyrometer with emissivity set to 0.95. Pictures of the thermal spray coating deposition are shown in Fig. 3.16.

Spray Distance: 3 inches
Air Back Pressure: 60 psi
Acetylene pressure/flow: 15 psi / 15 FMR
Oxygen pressure/flow 50 psi/13 FMR
Argon Carrier pressure/flow: 4 bar / 10 FMR
Air Shroud Pressure: 45 psi
Powder Wheel RPM: 15%
Gun Traverse Rate: F Value = 500

Table 3.6. Thermal spray coating summary with process parameters and resultant coating status.

Sample Number	Pre-Heat (°C)	Traverse Rate, (%)	No. of Cycles	Coating Temperature (°C)	Thickness (mils)	Comment
CBAB-230-0	None	50	1	150	4	Practice sample – not grit-blasted. Insufficient melting
CBAB-230-1	100	50	1	210	4	Too Hot, visibly degraded
CBAB-230-2	35	50	1	175	3	Mostly coalesced
CBAB-230-3	35	50	2	200	10	Too hot, visibly degraded
CBAB-230-4	35	70	2	170	5	Mostly coalesced, rough
CBAB-230-5	35	70	2	180	5	Repeat of #4
CBAB-230-6	35	90	3	180	7	Rougher, not fully coalesced
CBAB-260-7	35	70	2	160	9	Rougher, not fully coalesced
CBAB-260-8	35	60	2	170	11	Rougher, not fully coalesced
CBAB-260-9	35	50	1	175	7	Mostly coalesced
CBAB-260-10	35	50	1	170	6	Repeat of #9
C2A2-230-11	35	70	2	200	7	Fully Coalesced, glossy
C2A2-230-12	35	70	2	190	7	Repeat of #11
C2A2-230-13	35	50	1	165	4.5	Fully Coalesced, glossy
C2A2-230-14	35	50	1	170	4.5	Repeat of #13
C2A2-230-15	35	50	1	170	4.5	Repeat of #13
C2A2-260-16	35	50	1	165	5	Fully Coalesced, glossy
C2A2-260-17	35	50	1	170	5	Repeat of #16
C2A2-260-18	35	50	1	170	4.5	Repeat of #16
C2A2-260-19	35	50	1	160	5	Repeat of #16
C2A2-260-20	35	70	2	175	7	Fully Coalesced, glossy

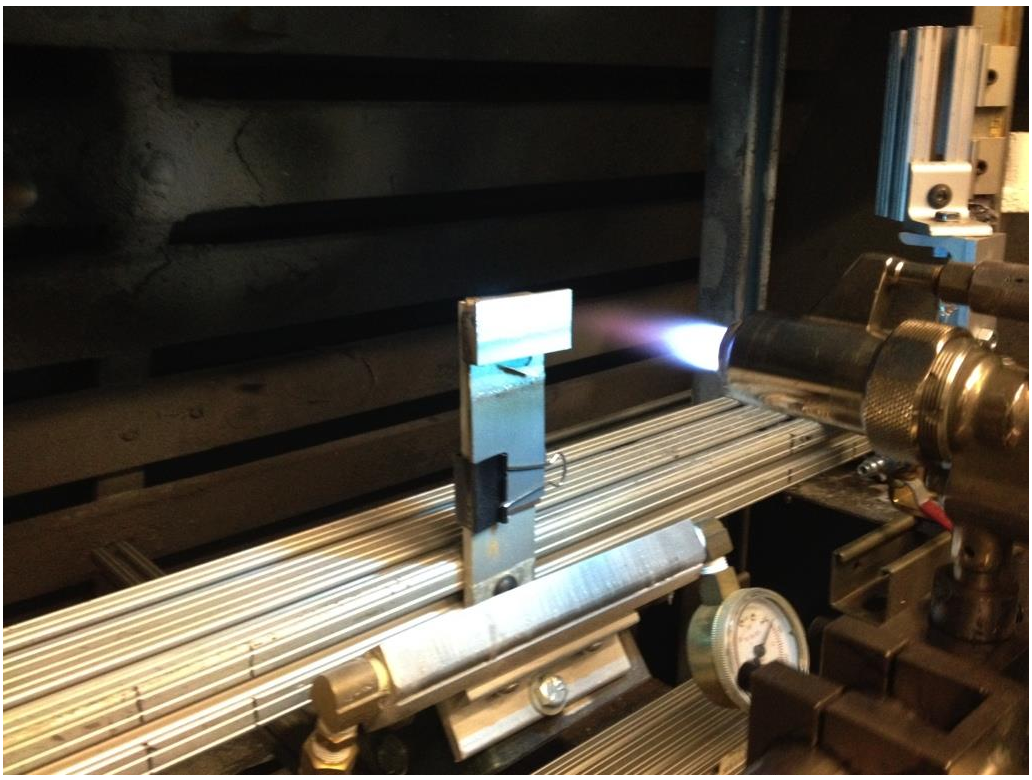

Fig. 3.16. Thermal spray deposition of ATSP copolyester powder onto steel coupons.

The CBAB-230 was the first powder used for establishing gun traverse rate and substrate preheat parameters. It was quickly observed that the new ATSP supplied powder had greatly improved melt flow compared to the powders used during the initial trials in 3.4. The powders did not require a pre-heat to induce melt flow. When the substrates were preheated to 100C, the coating got too hot as evident from the discoloration and visible degradation. A small processing window exists whereby coatings deposited around 175C were not fully coalesced yet coatings deposited around 200C were thermally degraded without being completely coalesced. It should be noted that the coating temperatures recorded by the infrared

pyrometer are approximate since the coating cools rapidly upon deposition but an attempt was made to record the coating temperature in a consistent manner immediately upon completion of the last spray pas. Traverse speed and number of spray cycles were varied to improve melting and maintain a thickness ~125 μm.

The CBAB-260 exhibited slightly less melt flow than the CBAB-230 powder. The same parameters for sample number CBAB260-7 were used as CBAB230-4 however, the CBAB260-7 was slightly rougher and less melted.

The C2A2-230 powder was deposited using the same 70% speed/2 cycles as noted above and resulted in a completely coalesced, glossy coating. Further parameter optimization resulted in decreasing the speed to 50% and depositing the coating in 1 cycle of passes, yielding a thickness of approximately 125 μms as measured with a micrometer. Coating temperatures measured ~ 170-180°C for the fully coalesced, glossy coatings. Similar results were also obtained for the C2A2-260 powder, yielding a fully coalesced coating.

3.7: Refinement of solvent-borne coating deposition

As one possible pathway towards practical deposition of ATSP coatings on inorganic substrates for tribologically-relevant polymeric coatings, solvent-borne deposition was explored more systematically after initial positive results shown above in 3.2 and 3.3 although it was necessary to greatly refine the process. It was

known in several instances of prior literature [43,51,105] that ATSP oligomers may be dissolved in NMP (n-methylpyrrolidone) and this was employed above. However, it was not clear that this was the ideal solvent for every situation. A range of available laboratory solvents were evaluated to determine which could solvate ATSP oligomers via a screening trial at 0.15 g/mL. For solvent-borne coatings, a higher concentration is better for the necessity of building a sufficiently thick dry coating layer. Deposition at lower concentration would require a very thick layer of solution which would preclude effective deposition on complex parts or vertical surface.

Solvents were acquired from Alfa Aesar and used without further treatment. C1A1 and C2A2 oligomer sets were prepared at a 1.1:1 mass-basis carboxylic acid-capped to acetoxy capped ratio. 1.5 grams of mixed oligomers were added to 10mL of solvents in a PTFE-capped 20mL scintillation vial and stirred by magnetic stirring either at 70°C or at 10°C below their boiling point (whichever was lowest) for 4 hours. The results are summarized in Table 3.7. Generally it was found that aprotic polar solvents were compatible with ATSP oligomers with 1,4-dioxane providing the only positive exception.

One obvious defect that was observed in early coatings of ATSP derived from the examined solvents was that low boiling point solvents tended to readily produce blisters on films of ATSP especially at higher oligomer loading concentrations. Solutions of 0.15g/mL C1A1 in compatible solvents were deposited onto articles of

scrap aluminum 6061 and cured under vacuum with a temperature cycle ramping 1°C/min to 330°C. Coatings were subsequently examined for blistering, which is the formation of either raised bubbles or depressions on a polymer coating. Blistering was found to decrease with increasing solvent boiling point with solvents that boil below 160°C generally found to cause blistering in ATSP coatings regardless of flash off process in coatings thicker than 5 μm. This is illustrated in Figure 3.17, with decreasing blistering associated with increasing solvent boiling point. Additionally, solutions of arbitrary concentration were found to be capable of producing blister-free coatings given a long enough flash off, however a blister-free flash off in less than 2 hours required either a solution concentration of <0.30 g/mL or a thickness lower than is typically found in tribological polymer coatings.

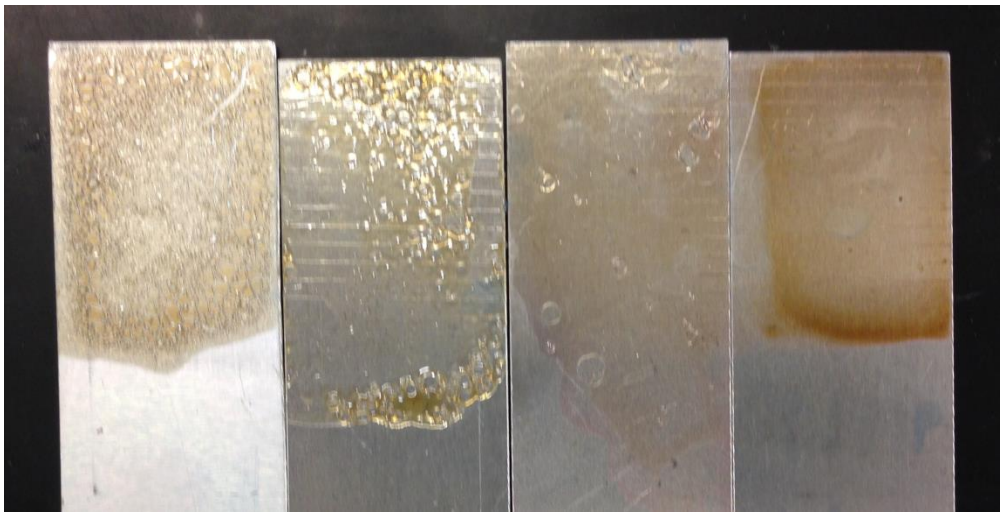

Fig 3.17. Coatings of 0.15 g/mL C1A1 oligomers in solvent. Solvent used from left to right: tetrahydrofuran, 1,4-dioxane, dimethylformamide, n-methylpyrrolidone in ascending boiling from left to right.

As described above, a wide assortment of reinforcing and lubricating are generally used in modern solid lubricant coatings. To 10 mL of dimethylformamide, dimethyl was added 0.075 g of available additives (equivalent to 5wt% of 0.15g/mL ATSP solutions commonly used in solve spray process). These included both DuPont's Zonyl® line of PTFE and select inorganic additives (aluminum silicate, molybdenum disulfide, and graphite). Results are summarized in Table 3.8. The 20 mL scintillation vials containing the solvent and additive were then shaken vigorously by hand for 60s and interaction of solvent and additive observed by eye. The Zonyl line of additives was chosen due to its small particle size in comparison to the Teflon® particle size ranges. A table of relevant properties of Zonyl based coatings is available in [109].

It was found that inorganic additives settled at the bottom of the scintillation vial in general conformation to Stoke's law on a time-basis by means of a stop watch as measured by eye and evidenced wetting in all of the three down-selected solvents. With guidance from tribological results above indicating that 5wt% concentration of PTFE resulted in the lowest COF and wear rate, solutions utilizing Zonyl MP1100 as it produced the lowest degree of agglomeration and dispersed well in high boiling point polar aprotic solvents. A proposed mechanism for this distinction is that Zonyl MP1100 and several others demonstrating at least mediocre dispersion within NMP are actually produced by first polymerizing a full molecular weight (1-4 * 10^6 g/mol) grade of PTFE which is then irradiated by electron beam under either an air or CO_2 atmosphere [109] which results in the presence of carboxylic acids as

functional end caps. This also significantly reduces the molecular weight of the product down to 0.5 * 10^6 g/mol. The bare presence of the COOH is thought to give it significantly more interaction with polar solvents in comparison to full MW PTFE examined such as Saint-Gobain's Norton® grade with a MW of 1*10^6 g/mol MW.

Solvated oligomer viscosity of neat oligomers or 1.1:1 matched sets in NMP was conducted a Cole-Parmer 98936 spindle-type viscometer with a LV-4 spindle at 60 rpm. Results are summarized in Figure 3.19. It was found that the COOH-capped oligomers created an increase in viscosity relative to the acetoxy-capped oligomers of similar configuration. This is likely straightforwardly due to the hydrogen bonding afforded by the carboxylic acids. An additional curious effect was found in the far higher viscosity of the C2 oligomer at 0.30 g/mL as compared to the C1 oligomer at the same concentration and a non-linear temperature dependence. The C2 oligomer actually possesses far less hydrogen bonding per unit mass (number of carboxylic acids per number average molecular weight – 0.0016 g^{-1}) versus the 0.0021 g^{-1} for C1. Additionally, the softening point determined by Frich [48] for C2 is nearly 30°C lower than that of C1. A clue might be found in the similar temperature dependence, though quantitatively lower viscosity found in A2. Both C2 and A2 had previously been found to evidence a nematic liquid crystalline phase. Unfortunately, a detailed causal mechanism has not been determined for this pattern of behavior. Another interesting phenomena is the viscosity profile of the mixed oligomers at 0.30 g/mol with temperature. As can be seen in the lower plots of Figure 3.19, the viscosity of C2A2 now largely loses its temperature dependence

below 50°C while the same conditions for C1A1 now has an entirely linear (with temperature) viscosity profile. A more detailed investigation with more variances in temperature, concentration, oligomer MW, COOH-concentration, neat un-solvated oligomer rheology, and LC-phase behavior would be necessary to understand the underlying mechanism.

At this point, trial coatings of ATSP were employed using an industrially relevant deposition device, namely a high volume/low pressure (HVLP) paint spray gun. The specific device was a Central Pneumatic 46718 HVLP touch up spray gun with a 120 mL top-fed cup size and a 0.8 mm adjustable nozzle.

Specimen substrates were first grit-blasted via 60 psi of compressed air carrying 40 mesh (400 μm) alumina grit. Specimen substrate for tribological testing were generally gray cast iron G2 Durabar in a 3” diameter disk with 4 beveled screw holes for implementation into a tribotest platform which will be discussed in section 3.9.

Table 3.7. Summary of ATSP oligomer solubility in assorted laboratory solvents. Boiling point (BP), density, dielectric constant and dipole moment obtained from [92].

Solvent	Structure	Class	BP (K)	Density (g/mL)	Dielectric constant	Dipole moment (D)	Miscible C1A1 to 0.15 g/mL	Miscible C2A2 to 0.15 g/mL
acetic acid		Polar, Protic	391	1.049	6.20	1.74	✗	✗
acetone		Polar, Aprotic	329	0.791	21.00	2.88	✗	✗
chloroform		Non-polar	334	1.483	4.81	1.04	✗	✗
1,2-dichloroethane		Non-polar	357	1.253	10.50	1.80	✗	✗
dimethylformamide		Polar, Aprotic	425	0.948	38.00	3.86	✓	✓
dimethylacetamide		Polar, Aprotic	438	0.937	37.78	3.72	✓	✓
dimethylsulfoxide		Polar, Aprotic	462	1.100	48.00	3.96	✓	✓
1,4-dioxane		Non-polar	374	1.033	2.30	0.45	✓	✓
ethanol		Polar, Protic	351	0.789	24.55	1.69	✗	✗
ethyl acetate		Polar, Protic	350	0.894	6.02	1.78	✗	✗
methyl ethyl ketone		Non-polar	353	0.805	18.51	2.76	✗	✗
n-methylpyrrolidone		Polar, Aprotic	475	1.028	32.20	4.09	✓	✓
pyridine		Polar, Aprotic	388	0.982	12.40	2.69	✓	✓
tetrahydrofuran		Polar, Aprotic	339	0.886	7.50	1.75	✓	✗
xylenes		Non-polar	~411	0.860	2.2-2.6	0.07-0.45	✗	✗
toluene		Non-polar	384	0.867	2.38	0.36	✗	✗
water		Polar, Protic	373	1.000	80.00	1.85	✗	✗

Table 3.8. Summary of additive suspensions in DMF, DMAc, and NMP. Suspensions were characterized based on tendency to accumulate at meniscus (↑) or bottom of scintillation vial (↓) and the degree of agglomeration was rated 0 to 5 with 0 being no visible macro agglomerates, 3 being a tendency towards a clear solution and up to mm-scale agglomerates, and 5 being instant clearing and up to cm-scale agglomerates.

	DMF		DMAc		NMP	
Additive	Accumulate ↑↓	Agglomerates (0-5)	Accumulate ↑↓	Agglomerates (0-5)	Accumulate ↑↓	Agglomerates (0-5)
Zonyl TE5069AN	↑	2	↑↓	2	↑	3
Zonyl MP1000	↑	4	↓	2	↑	4
Zonyl MP1100	↓	1	↓	0	↓	2
Zonyl MP1200SZ	↑	4	↑	4	↑	4
Zonyl MP1300	↑	4	↑	4	↑	4
Zonyl MP1500	↑	5	↑	5	↑	5
aluminum silicate	↓	0	↓	0	↓	0
MoS_2 (<2μm)	↓	0	↓	0	↓	0
graphite (44μm)	↓	0	↓	0	↓	0

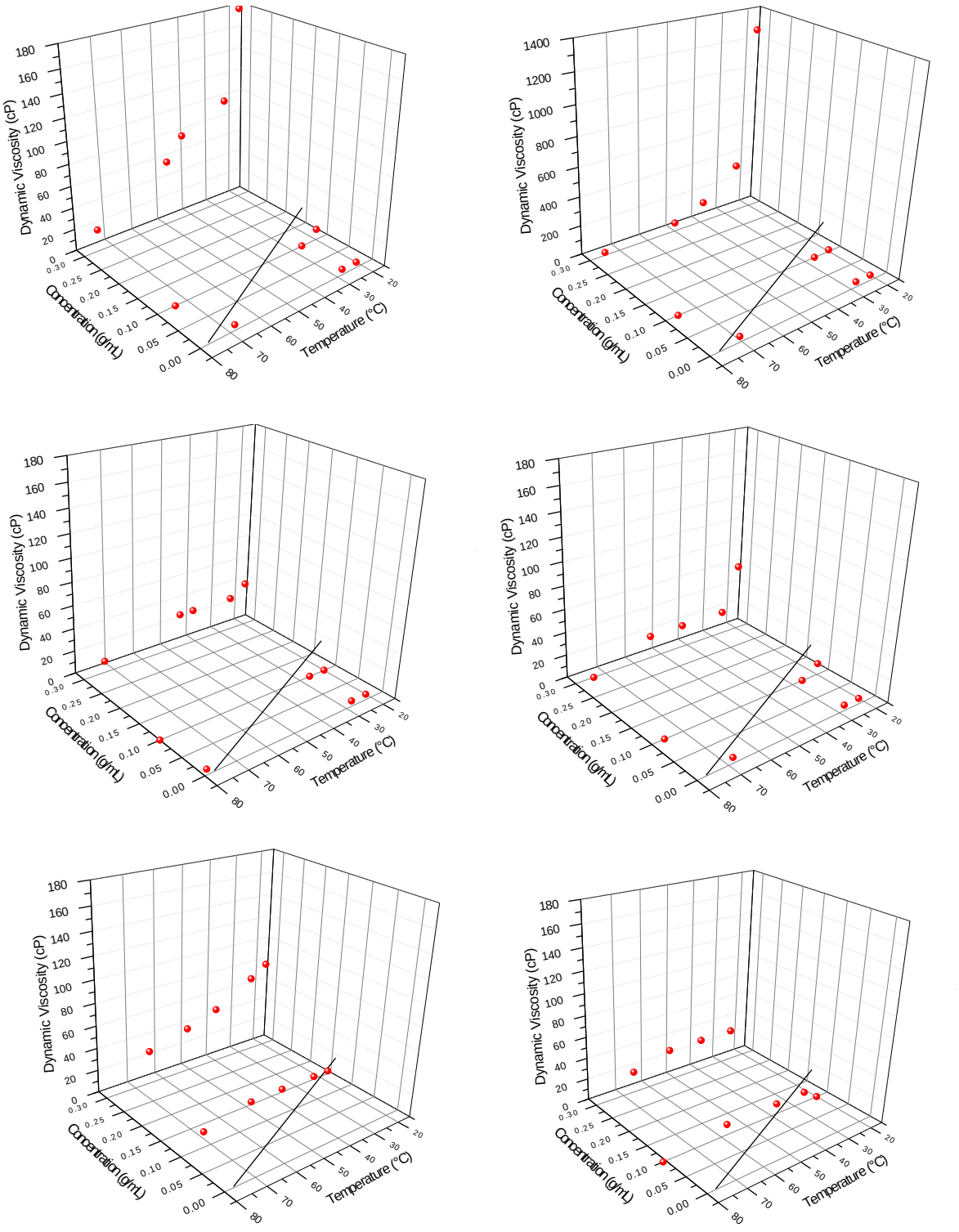

Fig. 3.18. Oligomer viscosities by spindle-type viscometer with temperature and concentration. (Top Left) C1, (Top Right) C2, (Middle Left) C1, (Middle Right) A2, (Bottom Left) C1A1, (Bottom Right) C2A2.

Figure 3.19 demonstrates what happens if a PTFE grade that does not disperse well in its solvent versus adequate dispersion. 0.30 g/mL of various ATSP oligomer/5wt% MP1100 in NMP generally remained dispersed indefinitely with mixture solidification occurring on the time-scale of weeks being the main mechanism of non-performance. All solvent-borne coating was generally conducted at 0.30 g/mL with the mixture warmed to 70°C. Figure 3.20 demonstrates an example roughness and thickness scan by Dektak-type profilometer with 1 µm conospherical tip on C1A1/5wt% MP1100. Table 3.9 contains a listing of surface roughnesses of various tradename coatings marketed for tribological performace.

Fig. 3.19. (Left) C1A1/5wt% TE5069AN deposited by HVLP on G2 Durabar substrate. (Right) C1A1/5wt% MP1100 deposited by HVLP on G2 Durabar substrate. The blue tape is used as a negative to establish coating thickness.

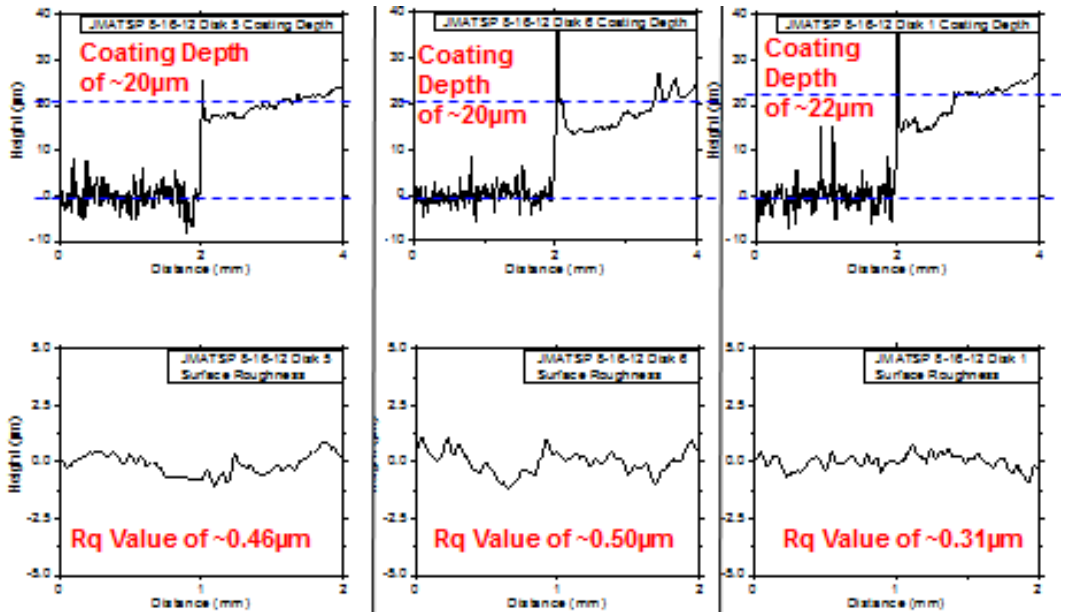

Fig. 3.20. Example roughness and coating thickness scans for batch of C1A1 / 5wt% MP1100 coatings deposited from a 0.30g/mL solution on roughened G2 Durabar substrate. Roughness step established by use of tape layer as negative.

Table 3.9. Tradename coatings marketed for tribological properties, their abbreviated names used here and in some prior literature on coating tribological performace and their R_q surface roughnesses.

Coatings (Spray-coated)	***R_q* (µm)**
DuPont® 958-303 (PTFE/Pyrrolidone-1)	2.28 (0.09)
DuPont® 958-414 (PTFE/Pyrrolidone-2)	0.61 (0.08)
Whitford Xylan® 1052 (Resin/PTFE/MoS_2)	1.71 (0.07)
Fluorolon® 325 (PTFE/MoS_2)	1.14 (0.05)
Impreglon® 218 (Fluorocarbon)	1.53 (0.15)
1704 PEEK/PTFE® (PEEK/PTFE)	1.00 (0.03)
1707 PEEK/Ceramic/PTFE® (PEEK/Ceramic)	0.92 (0.05)
Gray Cast Iron (Dura-Bar® G2) Substrate	0.3 ~ 0.5
Shoe and Pin	0.03~0.04

Coating thickness was also established via scanning electron microscopy (SEM) as shown in Figure 3.21. SEM imaging was generally conducted by Hitachi S4700 unless otherwise noted. The cross-section image in Figure 3.21 is also notable in that the cross-sectioning was performed by band-saw and as can be seen, there was no delamination at the substrate-coating interface, which indicates good adhesion to the substrate.

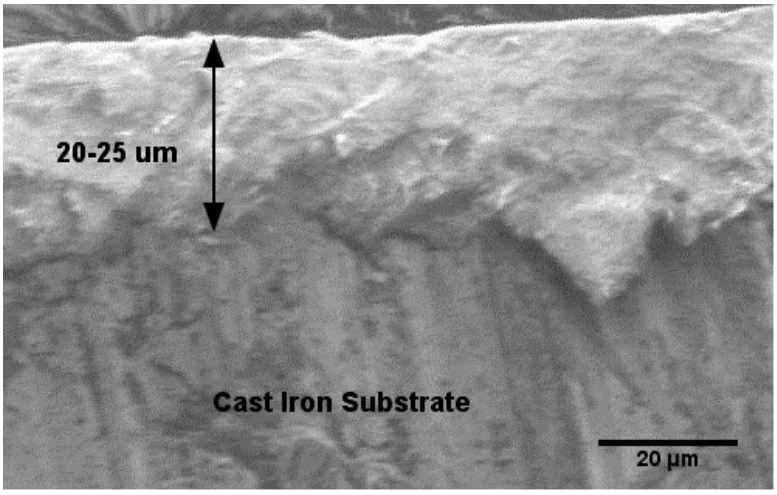

Fig. 3.21. SEM cross-section image of C1A1/5wt% MP1100 ATSP coating on G2 Durabar substrate. Coating thickness of 20-25 µm is demonstrated. Hitachi S4700 with acceleration voltage of 3 kV and working distance of 10 mm was used at a magnification of 450X.

The coating process demonstrated here was very flexible in terms of oligomer structure that could be used as feedstock for the coating. All of the original Frich and Economy [4] oligomers that have been examined to date are soluble in NMP to

at least 0.15 g/mL. It appears at least that below 2000 g/mol molecular weights this rule holds

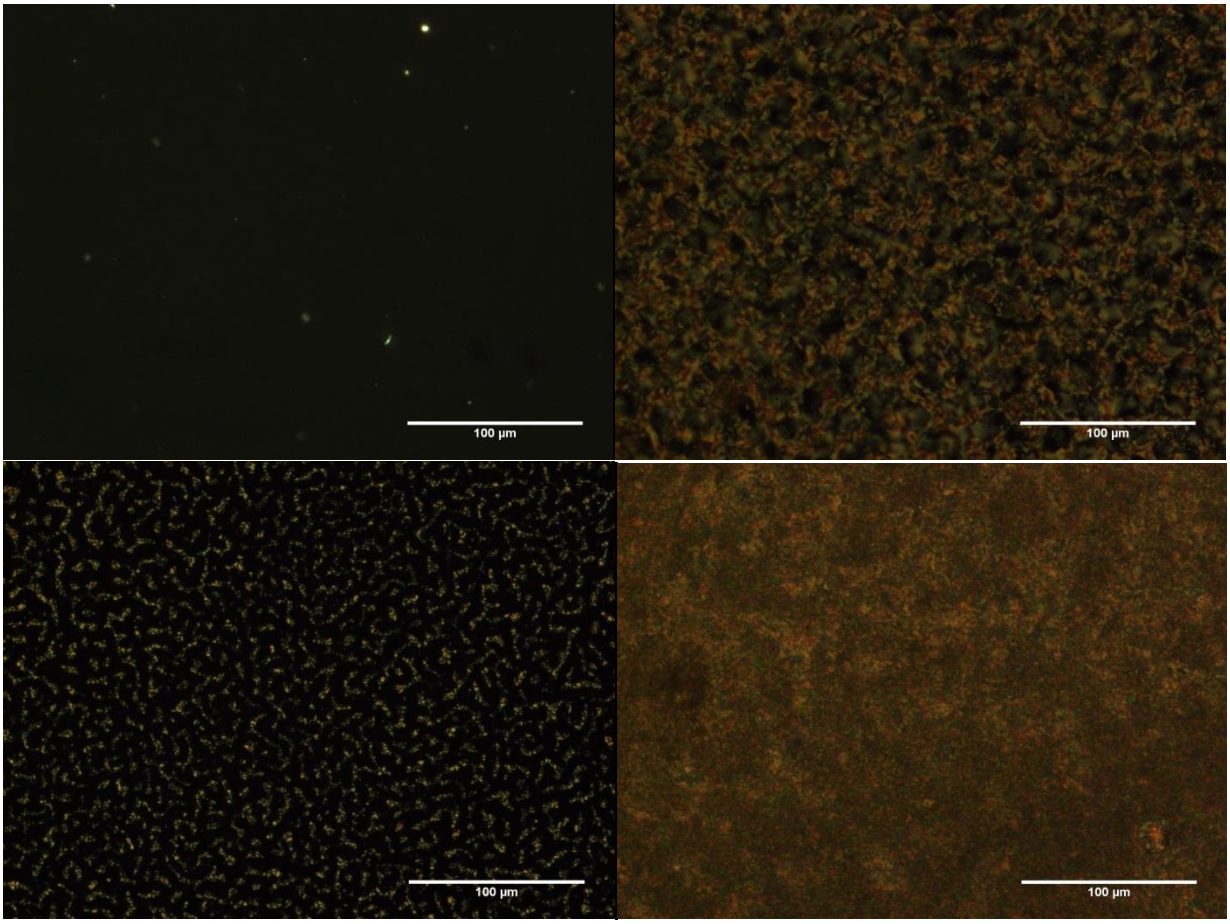

Fig. 3.22. Solvent-deposited cured ATSP coatings under cross-polarized transmitted light. (Top Left) C1A1, (Top Right) C1A2), (Bottom Left) C2A1, (Bottom Right) C2A2. All samples were 20 µm in thickness.

almost regardless of monomer unit including for oligomers bearing PFSA as a backbone unit. Oligomer structure has had substantial impact on coating microstructure and, as will be shown later, both coating micro- and macro-tribological properties. Figure 3.22 demonstrates the shift from amorphous to liquid-crystalline oligomer-based coatings and the apparent preservation of the

birefringence from into the cured structures. C1A1 demonstrates a completely amorphous structure while C1A2 and C2A1 show a phase segregation between amorphous and ordered regions. C2A2 possesses a fully birefringent morphology. Specific identification of ordered phase type may yield additional insight.

A C2A2 film was cast onto a glass slide and then the glass slide broken such that the film broke in tension at room temperature. This was examined via SEM as shown in Figure 3.23. Interestingly, this demonstrated substantial fibrillation at some domain orientations and brittle fracture at others. C2A2 sample shown in Figure 3.22 has a lower thickness than that of 3.23 and so the domains of 3.23 have a relaxed growth constraint and can grow to a larger length scale.

In addition to other experimental evidence towards ITR as a chemical process relevant to reordering and adhesive bonding, an interesting phenomena was observed (as shown in Figure 3.24) when a 50 μm C2A1 coating was observed on a glass slide after having been cured to 270°C for 30 minutes in a convection oven– which at this cure condition is already a crosslinked solid well below its glass transition temperature and which at no temperature evidences melting. After applying another 3 hours of cure at 330°C, we see an entirely different morphology within the same sample, from an “oil-in-water” phase segregation to a far more “spider web” morphology. This change in microstructure appears to be an entirely solid-state phenomena that proceeds via ITR.

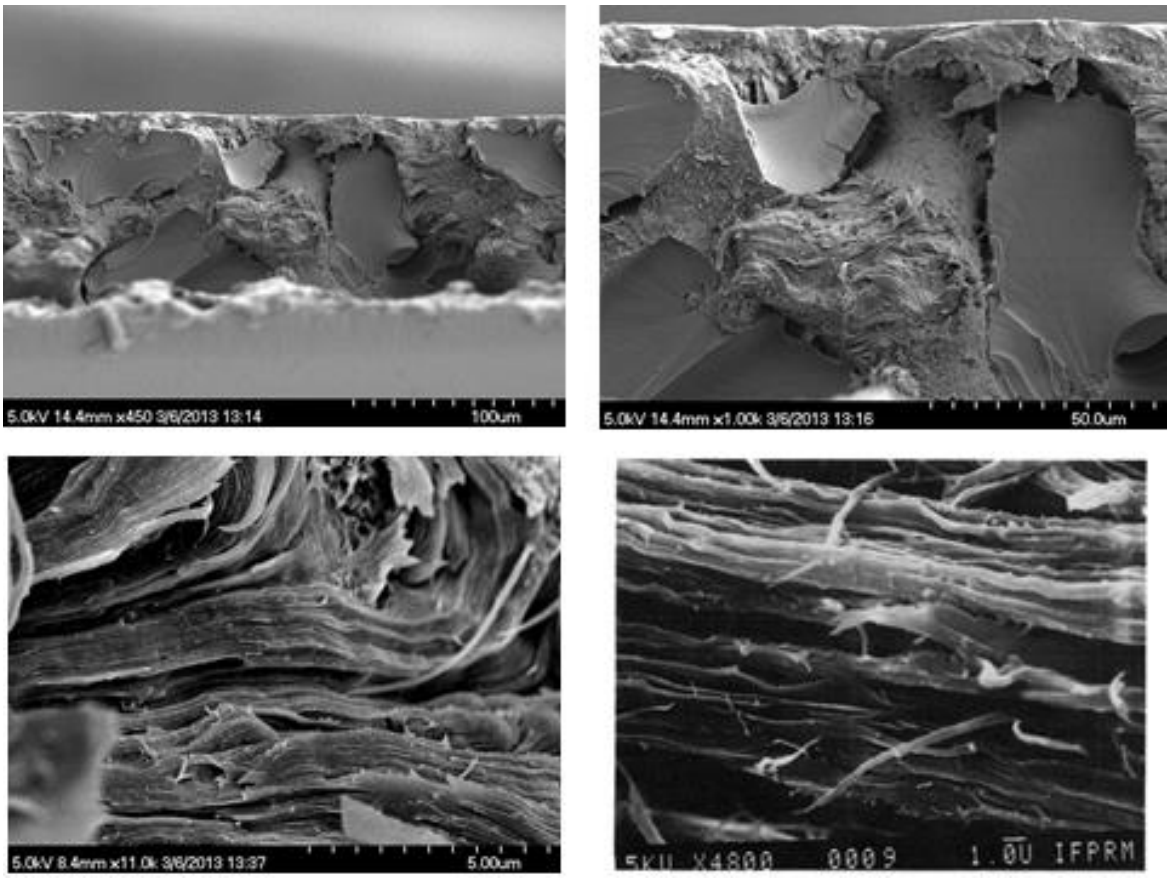

Fig. 3.23. (Top Left, Top Right, Bottom Left): SEM images of fibrillized region of C2A2 coating under increasing magnification. (Bottom Right) Surface of commercially-produced aromatic polyester Vectran fiber exhibiting similar morphology [2].

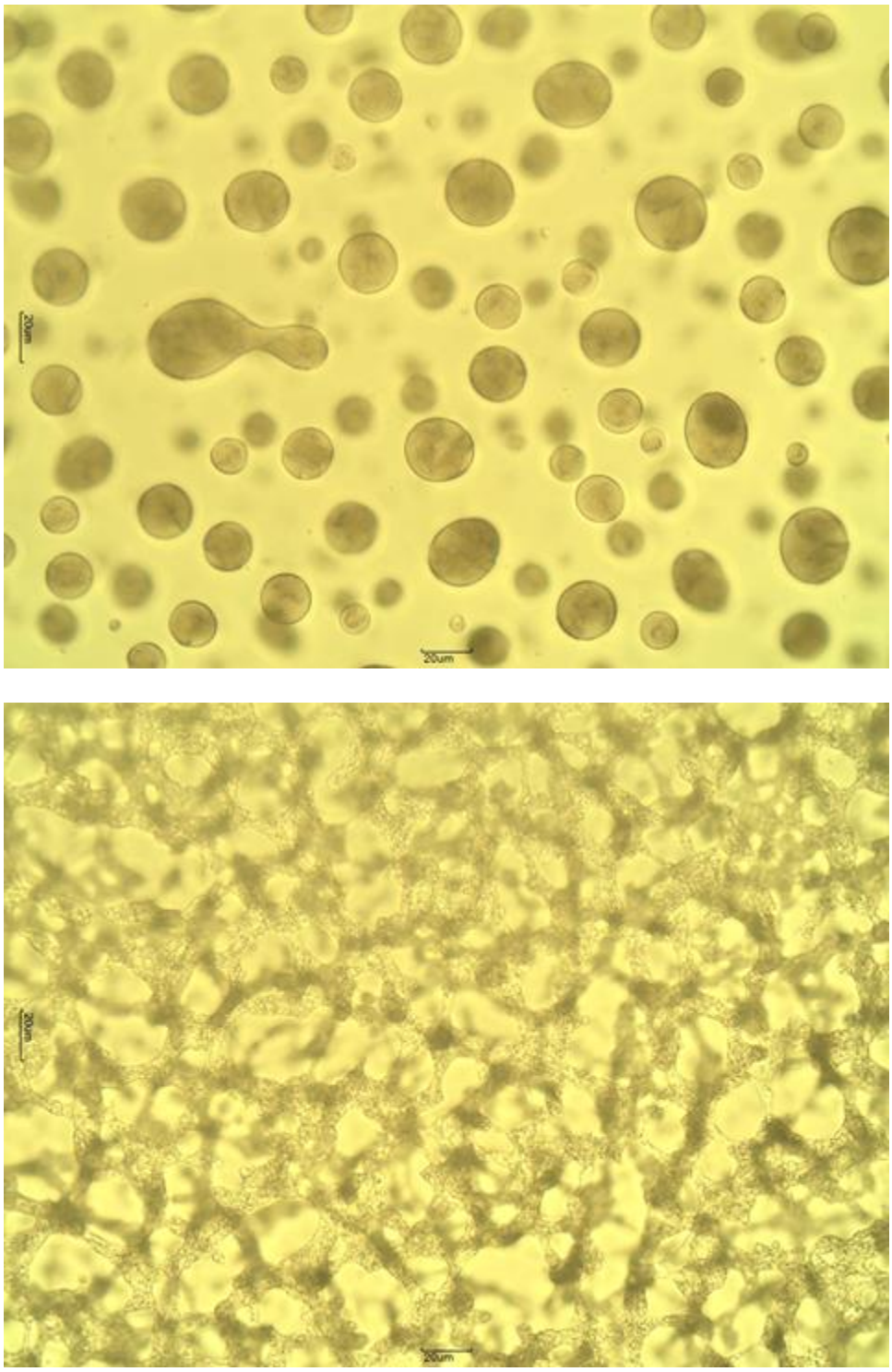

Fig. 3.24. The same 50 μm thick neat C2A1 film after (Top) 270°C, 30 min cure and (Bottom) an additional 330°C, 3 hour cure cycle.

3.8: Development of an electrostatic powder coating scheme for ATSP

To obviate the need for NMP, another coating pathway was examined. An initial trial was conducted wherein uncured CB and AB oligomer powders ground via a Col-Int Tech Laboratory Grinder and then sieved through a 90 μm screen via shaker table were blended at a 1:1 mass ratio and simply smeared across a roughened stainless steel substrate. The samples were placed into a convection oven heated to 250°C for 10 minutes and then removed. The oligomers had obviously melted and were adherent to the roughened substrate and passed the finger-nail test and otherwise indicated that they had acceptable adhesion.

Having passed that initial screening, a Gema bottom-fed electrostatic powder spray gun was used to produce a stream of positively-charged powder which was then picked up by a negatively-charged conductive plate. A 200V charge was utilized to build the uncured coating layer in all subsequent experiments. Here again CBAB powder at a 1:1 ratio, ground, and sieved through a 90 μm screen (representative particle size distribution shown below obtained by image analysis of transmitted light micrographs of dispersed powder).

Bin	Frequency
1	208
2	411
5	1124
10	542
20	159
40	38
Larger	4

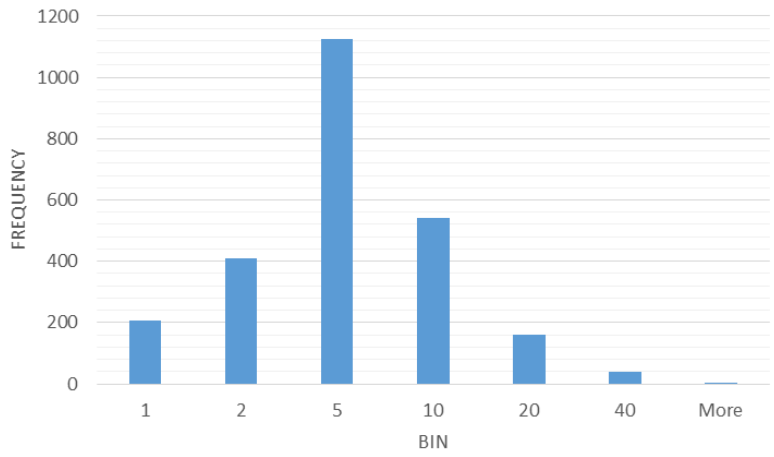

Fig. 3.25. Representative particle size distribution of ground CBAB powder.

Subsequent to electrostatic powder deposition, panels shown in Figure 3.26 were hung from a hook inside a convection oven and allowed to melt at 230°C. Resulting coating thicknesses as measured by magnetic coating thickness gauge (Reed Instruments CM-8822) are shown in Figure 3.27. It can be noted that the electrostatic powder coating experiment produced a glossy surface that easily passed the fingernail test on all panels, including unroughened panels. Figure 3.27 shows the cure cycle employed on all electrostatic-powder deposited coatings except where noted otherwise. For powder-coated samples, the cure cycle shown on Figure 3.28 in a Thermo-Fisher convection oven was used except where specified otherwise.

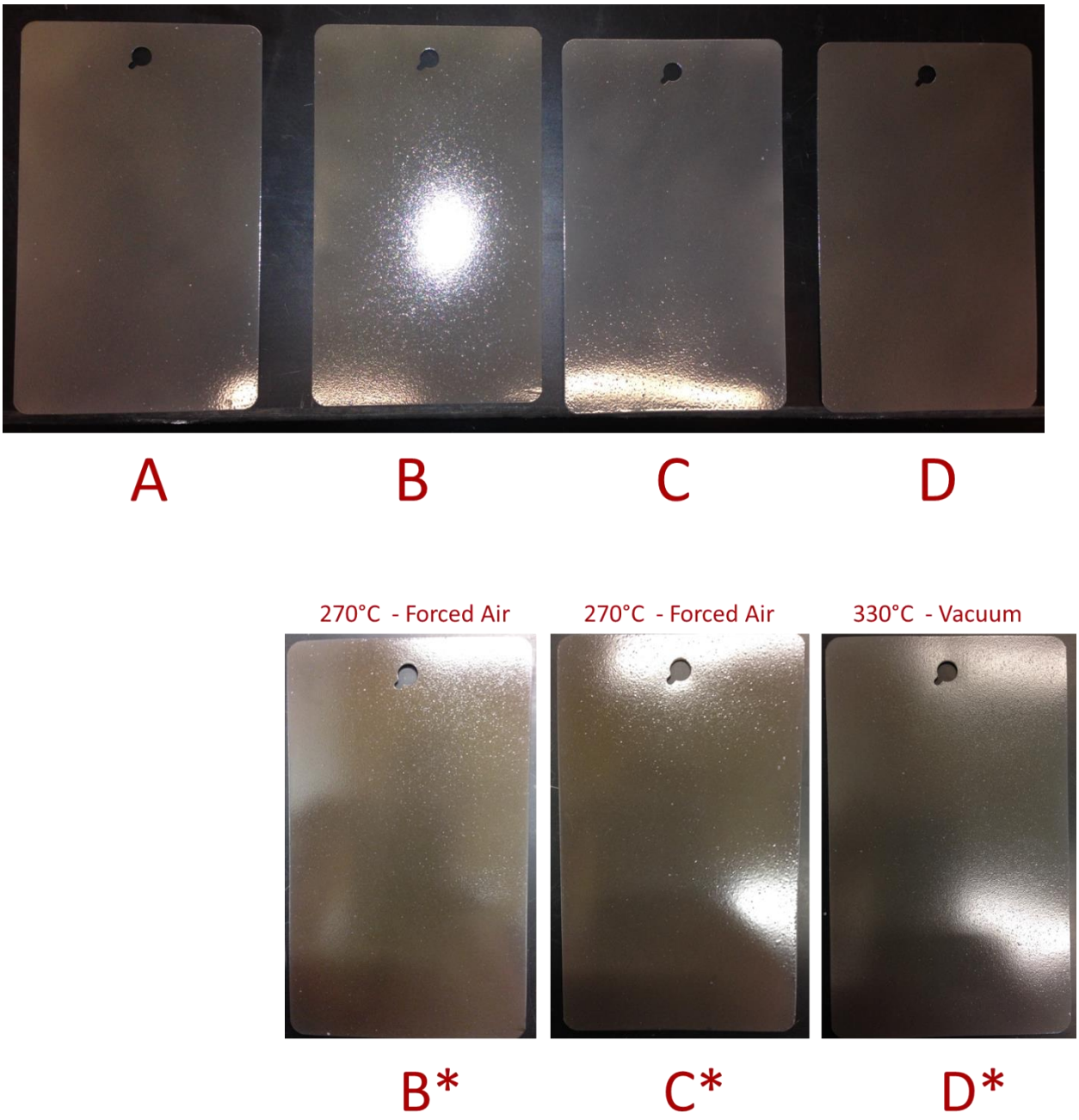

Fig. 3.26. (Top) Coated panels (2”x5”) after oligomer was allowed to melt for 10 minutes at 230°C. (Bottom) Curing conditions, where 270°C was held for 30 minutes and 330°C for 3 hours.

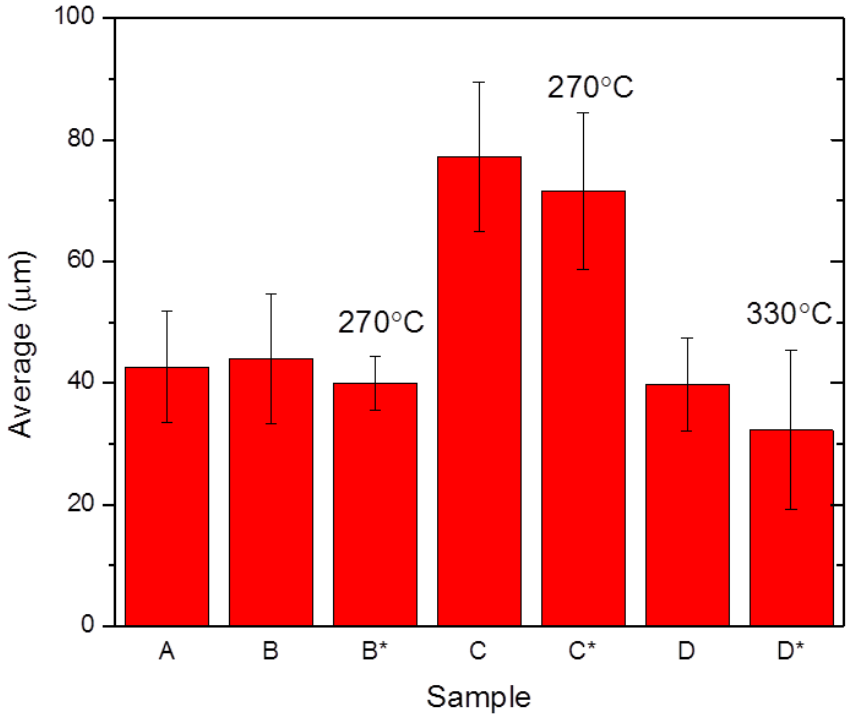

Fig. 3.27. Coating thickness for samples shown in Figure 3.27 as determined by magnetic coating thickness gauge and profilometer.

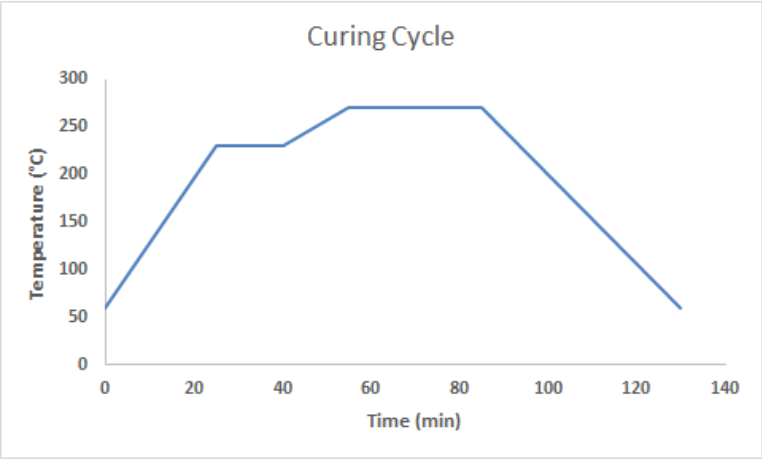

Fig. 3.28. Representative trace of cure cycle used for electrostatic ATSP powder coatings.

As can be seen in Figure 3.27, there was approximately an 8% loss in thickness upon cure for the initial CBAB coated specimens, which corresponds closely to the mass loss percentage upon cure. Similar to the solvent-borne coating deposition system described above, all of the oligomers attempted proved usable with this scheme. Prior to cure, all of the oligomers have very weak mechanical properties and are easily ground. As well, all of the oligomers enter an obvious molten state by 230°C although generally the melting point appeared quite diffuse. Lubricating addditives employed above were also generally usable however, a decrease in concentration turned out to be necessary. Figure 3.29 through 3.33 shows several cure experiments of ATSP oligomeric powder observed by reflected light hot stage experiment after electrostatic powder deposition onto aluminum foil. Samples were ramped to indicated temperatures where they were held for 5 minutes before proceeding to the next stage. It can be observed that there is a distinct morphology difference that evolves for the specimens that contain >4wt% of the MP1100 PTFE additive. This morphology was generally referred to as the “loose” morphology as it produces a rough surface texture. The loose morphology is created due to PTFE having a relatively high contact with the oligomer melt. As the oligomers melt, they contact the PTFE. As the oligomer contacts the (relatively fine particle size) PTFE, its flow and connection with other oligomer particles can be obstrcted due to the high contact angle and high viscosity of the oligomers. This creates voids in the microsctructure of the melt which get locked into place by the cure process. A higher PTFE concentration and a thicker layer of high PTFE concentration

C1A2/C2A1 tend to create the conditions for the loose structure. CBAB tends towards this set of circumstances at an even lower PTFE concentration due to the higher flow temperature of its constituent oligomers - hence why CBAB and CB2AB2 were generally used at <2wt% rather than the higher concentration used with the other oligomer systems. An example of the loose morphology can be seen in Figure 3.31.

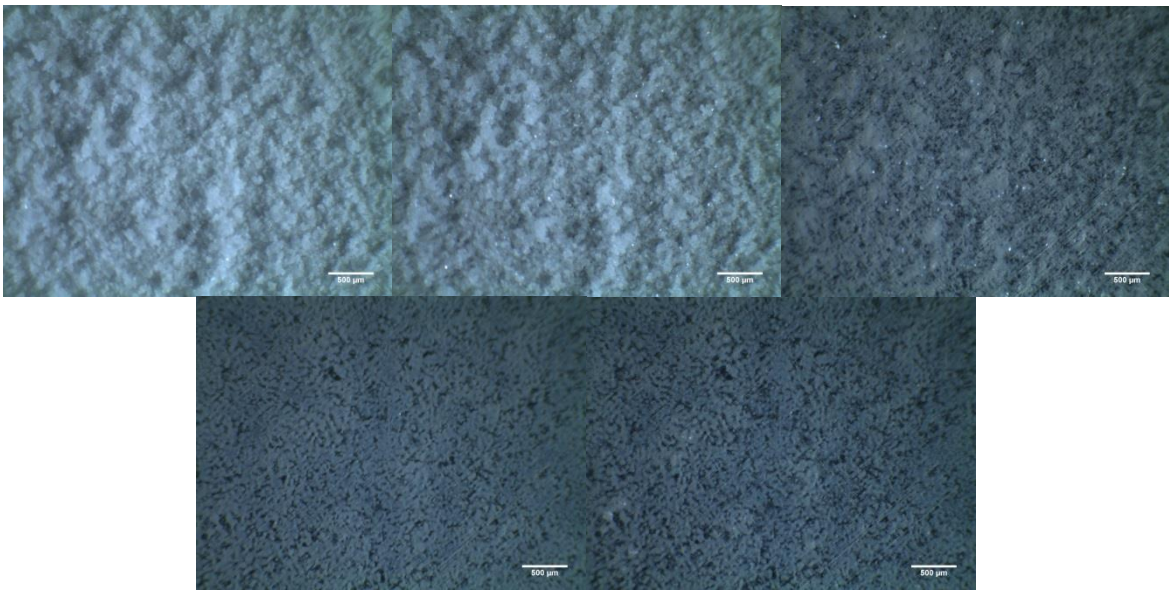

Fig. 3.29. Neat CBAB powder under reflected light hot stage experiment after 5 minutes at each temperature step. (Top Left) Deposited powder at RT. (Top Middle) At 150°C. (Top Right) 230°C showing substantial flow. (Bottom Left) 270°C. (Bottom Right) 330°C.

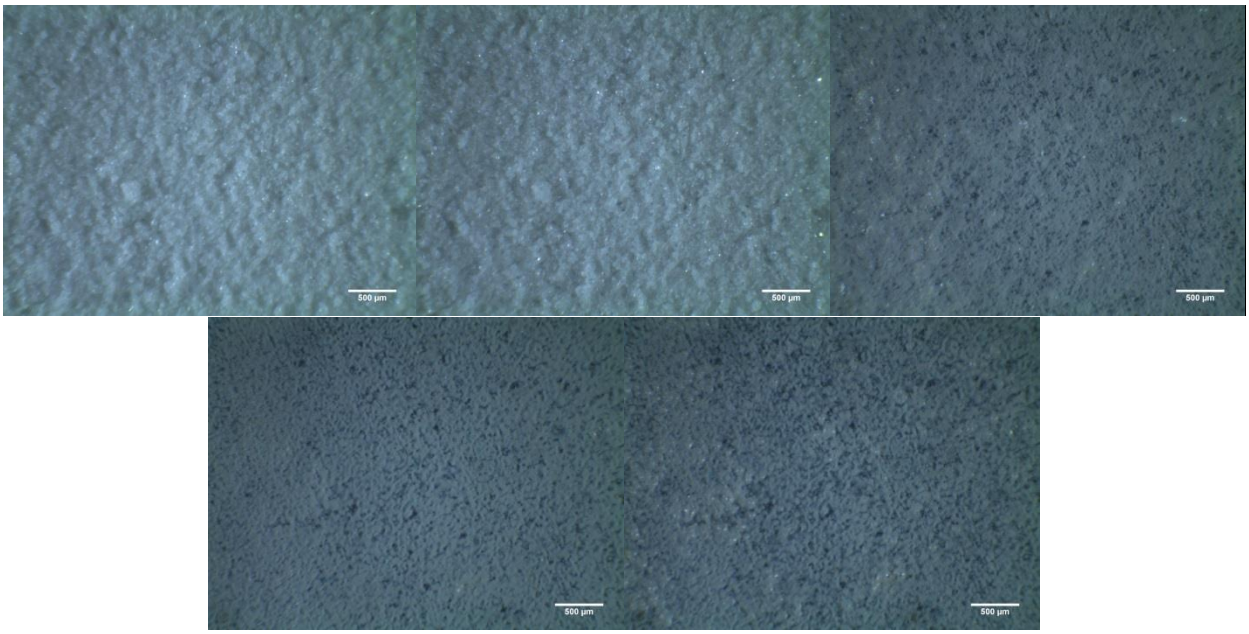

Fig 3.30. Figure 3.31. CBAB/2wt% MP1100 powder under reflected light hot stage experiment after 5 minutes at each temperature step. (Top Left) Deposited powder at RT. (Top Middle) At 150°C. (Top Right) 230°C showing substantial flow. (Bottom Left) 270°C. (Bottom Right) 330°C.

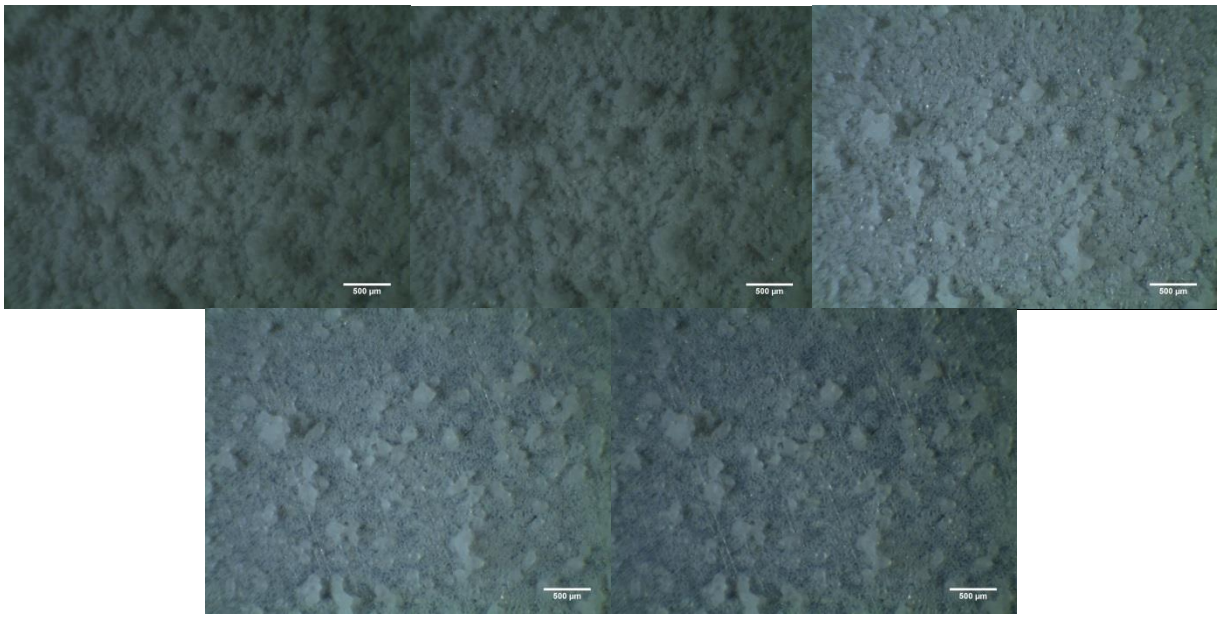

Fig. 3.31. CBAB/5wt% MP1100 powder under reflected light hot stage experiment after 5 minutes at each temperature step. (Top Left) Deposited powder at RT. (Top Middle) At 150°C. (Top Right) 230°C showing substantial flow. (Bottom Left) 270°C. (Bottom Right) 330°C.

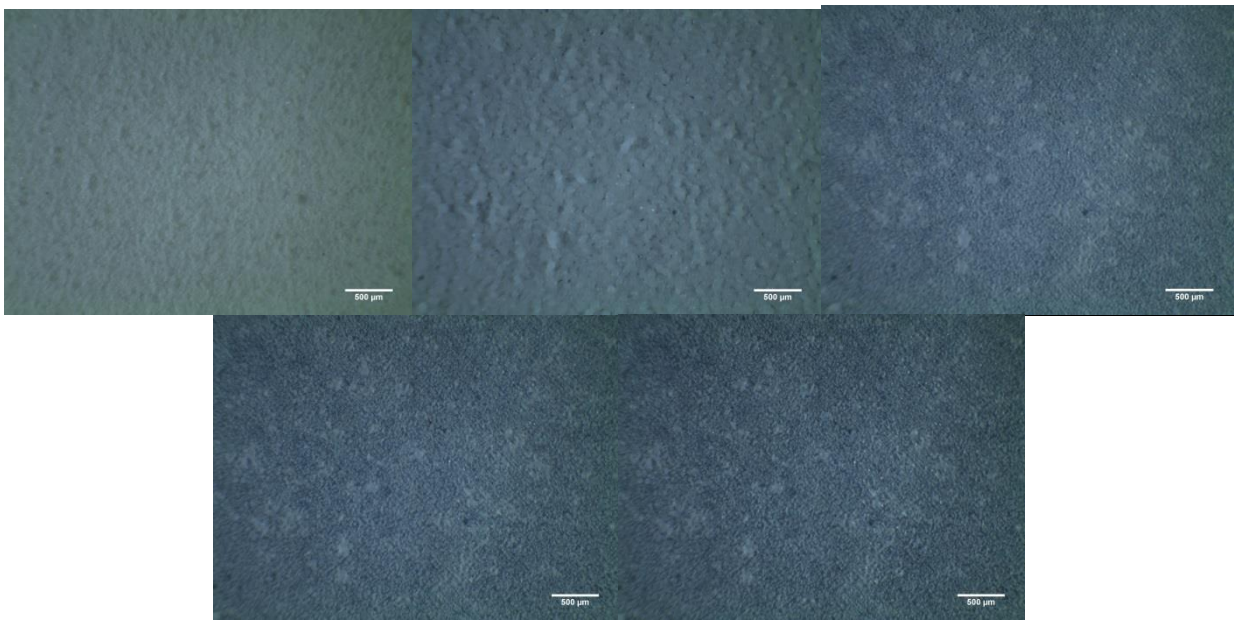

Fig. 3.32. CBAB/5wt% MP1100 powder under reflected light hot stage experiment after 5 minutes at each temperature step. (Top Left) Deposited powder at RT. (Top Middle) At 150°C there is obvious softening of the oligomer. (Top Right) 230°C showing substantial flow. (Bottom Left) 270°C. (Bottom Right) 330°C.

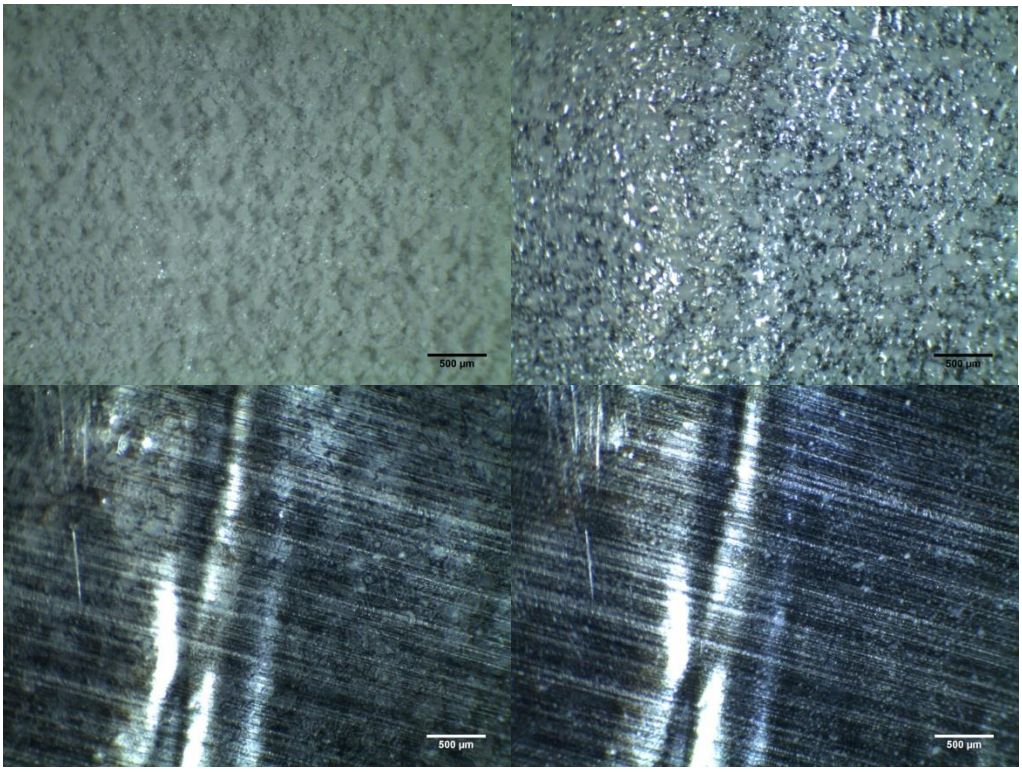

Fig. 3.33. Neat C1A1 powder under reflected light hot stage experiment after 5 minutes at each temperature step. (Top Left) Deposited powder at RT. (Top Right) At 150°C there is obvious softening of the oligomer. (Bottom Left) 230°C showing substantial flow. (Bottom Right) Coating at 270°C fully transparent.

Powder-coated specimens of aluminum foil were cured to 270°C after which their aluminum substrate was dissolved via 2N hydrochloric acid in deionized water. Following this, isolated freestanding films were thoroughly rinsed in deionized water followed by isopropyl alcohol and then dried at 70°C in air. Samples were then examined via cross-polarized transmitted light microscopy as shown in Figure 3.34. Again as in the case for solvent-deposited coatings, the trend towards increasing birefringence when using liquid crystalline, lower cross-link density oligomers is preserved.

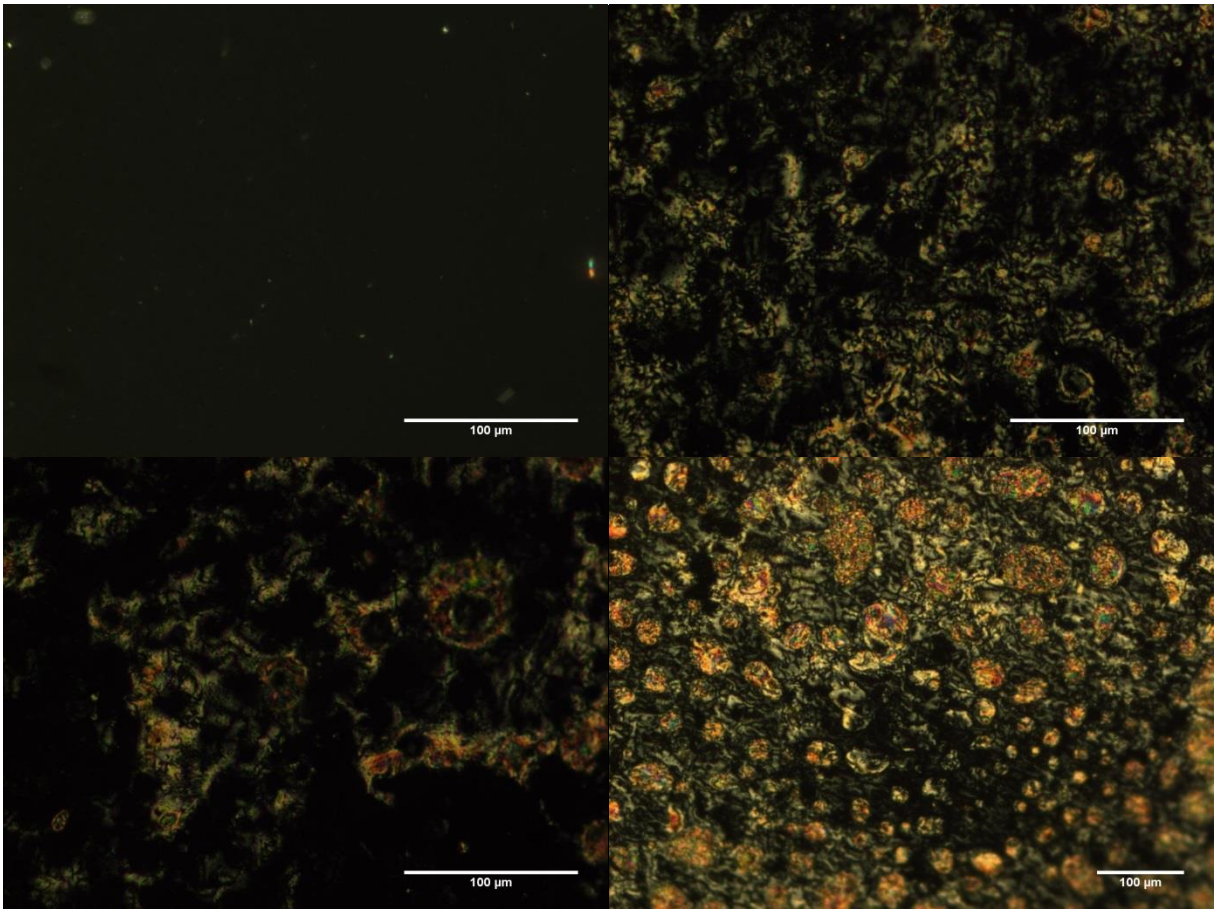

Fig. 3.34. Electrostatic powder-deposited cured ATSP coatings under cross-polarized transmitted light. (Top Left) C1A1, (Top Right) C1A2), (Bottom Left) C2A1, (Bottom Right) C2A2. All samples were 20 µm in thickness.

3.9: Macro-tribological Characterization of ATSP Coatings

Macro-tribological properties of ATSP-coated specimens (and therefore their suitability as protective coatings in the complex conditions experienced in the compressor environment) were determined primarily through accelerated, high pressure wear testing via high pressure tribometer (HPT). The HPT features a pressurized chamber which can be flooded with refrigerant gases as well as thermocouple measurement of the near contact temperature (NCT). A list of experimental parameters is featured in Table 3.10. HFO-1234yf is the trade name for 2,3,3,3-tetrafluoropropene a potential "drop in" replacement for R-134A (1,1,1,2-tetrafluoroethane) with a substantially lower GHG equivalent number [122-123]. Counterface was a 52100 hardened steel shoe, an actual compressor part used in automotive swash-plate compressors [86].

Table 3.10. Conditions for testing of solvent-deposited ATSP coatings.

Parameters	Unidirectional	Oscillatory
Normal Load	445 N	445 N
Rotational speed	1500 rpm (3.6 m/s)	-
Amplitude	-	60°
Frequency	-	4.5 Hz
Lubricant	Dry and PAG	Dry and PAG
Viscosity of Lubricant	300 SUS	300 SUS
Operating Temperature	90 °C	90 °C
Refrigerant	HFO-1234yf	HFO-1234yf
Chamber Pressure	0.3 MPa	0.3 MPa
Duration	30 min	30 min

Results generally demonstrate extraordinarily low cohesive wear of ATSP coatings in comparison to state-of-art (Table 3.9) commercial coatings marketed for tribological properties. For unidirectional motions, C2A1 with 5wt% MP1100 was found to exhibit the lowest COF under both dry and lubricated conditions, as shown in Figure 3.35. Figure 3.36 demonstrates superior surface integrity of both C1A2 and C2A1 coatings in unlubricated sliding conditions at 6 MPa of contact pressure. Moderate wear can be observed on the PTFE/MoS_2 surface and wear scratches observed on the Fluorocarbon and PTFE/PEEK surfaces. The PTFE/Pyrrolidone surface evidenced burnishing. Figure 3.37 shows the same coatings under the same conditions except now under boundary lubrication.

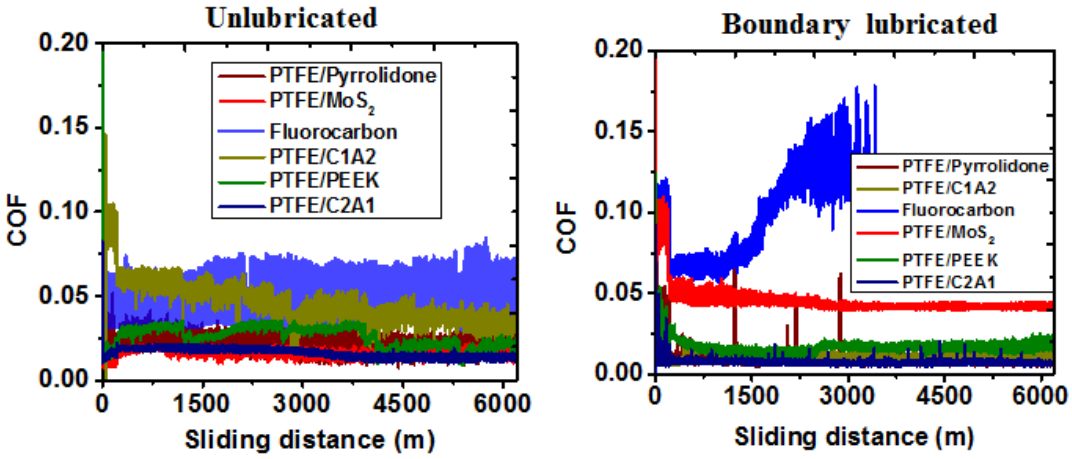

Fig. 3.35. COF versus sliding distance for various polymeric coatings on G2 Durabar as measured by unidirectional HPT with conditions in Table 3.10.

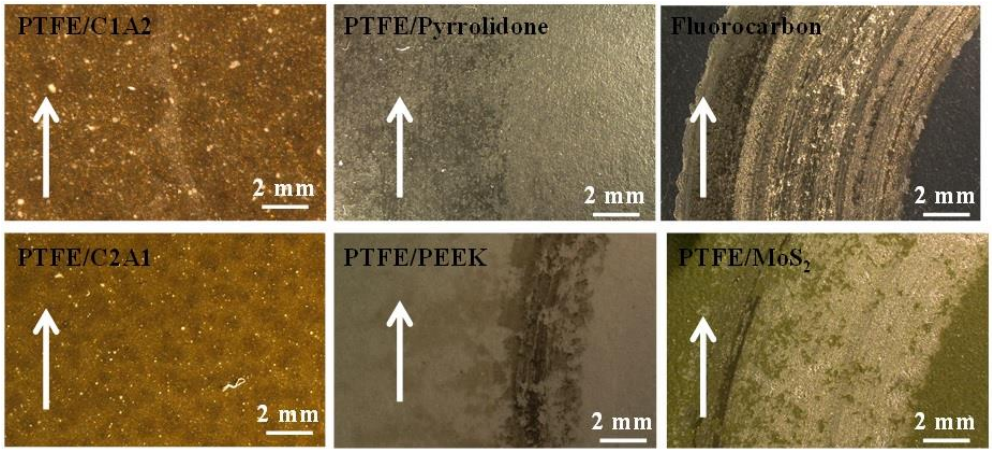

Fig. 3.36. Optical microscopic images of unlubricated coating surfaces subsequent to HPT wear experiments

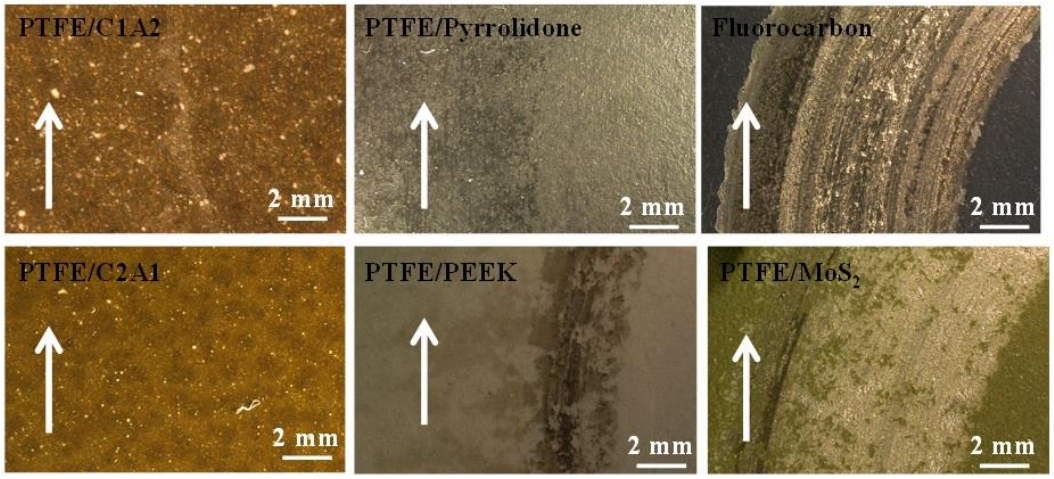

Fig. 3.37. Optical microscopic images of boundary-lubricated coating surfaces subsequent to unidirectional HPT wear experiments

Again, ATSP coatings exhibited a higher resistance to wear: no significant wear mark was observed. Fluorocarbon and PTFE/PEEK coatings demonstrated a worse performance than in the dry condition, which is thought to originate in the migration of the wear debris film under lubricated conditions. PTFE/Pyrrolidone

coating evidenced an almost identical performance under both dry and lubricated conditions. Wear depth tracks for both conditions of unidirectional wear, as observed by profilometry, are shown in Figure 3.38.

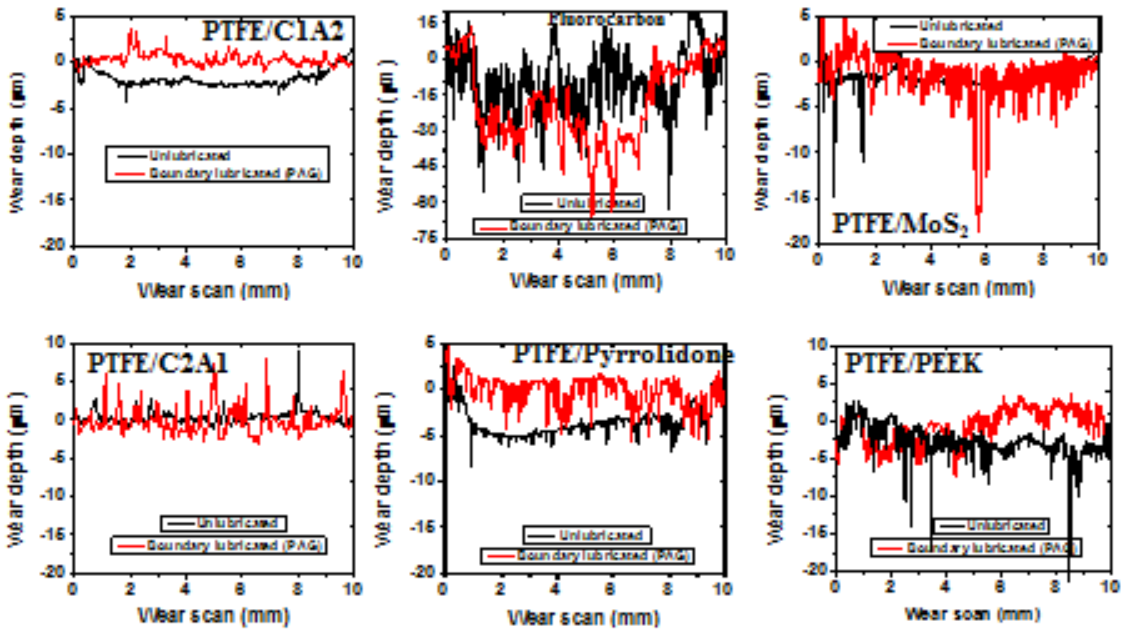

Fig. 3.38. Profilometry of tribological coatings after HPT wear experiment.

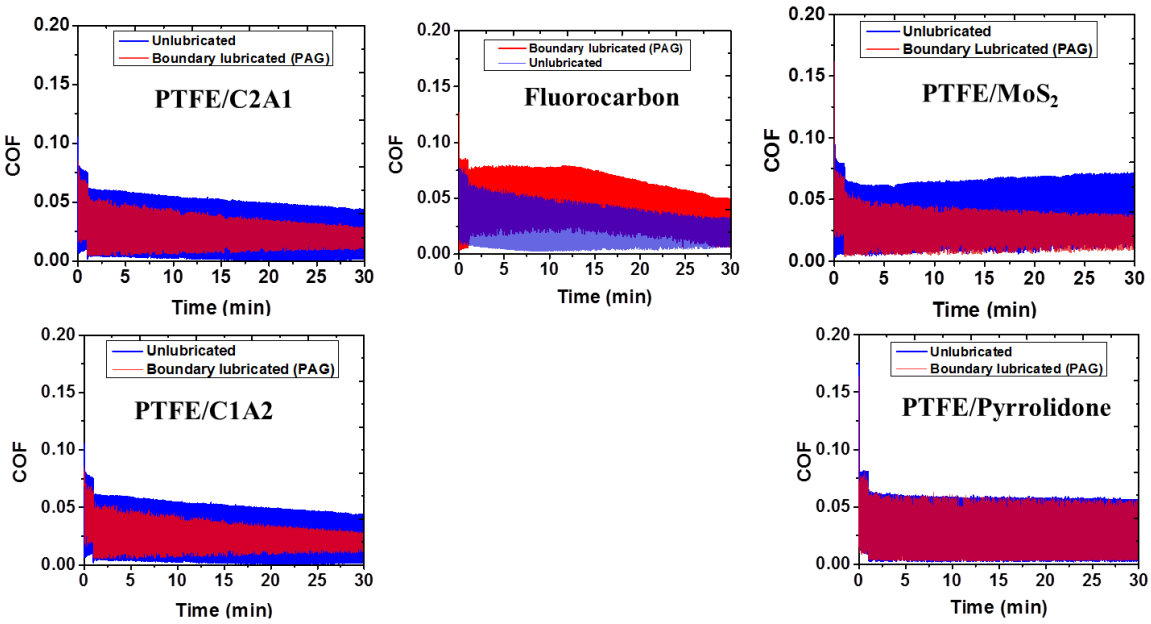

Fig. 3.39. COF versus sliding time for various polymeric coatings on G2 Durabar as measured by oscillatory HPT with conditions in Table 3.10.

A significant reduction in friction (both in average and standard deviation) was observed for the ATSP-based coatings. This suggests a synergistic effect between the lubricant and coating in these cases. PTFE/Pyrrolidone evidenced almost identical performance between unlubricated and boundary lubricated conditions, indicating no real benefit from the presence of lubricant. The COF increased for PTFE/MoS_2 and PTFE/PEEK coatings again likely due to wear debris films migration via the lubricant. No surface damage was observed for the ATSP films in the either lubricated or unlubricated conditions. Moderate wear was observed on all other coatings.

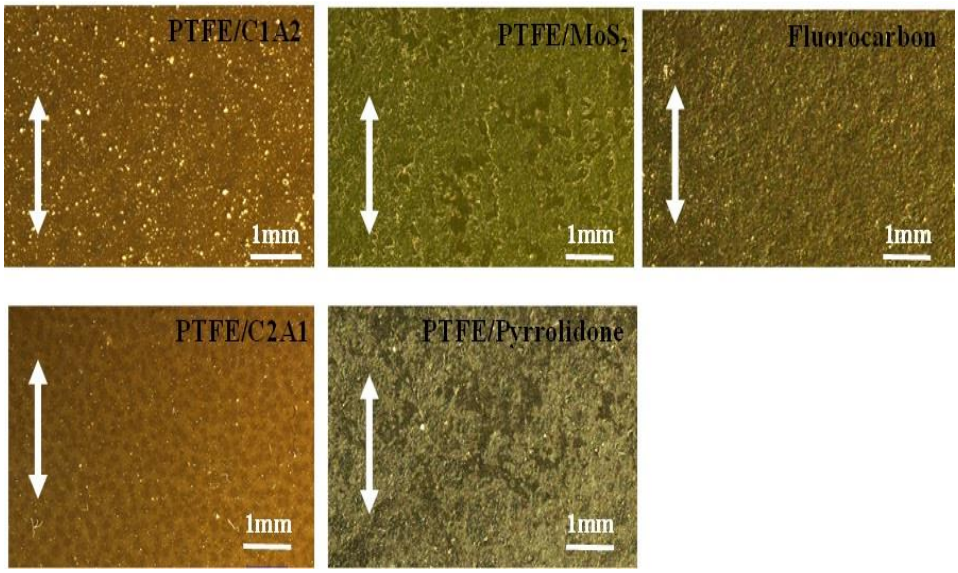

Fig. 3.40. Optical microscopic images of boundary-lubricated coating surfaces subsequent to oscillatory HPT wear experiments

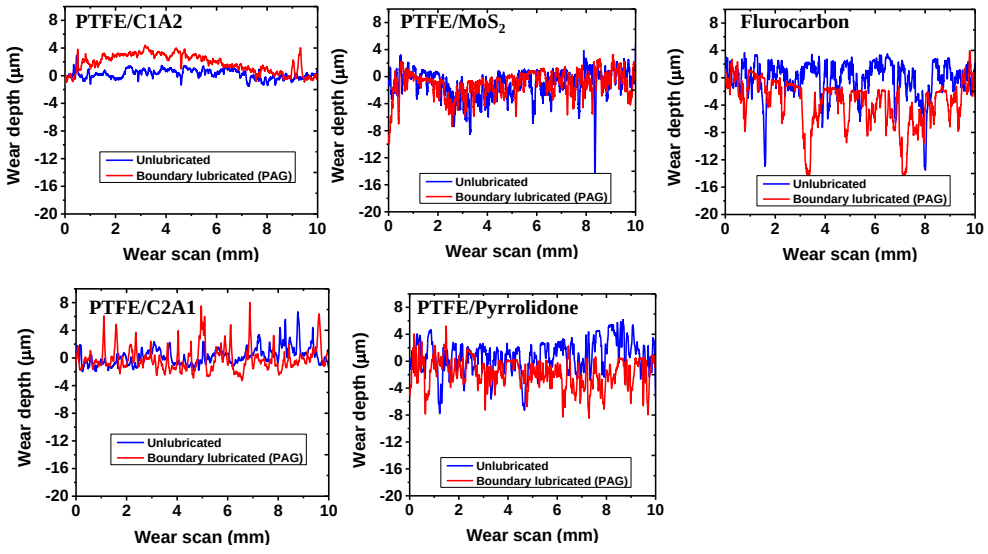

Fig. 3.41. Profilometry of tribological coatings after oscillatory HPT wear experiment.

Figure 3.42 summarizes the COF and wear results (as determined by integration of the volume of the wear tracks with time and load) of all coatings undergoing HPT testing and shows that ATSP-based coatings occupy an excellent position with respect to both parameters.

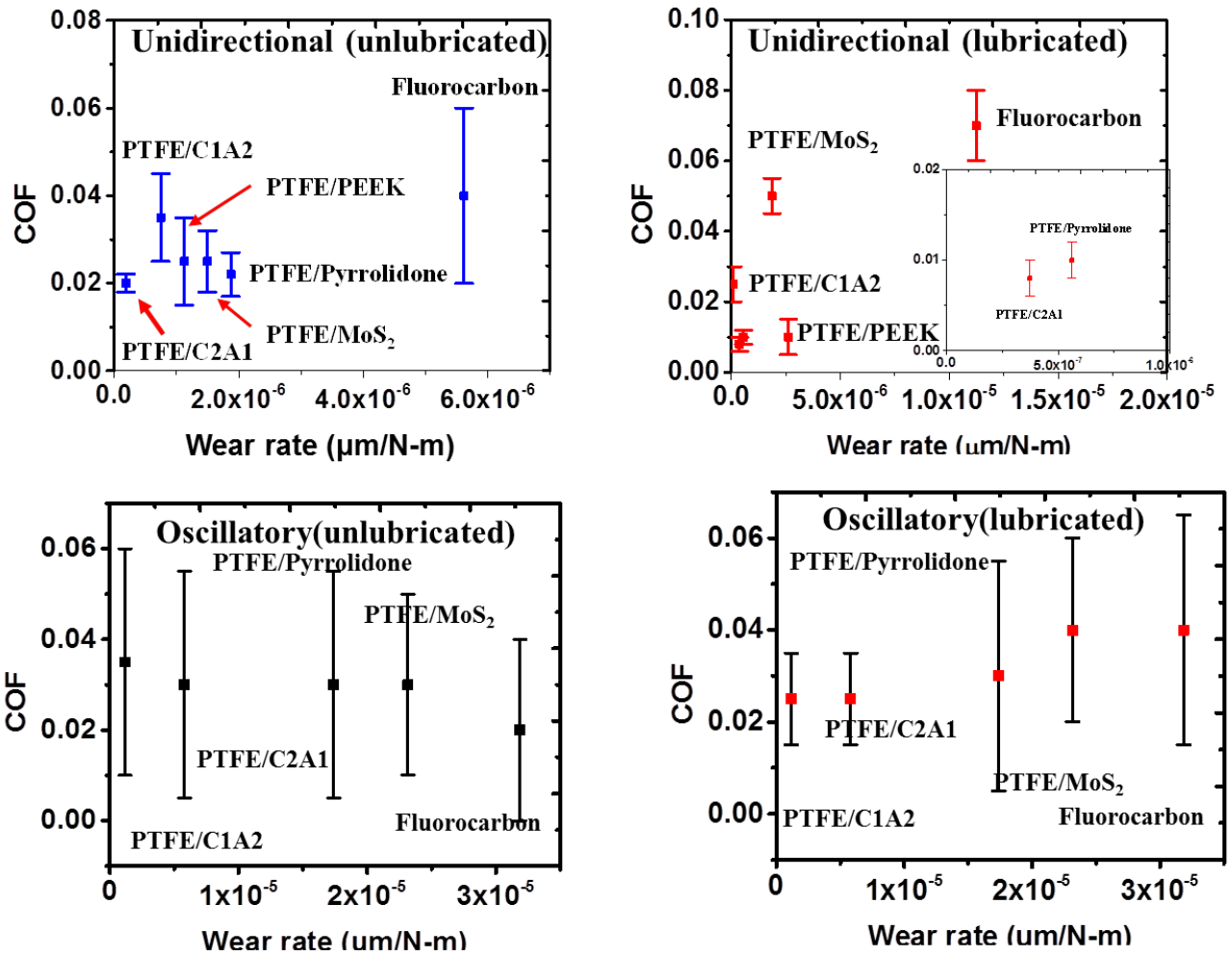

Fig. 3.42. Summary of ATSP and assorted tradename polymeric tribological coatings.

As part of the origins of the superior performance of the ATSP-based coatings, coatings at various stages of testing were examined. The phase segregation observed under cross-polarized transmitted light manifested as surface segregation with the more ordered and birefringent phase serving as the globular surface portrusions (Figure 3.43). After a relatively short sliding distance, the segregated peaks become sheared off and the material amalgamates and initiates formation of a layer on the polymeric surface. After continuous sliding, this results in a deformed and stable film layer on the polymer. This same behavior is seen on the counterface (Figure 3.44), where a non-fluorinated stable layer forms part of the counterface debris film which in this case forms a very stable and consolidated film. This suggests that ITR was involved in this mechanism as near contact temperatures were frequently observed to be up to 200°C throughout these experiments. As well, blue-ing of the steel shoe provides a qualitative indication of actual contact temperature (NCT will tend to underestimate this number).

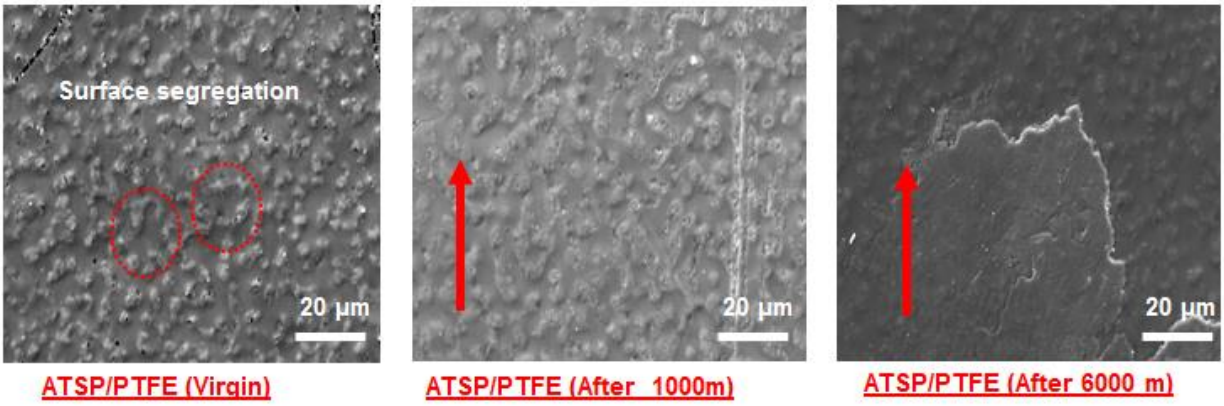

Fig. 3.43. Morphological analysis of solvent-deposited C1A2 + 5wt% MP1100 coating after unidirectional wear experiments.

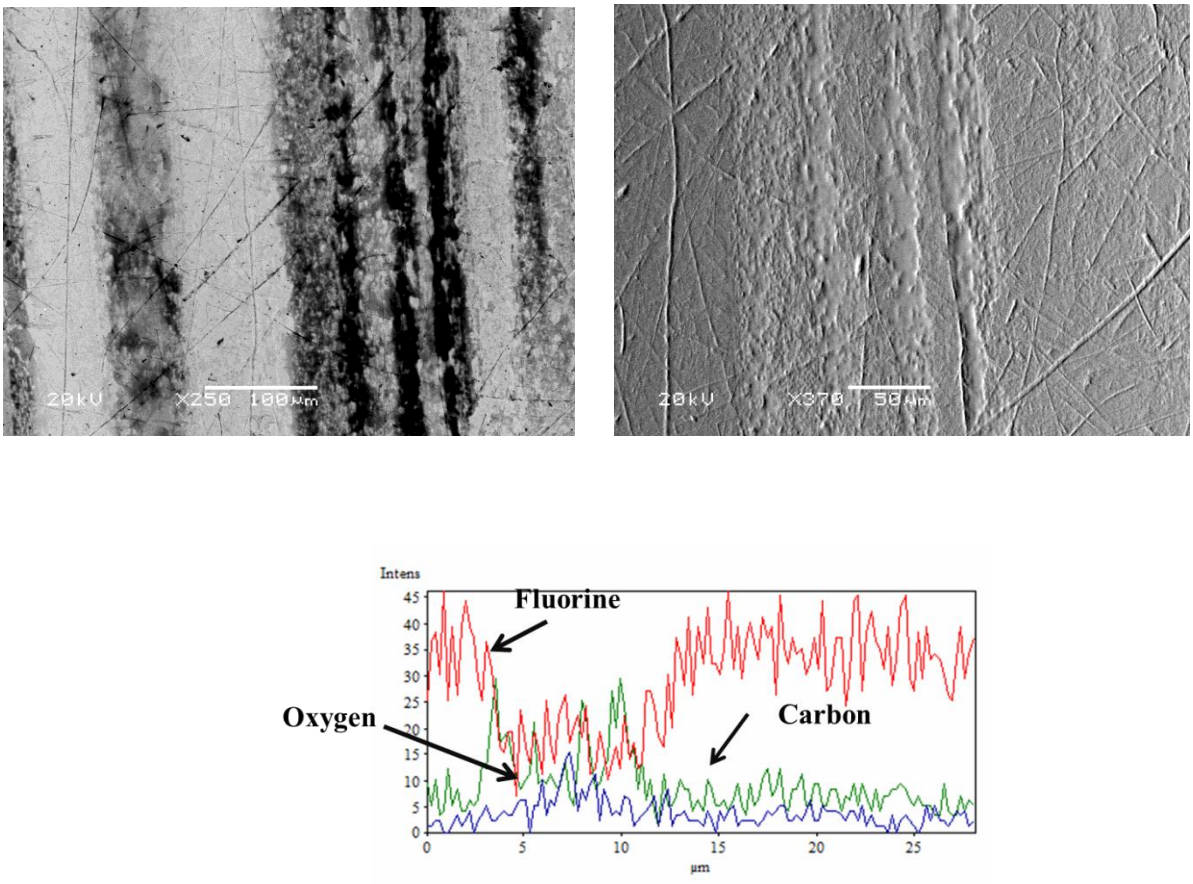

Fig. 3.44. (Top Left) SEM back-scatter imaging of 52100 steel counterface surface. (Top Right) SEM image of 52100 steel showing topography. (Bottom) electron dispersive spectroscopic scan of debris film indicated presence of CHO polymer (ATSP) present and forming a stable film layer.

A similar study was undertaken on electrostatic powder coatings of ATSP. Contact geometry was changed to a narrower pin such that contact pressure increased to 15.6 MPa and the pin metal was changed to 4340 steel. A similar process was used

as above for unidirectional wear, results are summarized in Fig. 3.45. All specimens aside from C1FA2F and C2FA1F were used with MP1100 as lubricating phase.

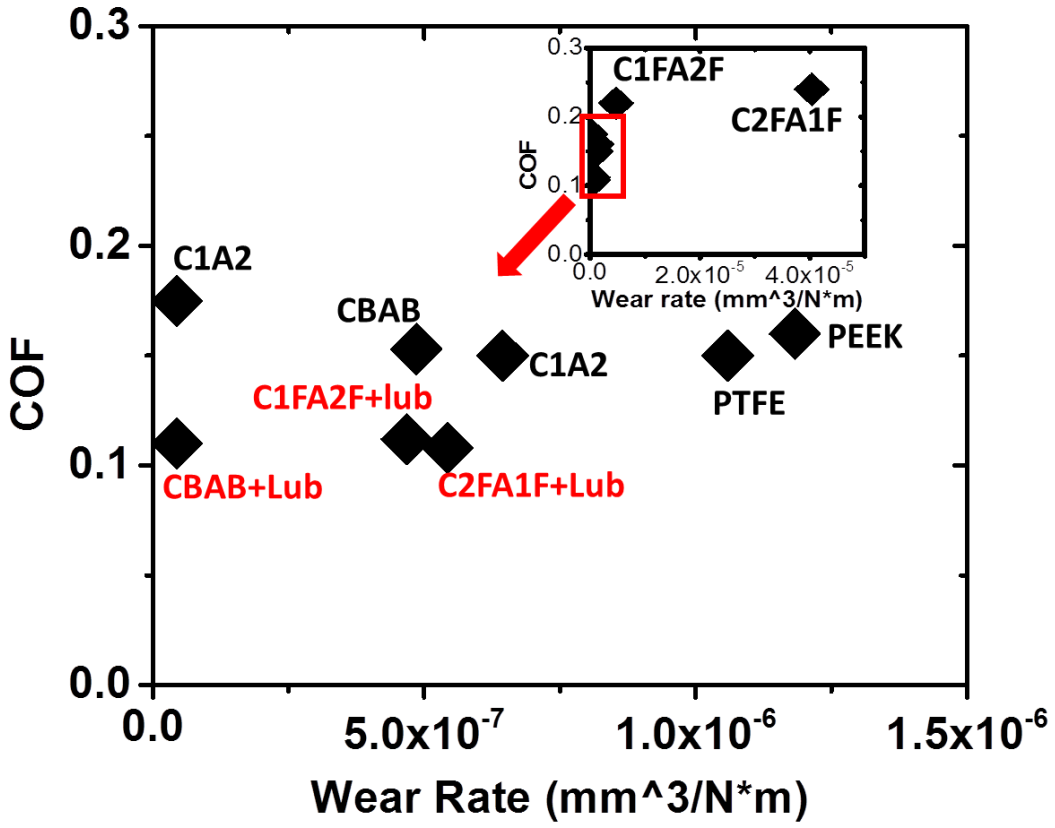

Fig. 3.45. Summary of powder-deposited ATSP and assorted tradename polymeric tribological coatings. Black labels are for unlubricated and red labels are for lubricated conditions.

An extended duration unidirectional HPT experiment was undertaken with CB2AB2 oligomer coated on a C932 bronze substrate for conditions intended to replicate submersible pumps utilized in the offshore energy-extraction industry. An extraordinarily high Pressure x Velocity-stability was observed for this system with

an incredibly low and stabilizing wear depth, which translates to a remarkable low wear rate. Results and high level of surface integrity after these incredibly severe and extended experiments are show in Figure 3.46. Table 3.11 summarizes these results in terms of PxV values.

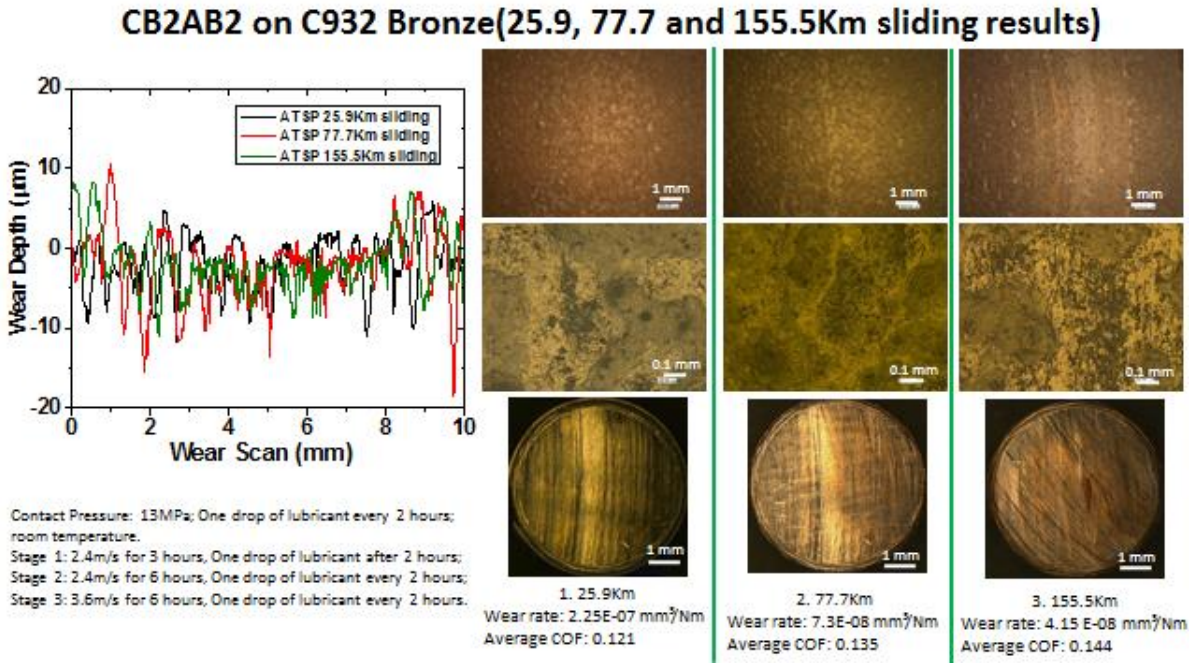

Fig. 3.46. Extended unidirectional HPT test on CB2AB2 + 1.4wt% MP1100 on C932 Bronze

Table 3.11. Summary of results on extended duration unidirectional testing.

Pressure x Velocity MPa*m/s (psi*ft/min)	Duration (hours)	COF	Total wear rate $mm^3/N*m$
$3.12*10^7$ ($8.91*10^5$)	3	0.121	$2.25*10^{-7}$
$3.12*10^7$ ($8.91*10^5$)	6	0.135	$7.3*10^{-8}$
$4.68*10^7$ ($1.34*10^6$)	6	0.144	$4.15*10^{-8}$

3.10: Conclusions

ATSP solvent-borne and electrostatic powder coatings offer performance superior to state-of-art tradename coatings. ATSP electrostatic powder coatings are now (with a Tg of up to 307°C (compared to PEEK at 143°C) are now the highest temperature electrostatic powder coatings seen in literature or available commercially by more than 150°C, which offers new ranges of utility and performance to diverse mechanical components.

CHAPTER 4

MICROMECHANICAL PROPERTIES AND ELASTIC RECOVERY OF AROMATIC THERMOSETTING COPOLYESTERS

4.1: Introduction

Using a combination of large force range (~ 300 mN) and large displacement range (~ 7 μm) indentation, the complete coating response could be measured together with the effect of the hard substrate. The microstructural differences between imposed by changes in the oligomer architecture were used to explain differences in the micromechanical properties of ATSP coatings. The measured micromechanical properties, which could be readily obtained by performing simple laboratory indentation tests, were successfully correlated with compressor specific tribological experiments.

Seven different commercial polymeric coatings, namely, PTFE/Pyrrolidone-1 (DuPont™ Teflon® 958-303), PTFE/Pyrrolidone-2 (DuPont™ Teflon® 958-414), Resin/PTFE/MoS_2 (Whitford Xylan® 1052), PEEK/PTFE (1704 PEEK/PTFE®), PEEK/Ceramic (1707 PEEK/Ceramic®), Fluorocarbon (Impreglon® 218), and PTFE/MoS_2 (Fluorolon® 325) were used in this chapter. Coatings blended with MoS_2 can normally sustain high normal loads and may offer, at the same time, low shear strength due to lamellar structure of MoS_2, thus resulting in a lubricious low friction surface. Several coatings based on ATSP were also selected for this comparative study. These coatings were blended with Zonyl-type PTFE additives and MoS_2 to implement a lubricating phase. ATSP was also varied from a low to a high crosslink density by adjustment of feed ratio of trimesic acid from C1A1 to C2A2.

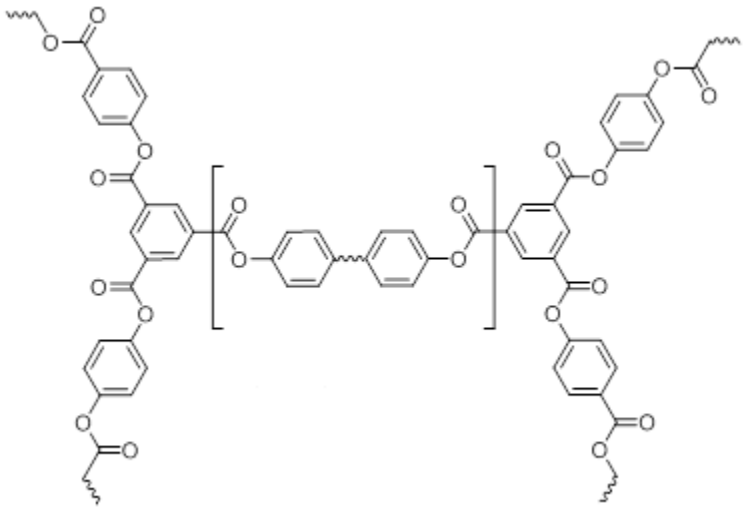

Sample	Oligomer mass feed ratio (C#/A#)	Oligomer molar feed ratio (C#/A#)	COOH / AcO	x_n	$(\bar{M}_c)_N$
ID#					(g)
C1A1	1.105	1.000	1.00	0.1440	834.10
C1A2	1.140	1.000	1.33	0.1051	1142.82
C1A2+	1.243	1.087	1.45	0.1063	1129.92
C1A2-	1.029	0.900	1.20	0.1030	1166.12
C1A2=	0.857	0.750	1.00	0.1010	1189.21
C2A1	1.080	1.000	0.75	0.1100	1117.30
C2A1-	1.224	1.133	0.85	0.1075	1117.30
C2A1=	1.440	1.333	1.00	0.1040	1091.91
C2A1+	1.584	1.467	1.10	0.1020	1177.55
C2A2	1.117	1.000	1.00	0.0718	1672.84

Fig. 4.1 Variation of Mc with oligomer choice. Branch parameters as described in Chapter 2.

To better understand the overall tribological behavior, an attempt was made to investigate how the frictional force is determined for sliding wear of a polymer surface against a metallic counterpart. From the well-known model by Briscoe [81], the surface layer of the polymer involved in the frictional process can be classified into two zones: the interfacial zone with a depth of about 100 nm and the cohesive (subsurface) zone corresponding to the depth of the coating thickness. Therefore, the frictional force resulting from the adhesion equals the product of the "real contact area" of the interfacial zone (with the counterpart) and the "shear stress" of the subsurface zone. This is assuming that the counterface is sufficiently hard in comparison to

the polymer-mating surface and undergoes only mild or no elastic deformation. Figure 4.2 shows a schematic diagram of the two-term friction model of polymeric surface.

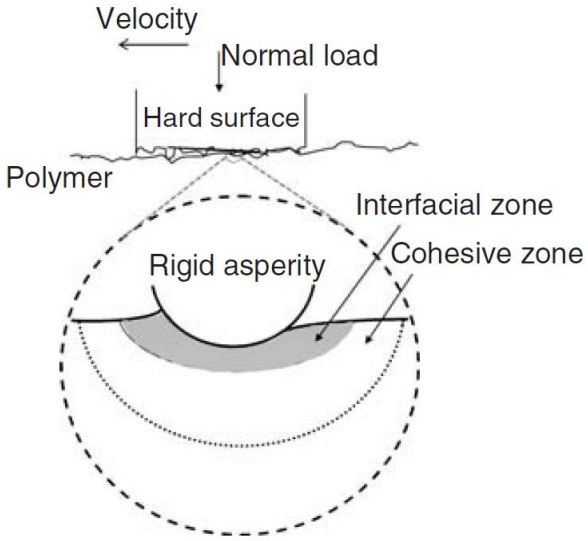

Fig. 4.2. Briscoe's two-term model of polymer interface showing interfacial and cohesive zones [81].

The frictional work at the interface is the result of adhesive interactions between the polymer surfaces and the rigid asperities which depend on factors such as: the hardness of the polymer, molecular structure, glass transition temperature, crystallinity of the polymer, surface roughness of the counterface and chemical/electrostatic interactions between the counterface and the polymer. For example, a soft elastomeric solid with a glass transition temperature well below room temperature, would have a large adhesive component leading to increased friction. Beyond interfacial work is the contribution of the cohesive term, which is a result of the plowing actions of the asperities of the harder counterface into the polymer. The energy required for the plowing action will depend primarily on the tensile strength and the elongation before fracture (or toughness) of the polymer and the geometric parameters (height and the cutting angle) of the asperities on the counterface [81]. In a normal sliding experiment, however, it is hard to

completely decouple the two terms (interfacial and cohesive) and therefore most of the data available in the literatures generally include a combined effect.

A critical component of indentation measurements is the calibration of the tip, known as area function. The classic tip area function routine, known as the Oliver-Pharr method [88], is a compliance method wherein the mechanical properties are determined based on the previously observed contact area of the probe tip to the sample, under a certain load. Since indentation measurements give us only contact depth information, the tip area function correlating the contact area and the contact depth needs to be determined/ known for the tip used in the measurements. Note that contact depth h_c is defined as the vertical distance along which contact is made by the tip during loading, and is less than the maximum penetration depth (h_{max}) due to the elastic property of the indented surface [88]. If the tip was manufactured to be perfect without any defects (which is not the case), the area function will be simply the geometrical shape function of a pre-specified tip such as: $A_c(h_c) = 24.5\ h_c^2$ in the case of the Berkovich tip. However, due to tip imperfections, the area function usually takes the following polynomial form. To determine the coefficients of the above equation, indentations at varying penetration depths (corresponding to similar depth range as the desired measurements) are performed on a standard material. Then, since the modulus of the standard material is known, the contact area corresponding to each contact depth (A_c, h_c) can be calculated and plotted as in Figure 4.4, and finally, the coefficients are determined by polynomial curve-fitting.

Two important elements that affect the tip calibration and thus the material property values are 1) the choice of the standard sample and 2) the contact depth range of calibration. In this study, a modified bismaleimide polymer (manufactured by BASF Corp) with a reduced

modulus value of 5.0 GPa was used as the calibration standard, as its value is similar to the polymeric coatings to be tested in this work. Note that we did not use the widely used fused Quartz standard because its reduced modulus is significantly higher than our interest, namely 69.6 GPa. Calibration was performed with 22 varying loads from 1 mN to 800 mN (under the exact same loading conditions as the measurements detailed later) resulting in 0.5 to 6.5 μm of contact depths (Figure 4.3) which were of similar range to those of the actual measurements. Once the tip is completely calibrated with the coefficients seen in Figure 4.3, this tip area function is directly used for the calculation of the mechanical properties during the indentation measurements. The detailed calculation process using the compliance method which involves the determination of the elastic modulus and hardness exclusively from the initial unloading portion of the load-displacement curve can be found in the literatures [88,140].

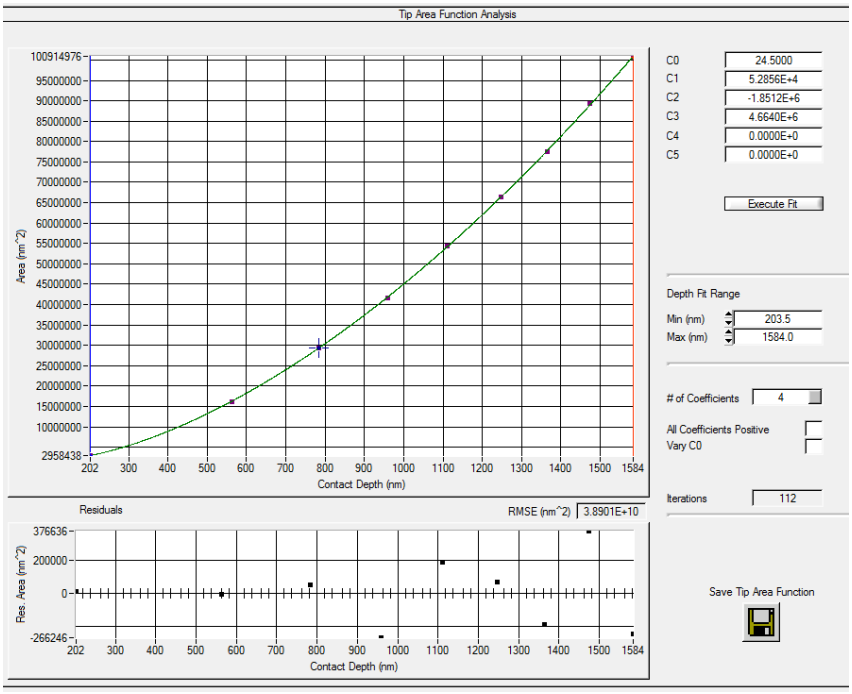

Fig. 4.3. Polynomial curve-fitting of measured contact area versus contact depth to determine the coefficients of tip area function. Screenshot of Hysitron Triboscan analysis software.

A typical indentation experiment on a polymeric material involves engaging the probe tip to the sample surface under a light load (2 μN), indenting to a pre-specified maximum load at a constant loading rate (10 mN/s), holding at the peak load (5 sec in this case) to reduce creep effects [81], and then withdrawing the tip at the same rate as during loading (~10 mN/s). This is called trapezoidal loading profile, compared to the most commonly used triangular profile which does not have a hold-time at the peak load. The initial set of indentations were performed on PTFE/Pyrrolidone-2 coatings using both trapezoidal and triangular loading profiles with a maximum load of 70 mN to examine possible creep behavior. For the triangular loading, three different loading/unloading rates (2, 10 and 30 mN/s) were used to determine their effect on the slope of the initial part of the unloading curve (and thus the calculated property values). For the main indentation measurements: a trapezoidal loading profile at a constant loading/unloading rate of ±10 mN/s was used for about 10 varying maximum loads between 5 to 400 mN (which correspond within the calibration range). For each maximum load, six indentations were repeated at different areas (resulting in approximately 60 indentations for each coating sample), thus resulting in 420 indentations in total. Although this method of using single loading/unloading indentations is time consuming, compared to the partial unloading method, it is preferred for precise examination of polymer material properties. Also, in this work, single indentations showed valuable phenomena for each coating, which correlated their structural properties with their tribological behavior.

Figure 4.4 depicts typical ramp-loading scratch experiments that were used for characterizing the coating's. Pre- and post-scratch scans of the surface topography were also performed due to the

viscoelastic behavior and the relatively high hardness of the coatings. Therefore, each scratch experiment consists of three steps: (1) a pre-scratch scan to measure the topography of the original surface to be scratched, (2) an actual ramp loading scratch, and (3) a post-scratch scan to measure the residual deformation of the scratched surface. All three steps were performed at the exact same location. At the beginning and end of each step, a pre- and a post-profile scan, which is about 12 % of the scratch length, is performed to correct the alignment of the data, as shown in Figure 4.4(a). After the completion of a scratch test, the scratch profile (red line) and the residual profile (green line) are normalized based on the reference original surface (black line) to precisely quantify the true depth of scratch as well as the elastic and plastic deformations of each coating surface, as seen in Figure 4.4(b). Along with the displacement plots, the *in-situ* lateral and normal forces are recorded, thus resulting in the *in-situ* friction coefficient of the scratched surface.

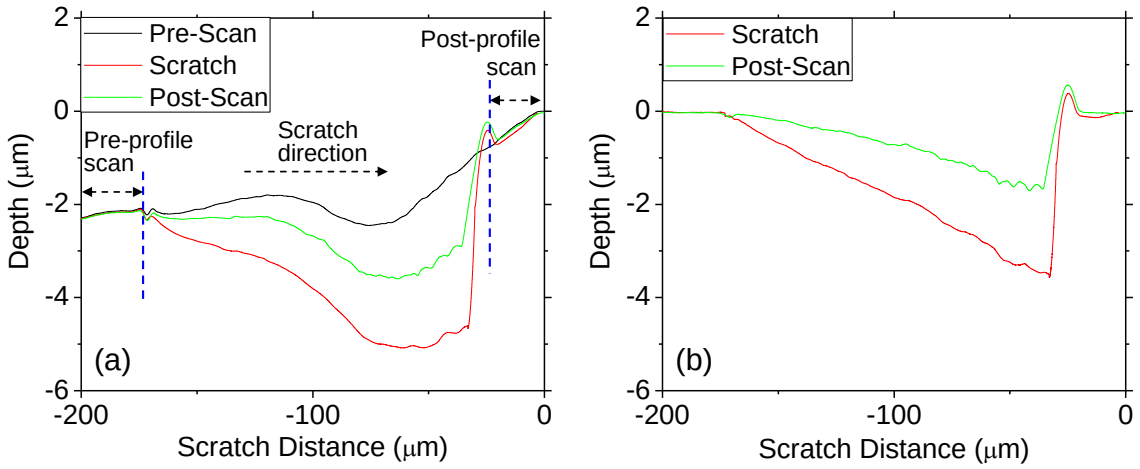

Fig. 4.4 Representative ramp-loading microscratch curves showing (a) low load pre-scratch scan (black), in-situ scratch displacement (red), and low load post-scratch scan (green); (b) normalized scratch and post-scratch scans.

A constant normal load of 200 μN was applied for both the pre- and post-scratch scans. Each sample was scratched 4 times for each maximum load (three different maximum loads of 10, 20, and 30 mN, thus resulting in 12 scratches for each sample) to ensure repeatability and establish the scatter in the results. The tip used for the scratch tests was a 60° conical tip with a tip radius of 4.3 μm as seen in Figure 4.5.

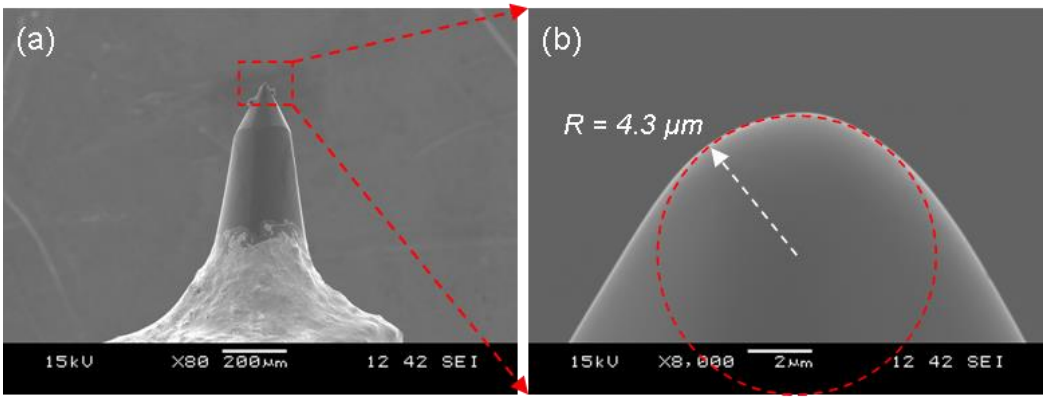

Fig. 4.5 (a) Scanning electron microscopy (SEM) image of conical tip used for scratch testing in this work, (b) zoomed in image showing the tip radius.

Analysis was performed on two representative PTFE- (PTFE/Pyrrolidone-2) and PEEK-based (PEEK/PTFE) coatings to examine the main differences in their micromechanical properties and correlation with their microstructure, as well as correlation with their tribological performance (section 4.3.3). Figure 4.6(a) and 4.6(b) show the load-displacement curves of PTFE/Pyrrolidone-2 and PEEK/PTFE coatings, respectively. The elastic modulus and hardness values determined from these curves (six measurements for each maximum load instead of the two shown in the figure) are plotted in Figure 4.6(c) and 4.6(d), respectively. Clear differences on load-displacement curves between the two coatings could be observed; PTFE/Pyrrolidone-2 in Figure 4.6(a) exhibited repeatable load-displacement behavior, namely, the two curves at the same maximum load showed exactly the same path. Also, note that the loading curves in this

case are almost identical, for all peak load experiments. Considering that each indentation was performed at a different area of the coating surface, this repeatability implies very uniform structure and mechanical properties over the whole coating surface area. At the same time, the smoothly increasing loading curve shows their structural uniformity through the coating thickness. These characteristics explain the small x- and y-axis error bars of the elastic modulus and hardness of PTFE/Pyrrodlidone-2 coating, as seen in Figure 4.6(c) and 4.6(d). Thus, PTFE/Pyrrolidone-2 coating can be thought to have amorphous-like microstructure.

In the case of PEEK/PTFE coating, the load-displacement curves showed completely different paths for all indentations, and the slopes of the loading curves differ significantly. This implies that the mechanical properties of PEEK/PTFE coating differ from location-to-location on the surface, which can also be seen by the large error bars of elastic modulus and hardness of PEEK/PTFE coating in Figure 4.6(c) and 4.6(d). Also, examining the loading curve, its slope is not smoothly increasing, but changing at some penetration depth, which means its microstructure is not uniform through the coating thickness. As the tip is penetrating the coating, it finds a nonhomogeneous material, with different mechanical properties (either amorphous or crystalline), showing the semi-crystalline microstructure of PEEK/PTFE coatings.

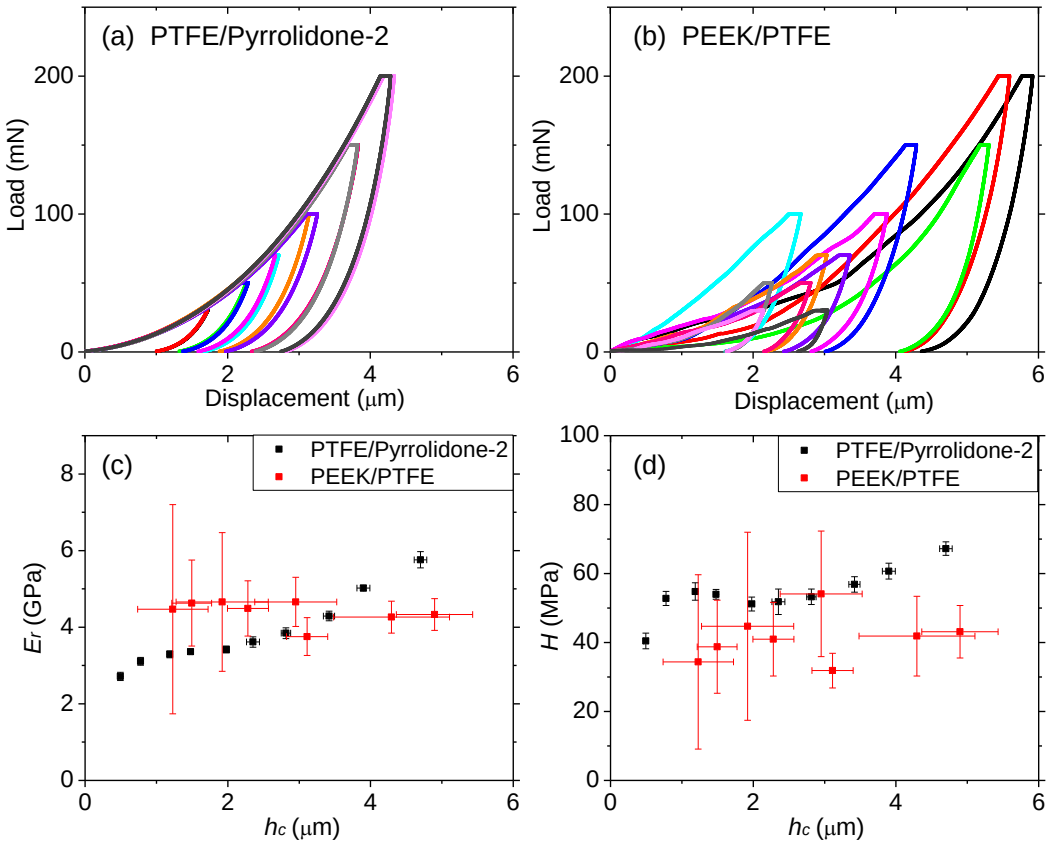

Figure 4.6 Load-displacement curves of (a) PTFE/Pyrrolidone-2 and (b) PEEK/PTFE coatings showing their load-bearing properties. Extracted (c) reduced modulus and (d) hardness values.

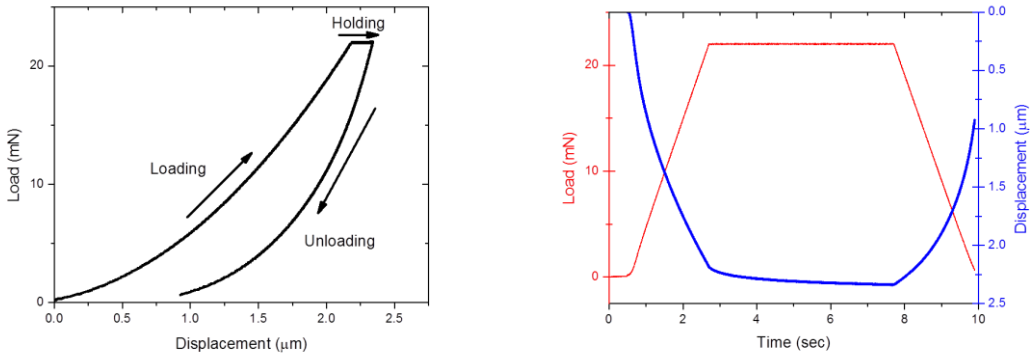

Figure 4.7 Schematic of load-displacement curves with hold (a) and regraphed as a function of time (b).

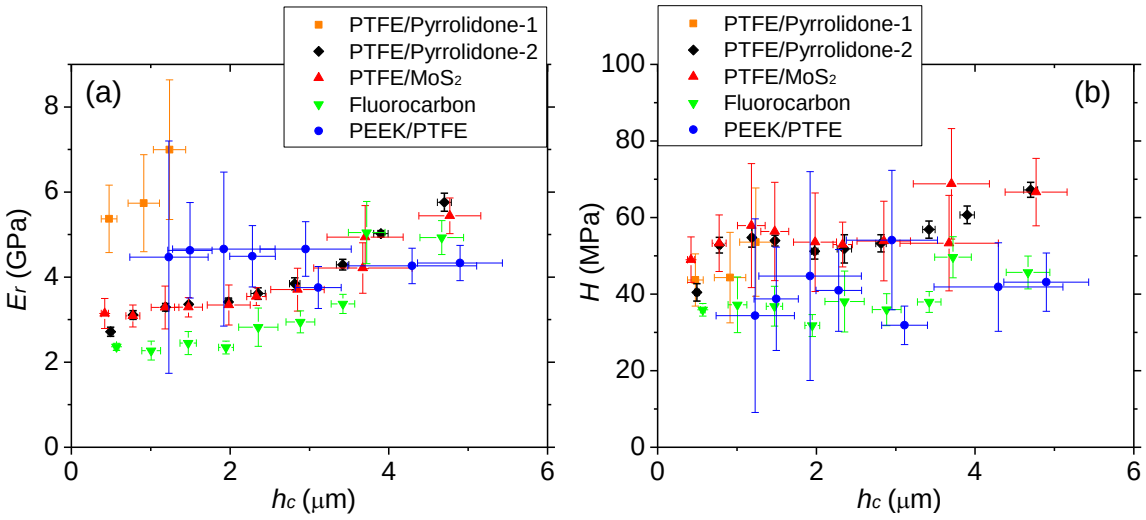

Figure 4.8 Extracted (a) elastic modulus and (b) hardness values with respect to contact depth.

Figure 4.8 shows the elastic modulus and hardness values of 5 different coatings as a function of contact depth. Each data point shows an averaged elastic modulus (y-axis) and contact depth (x-axis) along with their standard deviations (error bars in both axes) from six indentation measurements at a given maximum load. In all cases except PEEK/PTFE, the elastic modulus exhibits constant values at lower contact depths around 1.5 to 2 μm, and then increases with increasing contact depth due to the substrate effect as above. In the case of PEEK/PTFE coating, due to its porous structure, the elastic modulus is rarely affected by the substrate, thus resulting in constant values with increasing contact depth. Interestingly, it can be observed that the elastic modulus of PTFE/Pyrrolidone-1 coating is significantly higher than that of other coatings as seen in Figure 4.8(a) (note that values at higher than 1 μm contact depths were not included in the figure due to excessive pile-up during indentation, and thus inaccurate values). Note that excessive pile-up phenomenon was only observed with PTFE/Pyrrolidone-1 as seen in Figure 4.13. The underestimated contact area due to the pile-up effects was clearly observed for PTFE/Pyrrolidone-1 coating in Figure 4.9(a), compared to other coatings with no pile-up, for

example, PTFE/Pyrrolidone-2 shown in Figure 4.9(b). Usually, for polymer materials, a blunt tip with around 20 μm nominal radius is recommended to simply compress the material under the tip to avoid any plastic deformation. However, when sharp indenters like the Berkovich are employed, indentation becomes both elastic and plastic, thus resulting in such plastic deformation as pile-up or sink-in. In the case of pile-up where material plastically uplifts around the contact impression, the actual contact area is larger than that predicted by the area function discussed above. Therefore, both elastic modulus and hardness values are overestimated as can be seen in Figure 4.8 for PTFE/Pyrrolidone-1 [ref]. Finite element simulations for conical indenters (Bolshakov and Pharr, 1998) have shown that the ratio of final indentation depth, h_f (the depth of the indentation impression after unloading) to the depth of the indentation at peak load, h_{max} can be used as an indication of when pile-up is an important factor. Pile-up is significant only when $h_f / h_{max} > 0.7$ and the material does not appreciably work harden. For such materials, failure to account for the pile-up can lead to an underestimation of the contact area deduced from indentation load-displacement data by as much as 60%, thus resulting in an overestimation of the hardness and elastic modulus. When $h_f / h_{max} < 0.7$, or in all materials that moderately work harden, pile-up is not a significant factor, and the Oliver–Pharr model can be expected to give reasonable results. In this work in all coatings, except PTFE/Pyrrolidone-1, the latter is the case and thus pile up effects can be safely ignored.

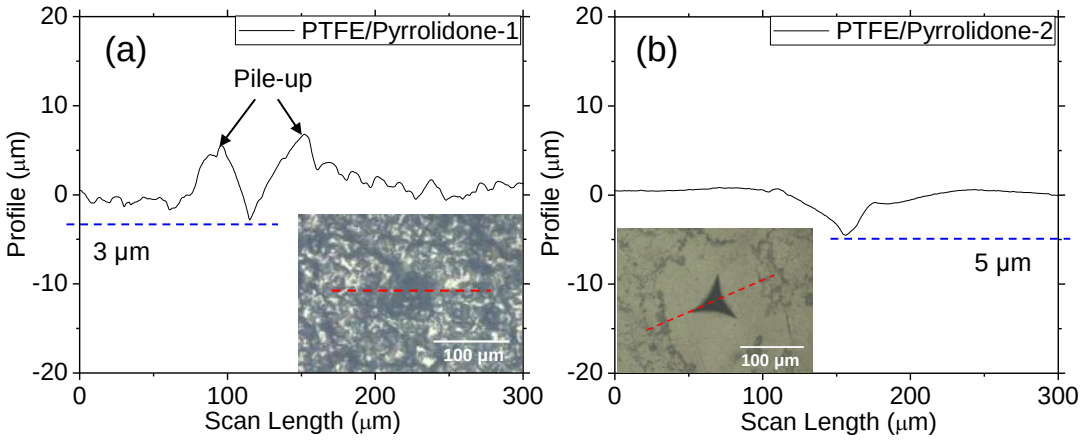

Figure 4.9 Cross-section line profile of indentation residual impressions: (a) PTFE/Pyrrolidone-1 and (b) PTFE/Pyrrolidone-2 coatings.

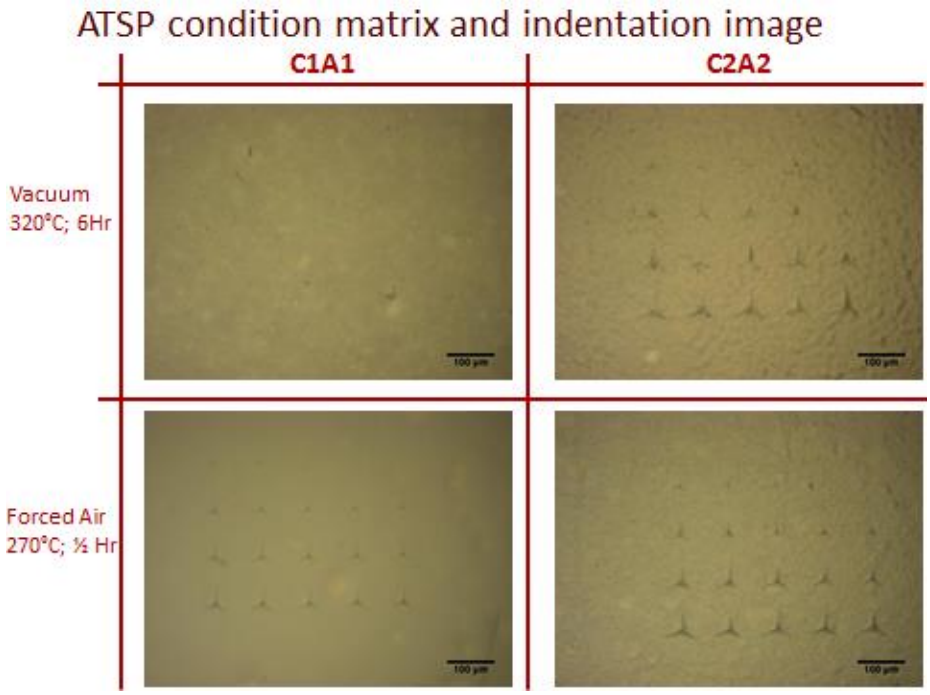

Figure 4.10 ATSP Condition matrix and indentation images. Top left (a) C1A1 cured in vacuum for 6 hr at 320°C. Top right (b) C2A2 cured in vacuum for 6 hr at 320°C. Bottom left (c) C1A1 cured in forced air at 270°C for ½ hr. Bottom right (d) C2A2 cured in forced air at 270°C for ½ hr.

PTFE-, PEEK-, and ATSP-based polymeric coatings were subjected to microscratch testing to investigate their viscoelastic (recovery) properties and to correlate these results with their tribological behavior. Figure 4.11(a,c,e) and Figure 4.11(b,d,f) show representative microscratch results obtained with ramp loading up to 10mN for PTFE/Pyrrolidone-2 and PEEK/PTFE coatings, respectively. As described in section 5.2.3, the in-situ scratch profiles were normalized using the pre-scan to correct for the surface topography. Shown in the Figure 4.11(c) and 4.11(d) are the in-situ deformations with red color (that includes both elastic and plastic deformation) as well as the post scan with green color that shows the permanent (or plastic) deformation only (the difference being the elastic recovery). In the case of PEEK/PTFE, most deformation was plastic as seen in Figure 4.11(d). Also, compared to the smooth scratch curves of PTFE/Pyrrolidone-2, Figure 4.11(c), PEEK/PTFE showed significant fluctuations. This can be attributed to both its rougher surface, and also to its non-uniform (semi-crystalline) structure which was also examined in Chapter 4. Along with the displacement curves, the in-situ COF corresponding to the displacement curve (red) was also measured as seen in Figure 4.11(e) and 4.11(f). A relatively stable COF was observed for PTFE/Pyrrolidone-2 coating, while PEEK/PTFE coating showed some fluctuation due to a rougher surface and possibly its semi-crystalline microstructure as well.

Figure 4.12(a,c,e) and Figure 4.12(b,d,f) show the microscratch results obtained with ramp loading up to 20 mN for 1% ATSP/PTFE and 5% ATSP/MoS_2 coatings, respectively. Compared to PTFE- and PEEK-based coatings, these coatings showed relatively smoother scratch curves and thus stable friction coefficient during the scratch. Also, it was observed that

most of deformation was elastic for ATSP-based coatings showing significant amount of recovery of deformed surfaces.

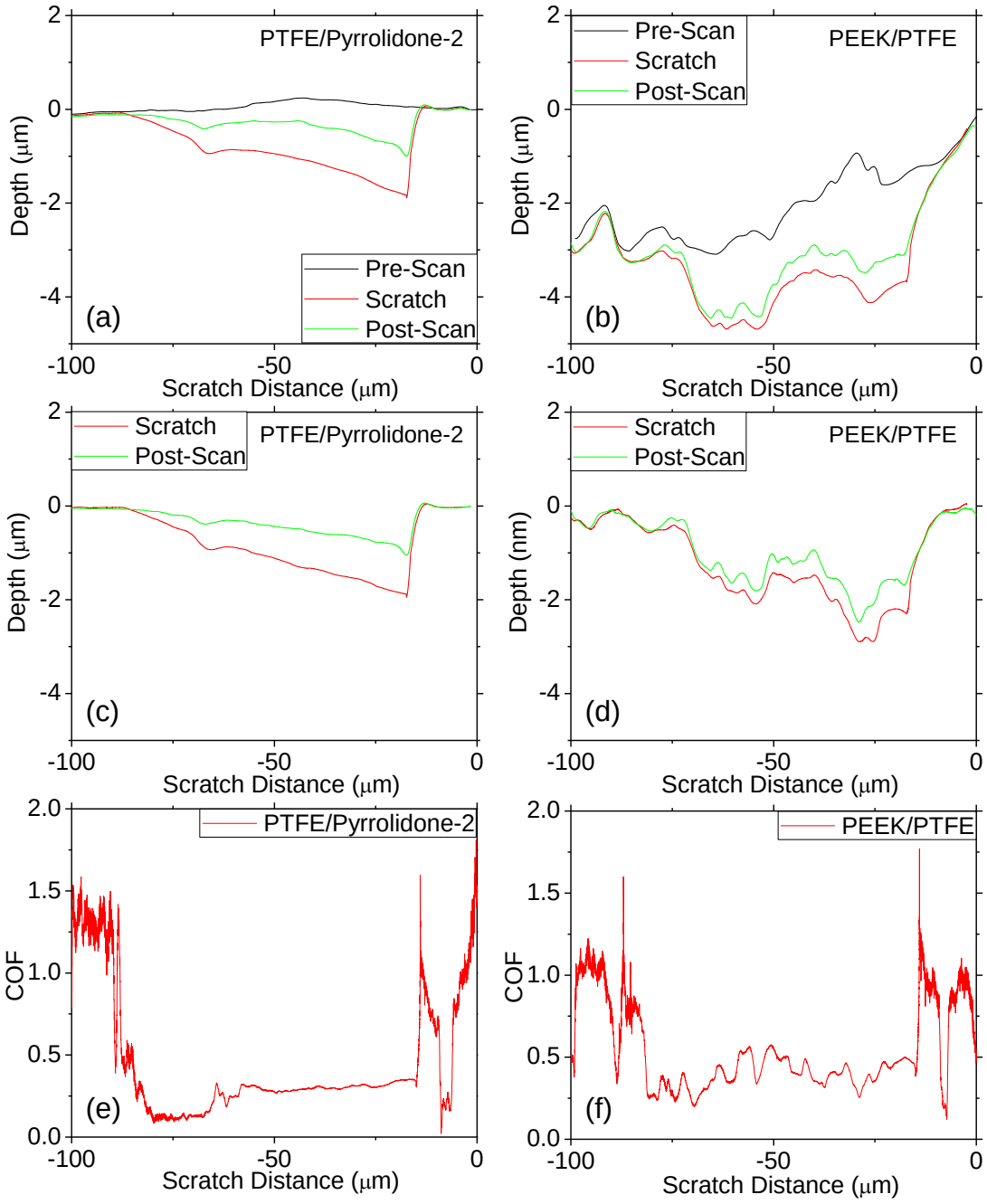

Figure 4.11 Microscratch curves from ramp-loading up to 10 mN for (a) PTFE/Pyrrolidone-2 ((c) after normalization), and (b) PEEK/PTFE ((d) after normalization). *In-situ* friction coefficient of (e) PTFE/Pyrrolidone-2 and (f) PEEK/PTFE coatings monitored during the actual scratch cycle.

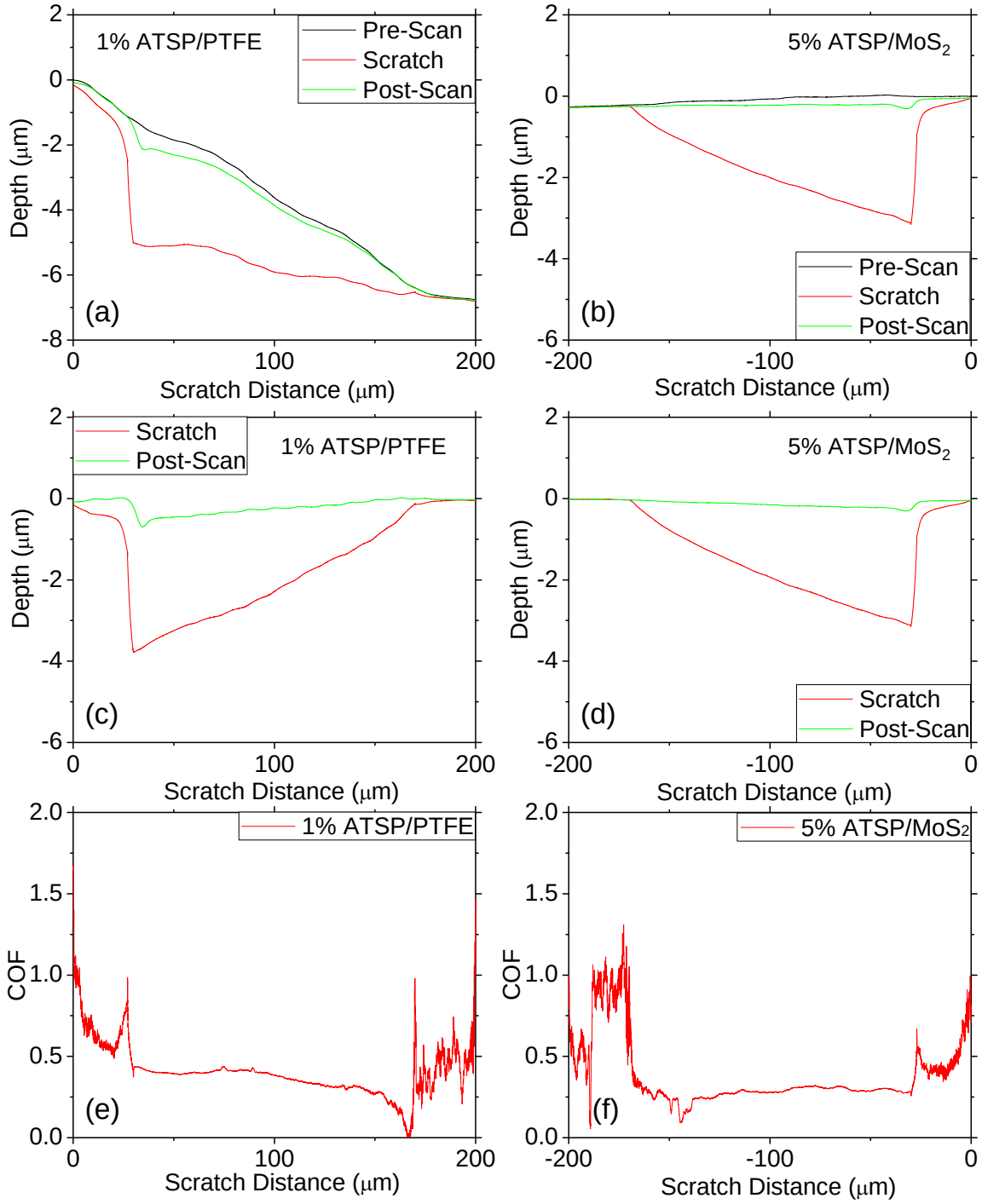

Figure 4.12 Microscratch curves from ramp-loading up to 10 mN for (a) 1% ATSP/PTFE ((c) after normalization), and (b) 5% ATSP/MoS_2 ((d) after normalization). *In-situ* friction coefficient of (e) 1% ATSP/PTFE and (f) 5% ATSP/MoS_2 coatings monitored during the actual scratch cycle.

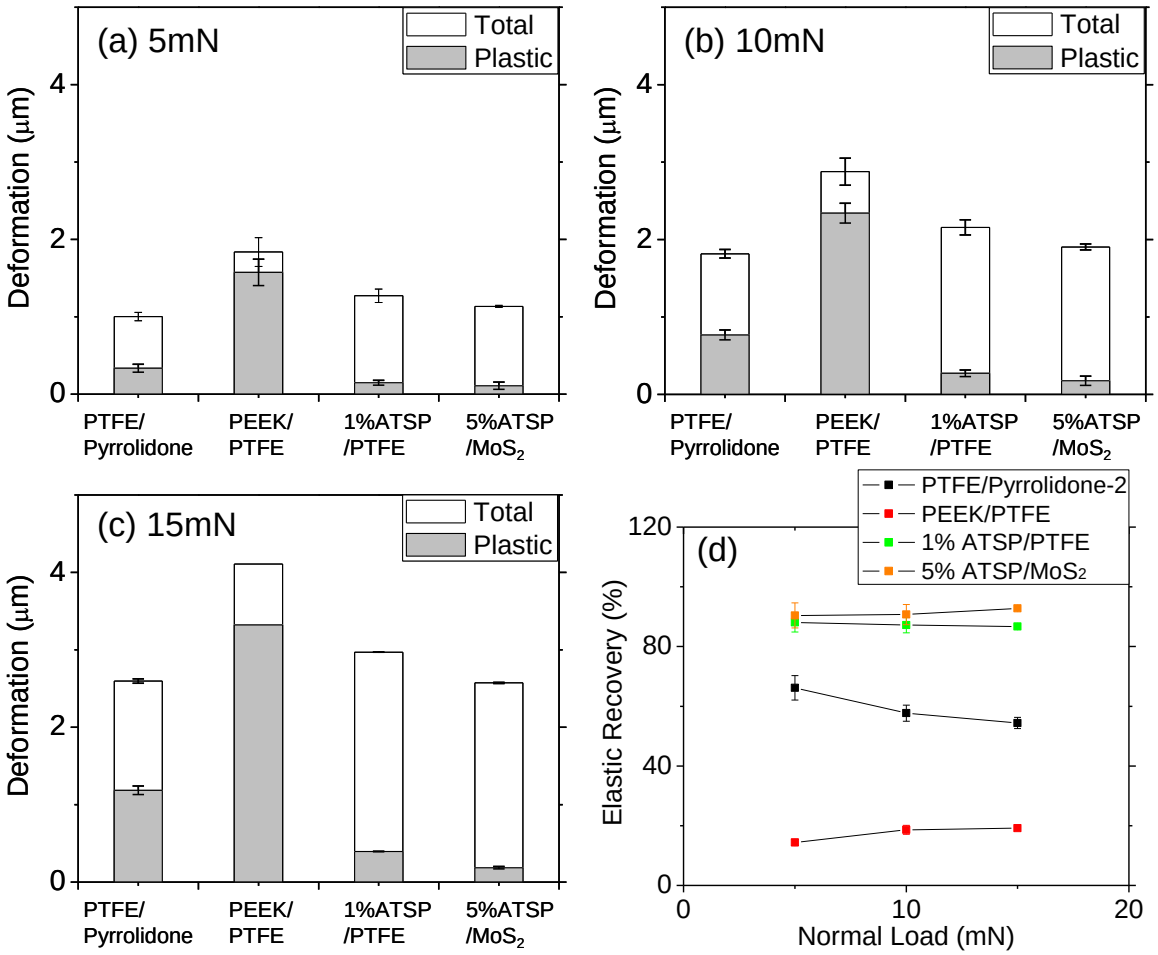

Figure 4.13 Total (penetration depth) and plastic (permanent) deformation of four different polymeric coating surfaces at (a) 5mN, (b) 10mN, and (c) 15mN normal load; (d) elastic recovery of coatings with respect to normal loads.

Triboindenter testing up to high loads (Figures 4.15 through 4.17) demonstrates that there exists for ATSP a specific contact stress through which deformation is recovered in both indentation and scratch-type experiments. This is compared in Table 1 for C1A1 with several other neat polymers and tradename coatings a discrete event wherein a high level of elastic recovery switches to a plowing mode (illustrated in Figure 4.19). Figure 4.18 shows an example from this table of a neat P84 polyimide coating verus C1A1. This generally demonstrates that C1A1 has an incredibly high cohesive strength and will recover

deformation. This is thought to be in part due to the high cross-link density and the available microscopic deformation mechanisms shown in Figure 1.1 around the ester bond creating a constrained conditioned that requires a very high stress to produce rupture and a transition to a plow-deformation.

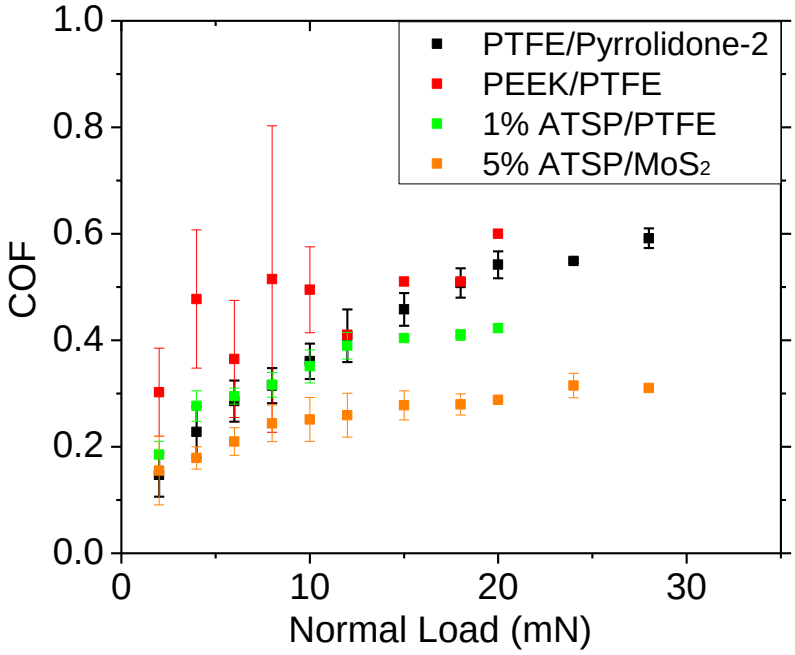

Figure 4.14 *In-situ* friction coefficient vs. normal loads of 4 different polymeric coating surfaces measured during actual scratch cycle.

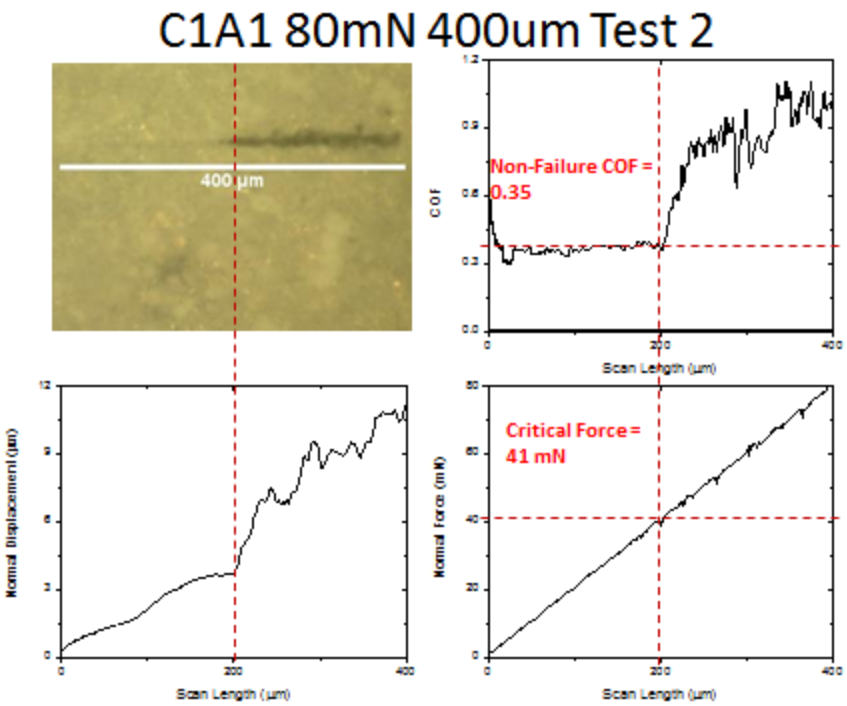

Figure 4.15 Example nanoscratch data from Hysitron triboindenter on C1A1-type coating with 5wt% PTFE. Top left is reflected light optical image at 20X. Top right is COF versus scan length. Bottom left is normal displacement of indenter tip versus scan length. Bottom right is normal force applied by indenter tip versus scan length. Specimen displays stead-state non-failure wear COF and sharp critical force.

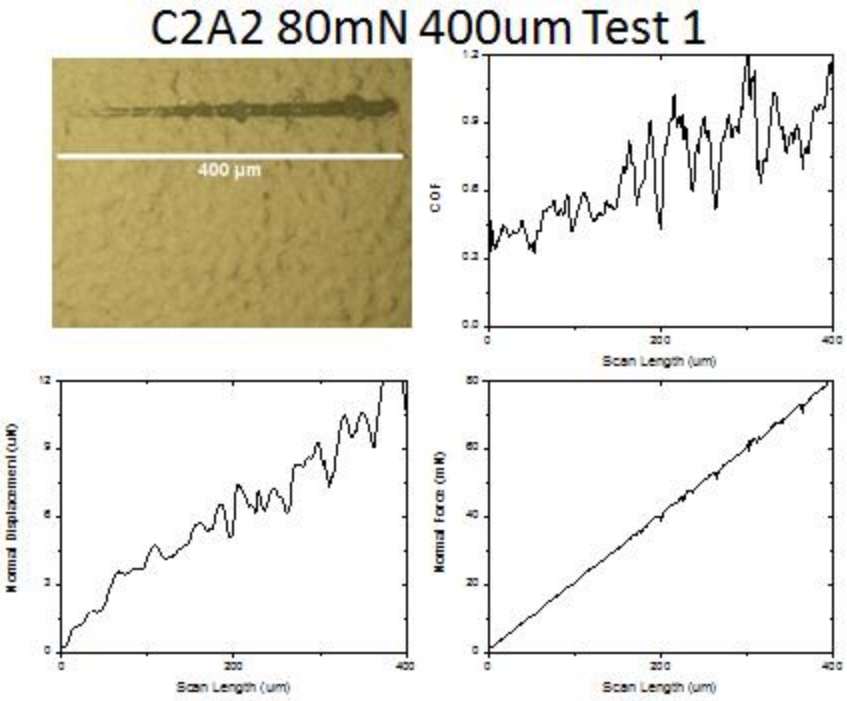

Figure 4.16 Example nanoscratch data from Hysitron triboindenter on C2A2-type coating with 5wt% PTFE. Top left is reflected light optical image at 20X. Top right is COF versus scan length. Bottom left is normal displacement of indenter tip versus scan length. Bottom right is normal force applied by indenter tip versus scan length. Specimen does not display a stead-state non-failure wear COF and evidences no sharp critical force.

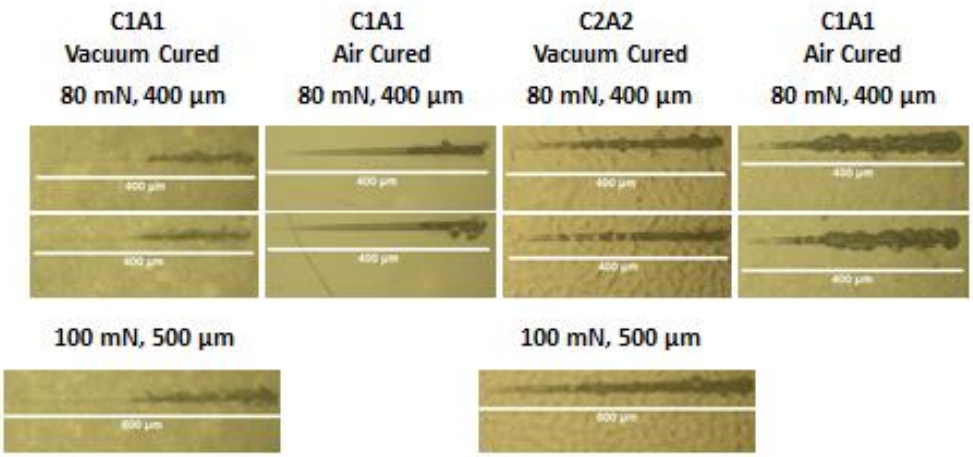

Figure 4.17 Scratch image summary for ATSP coatings.

Table 4.1. Condensed scratch parameters versus fully cured (under vacuum) C1A1.

Coating Type	Testing Conditions	Critical Force (mN)	Non-failure COF	Elastic Recovery (%)
C1A1	80mN / 400um	69-80+	0.3-0.33	92-98
C1A1/PTFE	80mN / 400um	45-48	0.34	90-95
ABS	80mN / 400um	N/A	N/A	---
PC	80mN / 400um	56	0.96	---
PTFE	80mN / 400um	N/A	N/A	---
PAI/PTFE	80mN / 400um	N/A	N/A	50-65
DGEBPA Epoxy	80mN / 400um	N/A	N/A	40-60
PMDA-ODA PI	80mN / 400um	50	0.50	60-86
P84	80mN / 400um	38	N/A	40-60
PEEK/PTFE	80mN / 400um	N/A	N/A	15-20

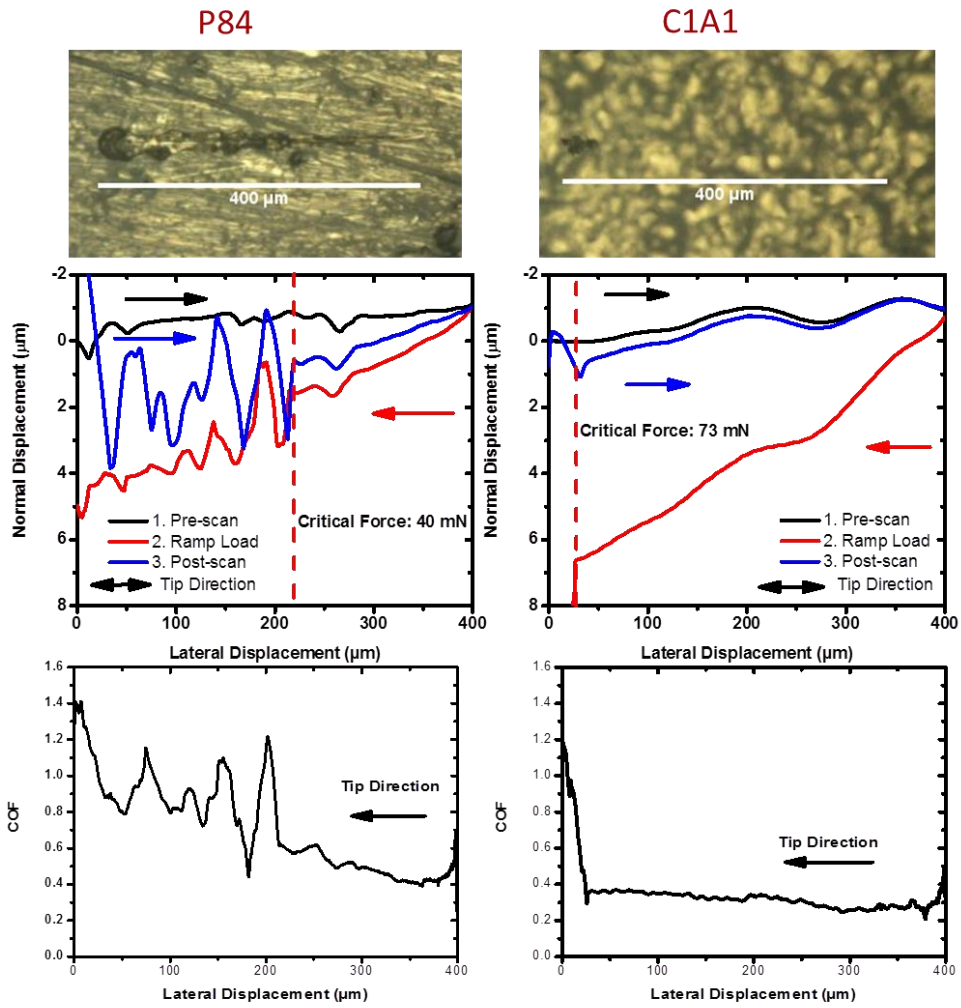

Fig. 4.18. Example scratch for P84 versus C1A1 ATSP. Tip direction proceeds as arrow indicates.

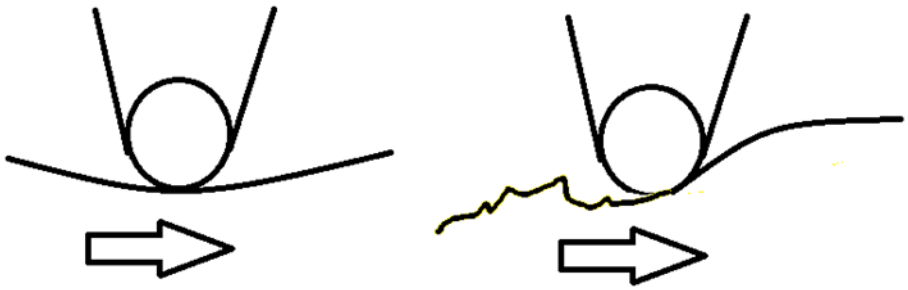

Fig. 4.19. Cartoon of transition from an elastic and recoverable mode to plowing deformation mode in ATSP coatings.

Electrostatic and solvent-borne deposition of a variety of different ATSP formulations (C1A2, C2A1, C1A1, C2A2 and CB2AB2 with 5% PTFE) were also examined. Figure 4.20 illustrates the results of scratch experiments performed on ATSP solvent-borne and electrostatic spray-coated panels. The COF results for electrospray coated panels are qualitatively in-line or even better indicating that the electrostatic deposition technique can produce tribologically robust coatings.

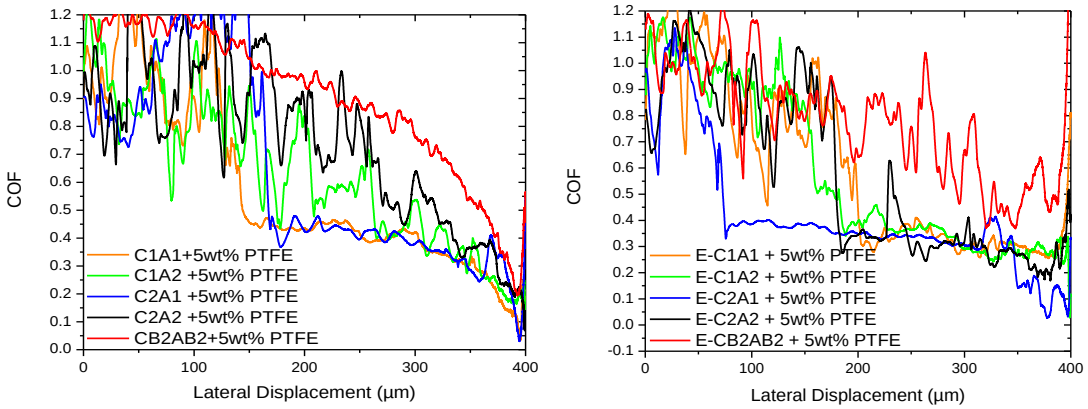

Fig. 4.20. Scratch experiments results conducted on ATSP-coated Q-panels; (left) solvent-borne, (right) electrostatic deposition.

CHAPTER 5

ADVANCED CHARACTERIZATION OF CONTINUOUS FIBER / ATSP COMPOSITES

5.1: Introduction and Background

As discussed in Chapter 1, the high mechanical properties of these materials are seen to arise from their orientational self-ordering [1] and high rigidity of their constituent units. Examining the simplest of the class of LCPs, poly(HBA) as shown in Figure 1.1, the phenylene units are prevented from rotating and conformational freedom is only available through crankshaft motion about the ester bond [38].

In addition to their robust mechanical properties (see Chapter 1), LCPs are also known to have excellent chemical resistance, high heat deflection temperatures and flame resistance, and hydrolytic stability [1, 2,9,11]. These features make them attractive as matrices in high performance composites. To date though, no LCP is known to have been successfully marketed as a matrix for continuous fiber reinforced composites.

A number of oligomeric systems with varying functionality and molecular weight have been developed and characterized. The oligomers can be tailored to be liquid crystalline by adjusting the molar ratio, thus providing unique advantages compared to conventional polymers. In addition, the number of functional groups can be modified to affect the crosslink density. Varying the molecular weight adjusts the mechanical properties of the neat resin and composite .

ATSP can be produced in either amorphous or liquid crystalline formulations by selection of appropriate oligomers. Oligomers which do not display birefringence individually in their melt form amorphous polymers when cured while those that do display birefringence produce polymers which are birefringent after full curing[38,51]. Birefringent oligomers have similar molecular weights as isotropic oligomers but with a lower feed ratio of the crosslinker (TMA) which results in a longer chain length between

crosslinks, as shown in Table 2.2. Figure 1.4 displays the difference in birefringence between amorphous and liquid crystalline fully cured ATSP.

One aspect where the tendency of LCPs to locally match coefficients of thermal expansion to carbon fibers (as discussed in Chapter 1) may find utility is in areas where a composite structure is exposed to a high degree of thermal cycling. An example application of this is reusable composite cryogenic fuel storage tanks. These are large filament wound structures (see Figure 5.1), while composite articles in this study will not be filament wound, generally comparable properties can be obtained and resin-dominate failure mechanics still hold [95,110].

Fig. 5.1. Composite filament wound cryogenic storage tank under fabrication for NASA's Space Launch System (SLS). From [131].

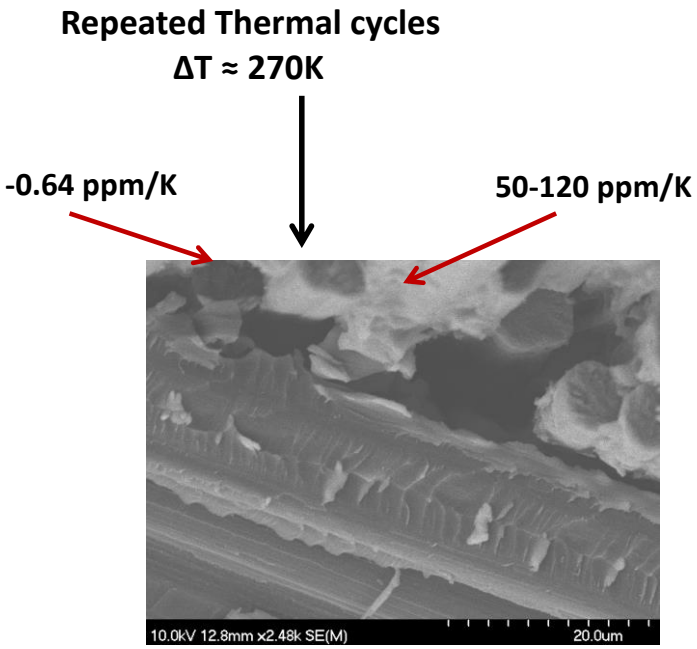

Fig. 5.2: Microcracks in an Epon 828/IM-7 carbon fiber composite produced by thermal cycling.

Local orientation of LCPs around carbon fibers has been observed in the literature via x-ray diffraction (XRD) [18], as we all nuclear magnetic resonance (NMR) [38] and polarized light microscopy [17,51]. XRD Observations by Chung, et al observed that the degree of orientation is very similar for both the LCP molecules and the carbon basal plane. They note that alignment parallel to the carbon surface is the most stable state for liquid crystal domains. This then presents the question of whether there is any difference in the mechanical bonding between fiber and matrix for matrices which are chemically similar to the LCP but are amorphous in the bulk material. The objective of this study is to investigate whether there is any significant difference in the strength of the bond between fiber and matrix as distinguished between amorphous and liquid crystalline formulations of ATSP and whether a highly oriented fiber surface (such as found on graphite fibers) is a strongly influencing factor. That is, do amorphous fibers (in this case glass) evidence the same difference, if any, in the strength of the bond between fiber and matrix when the ATSP composition is varied between amorphous (C1/A1) and liquid crystalline (C2/A2).

As well, lightweight structural concepts are necessary to enhance and enable space transportation for future exploration and science missions. Reduced mass of launch vehicles yields increased payload mass fraction, which is a critical need for all in-space systems. In addition, resilient cryo-tank concepts will also improve launch vehicle safety and potentially lead to orbital fuel storage tanks.

Advanced composite materials processable by cost-effective manufacturing play an important role in developing lightweight structures for future space and planetary systems. With the growing demand for improved performance, especially in aerospace, advances in polymer systems with extreme thermo-mechanical properties are critical in providing: (1) excellent retention of mechanical properties in high temperature environments and (2) high resistance to microcracking at cryogenic temperatures for advanced NASA requirements as described in NASA's Roadmap Technology Area 12 [133].

Development of material technologies for lightweight structures is critical for the aircraft industry to facilitate next generation aerospace missions. Although polymer resins like epoxies are used extensively, there is still a need for improved high temperature systems that are stable in aggressive environments. Design of thermally stable polymer matrices > 350 °C is an important key in production of structural components for high-speed aircraft and lightweight components near the engine [12-13,110]. The most widely used resins, epoxies, are stable only up to 100-120 °C for long-term usage [95]. The phenylethynyl terminated imide oligomers developed at NASA Langley have a degradation mechanism which is evident as low as 177 °C [134]. Additionally, the imidized oligomers employed in several NASA studies [13-17] have high melt viscosities (~ 4,200 cP) compared to that needed for successful vacuum assisted resin transfer molding (VARTM) that yields low porosity and high mechanical properties. Other polymeric resin systems that have been designed for high temperature stability are phenyl based epoxies, polyimides, bismaleimides, PEEK and Vectran. However, these polymeric systems generally possess either limited thermal properties or have extremely high melt viscosities that preclude fabrication of low-porosity, high quality composites [9]. Additionally, thermoplastics like PEEK provide an advantage over commercially extant thermosets with improved fracture toughness but their Tg is limited to 150 °C.

Some applications, like future supersonic transportation, require composite materials that are not only stable at high temperatures but also with negligible microcracking when cycled over a range of temperatures (thermal fatigue resistance). Thus the design of next generation polymer composite fuel tanks as well as structural composites for supersonic vehicles relies on thermally stable systems that are also thermal fatigue resistant [1,10]. Fiber reinforced composites cured at elevated temperatures contain thermal residual stresses after fabrication because of a coefficient of thermal expansion (CTE) mismatch between the carbon fiber (negative CTE) and matrix (positive CTE), and a mismatch in the CTE between plies with different orientations, both of which cause formation of microcracks. Microcracking can cause degradation of mechanical properties such as strength and stiffness [11] and an increase in gas permeability [12].

5.2: Single Fiber Fragmentation

One of the most reliable microtest method available [132] that measures fiber-matrix interface strength is single fiber fragmentation test (SFFT), of which a schematic is shown in Figure 5.3. In SFFT, a dogbone of polymer bearing a single fiber at the centroid of the dogbone cross-section is strained to at least three times the elongation at failure of fiber it bear. The fragment length of the fiber is then observed. The fragment lengths (l), fiber tensile strength (σ_f), and fiber diameter (d) are then related to the interfacial shear strength.

$$\tau_i = K\frac{\sigma_f}{2}\left(\frac{d}{l}\right) \tag{1}$$

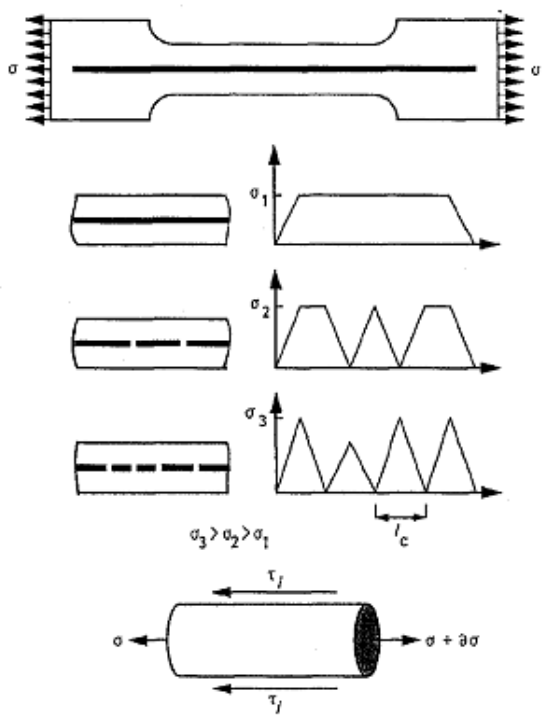

Fig. 5.3: Schematic representation of single fiber fragmentation process. From [132].

C1, C2, A1, and A2 oligomers (solids at ambient temperatures) were mechanically ground into a fine powder and purified using a 3:1 methanol:water solution in a Soxhlet extractor whose primary bulb was set by thermocouple-controlled heating mantle set at 70°C for 24 hours. The oligomers were then vacuum dried at 70°C for 48 hours.

Oligomeric solutions in N-methyl-2-pyrrolidone (NMP) were prepared by first blending dried carboxylic acid and acetoxy-end-capped oligomer powders at a 1.1:1 carboxylic:acetoxy to reflect the higher average molecular weight of the carboxylic oligomers. Oligomers were then weighed out to 0.3 g and dissolved into 10 mL of NMP stirred at 75°C.

Single filaments of Hextow IM-7 carbon from Hexcel and unsized Advantex fibers from Owens Corning were separated from their tows and individually laid onto one of the specially machined PTFE molds.

Great care was taken to only touch the ends of the separated fibers. Fibers were secured at the ends of the mold in a crevice that extends to the midpoint of the mold cavity using modeling clay.

Oligomer solution was carefully transferred to fiber surface using a fine metal-tipped syringe. Solution was observed to wet and coat the fibers within 15 seconds under a stereoscopic bench microscope. After coating all 8 fibers per mold, molds were placed in a thermocouple-controlled oven programmed with the temperature profile shown in Figure 5.9 under vacuum. Molds bearing ATSP-coated fibers were then removed from the vacuum oven. Previous investigation by AFM had shown coatings produced in this manner had a thickness of up to 600nm.

The molds were then filled with a degased 31:32:32:37 mixture of EPON 828, HELOXY 505, and Lindride 6K. Care was taken to pour slowly and minimally disturb the fiber. Epoxy dogbones were then cured at 120°C for 4 hours before removal by bending mold along the transverse direction.

Produced specimens were then examined for well-aligned fibers in the center of the dogbone. Specimens which failed to meet this criteria were discarded.

The specimens were then tested in a microstraining apparatus capable of applying sufficient load to fracture the coupons. Specimens were clamped at the ends and given an elongation of 20%. Fiber fragment lengths were then observed and recorded using a transmitted light polarizing microscope with one polarizer below and one polarizer above the test coupon to see birefringence.

Fiber fragment lengths (as in Figure 5.4) were digitally captured and analyzed using the pixel counter function in NSF Image J. Figure 5.5 shows the histogram of C1/A1 on Advantex glass fibers. This data is summarized in Table 5.1. Weibull analysis of the was performed in OriginPro 8.6 with the critical length estimated by equation (2):

$$\mathrm{E}[l_c] = \alpha\Gamma(1 + 1/\beta) \tag{2}$$

Where α is the scale factor and β the shape parameter computed via a gamma function to arrive at the mean $E[l_c]$.

The IFSS of the fibers was then calculated using equation (1) and are likewise reported in Table 5.1.

Table 5.1. Summarized mechanical properties of amorphous and liquid crystalline ATSP coupling agent.

	C1/A1	C2/A2*
Advantex Advantex 22 µm 3200 MPa	α = 0.49 β = 2.76 l_c = 0.436 mm τ_i = 63.9 MPa	α = 0.43 β = 3.11 l_c = 0.384 mm τ_i = 72.8 MPa
IM-7 IM7 5.1 µm 5310 MPa	α = 0.25 β = 3.55 l_c= 0.225 mm τ_i = 53.5 MPa	α = 0.16 β = 3.29 l_c = 0.143 mm τ_i = 84.2 MPa

IFSS for all ATSP coated fibers was very high compared to published values for other fiber/matrix systems for all combinations of the ATSP fiber/matrix interface. Previous to this study, there does not appear to be any published information for IFSS of LCP fiber/matrix interfaces. One study [136] of Kevlar 49 fibers embedded in an epoxy matrix presents IFSS values ranging up to 35 MPa, while IFSS values in the range of 20-30 MPa are fairly common for glass fiber and epoxy systems [137].

The primary trend observed in these values is that ATSP formulations that are liquid crystalline in the bulk polymer exhibit significantly higher IFSS values over their amorphous counterparts. The physical reasoning for this is that if the polymer at the surface has a higher degree of orientation (Q), as characterized by equation (3) and observable via XRD enables a stronger self-reinforcing effect.

$$Q = \frac{3\langle \cos^2 \theta \rangle - 1}{2} \tag{3}$$

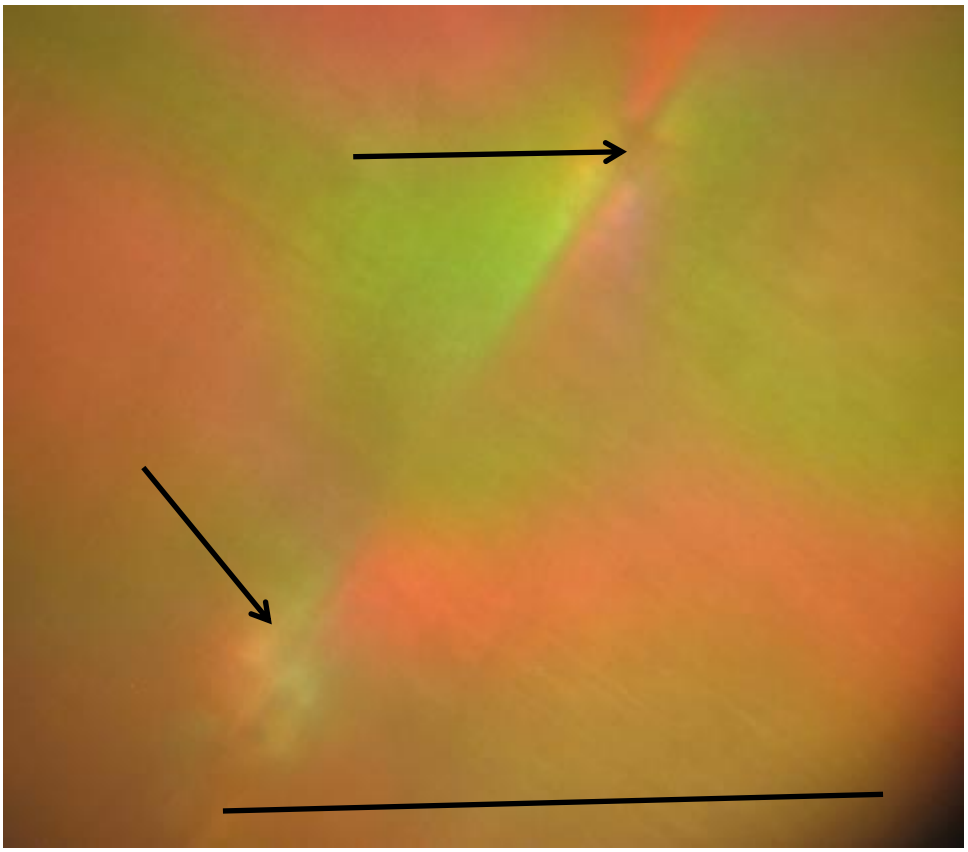

Fig. 5.4: Fiber fragment length by cross-polarized transmitted light microscopy. Arrows indicate fiber breaks. Scale bar is 500 µm.

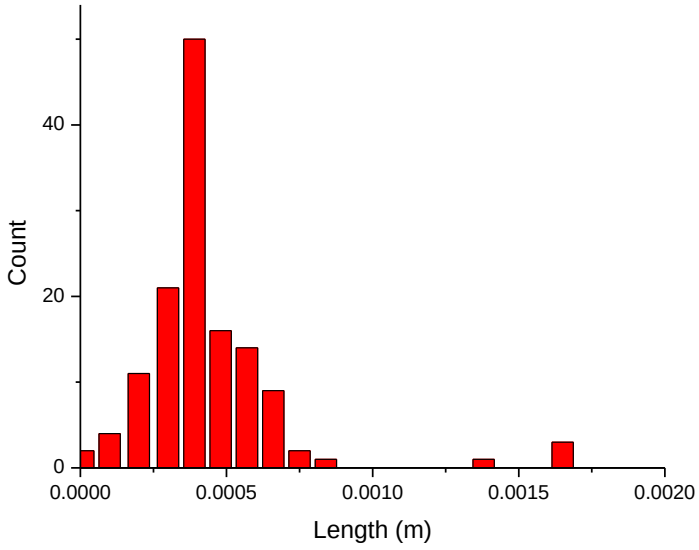

Figure 5.5: Histogram of C1/A1 on Advantex glass fiber fragment length.

One trend that is not definitively displayed is a significantly higher interfacial shear strength for highly oriented fibers (IM-7 carbon fibers) as compared to the amorphous Advantex glass fibers. This indicates that a highly oriented fiber surface does not appear to be required to induce local ordering of the LCP.

The very high IFSS values indicate that in continuous fiber composites based on ATSP, failure should be highly resin dominated rather than dominated by fiber debonding and pull-out. This is corroborated by SEM images of ATSP/C-fiber which show high cohesion of the matrix to individual fibers and fracture surfaces which indicate matrix dominated failure.

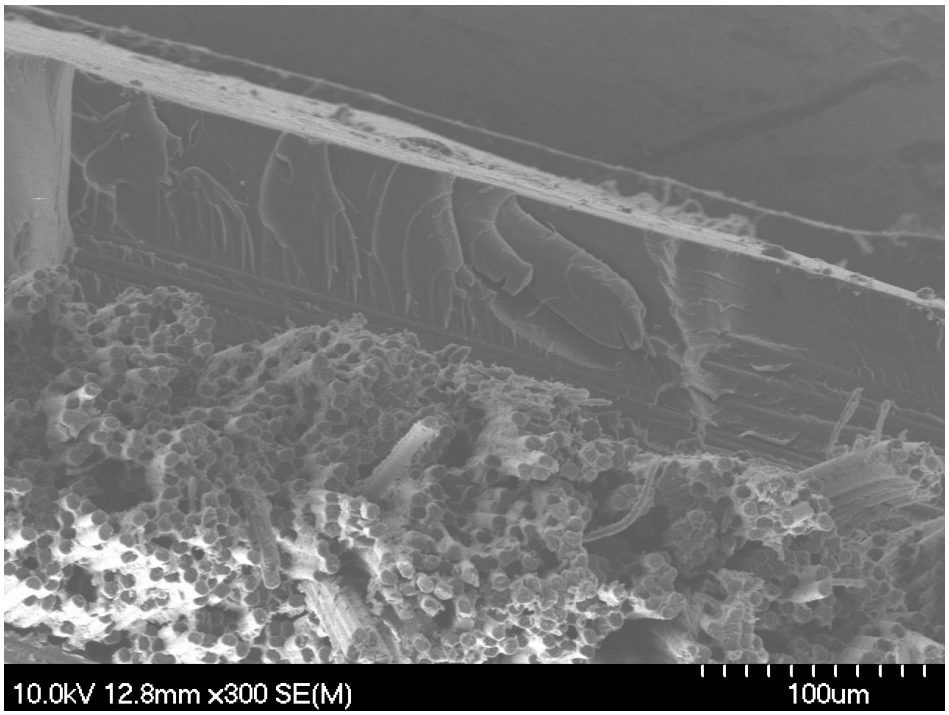

Fig. 5.6: Interface between 0° and 90° fiber tows showing river lines and good adhesion in the 0° tow.

In Figure 5.6, on the right of the 90° tow, the fracture occurred at a lower level than that on the left side. This results in more of the 90° fibers being visible. The fibers in the 0° tow are mostly held together as a single consolidated bundle with very few stragglers. This suggests that the bonding between the resin and the fiber surface was strong and was able to resist fracturing during the testing. The strength of the bond is likewise shown by the few fibers that have been slightly pulled out and still have resin adhered to them. Figure 5.7 likewise shows resin dominated interlaminar failure. In this case, a crack runs between the 0° and 90° plies in a resin-rich region. Figure 5.8 is a higher magnification view of Figure 5.6 showing good wetting of resin even near the fiber fracture surfaces.

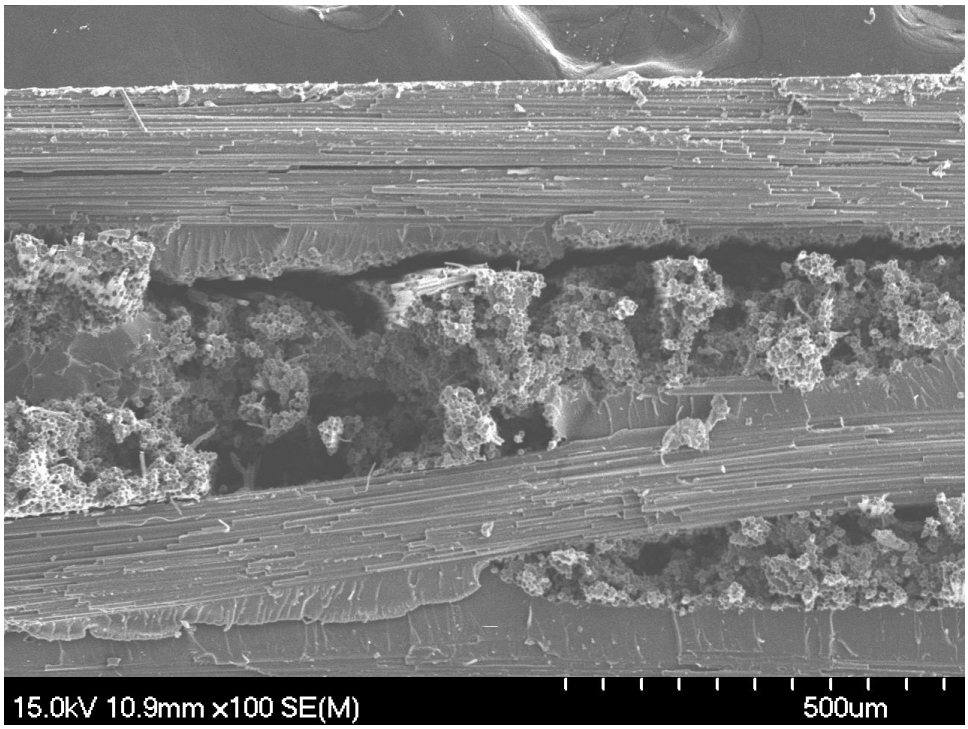

Fig. 5.7: Area where two plies meet, showing resin-rich areas between plies and a crack between the 0° and 90° of the top ply.

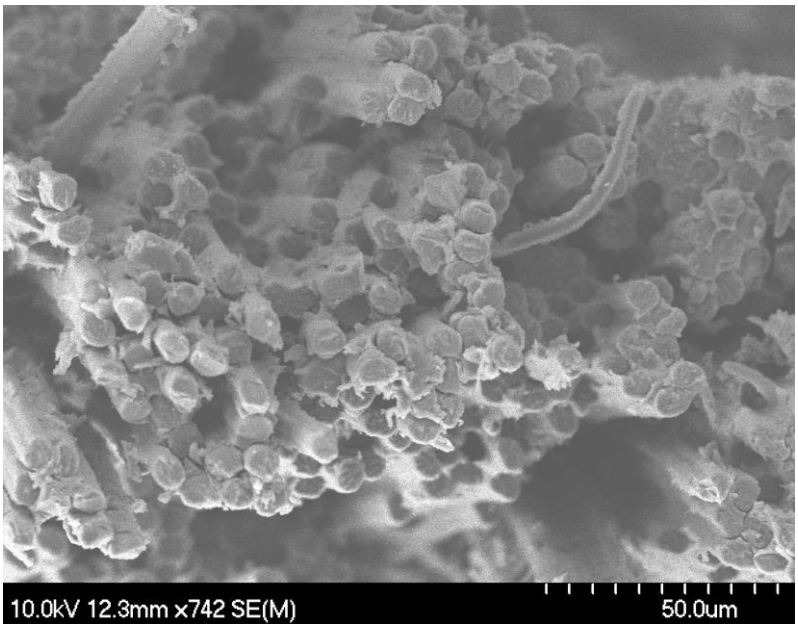

Fig 5.8: Higher magnification of 0° tow in Figure 9 with good wetting of resin between fibers.

5.3: Characterization of ATSP as the Resin-phase for Composite Cryogenic Storage Tanks

ATSP oligomer prepregs was prepared following closely from Parkar, et al [16]. Equimolar blends of ATSP oligomer powders was added to n-methylpyrrolidone (NMP) and stirred at 70 °C until a homogeneous solution is produced. It has previously been found [9,16,17] that solutions of 0.5 grams of oligomer per mL of NMP will produce composites with a 55 vol% fiber fraction when an excess of 20% oligomer mass (with a cured density of 1.35 g/cm3) to that necessary from mass balance. Therefore, 2.22 mL of ATSP oligomer solution was infiltrated into each gram of a unidirectional mat of IM-7 carbon fibers from Hexcel. Prepregs will then be desiccated of NMP to a leathery state wherein the composite prepreg has excellent drape.

To process the composites and remove the volatiles, a custom enclosed Carver hot press was used. Two 1.27 cm thick steel plates was used in order to protect the platens in the hot press. A Kapton film and fiberglass reinforced Teflon peel-ply was placed on either side of the composites to isolate it from the steel plates. The composite specimens will then be treated to the temperature cycle shown in Figure 5.9. At 205 °C, the vacuum pump was engaged to remove excess NMP. A pressure of 0.7 MPa was applied at a sample temperature of 330 °C. After the cycle is complete the sample was allowed to cool in the hot press to room temperature and then removed for characterization.

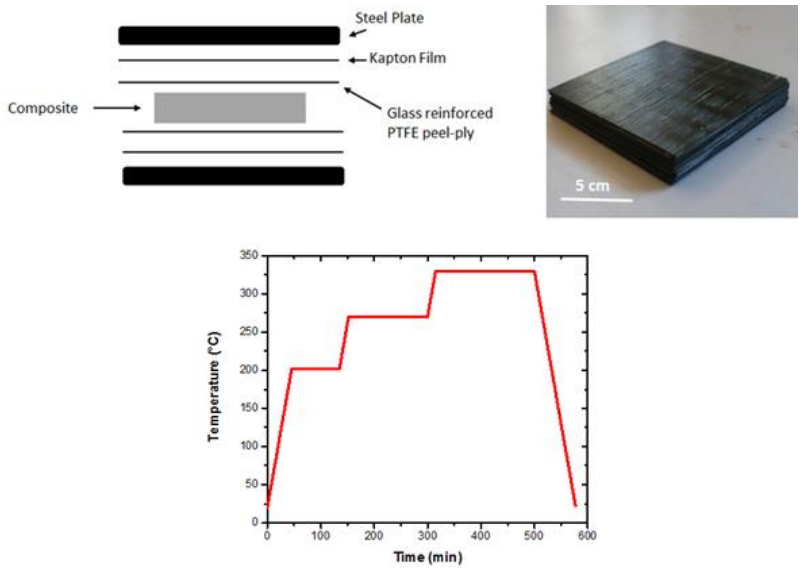

Fig. 5.9. Layup for ATSP composite cure (top, left), final thick cured ATSP composite specimen (top, right), and cure cycle for ATSP composite (bottom)

Composite specimens produced by this route will then be joined to desired specimen thickness by use of ITR to produce thick consolidated specimens. Individual plies were stacked together and exposed to the heat and pressure cycle described above, after which they will have a seamless bond with excellent Short Beam Shear Stress (SBS) (above 60 MPa) [9]. Plies were arranged to produce [0/90]s composites of approximately 2 mm in thickness as in Moll, et al [18] for comparative purposes.

VARTM was examined using the same unidirectional IM-7 carbon fibers and oligomer solutions from Task 2. The process will follow prior reports on VARTM of other high temperature polymer matrix composites [12-15] but modified to suit the chosen ATSP chemistry. Oligomer solutions were heated to 70 °C to yield viscosities ranging from 100-400 cP. This value is stable indefinitely as the cure reaction does not substantially advance at this temperature. The solution will then be infiltrated into a fiber preform using a VARTM apparatus. A stainless steel tool

plate was used as the base of the VARTM setup with Kapton polyimide film used for the inner and outer vacuum bag and Aluminum screen mesh as the flow media. High temperature sealant putty was used to ensure a vacuum-tight seal between tool plate and bagging. Tooling with fiber preforms (of [0/90]s layup) inside the polyimide bagging will then be transferred to a Thermo Scientific convection oven maintained at 70 °C and attached to vacuum apparatus and the heated container of oligomer solution. The valve connecting the apparatus to the vacuum pump was then be opened to allow the resin solution to be forced in and wet out the fiber preform. Once the resin infusion is complete, a cure cycle analogous to that shown in Figure 5.9 was initiated.

To determine the volume fraction of fibers, resin, and voids (following from ASTM D3171), a sample representative of each chemistry and processing method will first be weighed and its volume determined by an Archimedean procedure and then digested using concentrated sulfuric acid heated to about 80 °C. The samples were left in the acid for sufficient time (from prior experience 8-12 hours for ATSP resins) to remove all of the resin from the fibers. The solutions will then be filtered to recover the fibers and rinsed with copious amounts of water before being put in an oven to dry. The fibers will finally be weighed on a balance and the volume fraction of fibers, resin, and voids was calculated and reported.

ATSP is a unique high temperature matrix which shows potential for use as a high temperature stable matrix for carbon fiber composites for structural applications. Use of these composites for structural applications requires a thorough validation of the mechanical properties of bulk ATSP as well as ATSP/C composite lamina. Various test standards were used for characterizing this continuous fiber composite and neat resin. Tests are designed to study the behavior of composites in different thermal environments to provide insights for Phase II and other future works.

Dynamic mechanical analysis (DMA) was performed in a TA Instruments DMA Q800 on neat ATSP resins to obtain the storage modulus and Tg following ASTM standard D5023-07. After conditioning at 23 ℃ and 50% relative humidity for a minimum of 48 hours, the samples (12.5 mm x 25 mm strips) were loaded in 3-point bending configuration with a span of 25 mm. The cryogenic reservoir was filled with liquid nitrogen and the temperature of the sample was ramped from -196 ℃ to 150 ℃ at a rate of 1 °C/min. The storage and loss moduli was recorded as a function of temperature. The glass transition temperature (Tg) was reported based on the peak in the tangent of the phase angle between room temperature and 300 ℃. Any observation of a cryogenic-range Tβ and Tγ will likewise be reported based on lower tangent peak positions.

Thermal stability of representative clippings of ATSP composite specimens was measured in a TA Instruments TGA 2950 ramped at 10 ℃/min to 600 ℃ in air, N2, and CO2 to replicate a wide range of potential mission atmosphere conditions. The trace of the mass loss/temperature derivative curve as well as the total mass loss was reported. Additional high temperature hold experiments at 371 ℃ for one hour in air was conducted with mass loss as a percentage reported as point of comparison with VARTM polyimide composites from Cano et al. [13-14].

Mechanical strength and modulus of the composites was determined by short beam shear strength (SBS) following ASTM D2344, and flexural strength and modulus following ASTM D790. An Instron mechanical testing machine with temperature shroud was used with a test speed of 1.27 mm/min. Flexural tests will carried out at a test speed of 0.76 mm/min using the same load cell and temperature shroud. Temperature points of -90 °C, RT, and 180 °C was used for this matrix of experiments for comparison with state of art composite materials and published literature [13-17].

Fracture toughness was determined by double cantilever beam (DCB) configuration specimens with a pre-crack introduced during the cure process by thin polyimide film to conform to ASTM D5528. An Instron machine operating in displacement-controlled mode with a crosshead displacement speed of 0.67 mm/s was used with an end-tab configuration affixed by solid state bonded ATSP applied to the end tab to provide a high temperature adhesive [11]. Composite specimens was 20 to 25 mm wide and at least 125 mm long and 3 mm thick. Temperature points of -90 °C, RT, and 100 °C was used for the matrix of experiments.

CTEs for composite specimens was measured on a TA Instruments 2940 thermomechanical analyzer (TMA). Samples was sectioned into 10 mm square blocks and then ramped in the TMA at the rate of 10 °C/min from RT to 300 °C. A force of 50 mN was maintained throughout the test. CTE was examined in this fashion for both longitudinal and transverse sections of ATSP composites. This was compared to state of art composite materials for aerospace and especially cryogenic and high temperature applications.

Carbon fiber-reinforced composites used in aircraft engines and other space applications must be stable and capable of functioning in high temperatures. The main concern is the thermal decomposition and thermal oxidative degradations at their service temperature that will affect performance. In addition, microcracking can be observed during changes in temperature and repetitive thermocycling, which leads to degradation in mechanical properties and an increase in composite permeability. Microcrack development forms a penetrating network through the thickness of the composite leading to cryogens leakage through the tank wall and limiting their use in cryotanks [138].

Several composite specimens from each resin formulation was subjected to 200 h at 280 °C in air. Samples tested in this manner will then be subjected to short beam shear experiment.

The thermal fatigue characteristics of ATSP versus a reference high performance epoxy composite currently used in prototype cryogenic tanks (provided by NASA) was studied by thermal cycling over a range of temperatures. A schematic of the cycler is shown in Figure 5.10, which consists of an oven and a cryogenic bath. First an ATSP composite sample was examined under an optical microscope to verify that no cracks are present prior to thermal cycling. Then a composite sample is placed in a wire basket and cycled repeatedly from oven to cryogenic bath. A heated copper barrel can be used to heat up the sample. The temperature of the barrel is set using a temperature controller and a thermocouple. The sample was heated up to the ambient oven temperature (35 °C) in 8 minutes (based on prior experience), and then cooled to liquid nitrogen temperature (-196 °C) again for another 8 minutes.

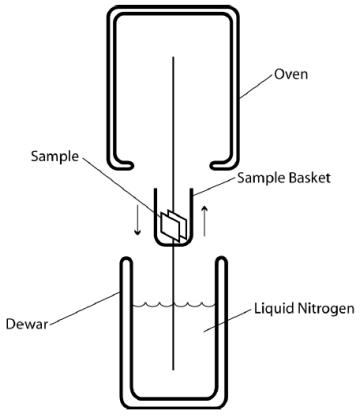

Fig. 5.10. Schematic of the thermal fatigue apparatus.

Sample permeability was evaluated in a pressure cell apparatus. In this experiment, nitrogen is flowed into the cell at a preset pressure recorded by a transducer. If a network of cracks is present in the sample, nitrogen gas will flow through the sample and results in an increased output pressure on the opposite side of the sample. The output pressure is measured and recorded by a second pressure transducer. The test was run for several minutes to monitor the development of the output pressure evolution with time. First the manufactured samples was tested for leaking then the process of cryogenic cycling and permeability testing was repeated until the sample leaks. Before performing the leak test, samples was placed in a desiccator for several hours to ensure all condensation is eliminated.

Current production of ATSP composites has been via a cured prepreg route, which are then solid-state bonded into fully condensed laminates via ITR, all the mechanical characterization, TGAs and volume fraction calculations reported here are for the ATSP/C composites made via prepreg route. However for many larger structures with complex shapes, vacuum-assisted resin transfer molding (VARTM) is preferable in terms of ease-of-fabrication. In this study, VARTM process will be also examined.

Figure 5.11 shows the schematic diagram of fabricating ATSP carbon fiber composite. A lamina of ATSP was made by first wetting the fibers (unidirectional fabric of Sikawrap 103C by Hexcel) with a 50% w/v ATSP solution in NMP and then curing the fabric using the cure cycle shown in Figure 5.9 in a custom-built vacuum-enclosed hot press. A Kapton film and fiberglass reinforced Tefon peel-ply was used to isolate the composite from the steel plates (Figure 5.9). The steel plates were brought together at the middle of step 2 (202 °C). A minimal amount of pressure was applied to remove any residual solvent present. Pressure of 100 psi was applied at the start of the last step (330 °C). The curing reaction was carried out in vacuum to facilitate

removal of the byproduct acetic acid and the solvent. Figure 5.13 shows a solvent impregnated carbon fabric with ATSP resin before and after curing. The average thickness of the cured composite lamina is 0.5 mm.

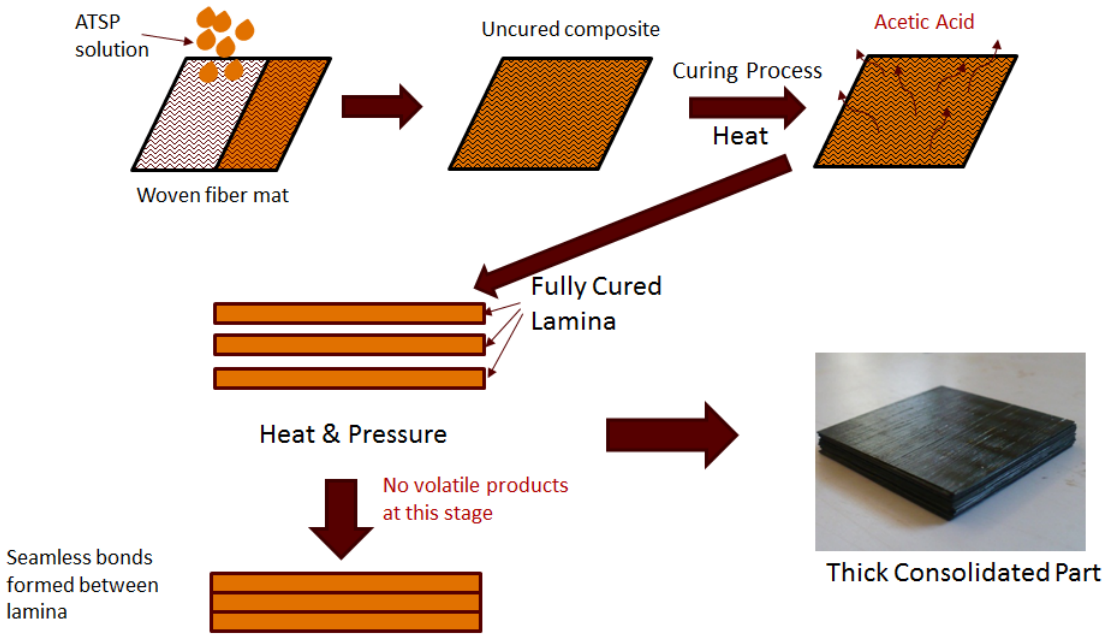

Fig. 5.11. Schematic diagram of fabricating ATSP carbon fiber composite.

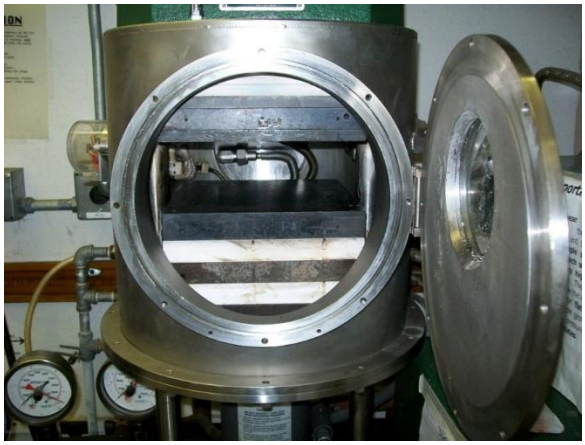

Fig. 5.12. Enclosed hot press used for composite processing.

Composite specimens produced by this route are then joined to desired specimen thickness by use of interchain transesterification reactions (ITR) to produce thick consolidated specimens. Individual plies are stacked together and exposed to the heat and pressure cycle described above, after which they will have a seamless bond (Figure 5.11). This was done by heating the plies under pressure for 4 hours at a pressure of 400 psi. Figure 5.11 shows a 6 mm thick sample formed by ITR.

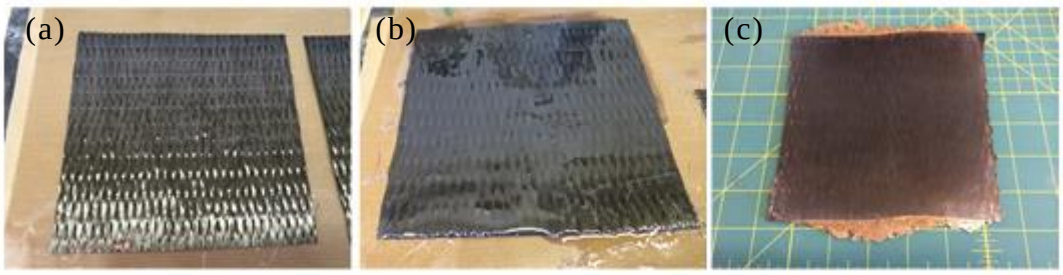

Fig. 5.13. Unidirectional fabric, uncoated (a), coated with ATSP solution (b), cured lamina (c).

Prior to the VARTM process, the vacuum bagging techniques were tested to fabricate an ATSP/C lamina using an ATSP prepreg. A 0.32 cm thick Aluminum tool plate (12" x 12") was utilized as the base of the setup. Kapton polyimide bagging material and high temperature sealant (A-800-3G, from Airtech) were used to seal the bag that contained the fiber preform, PTFE coated fiberglass (from CS-Hyde) and breather material. A breather cloth (Airweave-UHT-800) was also used to allow air and volatile escape (Figure 5.14).

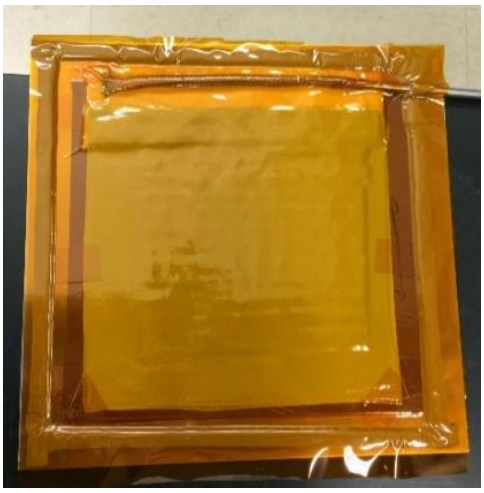

Fig. 5.14. Vacuum bagging sample, after pulling vacuum.

The fiber-reinforced composite panel was cured at 202 °C for 30 min, 270 °C for 1 hour and finally at 330 °C for two hours by applying 26 in Hg vacuum. The obtained cured lamina was fully impregnated with ATSP and the resin content of cured composite was about 44%, but the void content was about 23%. Vacuum bagging of ATSP impregnated weave fabric was also explored, which resulted in void content of 12% (Figure 5.15). This is a reasonable value considering that the fiber weave employed in this experiment was extremely loose (areal density of 197 g/m^2 [5.81 oz/sq. yd.]) and generally produced a high surface roughness of approximately ~100 μm of depth with lateral features of one millimeter in dimension. As the measurement of this density relied on a micrometer with a 0.25" flat sampling surface, the thickness measurement did not capture these depth features and the total sample thickness was only 0.9 mm, the surface roughness was likely a significant component of total thickness and so the 12 vol% of void content serves as an upper estimate.

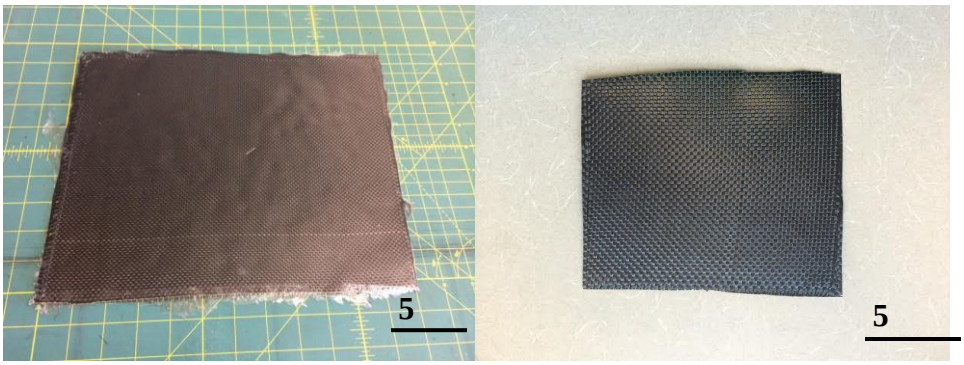

Fig. 5.15. Weave fabric, uncoated (a), and cured lamina (b).

VARTM process was also conducted using the same unidirectional carbon fiber mat and oligomer solutions used for prepreg route. C1A1 oligomer solution was heated to 70 °C to yield viscosity of 50 cP. Figure 5.16 shows the values of C1A1 viscosity at different temperature measured using a spindle type viscometer (Cole-Parmer, 98936 series). These values are stable indefinitely as the cure reaction does not substantially advance at these temperatures. An Aluminum tool plate was used as the base of the VARTM setup and Aluminum screen mesh as the flow media. The high temperature materials that used for vacuum bagging process was utilized for VARTM process (Figure 5.17). Tooling with fiber preforms (of $[0/90]_2$ layup) inside the polyimide bagging was then attached to vacuum apparatus and the heated container of oligomer solution. The valve connecting the apparatus to the vacuum pump was then opened to allow the resin solution to be drawn into the preform.

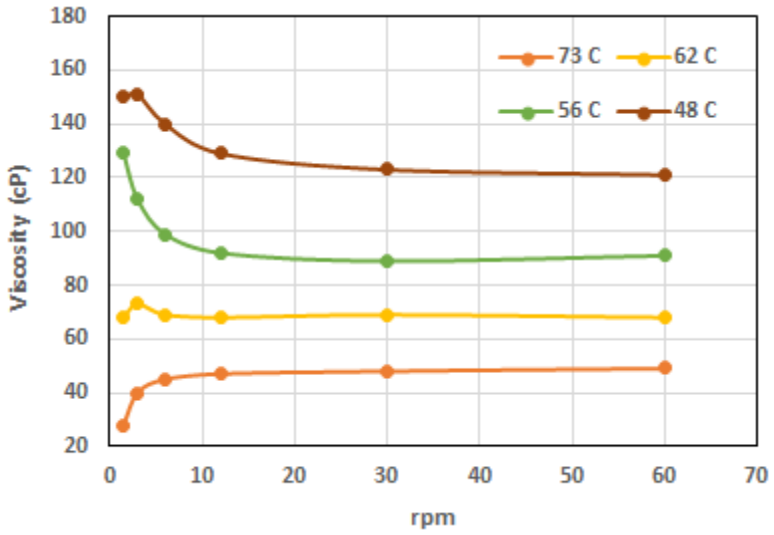

Fig. 5.16. Viscosity values of 50% C1A1 solution at different temperature, using LV-1 spindle

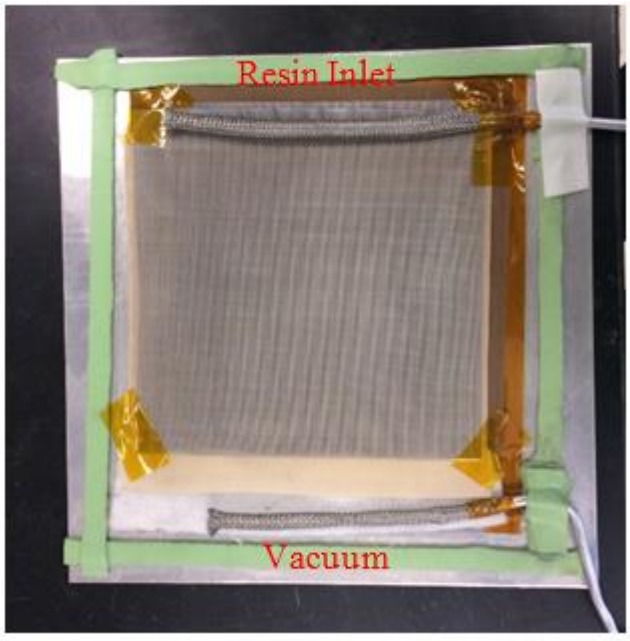

Fig. 5.17. VARTM setup sample, before addition of final Kapton sealant layer.

We were not successful in completely wetting out the fibers with ATSP resin during VARTM process. This was determined by observing the weight increase after 1 and then 2 hours of infiltration time. After one hour of infiltration time, sample evidenced a 21wt% increase in resin content, with visually more resin concentrated on in-flow side of preform. This quantity did not appreciably change after 2 hours of infiltration time. This was due, firstly, to unsuitability of available fiber preforms. Sikawrap 103C was observed to have extremely large tow sizes stitched with nylon thread. The unidirectional preform had a relatively low permeability within the tows that likely prevent successful infiltration of more viscous resins. Secondly, ATSP resin solutions have an increase in viscosity as temperature is decreased towards room temperature. Employed setup did not utilize a temperature zone at the preform. This configuration allowed the ATSP solution to cool to room temperature thus allowing an undesirable increase in viscosity and preventing successful infiltration. Rectification of this issue could include: a modest decrease in resin loading within solution, use of fabrics known to be amenable from literature to be VARTM appropriate, and implementation of a temperature zone at the preform.

To determine the volume fraction of fibers, resin, and voids (following ASTM D3171), representative samples of C1A1/C and C2A2/C, made via prepreg route, were first weighed and the overall density of the samples was determined. The specimen were then digested using concentrated sulfuric acid heated to about 80 °C. The samples were left in the acid for 6 hours to remove all of the resin from the fibers. The solution was then filtered to recover the fibers and rinsed with copious deionized water followed by isopropanol before being dried in a convection oven at 60°C. The fibers were finally weighed and the volume fraction of fibers, resin, and voids calculated. The results for C2A2/C composite sample are as follows:

Reinforcement content, volume percent:

$$(1) \qquad V_r = \left(\frac{M_f}{M_i}\right) \times 100 \times \frac{\rho_c}{\rho_r} = 56.7$$

Matrix Content, volume percent:

$$(2) \qquad V_m = \left(\frac{M_i - M_f}{M_i}\right) \times 100 \times \frac{\rho_c}{\rho_m} = 42.9$$

Void Volume, in percent:

$$(3) \qquad V_v = 100 - (V_r + V_m) = 0.4$$

Where, M_i (initial mass of the specimen) = 1.1932 g, M_f (final mass of the specimen after digestion) = 0.7614 g, ρ_r (density of the reinforcement) = 1.8 g/cm^3 [22], ρ_c (density of the specimen) = 1.61 g/cm^3, and ρ_m (density of the matrix) = 1.35 g/cm^3.

The void content of ATSP/C composites reported in Table 5.2. C1A1 and C2A2/C composites had relatively low void volume. Results observed in Table 5.2 are explainable given (1) the higher acetic acid yield of the CBAB resin (7.5wt% vs 6.5wt% for C1A1 and 5wt% for C2A2), (2) the broader Tg curve for C2A2 (indicating greater compliance during cure) as compared to C1A1 and both C1A1 and C2A2 significantly lower cured Tg as compared to CBAB (see Figure 5.18), and (3) practical reality that all specimens were cured to a maximum of 330°C due to equipment limitations. This means that CBAB evolved volatiles that due to sample rigidity during cure and subsequent ITR steps that were not fully removed.

Table 5.2. Fiber, resin and void volume for ATSP composites

Sample	Carbon Fiber	Sample Density (g/cm^3)	Fiber Volume Fraction (%)	Resin Volume Fraction (%)	Void Volume Fraction (%)
C1A1/C $[0/90]_s$	Unidirectional	1.58	63.7	32.4	3.9
C2A2/C $[0/90]_s$	Unidirectional	1.61	56.7	42.9	0.4
CBAB/C $[0/90]_s$	Unidirectional	1.42	49.7	38.8	11.5

Dynamic mechanical analysis (DMA) was performed in a TA Instruments DMA Q800 to obtain the storage modulus and Tg of ATSP via a 3 °C/min temperature ramp with a 1 Hz oscillation. Neat ATSP specimens were cut to 25 mm long by 7 mm wide by 1 mm thick and were loaded in a tensile clamp configuration. Dynamic thermal mechanical data as the storage modulus, loss modulus and tan δ as a function of temperature are shown in Figure 5.18. The glass-transition temperature (Tg) reported based on the tan δ peak was about 239.3 °C for C1A1 and 253.5 °C for C2A2, and 307 °C for CBAB. As expected, the Tg of the material decreased with an increase in molecular weight. As molecular weight increases, the resultant crosslink density decreases which will result in a lowering of the Tg.

Cryogenic dynamic thermal mechanical data as the tan δ as a function of temperature for C1A1 and C2A2 neat polymers at different frequencies are shown in Figure 5.19. The tan δ peak at around 0 and -50 °C was observed for C1A1 and C2A2, respectively.

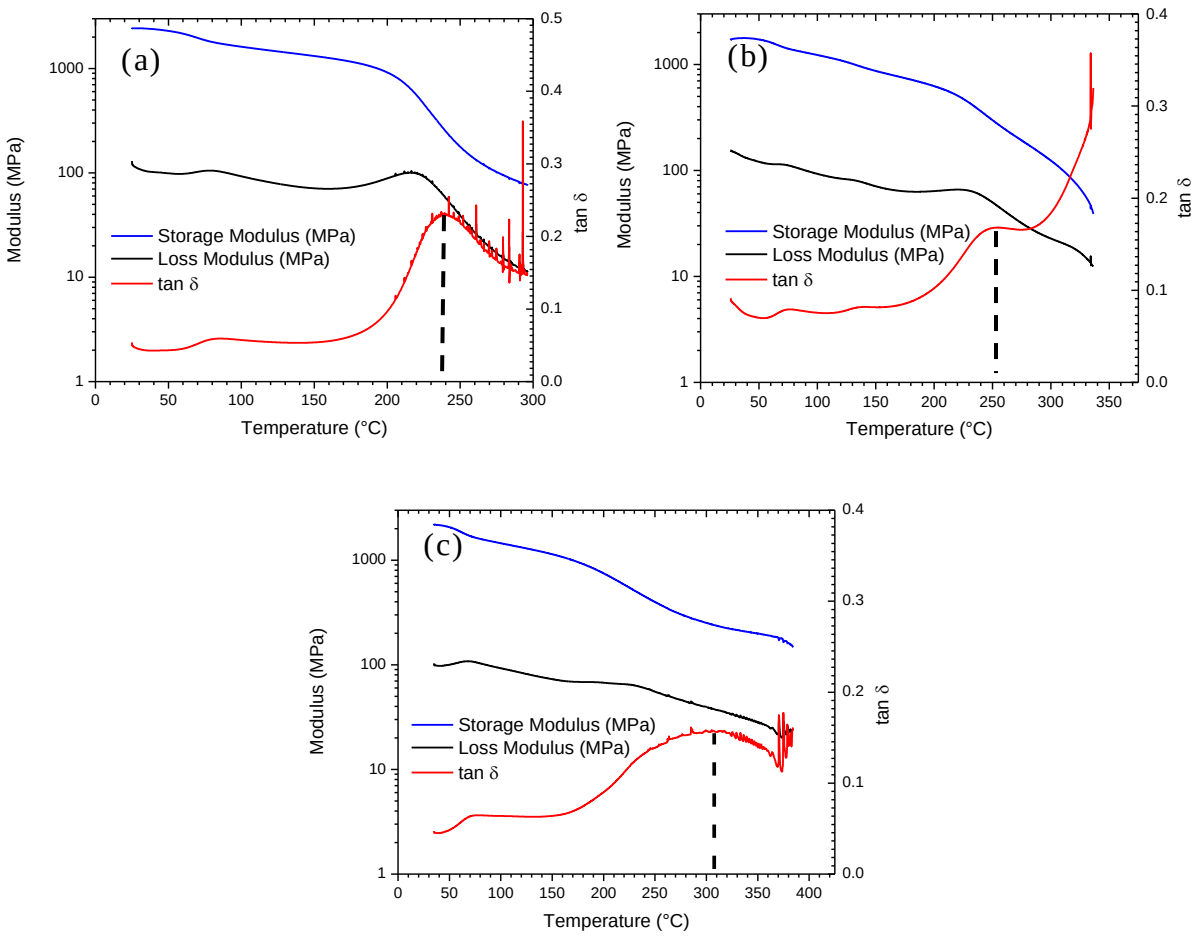

Fig. 5.18. DMA results for neat ATSP samples, (a) C1A1, (b) C2A2, and (c) CBAB.

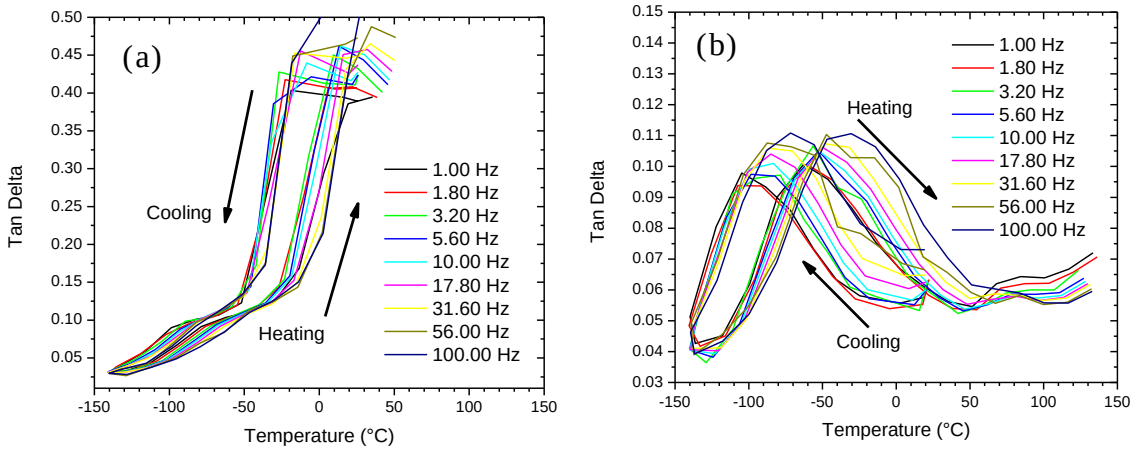

Fig. 5.19. Cryogenic DMA results for neat ATSP samples, (a) C1A1, (b) C2A2.

Thermogravimetic analysis (conducted on a TA Instruments TGA 2950) was also used to study the thermal stability of the C1A1/C, C2A2/C and CBAB/C composites. ATSP composites were cut and tested in the TGA under nitrogen and air at heating rates of 10 °C/min. Figure 5.20 shows the trace of the mass loss/temperature derivative curve as well as the total mass loss. The composites were stable even above 400 °C which reiterates the high temperature stability of this resin system. The weight loss was about 60, 67 and 62% for C1A1/C, C2A2/C and CBAB/C composites at 800 °C, respectively in air and about 27% for all composites in nitrogen.

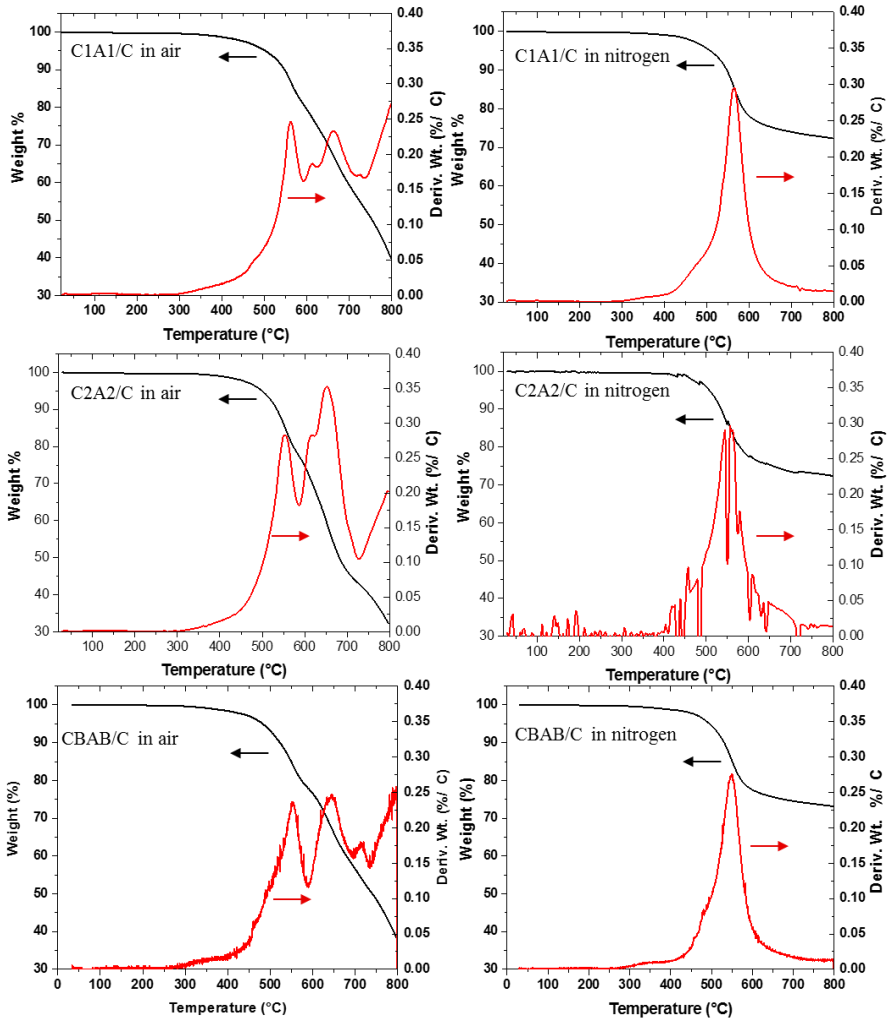

Fig. 5.20. TGA curves of C1A1/C, C2A2/C and CBAB/C composites in air and nitrogen.

Isothermal heat stability of ATSP at 371 °C was also characterized for C1A1/C, C2A2/C and CBAB/C composite. The ATSP/C samples were ramped up to 371 °C at a rate of 10 °C/min and then held isothermally at that temperature for 1 hour in an air atmosphere. The weight loss at this temperature was about 3.52, 3.05, and 1.33% for C1A1/C, C2A2/C and CBAB/C composites, respectively (Figure 5.21). Note that in the temperature range of testing, carbon fiber is stable and should not contribute to the weight loss. Some high temperature polyimides mass loss are presented in Table 5.3. As shown, CBAB/C lost just 1.33% of its weight was. Even though C1A1 and C2A2/C mass loss at 371 °C was about 1 % higher than that of polyimides (Table 5.3) [7], one should note that the polyimides were cured at 371 °C for one hour during processing while ATSP final cure temperature was at 330 °C.

Table 5.3. Cured Tg after 1 hour at 371°C and mass loss.

Material	Tg (°C)	Mass Loss (%)
PETI-8/1000	301	2.78
PETI-8/1125	293	2.24
PETI-8/1250	275	1.42
C1A1/C	239	3.25
C2A2/C	253	3.05
CBAB/C	307	1.33

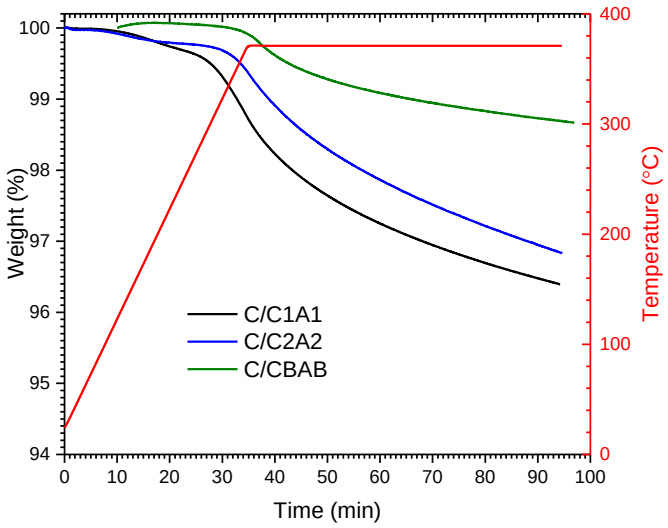

Fig. 5.21. Isothermal heat stability of ATSP/C composites.

CTEs for composite specimens was measured on a dilatometer. ATSP (C1A1/C and C2A2/C) and 8551-7/C (provided by NASA) samples were sectioned into 3 x 3 x 25 mm blocks. The specimen was placed in a dilatometer between a quartz fixture with a constant normal force that held onto the sample. The temperature was increased at a rate of 5°C/min from RT to 300 °C. Change in displacement with increasing temperature curves for ATSP and NASA samples are shown in Figure 5.22. CTE for both longitudinal and transverse sections of ATSP composites as well as $[0/90]_{2s}$ layup of ATSP and 8551-7/C are reported in Table 5.4.

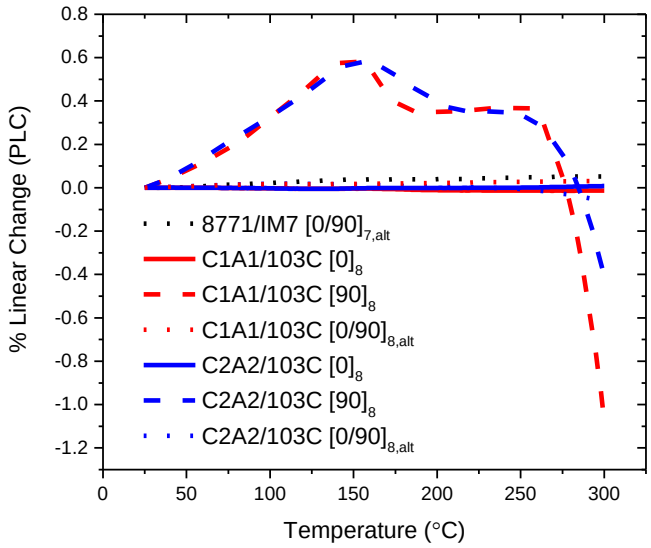

Fig. 5.22. Change in displacement with increasing temperature plot for ATSP and NASA composites.

Table 5.4. CTE of ATSP and 8551-7/C composites

Composite	Fiber Volume (%)	Longitudinal CTE (1/K)	Transverse CTE (1/K)	$[0/90]_s$ CTE (1/K)
C1A1/C	63.7	-4.73×10^{-7}	46×10^{-6}	1.17×10^{-6}
C2A2/C	56.7	2.98×10^{-7}	50×10^{-6}	1.4×10^{-6}
8551-7/C	60	-	-	1.91×10^{-6}

The CTE of 8551-7/C is higher than that of ATSP/C composites. We expect that the residual stresses induced in ATSP/C composites will be lower than that of 8551-7/C, thus ATSP/C can help in providing reliable composite structures when used over a range of temperatures.

Four point flexural tests of the ATSP composites were conducted according to ASTM D7264 at room temperature with the loading rate of 2 mm/min, as shown in Figure 5.23. This procedure involved arranging cured lamina in unidirectional configurations [0°] which were then solid-state bonded using ITR at a temperature of 330 °C for 4 h under a compressive pressure of 100 psi under vacuum. Finished laminates were then cut into specimens of 130 mm in length for testing.

The width and thickness of samples are shown in Table 5.5. Flat rectangular specimens, 8-ply unidirectional fabrics, of (C1A1/C and C2A2/C) composites were loaded in 4-point bending Instron machine.

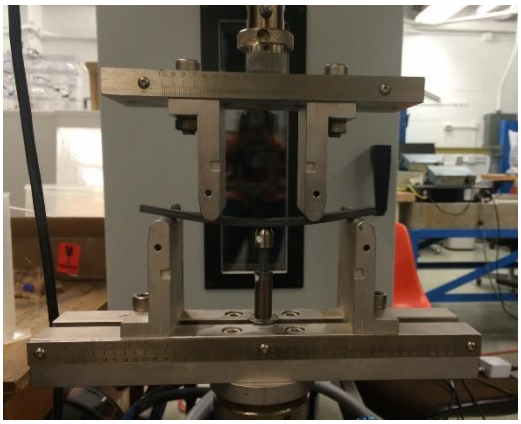

Fig. 5.23. Flexural testing being conducted.

Flexural strength, σ, and modulus, E_f, of the composites were calculated using the following equations:

$$\sigma = \frac{3PL}{4bh^2} \quad (4)$$

where, P is the breaking force of the specimen, L is the span support (105 mm), b is the width and h is the thickness.

The flexural modulus, E_f, is calculated by drawing a tangent to the steepest initial straight-line portion of the load deflection curve and using the following equation:

$$E_f = \frac{0.17L^3m}{bh^3} \quad (5)$$

where m is the slope of tangent of the initial straight-line portion of the load deflection curve.

A minimum of five tests were conducted for each chemistry, and the average values and variations are presented in Table 5.5. The stress–strain curve from sample # 1 is also shown in Figure 5.24. Note that the load increases linearly until the failure point.

Table 5.5. Flexural properties of C1A1/C and C2A2/C composites.

Sample	Resin	Flexural Stress	Flexural Modulus	b	h	span/thickness
ID#	**Chemistry**	**(MPa)**	**(GPa)**	(mm)	(mm)	L/h
1	C1A1	993.7	120.5	13.03	4.00	26.25
2	C1A1	1161.0	114.1	12.10	3.97	26.45
3	C1A1	1262.0	127.7	12.88	3.88	27.06
4	C1A1	877.9	108.7	12.76	3.80	27.63
5	C1A1	1111.1	125.2	12.50	3.90	26.92
Mean	**C1A1**	**1081.1**	**119.2**	**12.7**	**3.9**	**26.9**
Standard deviation	**C1A1**	**149.1**	**7.8**	**0.4**	**0.1**	**0.5**
7	C2A2	879.0	119.4	12.22	2.25	46.67
8	C2A2	712.9	108.1	13.22	2.97	35.35
9	C2A2	660.9	109.8	13.80	2.82	37.23
10	C2A2	759.5	108.3	13.10	2.20	47.73
11	C2A2	770.9	115.4	12.25	2.23	47.09
12	C2A2	841.1	109.2	14.11	2.34	44.87
Mean	**C2A2**	**770.7**	**111.7**	**13.1**	**2.5**	**43.2**
Standard deviation	**C2A2**	**80.3**	**4.6**	**0.8**	**0.3**	**5.4**

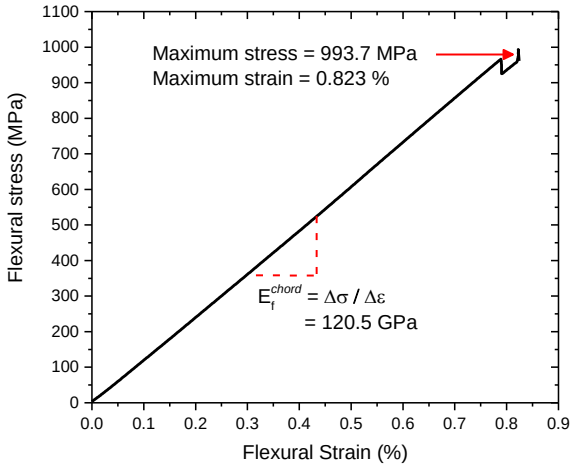

Fig. 5.24. Stress-strain curve from flexural test (sample #1).

Following the testing, all specimens were inspected. As shown in Figure 5.25, the most common failure in nearly all composites was compressive local buckling at the outer (top) surface between the loading noses. The C1A1/C composites evidenced a flexural strength and moduli of 1081.1±149.1 MPa and 119.2±7.8 GPa, respectively which is comparable or better than that of polyimide and epoxy/carbon unidirectional composites available in literature [7, 23-24]. Therefore, we can gain the qualitative observation that out-of-plane shear moduli and strength should be fairly high. This becomes an effective demonstration of the ability of fully-cured ATSP laminae to be bonded together via interchain transesterification reactions (ITR) into an effective multi-ply laminate.

C2A2 composites evidenced a somewhat lower flexural strength than C1A1-based composites for one of two reasons: produced C2A2 composites were generally thinner in the thickness dimension that C1A1 composites while the test was still conducted with a specified span length, resulting in a change in span ratio (span length versus thickness, Table 5.5). This may have created an earlier onset of failure events due to an increase in compressive stress concentration at the upper surface (inside curvature) due to overall great deflection of the C2A2 samples during testing.

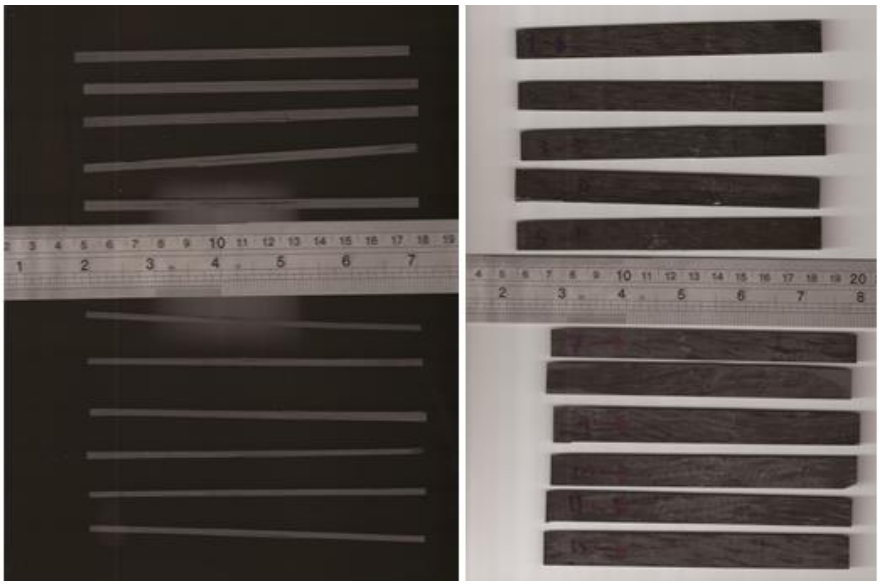

Fig. 5.25. C1A1 (top) and C2A2 (bottom) specimens after flexural tests.

The fracture toughness and damage resistance of ATSP composites was characterized as shown in Figure 5.26. Composite specimens, 20 mm wide, 3 mm thick and at least 125 mm long, with $[0/90/0]_s$ layup pattern was used for testing ATSP matrices. A precrack was introduced in the sample during the ITR cycle by placing a PTFE ply between the lamina. The samples were loaded under tension and the two faces were pulled apart at a constant rate of 2 mm/min. The fracture toughness of C1A1/C and C2A2/C was determined by loading a double cantilever beam sample under tension at -90, RT and 100 °C. Samples were allowed to equilibrate with their environment for 5 minutes prior to testing. A representative curve of the load vs displacement is shown in Figure 5.27. For each sample the load was calculated as the average of the loads for up to 90 mm of delamination length.

The G_{Ic} values of the various samples were calculated. The results are summarized in Table 5.6, and a representative Mode I fracture toughness versus delamination length curve for C2A2/C composite is shown in Figure 5.28.

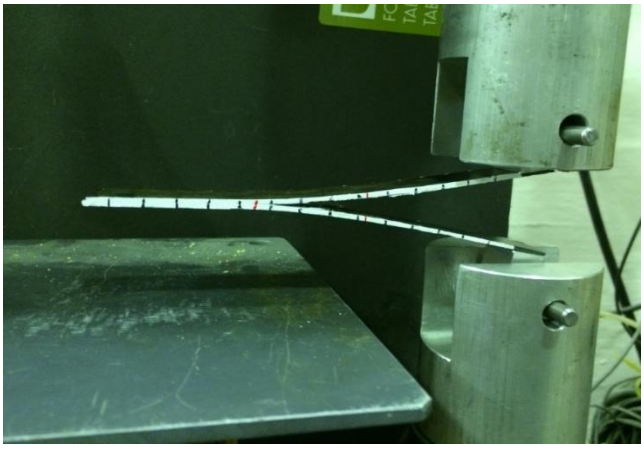

Fig. 5.26. Fracture toughness testing being conducted.

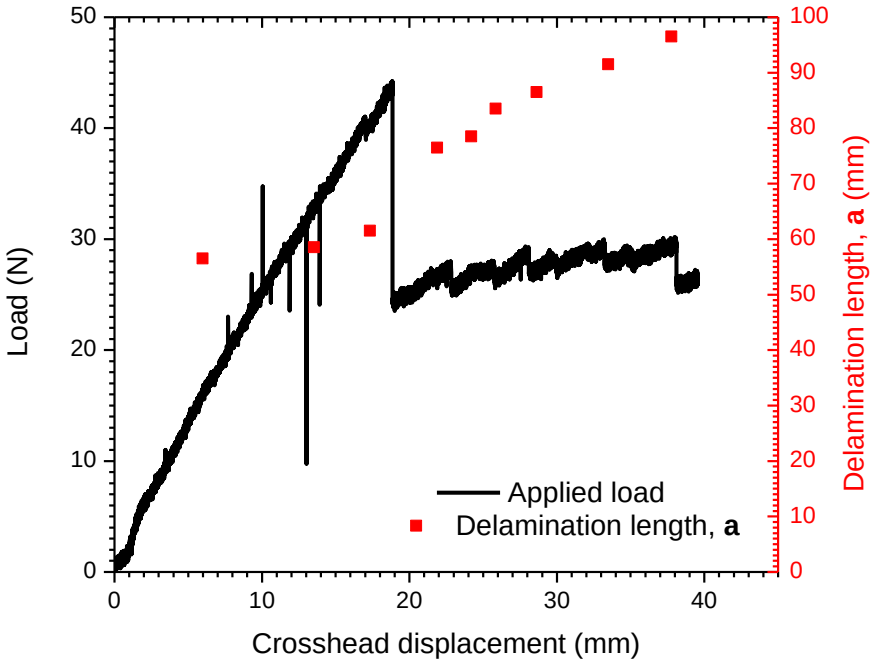

Fig. 5.27. Representative load vs displacement and delamination length vs displacement curves for C2A2/C composite obtained during fracture toughness testing a 100 °C.

Table 5.6: Interlaminar fracture toughness properties of ATSP/C composites

Composite	Layup	Temperature °C	G_{Ic} KJ/m^2 (Mean)
C1A1/C	$[0/90/0]_s$	RT	320.0
C2A2/C	$[0/90/0]_s$	RT	429.8
C1A1/C	$[0/90/0]_s$	100 ± 5	653.0
C2A2/C	$[0/90/0]_s$	100 ± 5	749.6
C1A1/C	$[0/90/0]_s$	-90 ± 5	332.5
C2A2/C	$[0/90/0]_s$	-90 ± 5	457.7

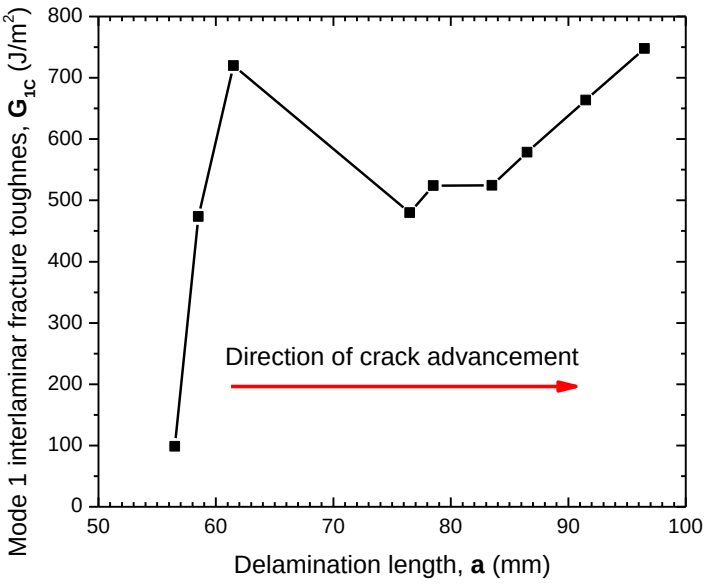

Fig. 5.28. Representative Mode I fracture toughness vs delamination length curve for C2A2/C composite at 100 °C.

Calculated G_{Ic} values were obtained via modified beam theory (MBT) as given in section 13.1.1 in ASTM D5528 with modifications for compliance and loading block geometry recommended in Annex A1. Results indicate that both C1A1 and C2A2-based composites based on laminae joined via solid-state ITR reactions evidenced fracture toughness values comparable or better

than an assortment of commercially-produced epoxy prepreg composites reviewed by Barikani et al [116]. This demonstrates the viability of solid-state bonding via the ITR mechanism for fabrication of composite structures. Both C1A1 and C2A2, as well, evidenced no significant decline at cryogenic and elevated temperatures, indicating the potential for their use within elevated temperature and cryogenic conditions. There was a modest enhancement of properties observed for C2A2 (which was based on liquid crystalline oligomers and which continues to evidence birefringence in the fully cured state) versus amorphous C1A1. This is thought to have physical origin in one or both of (1) elevated void content for C1A1 composites, or (2) local microfibrillation and enhanced cusping in C2A2 as suggested by the persistence of markers of liquid crystallinity from the oligomeric to the fully cured state and ex situ observations of fracture surfaces of C2A2 relative to C1A1.

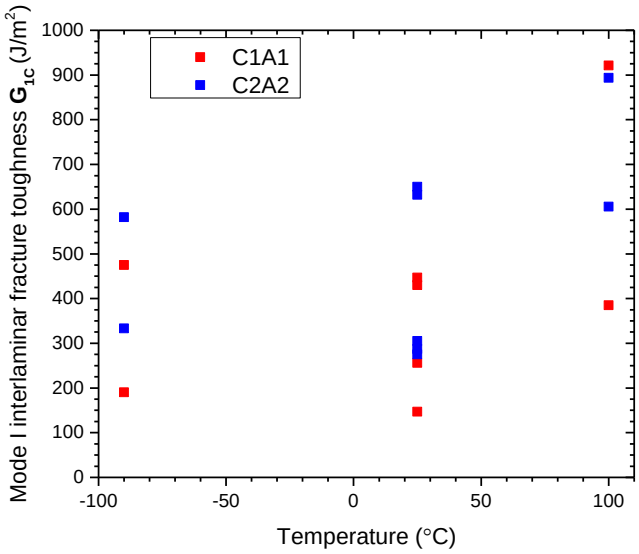

Fig. 5.29. Temperature dependence of Mode I interlaminar fracture toughness of ATSP/C composites

Short beam bending tests were used to introduce interlaminar cracks of the ATSP/C $[0/90]_{4s}$ composites. ASTM D2344 was closely followed during testing. Samples with dimensions of about 36 mm x 12 mm x 6 mm were tested on an Instron machine with a 50 kN load cell at -90, RT and 180 °C. A span length of 24 mm was used for all the testing and the experimental setup is shown in Figure 5.30. ATSP $[0/90]_{4s}$ composites were loaded at a rate of 1 mm/min until interlaminar cracks developed. Load versus displacement curves for a C1A1/C and a C2A2/C sample at RT was plotted (Figure 5.31). The point of appearance of interlaminar cracks or reduction of the load by 20% was noted as the interlaminar shear strength (ILSS) of the sample. The summary of SBS experiments for 5 samples of each chemistry is shown in Table 5.7. These values are comparable or better than polyimide and epoxy composites [13-15,116] of similar layup.

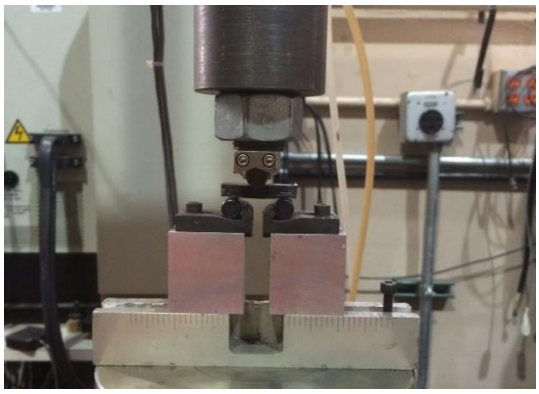

Fig. 5.30. Short Beam Shear testing being conducted.

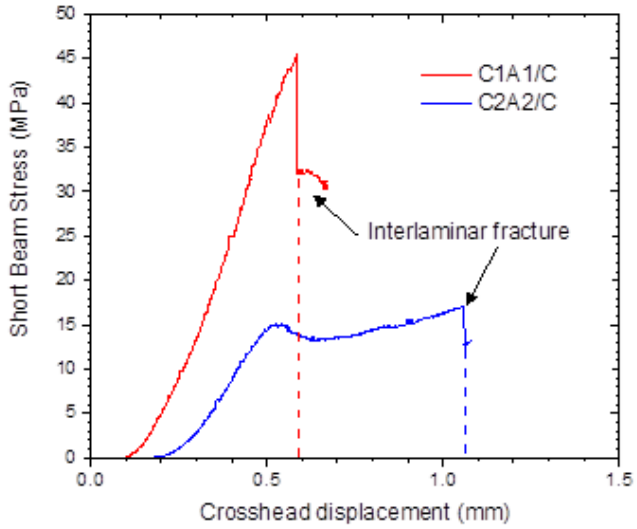

Fig. 5.31. Representative displacement vs load curve for C1A1/C and C2A2/C composites at room temperature.

Table 5.7. Summary of ATSP/C SBS experiments at different RT.

Sample ID#	Resin Chemistry	Crosshead displacement to interlaminar failure (mm)	ILSS (MPa)
1	C1A1	0.54	51.05
2	C1A1	0.58	44.64
3	C1A1	0.57	42.28
4	C1A1	0.52	43.17
5	C1A1	0.58	45.49
Mean	**C1A1**	**0.56**	**45.33**
Standard deviation	**C1A1**	**0.03**	**3.43**
6	C2A2	1.66	13.23
7	C2A2	1.26	15.76
8	C2A2	1.08	17.25
9	C2A2	1.23	15.73
10	C2A2	1.06	17.06
Mean	**C2A2**	**1.26**	**15.80**
Standard deviation	**C2A2**	**0.24**	**1.61**

Interlaminar shear strength of ATSP composites was also measured at different temperatures (Table 5.8). It can be seen that there is an interesting phenomena evident in the difference between the RT properties of the amorphous C1A1 resin and the liquid crystalline C2A2 resin. In the first part, the amorphous ATSP resin has a strongly enhanced ILSS value relative to

published values for non-unidirectional (parallel to the span direction) SBS experiments. These values were then observed to decrease significantly in cryogenic conditions. On the other hand, C2A2 had values in line with its low degree of unidirectionality (<50%) and in fact had enhanced ILSS values at cryogenic conditions. Its high temperature ILSS values were as well qualitatively in line with relative decline in storage modulus observed in the DMA curve.

Table 5.8. Summary of ATSP/C $[0/90]_{alt}$ SBS experiments at different temperatures.

Composite	Temperature (°C)	Interlaminar Shear Strength (MPa)
C1A1/C	RT	45.33 ± 3.43
C2A2/C	RT	15.80 ± 1.61
C1A1/C	180 ± 5	-
C2A2/C	180 ± 5	9.03 ± 3.32
C1A1/C	-90 ± 5	17.76 ± 4.18
C2A2/C	-90 ± 5	25.68 ± 9.57

A common damage type of polymer matrix composites is matrix cracking, which may lead to delamination and ultimately failure. Thermal residual stresses due to exposure time at different temperatures are among the many factors that can influence the development of microcrack damage. Even if microcrack density is not sufficient to diminish structural properties, the presence of microcracks leads to the risk of permeation. Leakage of cryogenic fluids is among the greatest concerns in the utilization of PMC's for cryogenic-fuel tanks.

C2A2/C composite specimens were subjected to 170 h at 280 °C in air in a Lindberg tube furnace. Samples tested in this manner were then subjected to short beam shear strength. A

representative displacement versus load curve for ATSP composites is plotted in Figure 5.32. Interlaminar shear strength of C2A2/C composite was 16.05 ± 1.74 MPa after aging.

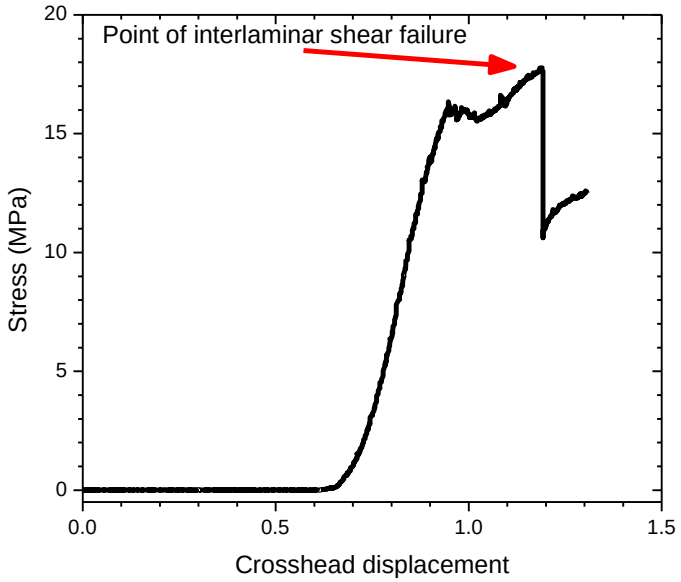

Fig. 5.32. Representative displacement vs load curve for C2A2/C composite.

Isothermal aging conducted at 280 °C for 170 h indicates that C2A2/C composite display complete property retention.

The thermal fatigue characteristics of ATSP/C composites, as compared to 8551-7/C composites (provided by NASA), were studied by thermal cycling over a range of temperatures. Cured ATSP/C laminas with $[0/90]_{2s}$ layup were cut into 4.5 x 4.5 cm squares to be compared to 8551-7/IM7 carbon fiber composite.

The ATSP Thermal Cycling Machine (TCM) was built and installed (Figure 5.33). The TCM is comprised of an upper square aluminum "oven" (heated by twin 240 Watt 3" x 12" strip heaters and controlled by a single-input PID through twin solid state power relays), a sample holding sled coupled to a drive motor system, a series of guide tubes, and a liquid nitrogen dewar. The samples are held in a set of three waterjet-cut aluminum plates. The 304SS wire rope connecting

the reel to the sample sled assembly is 1/32" in diameter to minimize thermal mass and maximize flexibility. The sled assembly is guided by four long 3/8" PTFE guide tubes, each mounted on one end to a bottom plate and on the other end to the top plate shaft collars. The total length of wire does not allow the sled to travel further down than a prescribed distance off the bottom of the liquid nitrogen dewar.

Fig. 5.33. The ATSP Thermal Cycling Machine.

Four samples each of C1A1/C, C2A2/C and 8551-7/C ($[0/90]_{2s}$) composites were cycled from cryogenic bath to the oven. The sample were cooled in liquid nitrogen temperature (-196 °C) for 8 minutes and then heated up to the ambient oven temperature (35 °C) again for another 8 minutes.

To measure permeability of samples, each specimen was pressurized to 50 psi with nitrogen and the pressure transducer in the leak tester (Figure 5.34) measured pressure changes. A drop in pressure indicated a leak in the sample. Thermal cycling (-196^0C to 35^0C) of these of

ATSP/C specimens lead to the formation of microcracks, over time, formed a percolating crack network from one side of the composite to the other, resulting in a gas permeable specimen after 80 cycles. To quantify the healing ability of the ATSP/C composites, samples were heated to 330 °C under 400 psi to induce ITR (as discussed earlier). Figure 5.35 shows the permeability of samples after cycling as well as after heating under pressure. As seen, ATSP shows a unique capability to repair microcracks upon application of heat and pressure.

Fig. 5.34. Pressure cell apparatus.

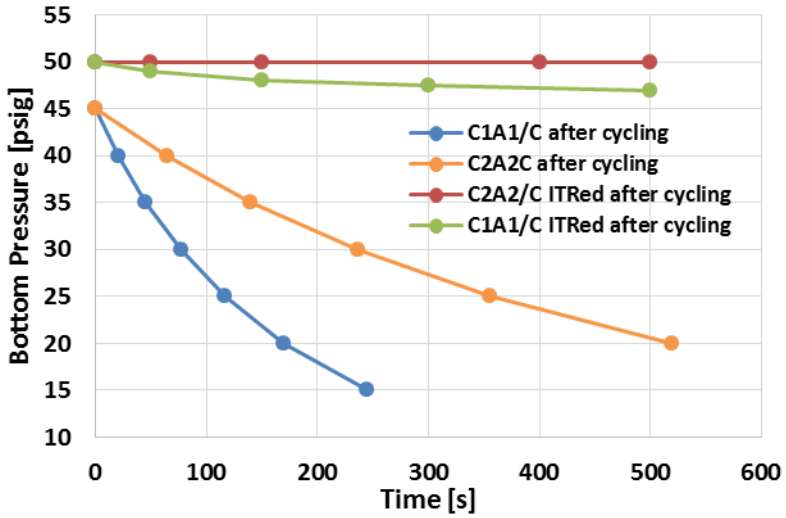

Fig. 5.35. Leak testing after 80 thermal cycles on ATSP composites, both as processed and healed.

In another set of experiments, ATSP composites were fabricated using $[0]_7$ layup and tight weave E-glass fiber 7781 mat. Composites were then cycled from cryogenic bath to the oven. The samples were cooled to liquid nitrogen temperature (-196 °C) in 5 minutes, then heated up to the oven temperature at 90 °C, which accelerated heating process of the samples, thus samples reached 35 °C in 5 minutes. Therefore, we managed to perform more cycling by decreasing the half cycle time from 8 to 5 minutes.

After 300 cycles, none of the samples showed any leakage. Thermal fatigue testing suggests that ATSP is resistant to microcracking. ATSP also shows a unique capability for healing of interlaminar cracks on application of heat and pressure. These features, along with the high strength-to-weight ratio, should make ATSP a prime candidate material to address a wide range of current and future NASA missions and enabling technology for building lighter, highly reusable, and more robust propellant tanks, thus reducing need for maintenance between flights.

The explanation for leaks seen in the first set of experiments for ATSP $[0/90]_{2s}$ composites can be accounted for in the particulars of the weave of the 103C fiber mat used versus the 8551-7 prepreg-derived composite specimens used as comparison. The 103C mat received by ATSP in 2014 had a relatively large tow size compared to 8551-7 and this allowed (1) more substantial net thermal stresses between tows which allowed more extensive inter-tow cracking and (2) during cure, occasional gaps were opened during cure. This was not the case with the version of unidirectional Sikawrap 103C received in 2009 and used previously and which possessed a far smaller tow size. If one takes another example of even a very loose plain weave mat (see Figure 5.15), pressure cell testing evidenced a substantially reduced permeability despite a tow-tow spacing of over a mm. Extending this to a very tightly woven glass fiber 7781/C1A1 and

7781/C2A2 composite we can also see that neither of these have leaked as well. This suggests that the origins of the permeability in $[0/90]_{2s}$ ATSP composites used to date were most likely (1) hand impregnation of the fiber mat prior to making composite and (2) large tow size of the fiber mat. Future experiments along this line towards testing resin effect on composite permeability should use fiber mats as similar as possible with only fiber sizing for compatibility with particular resin acting as the only allowable variance.

CHAPTER 6

INTERCHAIN TRANSESTERIFICATION AS A SOLID-STATE FABRICATION TOOL

6.1: Introduction and Background

Weight reduction is a benchmark that has always been critical to the aerospace and automotive industries and metal replacement is often key to reducing weight, cost, production times and processing cycles [110]. Polymers can be considered for metal replacement for wide variety of applications in a range of uses such as manufacturing equipment to automotive engines, aircraft components, oil and gas process and extraction equipment, bushings, bearings, seals and gears. Here, we outline results to date for a new technique to use interchain transesterification for solid-state fabrication of polymeric structures and propose several more. Fully dense ATSP plates as well as bulk ATSP with different densities are fabricated by mixing ATSP oligomers, curing to make foams, grinding the cured material and sintering the cured powders by applied heat/pressure. As well, rigid and mechanically robust ATSP foams (from which the bulk plates are derived) are also characterized in terms of thermal and mechanical properties for the first time.

Solid-state bonding of aromatic thermosetting copolyesters was previously demonstrated by Frich [10,11] wherein two fully cured coated layers were bonded to each other and demonstrated lap shear strengths competitive with commercial state-of-art. It was also revealed by SIMS that the interdiffusion depth between the

cured layers (distinguished by use of deuterium-tagged oligomers) was less than 50 nm. As this is significantly below length scale understood to be needed for a purely physical bond [18], it suggested a solid state chemical reaction at the bondlines. Along with experimental demonstration of a chemical basis for sequence reordering in hydroxybenzoic acid/hydroxynapthoic acid (HBA/HNA) copolymers [54], interchain transesterification reactions (ITR) were proposed as the operative chemical mechanism for several related phenomena within the aromatic polyester family. Following work utilized bonding schemes based on ITR to fabricate continuous fiber composites [5] and polytetrafluoroethylene (PTFE)-filled tribological materials [19,20,107] from ATSP synthesized as a cured powder via a solution-suspension polymerization. Here, we describe production of firstly a high performance foam that is then recycled via grinding into a powder and sintered via hot press into a fully dense (and presumably chemically contiguous) bulk polymer structure. Thermal and mechanical properties of the foam and bulk material, including PTFE are characterized and reported.

Among the various solid state adhesive or reversible organic systems (encompassing materials capable of schemes based on polymer shape memory [26-28], transreactions [4,96,112], hydrogen bonding [29], and others [24,30-31]), all-aromatic ATSP appears to have the highest glass transition so far reported in literature (310°C) for any material that has access to such a scheme.

Four additive manufacturing schemes and one welding scheme utilizing ITR are also proposed for future work.

6.2: Synthesis and Properties of Foamed ATSP

Dynamic mechanical analysis (DMA) was performed in a TA Instruments DMA Q800 to obtain the storage modulus and Tg of ATSP via a 3 °C/min temperature ramp with a 1 Hz oscillation. Neat ATSP specimens were cut to 25 mm long by 7 mm wide by 1 mm thick and were loaded in a tensile clamp configuration.

Thermal stability and isothermal heat stability of ATSP were characterized in a TA Instruments TGA 2950 for fully dense C2A2 and CBAB structures. The ATSP samples were heated to 600 °C with the heating rates of 10 °C/min for the former and ramped up to 371 °C at a rate of 10 °C/min and then held isothermally at that temperature for 3 hours in an air atmosphere, for the later experiments.

Coefficient of thermal expansion (CTE) of ATSP materials was measured on a Orton Dilatometer. ATSP samples were sectioned into 3 x 3 x 25 mm blocks. The specimen was placed in a between quartz fixtures with a constant normal force that held onto the sample. The temperature was increased at a rate of 3°C/min from RT to 300 °C. Observed percent linear change values below glass transition temperature were used to develop coefficients of thermal expansion.

Compression tests on the ATSP foam and fully dense structures were conducted according to ASTM D1621-10 and ASTM 695-10, respectively at room temperature with the loading rate of 1 mm/min in an Instron mechanical testing machine. For

foam structures, test specimen were square in cross section, 25.8 cm2 in area and 2.54 cm thick, and for the fully dense materials, cylindrical samples (5 mm in diameter and 10 mm in length) were obtained.

The tensile strength of ATSP foams and fully dense materials was determined with guidance from ASTM D638-14. The Type I sample specimen with the dumbbell shape and thickness of 7 mm were used for fully dense material and tested in tension in an Instron mechanical testing machine. The straight gage section has a length of 50 mm and a width of 13 mm. For the foam structures, Type IV specimen with gauge widths of 4 mm and thickness of 2 mm were used.

Samples for scanning electron microscopy were prepared via sectioning fracture surfaces from specimens and sputtering on a conductive layer of Au-Pd. A Hitachi S-4700 scanning electron microscope (SEM) was used to obtain the micrographs.
ATSP foam structures were obtained by simply mixing two matched set oligomer powders together (C2A2 and CBAB) via vigorous shaking in a container by hand followed by application of heat. C2 and A2 oligomers were mixed C2:A2 at 1.1:1 weight ratio while CB and AB oligomers were mixed CB:AB at 1:1 and cured at 200 °C for 1 hr, 270 °C for 2 hr followed by 330 °C for 3 hr. Curing was performed under vacuum to reduce oxidation. Mold release solid is necessary and only PTFE was found to actually be compatible and provide adequate release. Complex solids of revolution were easily fabricated.

Acetic acid is the by-product upon crosslinking of carboxylic end group and acetoxy end group oligomers. The low density/ high strength closed-cell foamed structures of ATSP were obtained by evolution of acetic acid (Figure 6.1). Product foam density was about 0.36 g/cm^3 by water displacement of faced (uncut) foam, which was generally water-tight. The foam exhibited high thermal stability up to 250 °C as shown in Figure 6.2.

Figure 6.2 shows thermal stability of ATSP foams ramped up and held for 8 hours at 100, 150, and 250 °C and 4 hours at 200 °C in air. The samples evidenced no weight loss at 100 and 150 °C, with a weight loss of 0.003% and 0.3% at 200 and 250 °C, respectively.

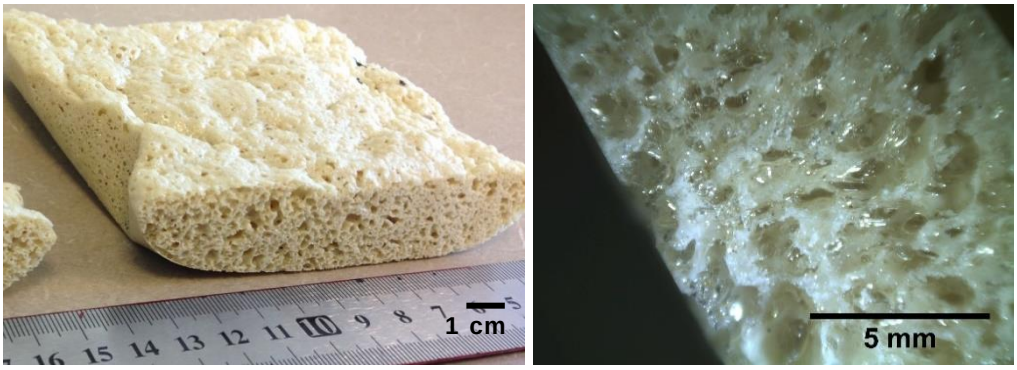

Fig. 6.1. Photograph of foamed ATSP sample.

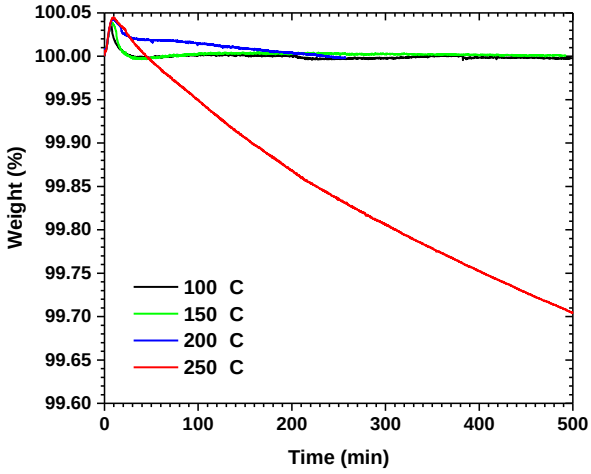

Fig. 6.2. TGA isothermal hold experiment curves of ATSP foam in air.

The compression strength of ATSP foamed structures was determined following ASTM D1621-10. The test specimen square in cross section, 25.8 cm2 area and 2.54 cm thick, obtained and were tested under compression in an Instron mechanical testing machine. A crosshead displacement of 2 mm/min was utilized and the compressive strength vs strain is reported in Figure 6.3 The C2A2 foam structures evidenced a yield strength of 3.62 ± 1.0 MPa, while the CBAB foam structures showed a yield strength of 7.51 ± 1.0 MPa.

The tensile strength vs strain of C2A2 foam structure and CBAB foam structure were plotted in Figure 6.4. Foam ultimate tensile strength, percent elongation, and modulus were reported in Table 6.1. Tensile strength was reported as the breaking load divided by sample cross-sectional area, percent elongation will be determined by extensometer, and modulus by dividing the difference in stress corresponding to any segment of section on this straight line by the corresponding difference in strain in the initial linear portion of the curve.

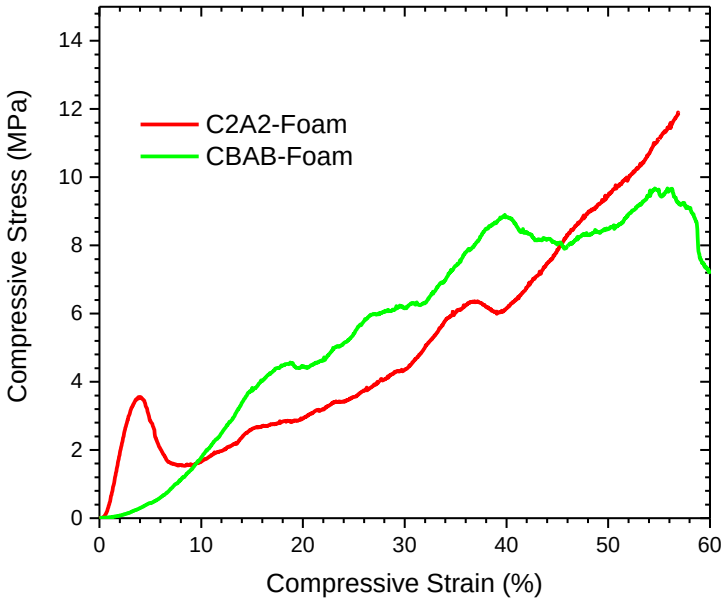

Fig. 6.3. Compressive stress vs strain of C2A2 and CBAB foam structures.

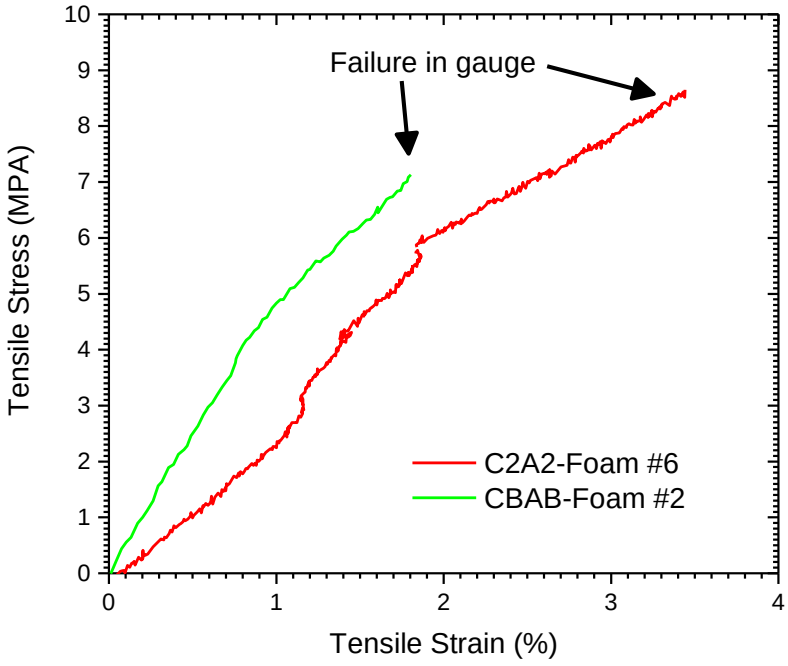

Fig. 6.4. Tensile stress vs strain of C2A2 and CBAB foam structures.

Table 6.1. Tensile and compressive properties of C2A2 and CBAB foam structures.

Material	Density (g/cm3)	Compression Strength at 10% (MPa)	Compression Strength at 20% (MPa)	Ultimate compressive strength (MPa)
C2A2 Foam	0.36	1.5	3.0	8.0
CBAB Foam	0.38	2.0	4.2	7.0
Vespel SF (Polyimide Foam) [129]	0.3 ± 0.1	2.0	3.4	4.4

ATSP foams occupy a potentially very interesting niche among polymeric foam materials. CBAB foams demonstrated comparable mechanical properties in both compression and tension as compared to Vespel SF [129] while not having the limitation of 2 mm thickness imposed to Vespel foams due to processing demands. Indeed, compression specimens utilized during this study were of significantly higher thickness than Vespel SF foams and even larger structures are seen as viable. As well, commercially scaled insulating materials found in the aerospace industry were found (Figure 6.25) to evidence quite oxidative stability in comparison to ATSP foams. It is forseeable that ATSP foam material may be employed as low density core materials in high performance applications where a high glass transition and enhanced mechanical properties in the core may be desirous.

Additionally, the relative modulus versus relative density (Figure 6.26) indicates that ATSP should deform via idealized bending behavior.

6.3: Synthesis and Properties of Fully Dense ATSP Structures via ITR

ATSP foamed structure was ground and sieved to produce powders with controlled particle size distributions in the range of <90 µm. A Col Int. Tech. FW 800 was used for crushing and grinding the C2A2 foam structure and the produced particles were automatically screened through mesh of 90 µm using a Retsch® Sieve Shaker machine. Figure 6.5 shows particle size distribution (weight and number frequency) of ground C2A2 and CBAB powder passed through 90 µm sieve.

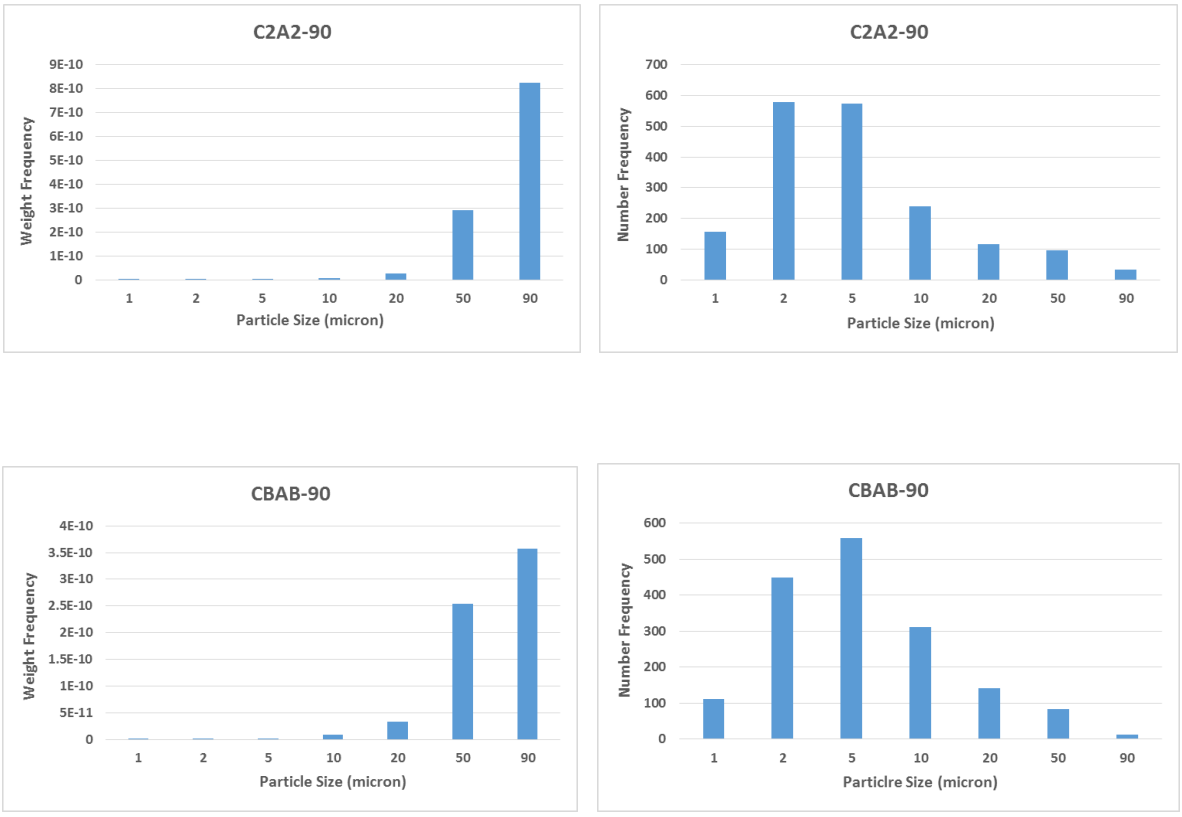

Fig. 6.5. Particle size (weight and number) distribution of CBAB passed through 90 µm sieve as analyzed by micrographic image analysis.

For making fully dense ATSP, the fine cured powders (< 90 um) were loaded into a (6 ¼" x 6 ¼") mold and compressed at 1000 psi in a hot press under vacuum. The sample was heated to 340 °C over 2 hr and then sintered at 340 °C for 2 hr (6hr for CBAB). In another experiment the sample was sintered at 340 °C for 6 hr. The final product was a fully consolidated part with the density of 1.32 g/cm^3 and 1.27 g/cm^3 for C2A2 and CBAB respectively.

Dynamic mechanical analysis (DMA) was performed in a TA Instruments DMA Q800 to obtain the storage modulus and glass-transition temperature (T_g) of ATSP via a 3 °C/min temperature ramp with a 1 Hz oscillation. Neat ATSP specimens were cut to 25 mm long by 7 mm wide by 1 mm thick and were loaded in a tensile clamp configuration. Dynamic thermal mechanical data as the storage modulus, loss modulus and tan δ as a function of temperature are shown in Figure 6.6. The T_g reported based on the tan δ peak was about 211 °C for C2A2, and 261 °C for CBAB. As expected, the T_g of the material decreased with an increase in the number average molecular weight between crosslinks M_c and lower rigidity of backbone units included within the oligomer set.

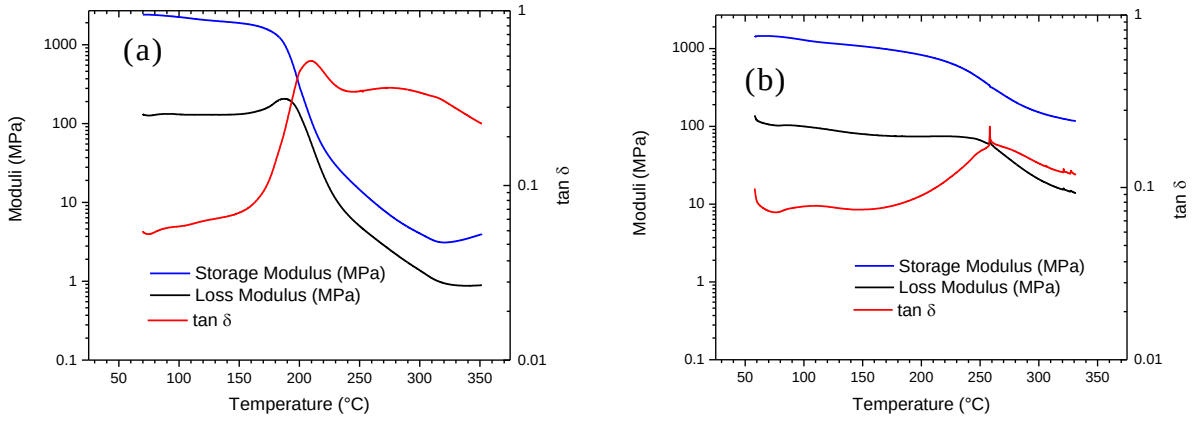

Fig. 6.6. DMA results for neat ATSP samples, (a) C2A2, and (b) CBAB.

Isothermal heat stability of ATSP at 371 °C was also characterized in a TA Instruments TGA 2950 for fully dense C2A2 and CBAB structures. The ATSP samples were ramped up to 371 °C at a rate of 10 °C/min and then held isothermally at that temperature for 3 hours in an air atmosphere. The weight loss at this temperature was about 8.17 % for CBAB and 6.66 %for C2A2, from (Figure 6.7).

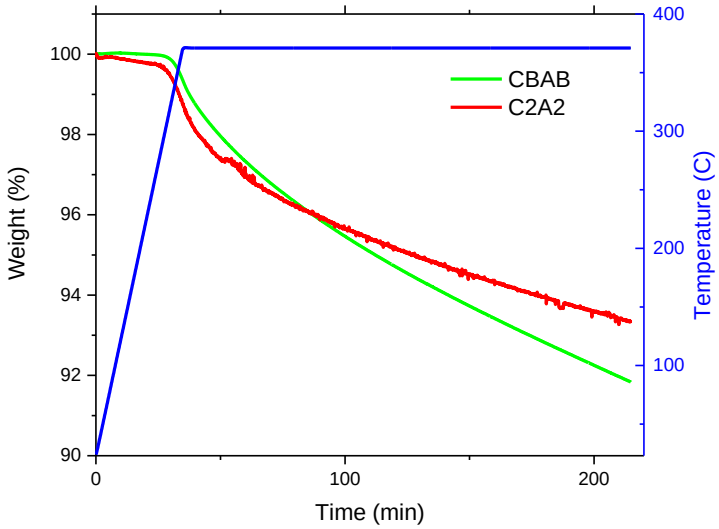

Fig. 6.7. Isothermal heat stability of neat ATSP, C2A2 and CBAB.

The compression strength of ATSP fully dense materials was determined with guidance from ASTM D695-10. Cylindrical samples (5 mm in diameter and 10 mm in length) were machined out of bulk ATSP specimens and tested under compression in an Instron mechanical testing machine. The compressive strength is reported in Figure 10. The ultimate compressive strength was 282.8 ± 31.4 MPa for C2A2 sintered for 2 hr, from Example 1.D, 333.7 ± 18.9 MPa for C2A2 sintered for 6 hr, and 303.8 ± 11.1 MPa for CBAB sintered for 6 hr.

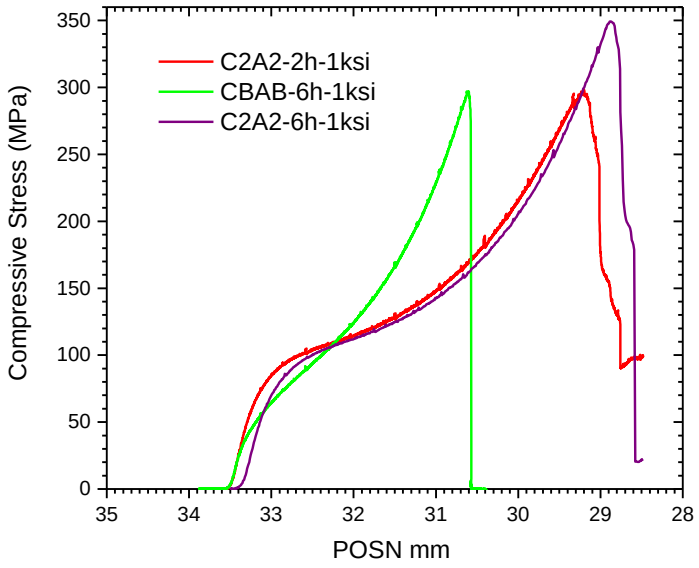

Fig. 6.8. The compression strength of C2A2 and CBAB fully dense structures.

The tensile strength of ATSP bulk materials was determined with guidance from ASTM D638-14. The Type I sample specimen with the dumbbell shape and thickness of 7 mm were used for fully dense material and tested in tension with an Instron mechanical testing machine. The straight gage section had a length of 50 mm and a width of 13 mm.

The tensile strength vs strain results are reported in Figure 6.9 and 6.10 for fully dense C2A2 and CBAB parts, respectively. Ultimate tensile strength, percent elongation, and modulus are reported in Table 6.2. Tensile strength was reported as the breaking load divided by sample cross-sectional area, percent elongation was determined by extensometer, and modulus by dividing the difference in stress corresponding to any segment of section on this straight line by the corresponding difference in strain in the initial linear portion of the curve.

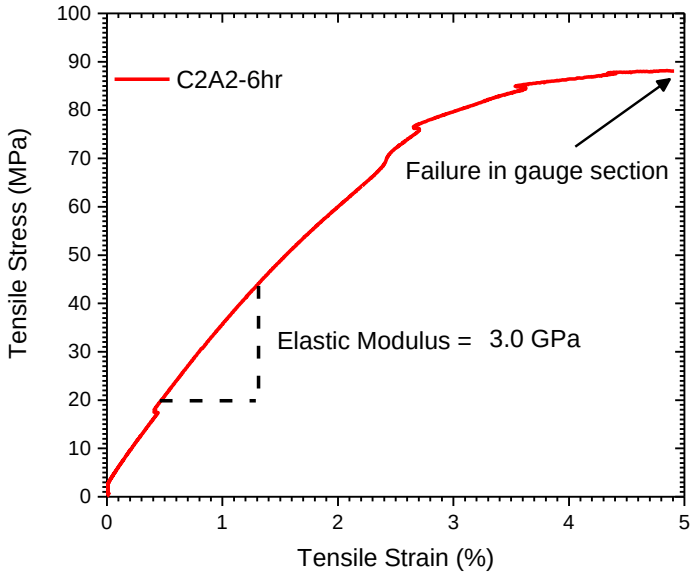

Fig. 6.9. The tensile strength vs strain of C2A2 fully dense structures.

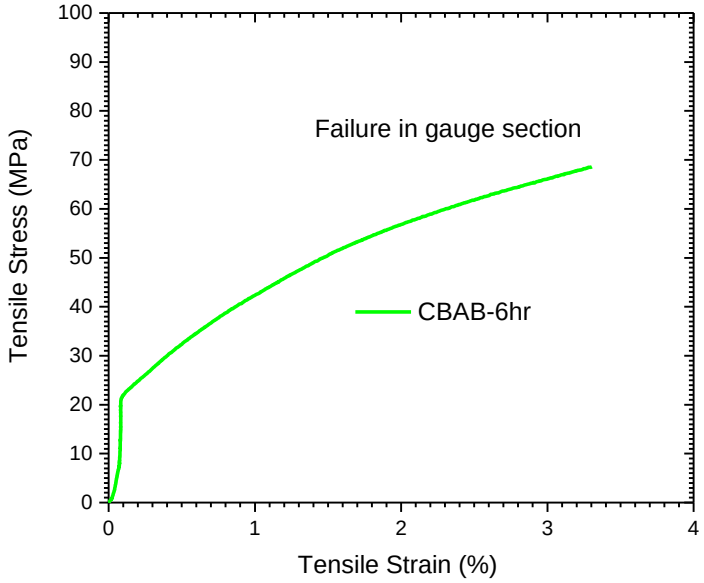

Fig. 6.10. The tensile strength vs strain of CBAB fully dense structures.

Table 6.2. Tensile properties of C2A2 and CBAB fully dense structures.

Formulation	Tensile Stress (MPa)	Modulus (GPa)	Elongation (%)
C2A2	87.2 ± 1.5	3.2 ± 0.3	7.0 ± 2.0
CBAB	66.9 ± 1.6	4.3	3.0 ± 0.5

Material	**Density (g/cm3)**	**Compression Strength (MPa)**	**Ultimate Tensile strength (MPa)**
C2A2	1.32	283	87.2
CBAB	1.27	304	66.9
VICTREX® PEEK 450G	1.43	125	98

The coefficient of thermal expansion (CTE) for bulk ATSP specimens was measured on an Orton Dilatometer. ATSP (C2A2 and CBAB) samples were sectioned into 3 x 3 x 25 mm blocks. The specimen was placed in a dilatometer between quartz fixtures with a constant normal force holding onto the sample. The temperature was

increased at a rate of 2°C/min from RT to 200 °C. CTE for ATSP samples is reported in Table 6.3.

Table 6.3. CTE of ATSP bulk materials.

Material	CTE (1/K)
C2A2	38×10^{-6}
CBAB	41×10^{-6}
PEEK 450G	55×10^{-6}
Vespel SP-1	54×10^{-6}

Tribological testing was conducted using a high-pressure tribometer (HPT) with a pin-on-disk contact geometry. The HPT simulates typical operating conditions found in an air-conditioning compressor. The disk samples were made of gray cast iron with a hardness of 95 HRB, while the pins were cut from the rectangular composite out of the mold. All experiments were performed at temperature of 25 °C and 60 °C under a load of 155 N. In order to make polymer pins for the pin-on-disk tribological tests, the ATSP fully dense specimen was machined down to pins with a diameter of 6.35 mm and a height of 11 mm.

Table 6.4. Tribological properties of neat C2A2 and CBAB pins.

Formulation	Pressure (MPa)	Distance (m)	Weight loss (gram)	Wear rate (mm^3/Nm)	COF	Temperature (°C)
Neat C2A2	4.95 (155N)	4320	0.0284	3.05 E-6	0.46	Fixed 25°C
Neat C2A2	4.95 (155N)	4320	0.00182	1.95 E-6	0.39	Fixed 60°C

ATSP fabricated in this method was also produced with variable density. C2A2 and CBAB foamed structures were ground and sieved to produce powders with controlled particle size distributions in the range of <90 µm and <250 µm. Powders were produced by grinding ATSP foam using a Col Int. Tech. FW 800 grinder and automated screening through mesh of 90 µm using a Retsch® Sieve Shaker machine. The larger powders were then sieved through 250 µm sieve.

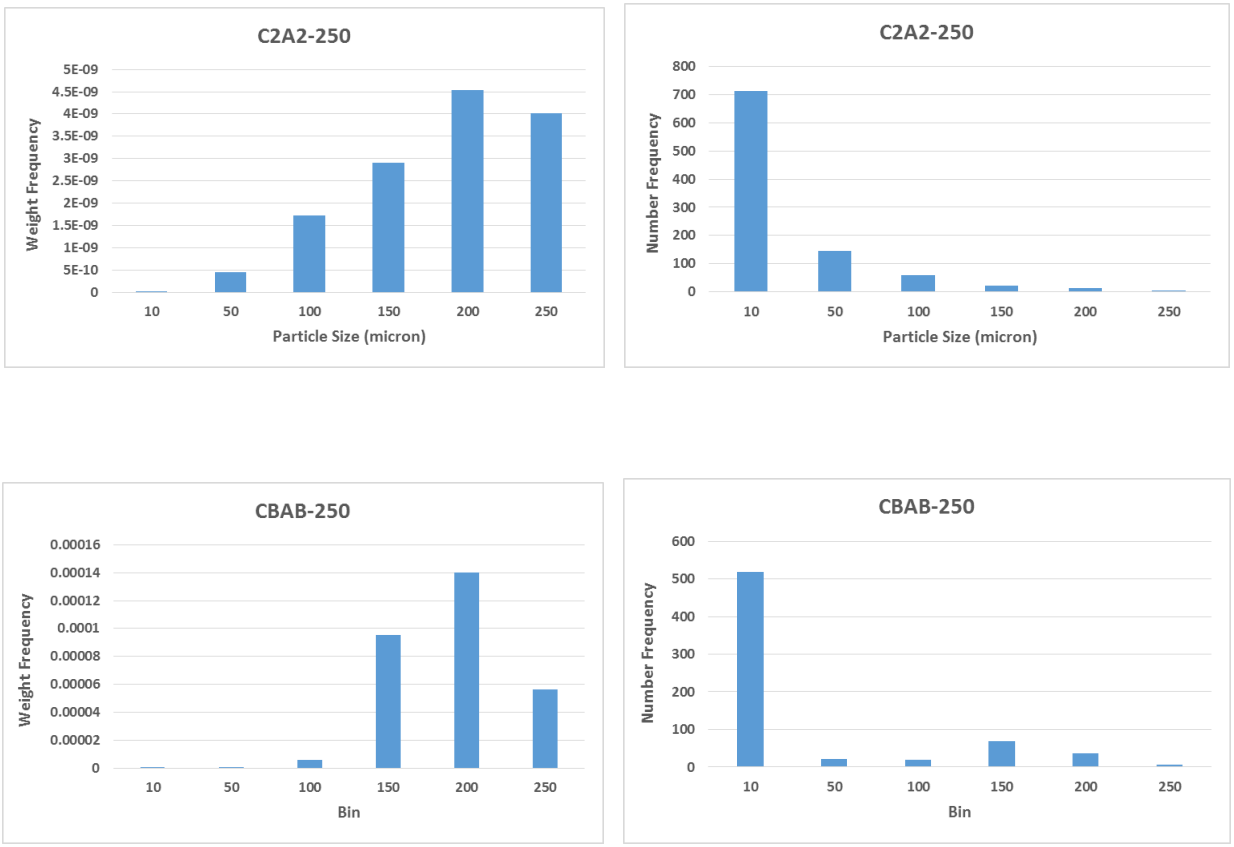

Figure 6.11. Particle size (weight and number) distribution of C2A2 and CBAB passed through 250 µm sieves.

For the bulk C2A2 and CBAB materials, the cured powders were loaded into a (½" x 2") compression mold and put in a hot press under vacuum. The samples were heated to 340 °C over 1.5 hr and then sintered at 340 °C for 0.5 hr with either no applied pressure or 1000 psi. Table 6.5 shows density based on particle size and applied pressure. The compression strength of ATSP variable density materials was determined with guidance from ASTM D695-10. Cylindrical samples (5 mm in diameter and 10 mm in length) were machined and tested under compression in an Instron mechanical testing machine. The ultimate compressive strength vs density is reported in Figure 6.12. This demonstrates a clear dependence between the compressive strength and the density of the fabricated ATSP components.

Table 6.5. Density of bulk ATSP per powder particle size.

Formulation	Particle Size	Density (g/cm^3)	Applied Pressure (psi)
C2A2	< 90 µm	1.32	1000
C2A2	< 90 µm	1.09	0
C2A2	< 250 µm	0.90	0
CBAB	< 90 µm	1.27	1000
CBAB	< 90 µm	0.89	0
CBAB	< 250 µm	0.81	0

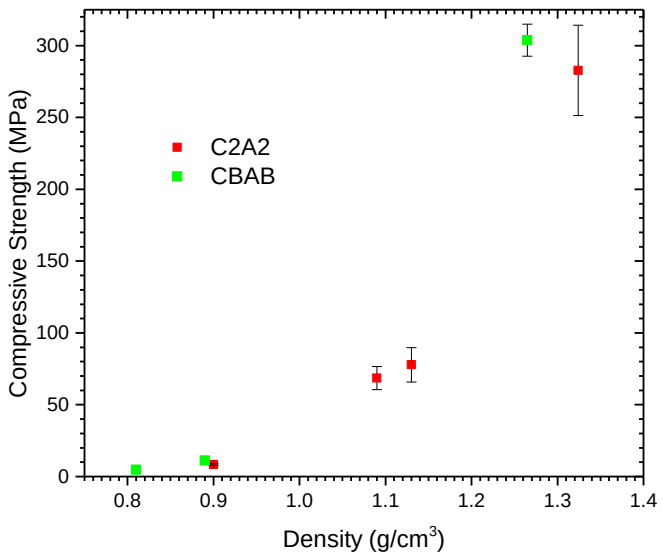

Figure 6.12. The ultimate compression strength vs density.

For the bulk C2A2/PTFE and CBAB/PTFE materials, the cured C2A2 and CBAB powders were mixed with PTFE powder, respectively, via vigorous shaking in a container by hand. ATSP/PTFE of 75/25 wt% and 95/5 wt% were loaded into a (2" x 2") compression mold and put in a hot press under vacuum and 1000 psi pressure. The samples were heated to 340 °C over 2 hr and then sintered at 340 °C for 6 hr. The final products were fully consolidated parts with density of 1.52 g/cm^3 and 1.50 g/cm^3 for C2A2/PTFE (75/25) and CBAB/PTFE (75/25) composites, respectively, and 1.37 g/cm^3 for both C2A2/PTFE (95/5) and CBAB/PTFE (95/5) composites.

The compression strength of ATSP fully dense materials was determined with guidance from ASTM D695-10. Cylindrical samples (5 mm in diameter and 10 mm in length) were machined and tested under compression in an Instron mechanical testing machine. The compressive strength is reported in Figure 15. The ultimate compressive strength was 84.04 ± 1.54 MPa and 126.38 ± 9.20 MPa for C2A2/PTFE (75/25) and CBAB/PTFE (75/25) fully dense composites.

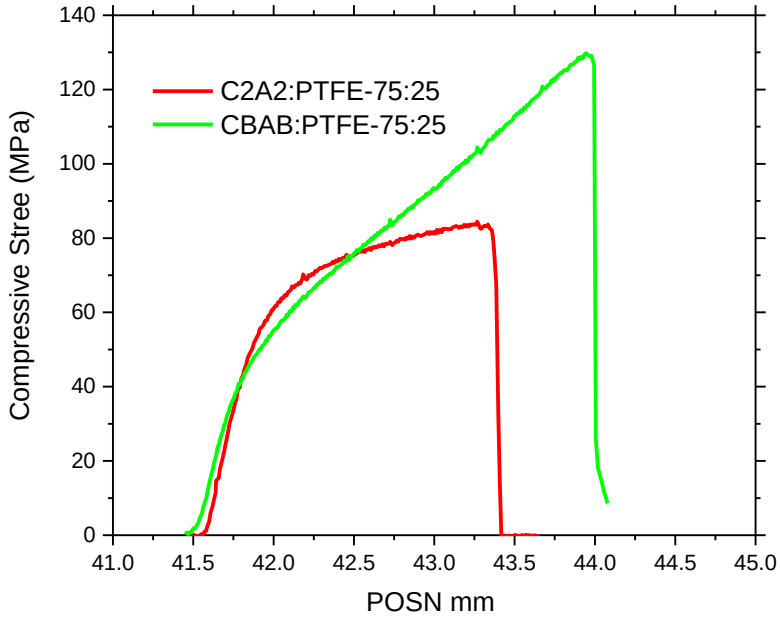

Figure 6.13. The compression strength of CBAB/PTFE and C2A2/PTFE fully dense structures.

Dynamic mechanical analysis (DMA) was performed in a TA Instruments DMA Q800 to obtain the storage modulus and T_g of ATSP/PTFE via a 3 °C/min temperature ramp with a 1 Hz oscillation. Neat ATSP specimens were cut to 25 mm long by 7 mm wide by 1 mm thick and were loaded in a tensile clamp configuration. Dynamic thermal mechanical data as the storage modulus, loss modulus and tan δ as a function of temperature are shown in Figure 16. The glass-transition temperature (T_g) reported based on the tan δ peak was about 218 °C for C2A2/PTFE (75/25), and 273 °C for CBAB/PTFE (75/25).

Storage modulus is an important parameter for the rigidity of materials. Figure 16 shows a very similar storage modulus curve to the pure ATSP. As seen, the storage modulus of the 75:25 composite is slightly lower than the neat ATSP sample over the entire temperature range

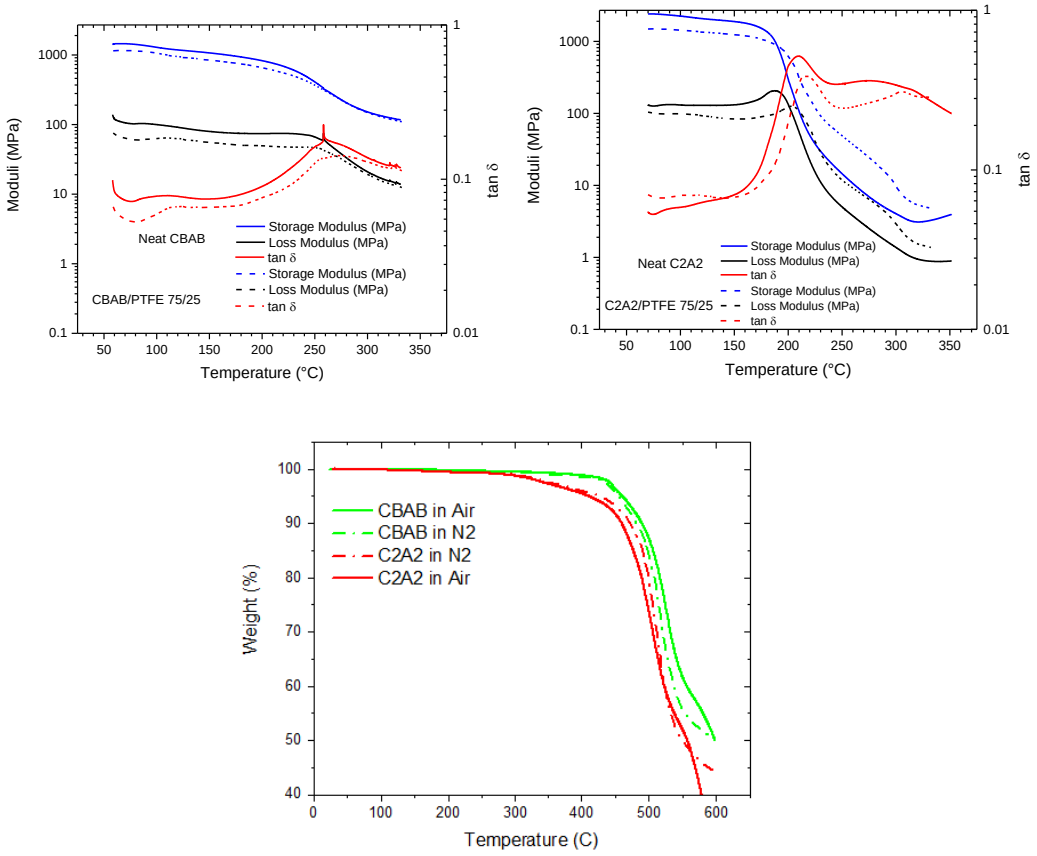

Figure 6.14. (Upper) DMA results for neat ATSP and ATSP/PTFE composite samples. (Lower) Ramped temperature TGA results in air and nitrogen for neat C2A2 and CBAB.

Tribological testing was conducted using a high-pressure tribometer (HPT) with a pin-on-disk contact geometry. The HPT simulates typical operating conditions found in an air-conditioning compressor. The disk samples were made of gray cast

iron with a hardness of 95 HRB, while the pins were cut from the rectangular composite out of the mold. All experiments were performed at temperature of 25 °C and 60 °C under a load of 230 N. The results are shown in Table 6.6.

In order to make polymer pins for the pin-on-disk tribological tests, the ATSP/PTFE composite was machined down to pins with a diameter of 6.35 mm and a height of 11 mm.

Table 6.6. Tribological properties of C2A2/PTFE and CBAB/PTFE pins.

Formulation	Pressure (MPa)	Distance (m)	Weight loss (gram)	Wear rate (mm^3/Nm)	COF	Temperature (°C)
C2A2/PTFE (95:05)	7.4	4320	0.00095	6.77E-07	0.365	25
C2A2/PTFE (95:05)	7.4	4320	0.00052	3.71E-07	0.249	60
C2A2/PTFE (75:25)	7.4	4320	0.00021	1.38E-07	0.264	25
C2A2/PTFE (75:25)	7.4	4320	0.0004	2.64E-07	0.241	60
CBAB/PTFE (95:05)	7.4	4320	0.0005	3.61E-07	0.491	25
CBAB/PTFE (95:05)	7.4	4320	0.0003	2.16E-07	0.468	60
CBAB/PTFE (75:25)	7.4	4320	0.00004	2.69E-08	0.314	25
CBAB/PTFE (75:25)	7.4	4320	0.00026	1.75E-07	0.265	60

Figure 6.15 shows the COF versus wear rate for neat C2A2, CBAB along with C2A2/PTFE and CBAB/PTFE composites at 25 and 60 °C. Where A1, A2, A3 denote pure C2A2, C2A2/PTFE (95:05), and C2A2/PTFE (75:25), respectively, and B2 and B3 denote CBAB/PTFE (95:05) and CBAB/PTFE (75:25), respectively.

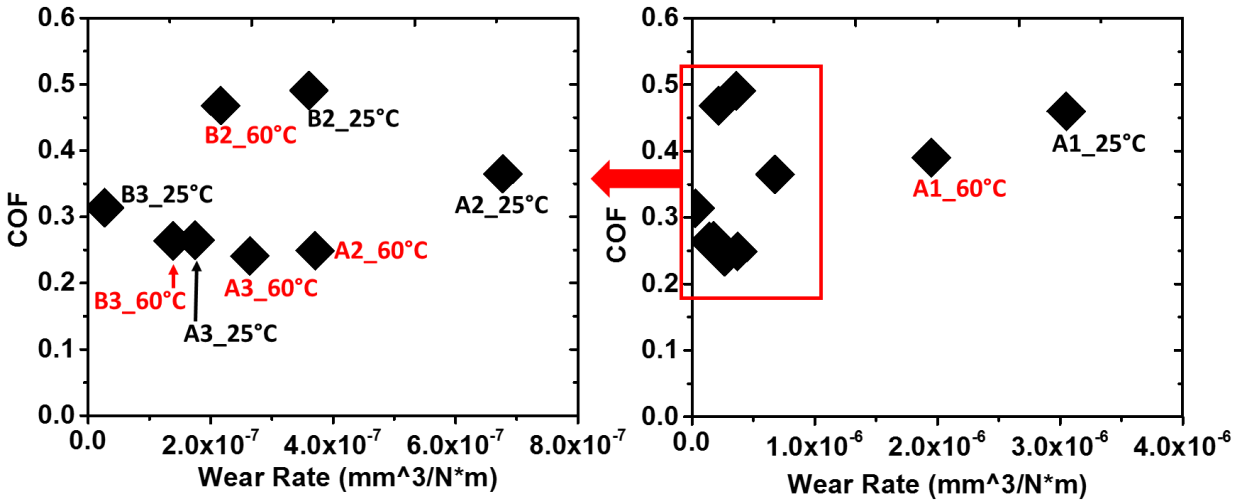

Figure 6.15. COF versus wear rate for neat C2A2/ PBAB and C2A2/PTFE and CBAB/PTFE composites pins.

Within the same temperature: higher percentage of PTFE results in lower COF and lower wear rate. For the 25% PTFE composites, higher temperature results lower COF but higher wear rate. The 5% PTFE composites, higher temperature results in lower COF and lower wear rate. CBAB/PTFE composites, in same temperature and concentration, have higher COF and lower wear rate compared with C2A2 composites.

Table 6.7. Network parameters and observed properties

Material	Branch density (x_c)	Average Flory branch coefficient (α_{AVE})	$(M_c)_n$ (g/mol)	Tan δ (°C)	5% Weight loss Temperature (°C)
C1A1 [19,20]	0.1436	0.5692	856.50	268	410
C1A1 [48]	0.1436	0.5692	856.50	224	450
C2A2 [48]	0.0718	0.4758	1692.13	209	--
C2A2	0.0718	0.4758	1692.13	211	405
CBAB	0.1333	0.45588	1112.33	261	460

The network parameters x_c and $(M_c)_N$ are defined earlier in Chapter 2. The Flory branch coefficient for each produced oligomer was calculated as [50,51]:

$$\alpha = \frac{rp_C^2\rho}{[1 - rp_C^2(1-\rho)]} = \frac{p_A^2\rho}{[rp_A^2(1-\rho)]}$$

where r is the initial formula ratio of carboxylic acid to acetoxy groups prior to oligomerization, ρ is the formula ratio of carboxylic acids belonging to the branching units (trimesic acid) to the total number of carboxylic acids prior to oligomerization. Extent of reaction for acetoxy and carboxylic groups was represented by pA and pC, respectively. Flory coefficients for acetoxy-capped oligomers (A1, A2, AB, AB2) were calculated using the equation for α on the left and carbolxylic acid-capped oligomers (C1, C2, CB, CB2) using the equation on the right. These carries the assumption of complete reaction of the counterpart functional groups during oligomerization and that therefore pC and pA could be assumed to be 1 after completion of the oligomerization process described above.

Average Flory branch coefficient was computed as the number average of the constituent oligomers.

$$\alpha_{AVG} = \sum \frac{\alpha_i N_i}{N_i}$$

In this case, we can see that a higher crosslink density (as indicated by several metrics in Table 6.7) in conjuction with observations of total elongation (Table 6.2) and observations of fracture structures of neat ITR'd specimens seen in Figures 6.16 and 6.17, that this increases brittleness in exchange for enhancement of glass transition temperature.

Well dispersed PTFE additives (as seen by fribrillar morphology across Figure 6.16 e & f, shows further that an ITR process is amenable to micron-scale additives and produces structures with outstanding mechanical properties that may have utility in anti-wear applications, as indicated in Table 6.6 and Figure 6.15.

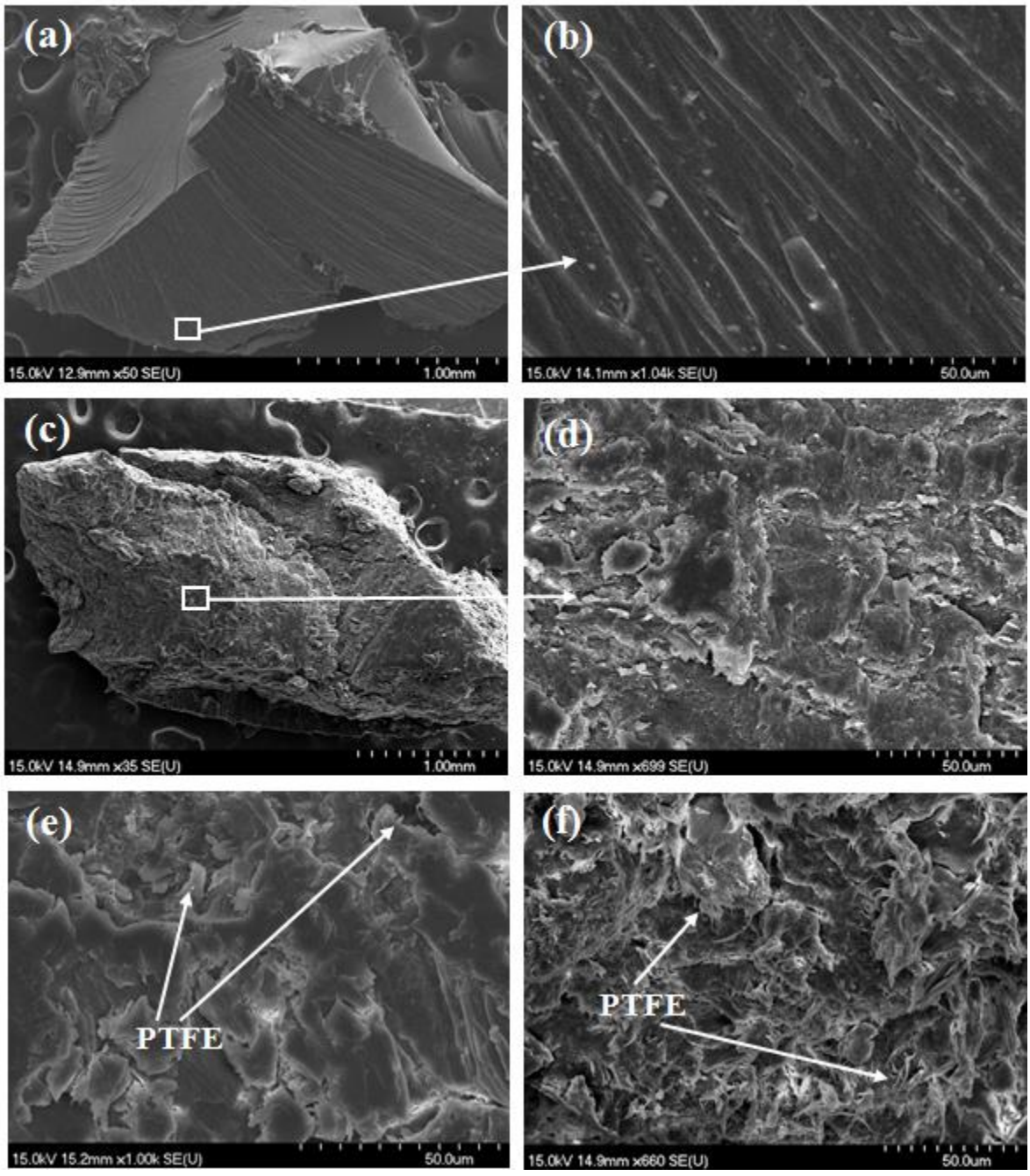

Fig. 6.16. SEM images of **(a, b)** neat CBAB, **(c, d)** neat C2A2, **(e)** CBAB/PTFE (75:25), and **(f)** C2A2/PTFE (75:25) after compression test.

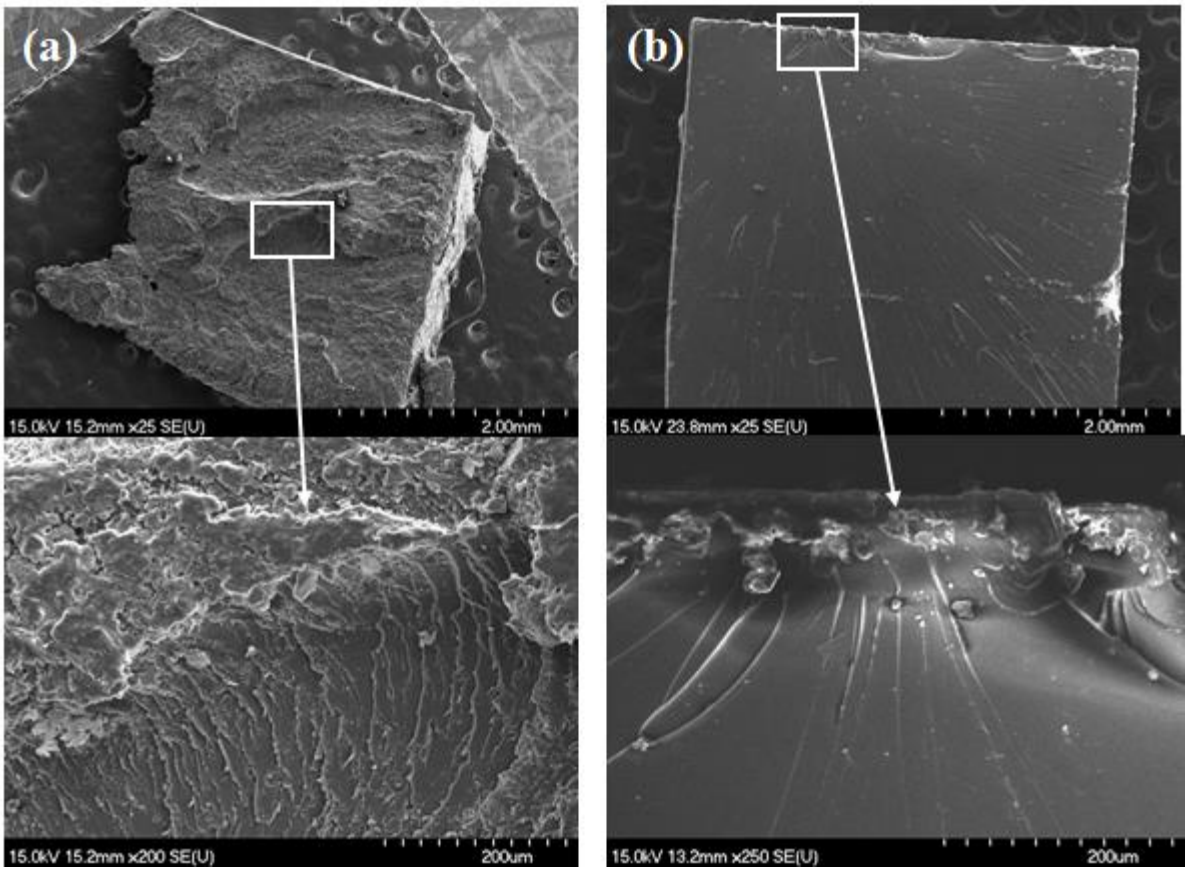

Fig. 6.17. Fracture surfaces of neat bulk tensile specimens. **(a)** C2A2, **(b)** CBAB.

6.4: Proposed Concepts for Use of ITR as a Solid-state Fabrication Tool

Composite tank joints, especially bolted joints, are particularly troubling area predisposed to leaks. Based on the success of using ITR in as a solid-state joining technique, we suggest the exploration of several techniques for solid state joining that are amenable to implementation both in continuous operation and for joining large components. Conventional joining techniques for both thermoset and thermoplastic matrices rely on either adhesive or mechanical fastening. Both techniques, though widely employed, have several limitations. These include

mismatches in CTE, high stress concentrations, and damage induced in drilling operation for mechanical fastening. For adhesive bonding, producing bondlines of appropriate strength and finding compatible adhesives can be challenging in the case of thermoplastic resins and can require substantial additional setting times in either case. One solution to this is to employ composite welding or fusion bonding as a joining operation. This has been substantially explored in the case of thermoplastic matrices [16, 35-38] and aspects of this approach have been found to be attractive to industry. For example, an earlier study by the Boeing Company indicated that a labor savings of up to 61% could be afforded by implementation of a welding approach as compared to a bolting approach [16].

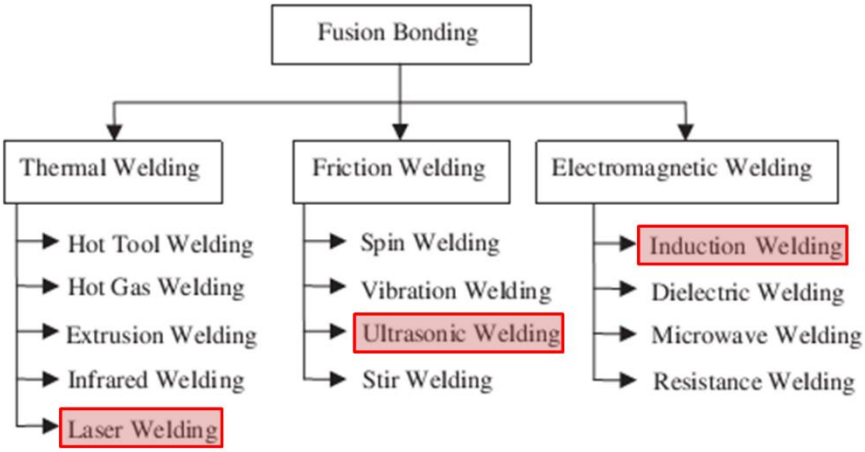

Fig. 6.18. Fusion bonding classification. Adapted from [16].

Techniques for welding of polymers can be divided into several categories based on the method of heat induced at the bondline (Figure 6.18). One technique from each category has been chosen to demonstrate applicability of this technique to aromatic thermosetting copolyester resins. Earlier in the document and in prior research in

the Economy group [5,51], it was demonstrated that carbon fiber reinforced ATSP single plies could be fabricated and then joined in the solid state by means of ITR in a hot press environment. Results in Chapter 5 indicate that ATSP/C composites produced with such a solid-state bonding method yielded interlaminar shear strengths, flexural strengths and moduli, and mode I fracture toughness at the bondline at least comparable to presently employed resin systems. In the future, we could demonstrate that techniques traditionally only employed on thermoplastic resins are now applicable to ATSP.

The High Power Direct Diode Laser (HPDDL), which is an ideal source for laser heat treating, ultrasonic welder, which applies high frequency ultrasonic acoustic vibrations, and/or localized induction heater will be examined to weld ATSP/C composite parts. These processes eliminate the use of large heating ovens since only certain areas of a part in large mold tools or engine parts need to be welded.

These localized heating processing making it possible to weld complicated geometries by using ITR. Furthermore, laser processing and induction heating are non-tactile: therefore, no non-thermal forces are applied to the workpiece. As well, prepreg would no longer have to be stored at structure integration facility, greatly simplifying equipment and ventialation needs. These methods have high automation potential for use in industrial manufacturing [33]. Thus if successful, they can be used to simplify production processes for large composite sections of launch

vehicles as well as having impact in a broader aerospace manufacturing context if successful.

Finally, the effect of welding on the strength of welded joints could be studied. Several coupons will be cut according to Figure 6.19 then welded together. Based on the high observed Mode 1 fracture toughness of ATSP composites produced by solid-state joining via the ITR mechanism, tensile testing of welded ATSP composite specimens could be conducted following ASTM D3039 [130]. Variations in notch length (L) could be explored to determine critical joining length for weldable thermoset composite parts. When combined with present data on fracture toughness of ATSP composites, this should present a compelling argument towards the utility of continuous fiber thermoset composites joinable in the solid state.

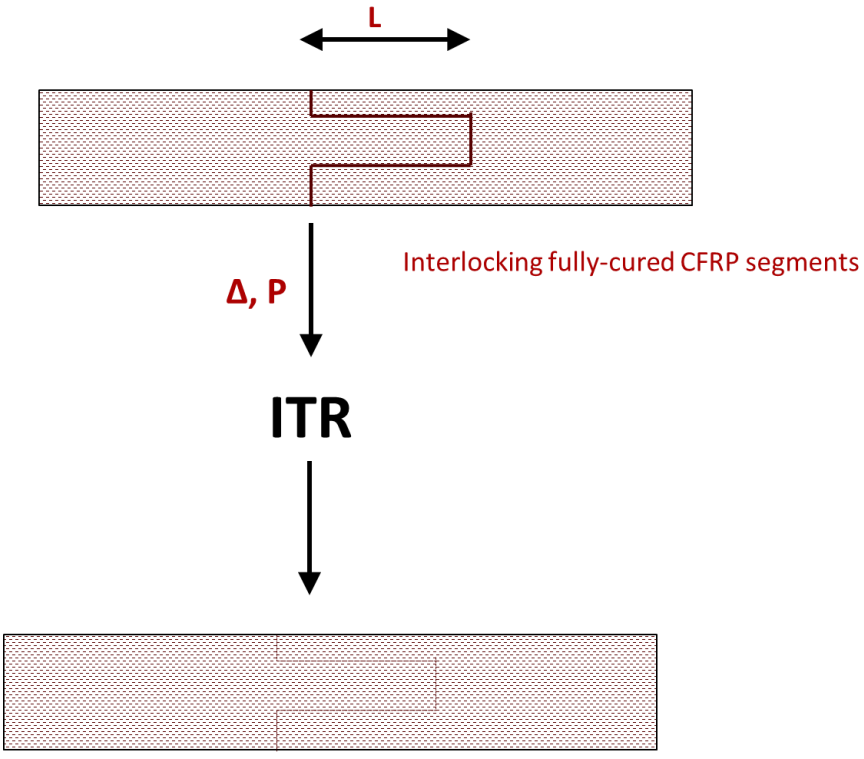

Fig. 6.19. Proposed welding scheme for fully cured ATSP laminates.

We also suggest four additive manufacture schemes (Schemes 1 through 4). Scheme 1 would be an analogous process to that currently employed for additive manufacturing of titanium and other refractory metals (selective laser sintering - SLS). With their common application in sintering of metals in mind, industrial sintering lasers can easily impart a heat flux of up to 450°C [124] to a polymer and so the exchange reactions at polymer surface and relaxation of the particle itself can happen extraordinarily fast.

Scheme 1:

1. Produce matched crosslinked COOH, AcO oligomer sets
2. Cure and/or partially cure
3. Grind/sieve to appropriate mesh
4. ↑Tg → softens/ITR → bonded → layer → repeat

Scheme 2 would be the most familiar approach for polymers although would require a higher temperature nozzle system than conventional polymers and would employ a build zone preheated up to 270°C

Scheme 2:

1. Produce matched COOH, AcO linear oligomers sets
2. React/extrude into filament
3. Melts/cures → cools → layer → repeat

Scheme 3 would be similar to Scheme 1 although would use observations from Chapter 3 wherein it was observed that acetic acid by-product gas would not be trapped at small enough section thicknesses. Subsequent to layer build, melted layer would be cured.

Scheme 3:

1. Produce matched crosslinked COOH, AcO oligomer sets
2. Grind/sieve to appropriate mesh
3. Laser or electron beam
4. Melts → cures → layer → repeat

Scheme 4 would utilize the ability of ATSP to undergo ITR between coated plates [11,12] and cured laminae [5,6,8,51] under heat and pressure. This process would allow use of arbitrary lamina as stock sheets so long as surfaces are capable of ITR and a laser can cut through the sheet.

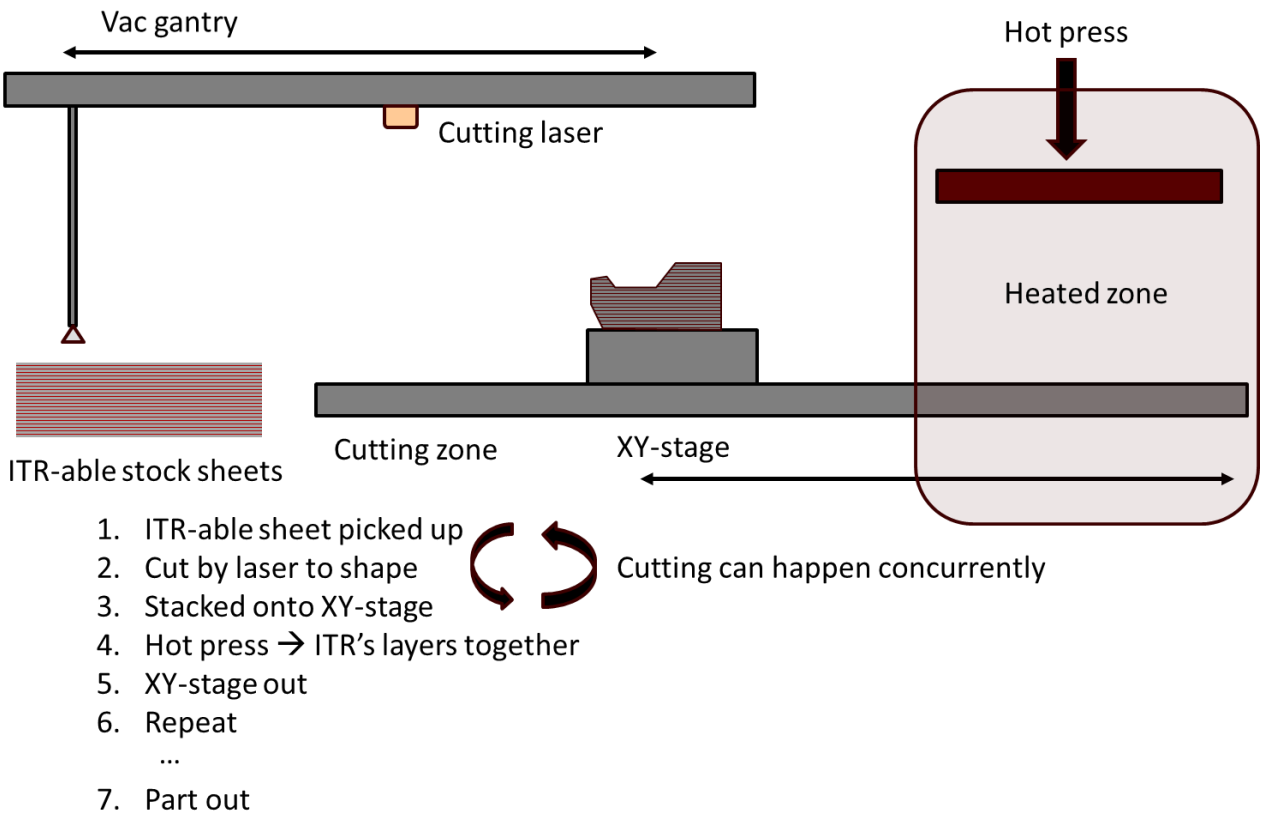

Fig. 6.20. Additive manufacturing scheme 4

This process would allow very rapid fabrication of laminates of complex geometry and arbitrary laminate order. It may have impact on rapid fabrication of injection molding cavities, microfluidics, hypersonic vehicles, general parts fabrication in the aerospace and automotive industries.

Examples of plausible laminae include:

1. Woven carbon fiber/ATSP composite
2. Woven E-glass/ATSP composite
3. ATSP Foam layers

4. Filled or unfilled bulk ATSP layers
5. ATSP-coated ceramic layers
6. Both-side-coated metal sheets (ferrous, Al, Ti)

6.5: Conclusions

It has been demonstrated that ATSP foams and ITR'd material derived from the foams possess attractive mechanical properties competitive with the highest values available from the literature within their overall form-factor. (Figures 6.21-6.19). It As well, Figure 6.24 demonstrates its amenability to precision machining. With these various aspects in mind, it seems clear that ITR is an extraordinarily powerful tool for polymer structural fabrication.

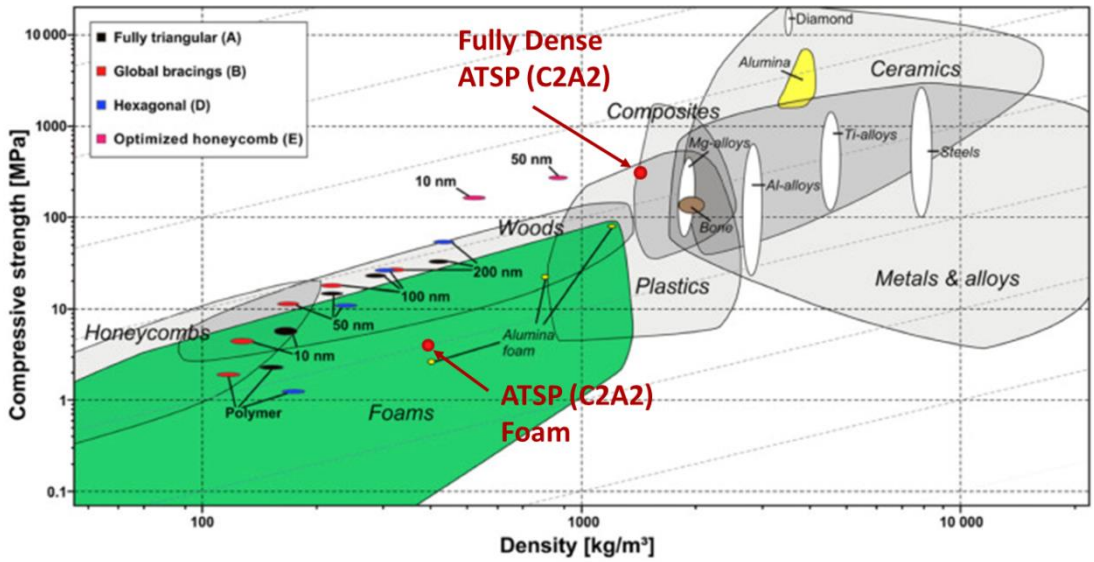

Fig. 6.21. Ashby plot of compressive strength versus density. Adapted from [127].

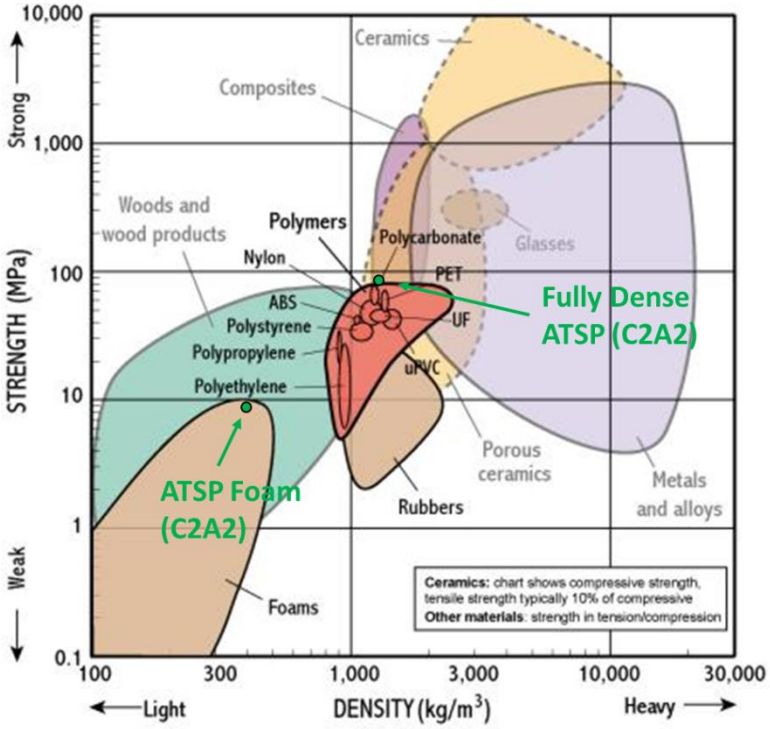

Fig. 6.22. Ashby plot of tensile strength versus density. Adapted from [126]

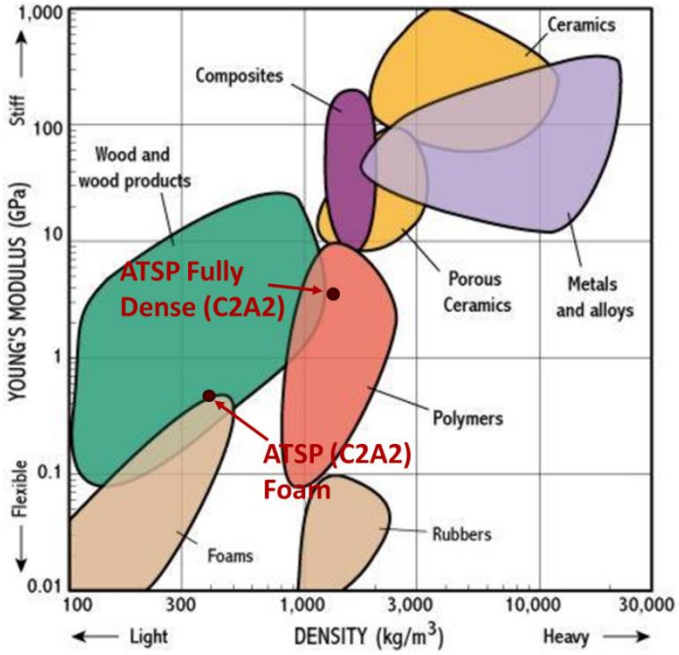

Fig. 6.23. Ashby plot of Young's modulus versus density. Adapted from [126].

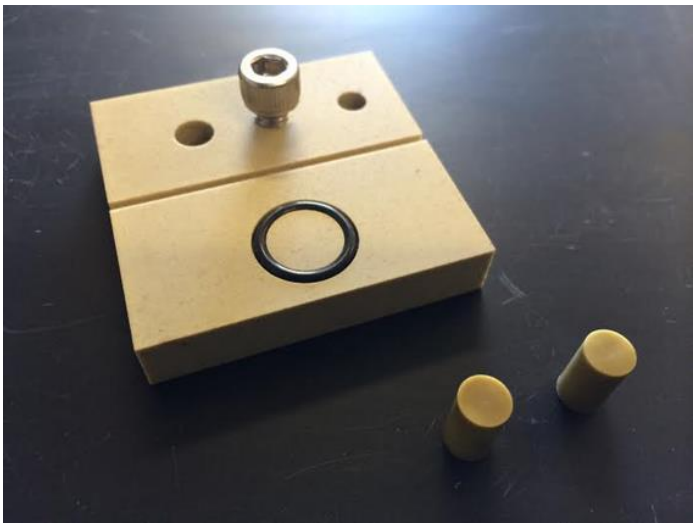

Fig. 6.24. Bulk C2A2 material with basic machining implemented including threading.

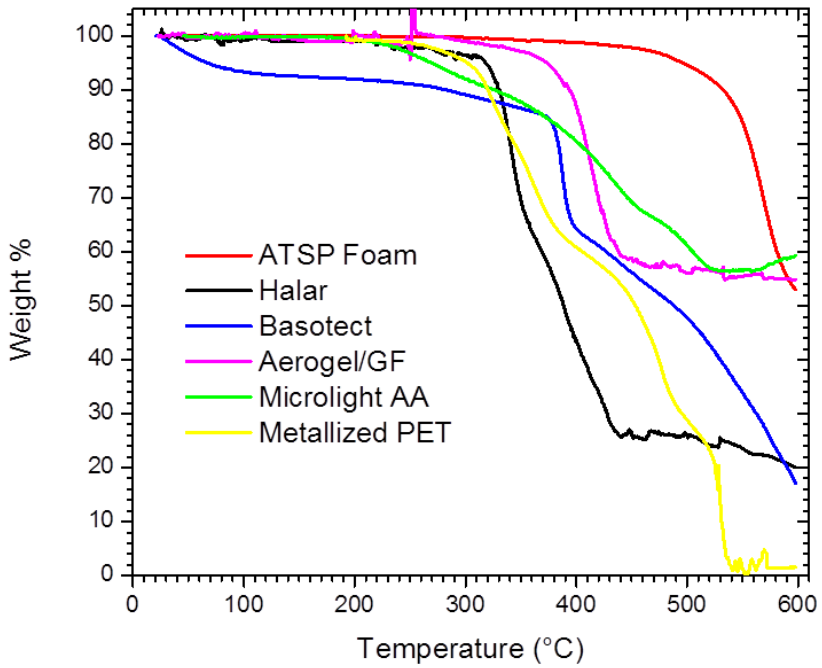

Fig. 6.25. ATSP foams in comparison to other state of art insulating and lightweight materials

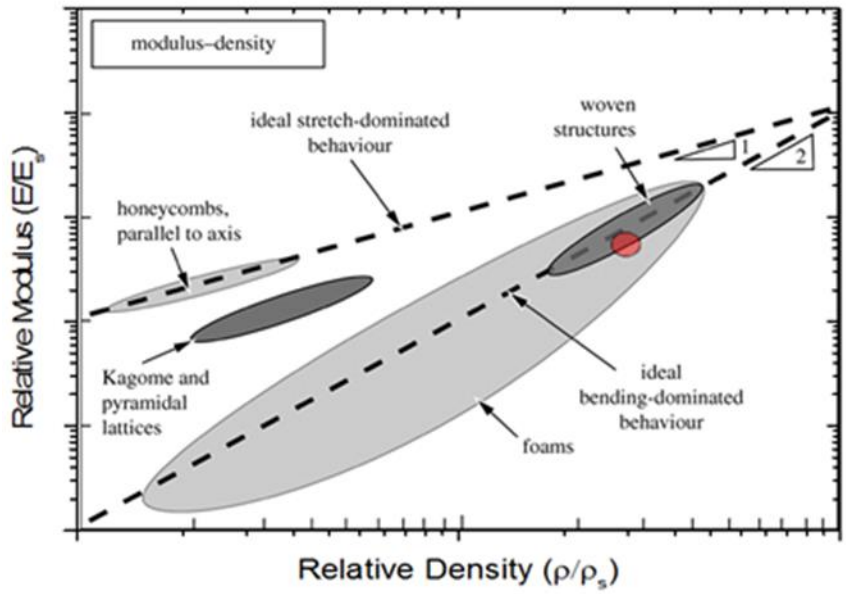

Fig. 6.26. Ashby schematic plot of relative density versus relative modulus with position ATSP foams indicated in red. Adapted from [128].

REFERENCES

1. A. Donald, Liquid Crystalline Polymers, Cambridge University Press, (2006).
2. J. Economy and K. Goranov, "Thermotropic Liquid Crystalline Polymers for High Performance Applications" *Adv. in Poly. Sci.,* 117, 222-255 (1994).
3. J. Economy, B. Nowak, "Polyester based on hydroxybenzoic acids", US Patent US3759870 A, (1970).
4. D. Frich, K. Goranov, L. Schneggenburger, and J. Economy, "Novel High-Temperature Aromatic Copolyester Thermosets: Synthesis, Characterization, and Physical Properties" *Macromolecules,* 29, 7734-7739 (1996).
5. A. Lopez and J. Economy, "Solid State Bonding of Graphite/Thermoset Composites via lnterchain Transesterification Reaction (ITR)" *Polym. Compos.,* 22, 444-449 (2001).
6. J. Economy, A. Polycarpou, and J. Meyer, "Polymer coating system for improved tribological performance" US Patent 20130337183 A1, (2013).
7. F. Shi and J. Economy, "Moisture Transport Studies on Newly Developed Aromatic and Aromatic / Aliphatic Copolyester Thin Films" *J. Poly. Sci. B: Poly. Phys.,* 36, 1025–1035 (1998).
8. B. Vaezian, J. Meyer, C. Mangun, J. Economy, "Aromatic Thermosetting coPolyester Composites for High Temperature and Cryogenic Applications" NASA SBIR Phase I NNX14CM10P – Final Report (2014).
9. Z. Parkar, C. Mangun, D. King, T. Field, G. Sutton, J. Economy, "Ablation characteristics of an aromatic thermosetting copolyester/carbon fiber composite" *J. Compos. Mater.,* 46, 1819-1830, (2012).
10. D. Frich, A. Hall, J. Economy, "Nature of adhesive bonding via interchain transesterification reactions (ITR*)", Macromol. Chem. Phys*. 199, 913-921, (1998).
11. D. Frich, J. Economy, K. Goranov, "Aromatic Copolyester Thermosets: High Temperature Adhesive Properties", *Poly. Eng. and Sci,* 37, 541-548, (1997).
12. K. Chuang, D. Revilock, J. Pereira, J. Criss, E. Mintz, "High Temperature Polyimide Composites Fabricated by RTM: Characterization and Impact Testing", *SAMPE Journal,* 49, 5 48-57, (2013).
13. S. Ghose, K.A. Watson, R.J. Cano, S.M. Britton, B.J. Jensen, J.W. Connell, H.M. Herring, and Q.J. Lineberry., "High Temperature VARTM using LARC-PETI-9 polyimide resin", *High Perf. Polym.,* 21, 653-672, (2009).
14. R.J. Cano, B.W. Grimsley, B.J. Jensen, and C.B. Kellen. "Processing and Characterization of PETI Composites Fabricated by High Temperature VARTM", *36th Int. SAMPE Conf.,* 459-68 (2004).
15. K. Chuang, J. Criss, E. Mintz, "Polyimide Composites Properties of RTM370 Fabricated by Vacuum Assisted Resins Transfer Molding (VARTM)" NASA Technical Report 20110008609, (2011).
16. C. de Ruijter, E. Mendes, H. Boerstoel, S, Picken, "Orientational order and mechanical properties of poly(amide-block-aramid) alternating block copolymer films and fibers" *Polym.,* 47, 8517-8526, (2006).
17. S. Bhama and S. Stupp, "Liquid Crystal Polymer-Carbon Fiber Composites: Molecular Orientation" *Poly. Eng. and Sci.,* 30, 228-234, (1990).

18. T. Chung, Z. Gurion, J. Stamatoff, "Induced Orientational Behavior of Liquid Crystal Polymer by Carbon Fibers", *Polym. Compos.*, 6, 181-184, (1985).
19. N. Demas, J. Zhang, A. Polycarpou, J. Economy, "Tribological Characterization of Aromatic ThermosettingCopolyester–PTFE Blends in Air Conditioning Compressor Environment", *Tribol. Lett.*, 29, 253–258, (2008).
20. J. Zhang, N. Demas, A. Polycarpou, J. Economy, "A new family of low wear, low
21. coefficient of friction polymer blend based on polytetrafluoroethylene and an aromaticthermosetting polyester", *Polym. Adv. Technol*., 19, 1105–1112, (2008).
22. Z. Parkar, J. Meyer, J. Economy "Repair of Interlaminar Cracks using Interchain Transesterification Reactions in an Aromatic Thermosetting Copolyester/Carbon Fiber Composite", *J. Compos. Mater*. submitted.
23. G. Gardiner. "Building TRUST in bonded primary structures", *Composites World*, http://www.compositesworld.com/articles/building-trust-in-bonded-primary-structures, (2015)
24. X. Luo, K. Lauber, P. Mather, "A thermally responsive, rigid, and reversible adhesive," *Polym.*, 51, 1169–1175, (2010).
25. V. Pisacane, "Fundamentals of Space Systems", Johns Hopkins University Applied Physics Laboratory Series in Science & Engineering, 424, (2005).
26. T. Xie, J. Hulway, X. Xiao, "Shape memory polymer and adhesive combination and methods of making and using the same", US 8685528 B2, (2009).
27. T. Xie, "Recent advances in polymer shape memory", *Polym.*, 52, 4985-5000, (2011).
28. H. Mengand G. Li, A review of stimuli-responsive shape memory polymer composites, *Polymer*, 54, 2199-2211, (2013).
29. M. Bartlett, A. Crosby, High Capacity, Easy Release Adhesives From Renewable Materials, *Adv. Mater.* 26, 3405-3409, (2014).
30. D. King, M. Bartlett, C. Gilman, D. Irschick, A. Crosby, "Creating Gecko-Like Adhesives for 'Real World' Surfaces", *Adv. Mater*., 26, 4345–4351, (2014).
31. M. Bartlett, A. Croll, D. King, B. Paret, D. Irschick, A. Crosby, "Looking Beyond Fibrillar Features to Scale Gecko-Like Adhesion" *Adv. Mater*., 24, 1078-1083, (2012).
32. A. Yousefpour, M. Hojjati, J-P Immarigeon, "Fusion Bonding/Welding of Thermoplastic Composites", *J. of Thermoplastic Compos. Mater*., 17, 303-341, (2004)
33. I. Villegas, "High-speed spot welding of continuous fibre reinforced thermoplastic composites", *CfK Valley Convention*, (2012).
34. I. Villegas, H. Bersee, "Ultrasonic welding of advanced thermoplastic composites: an investigation on energy-directing surfaces", *Adv. in Poly. Tech*., 2, 112-121, (2010)
35. R. Rudolf, P. Mitschang, M. Neitzel, "Induction heating of continuous carbon-fibre-reinforced thermoplastics", *Compos. A: App. Sci. and Manuf*., 31, 1191-1202, (2000).
36. J. Economy, US Patent No. 5,439,541, (1995).
37. D. Frich and J. Economy, "Thermally Stable Liquid Crystalline Thermosets Based on Aromatic Copolyesters: Preparation and Properties," J. *Polym. Sci. A: Polym. Chem.*, 35, 1061 (1997).
38. J. Hummel and P. Flory. "Structural Geometry and Torsional Potentials in p-Phenylene Polyamides and Polyesters", *Macromolecules*. 13 479-484, (1980).
39. K. Berger and M Ballauff. Structure and phase behavior of thermotropic poly(2-n-alkyl-1,4-phenylene terephthalate)s, *Molecular Crystals and Liquid Crystals*, 157, 109-23, (1988).

40. T. Chung, M. Cheng, G. Min, H. Suat, M. Jaffe; GW Calundann. Revisiting the crystallization mechanism of vectra, a liquid crystal polymer, J. *of App. Polym. Sci*., 72-9, 1139-1150, (1999).
41. S. Bhama and S. Stupp. Liquid crystal polymer-carbon fiber composites. molecular orientation, *Polym. Eng. and Sci*., 30-4, 228-234, (1990).
42. P. Mangalgiri, "Polymer-matrix Composites for High-temperature Applications", *Defense Sci. J.* 55, 175-187, (2005).
43. S. Bender, M.S. Thesis, University of Illinois, (2009).
44. A. Klepl, "Uber die Produkte der trocknen Destillation von Paraoxybenzoësäure", *J. Prakt. Chem*., 28, 193-219, (1883).
45. E. Fischer, "Über die Carbomethoxyderivate der Phenol-carbonsäuren und ihre Verwendung für Synthesen. II", *Berichte der deutschen chemischen Gesellschaft*, 42, 215-228, (1909).
46. R.Gilkey, J. Caldwell, "Polyesters of hydroxybenzoic acids", *J. Appl. Polym. Sci.*, 2, 198–202, (1959).
47. J. Economy and Z. Parkar, "High Temperature Aromatic Polyesters of p-Hydroxybenzoid Acid and Their Copolyesters", In "100+ Years of Plastics, Leo Baekeland and Beyond", 7, 93-103, (2011).
48. D. Frich, "The Effect of Interchain Transesterification on the Development of Aromatic Copolyesters", University of Illinois at Urbana-Champaign, (1996).
49. J. Gooch, "Encyclopedic Dictionary of Polymers", Springer, 182, (2010).
50. H. Duran, B. Yameen, M. Geuss, M. Kappl, M. Steinharte and W. Knollf, "Enhanced interfacial rigidity of 1D thermoset nanostructures by interface-induced liquid crystallinity", *J. Mater. Chem*. C, 1, 7758-7765, (2013).
51. Z. Parkar, "Design of Unique Composites Based on Aromatic Thermosetting Copolyesters", University of Illinois, (2011).
52. Y. Kim, J. Economy, "The Degradation Process Observed during Step Annealing of 73/27 HBA/HNA Copolyester", *Macromolecules*, 32, 2855-2860, (1999).
53. J. Economy, L. A. Schneggenburger, "Solid state interchain transesterification reactions in macromolecules", *Macromolecular Symposia*, 128, 1-12, (1998).
54. L. A. Schneggenburger, P. Osenar, and J. Economy, "Direct evidence for sequence ordering of random semicrystalline copolyesters during high-temperature annealing" *Macromolecules*, 30, 3754-3758, (1997).
55. T. Chung, Z. Gurion, and J. Stamatoff, "Induced orientational behavior of liquid crystal polymer by carbon fibers", *Polym. Compos*., 6, 181-184, (1985).
56. T. Davies, "Chemical Reactions of Polymers", Interscience, 553-561, (1964).
57. P. Flory, "Principles of Polymer Chemistry", Cornell University Press, (1953).
58. E. Bostick, "Chemical Reactions of Polymers", Interscience, 515-528, (1964).
59. M. Berenbaum, "Chemical Reactions of Polymers", Interscience, 528-548, (1964).
60. M. Stern and A. Tobolosky, Stress-Time-Temperature Relations in Polysulfide Rubbers, J. Chem. Phys., 14, 93, (1946).
61. M. Stevens, "Polymer Chemistry: An Introduction", 3rd Edition, Oxford University Press, (1999).
62. J. McMurry, "Organic Chemistry", 8th Ed., Brooks Cole, (2011).
63. P. Flory, "Kinetics of the Degradation of Polyesters by Alcohols", *J. Am. Chem. Soc*., 62, 2255-2261, (1940).

64. W. Jackson and H. Kuhfuss, "Liquid crystal polymers. I. Preparation and properties of p-hydroxybenzoic acid copolyesters", *J. Polym. Sci., Polym. Chem. Ed*. 14, 2043-2058, (1976).
65. J. Jin, S. Lee, H. Park and I. Kim, "Liquid Crystalline Properties of the Copolyesters Prepared from Resorcinol, p-Hydroxybenzoic Acid, and Terephthalic Acid", *Polym. J.*,21, 615-622, (1989).
66. H. Ramjit, "The Influence of Stereochemical Structure on the Kinetics and Mechanism of Ester-Ester Exchange Reactions by Mass Spectrometry", *J. Macomol. Sci.-Chem.*, A20, 659-673, (1983).
67. E. Tijsma, L. van der Does, A. Bantjes, and I. Vulic, "Interchange reactions with polypivalolactone", *Makromol. Chem.*, 194, 305-319, (1993).
68. P. Flory, "Fundamental Principles of Condensation Polymerization", *Chem. Rev.*, 39, 137-197, (1946).
69. K. Yoda, "Catalysis of trans-esterification reactions", *Makromol. Chem.*, 136, 311-313, (1970).
70. F. Hamb, "Copolyesters of glycols and bisphenols: A new preparative process", *J. Polym. Sci., Polym. Chem. Ed.*, 10, 3217, (1972).
71. E. Tijsma, L. van der Does, A. Bantjes, I. Vulic, G. Buning, "Interchange reactions with polypivalolactone", *Makromol. Chem.*, 194, 2807-2825, (1993).
72. P. Flory, "A Comparison of Esterification and Ester Interchange Kinetics", *J. Am. Chem. Soc.*, 62, 2261-2264, (1940).
73. J. Kugler, J. Gilmer, D. Wiswe, H. Zachmann, K. Hahn, E. Fischer, "Study of transesterification in poly(ethylene terephthalate) by small-angle neutron scattering", *Macromolecules*, 1116-1119, (1987).
74. V. Arrighi, J. Higgins, R. Weiss, A. Cimecioglu, "A small-angle neutron scattering study of a semiflexible main-chain liquid crystalline copolyester", *Macromolecules*, 25, 5297-5305, (1992).
75. A. Muhlebach, J. Economy, R. Johnson, T. Karis, J. Lyerla, "Direct evidence for transesterification and randomization in a mixture of homopolyesters of poly(4-hydroxybenzoic acid) and poly(6-hydroxy-2-naphthoic acid) above 450C" *Macromolecules*, 23, 1803, (1990).
76. E. George and R. Porter, "Novel approach for the processing of thermotropic liquid-crystal polymers. 1. Thermodynamics and solid-state transesterification" *Macromolecules*, 19, 97-105, (1986).
77. M. Stewart, A. Cox, D. Naylor, "Reactive processing of poly(ethylene 2,6-naphthalene dicarboxylate)/poly(ethylene terephthalate) blends" *Polym.*, 34, 4060-4067, (1993).
78. J. Economy, T. Gogeva, V. Habbu, "Liquid Crystalline Copolyesters as High Temperature Adhesives for Aluminum" *J. Adhesion*, 37, 215-224, (1992).
79. J. Economy, and A. Andreopoulos, "Factors Which Influence the High Temperature Adhesive Characteristics of Liquid Crystalline Copolyesters", 40, 115-125, (1993).
80. C. Klapperich, K. Komvopoulos, L. Pruitt, "Nanomechanical properties of polymers determined from nanoindentation experiments", *J. Tribol.* 123, 624-631, (2001).
81. B. Briscoe, L. Fiori, E. Pelillo, "Nano-indentation of polymeric surfaces", *J. Phys. D: Appl. Phys.*, 31, 2395-2405 (1998).

82. A. Strojny, X. Xia, A. Tsou, W. Gerberich, "Techniques and considerations for nanoindentation measurements of polymer thin film constitutive properties", *J. Adhes. Sci. Technol.*, 12, 1299-1321, (1998).
83. X. Xia, A. Strojny, L.E. Scriven, W.W. Gerberich, A. Tsou, C.C. Anderson, Constitutive property evaluation of polymeric coatings using nanomechanical methods, *Mater. Res. Soc. Symp. Proc.* 522 199-204, (1998).
84. N. Tayebi, A. Polycarpou, T.F. Conry, "Effect of substrate on determination of hardness of thin films by nanoscratch and nanoindentation techniques", *J. Mater. Res.* 19 1791-1802, (2004).
85. J. Hay, "Measuring substrate-independent modulus of dielectric films by instrumented indentation", *J. Mater. Res.* 24, 667-677, (2009).
86. E. Escobar Nunez, S. Yeo, K. Polychronopoulou, A. Polycarpou, "Tribological study of high bearing blended polymer-based coatings for air-conditioning and refrigeration compressors", *Surf. Coat. Tech.* 205, 2994-3005, (2011).
87. T. Solzak, A. Polycarpou, "Tribology of hard protective coatings under realistic operating conditions for use in oilless piston-type and swash-plate compressors", *Tribol. T.* 53, 319-328, (2010).
88. W. Oliver and G. Pharr, "An improved technique for determining hardness and elastic modulus using load and displacement sensing indentation experiments", *J. Mater. Res.* 7, 1564-1583, (1992).
89. T. Ohmura, S. Matsuoka, K. Tanaka, T. Yoshida, "Nanoindentation load-displacement behavior of pure face centered cubic metal thin films on a hard substrate", *Thin Solid Films* 385, 198-204, (2001).
90. M. Mata, O. Casals, J. Alcala, "The plastic zone size in indentation experiments: The analogy with the expansion of a spherical cavity", *Int. J. of Solids and Structures*, 43, 5994-6013, (2006).
91. A. Bolshakov, G. Pharr, "Influences of pileup on the measurement of mechanical properties by load and depth sensing indentation techniques", *J. Mater. Res.* 13, 1049-1058, (1998).
92. S. Murov, "Properties of Organic Solvents", http://murov.info/orgsolvents.htm, (2014).
93. D. Crawmer, Ed: J. Davis, "Handbook of Thermal Spray Technology", ASM International, 47-53, (2004).
94. D. Crawmer, Ed: J. Davis, "Handbook of Thermal Spray Technology", ASM International, 53-76, (2004).
95. I. Daniel, and O. Ishai, "Engineering Mechanics of Composite Materials" 2nd Ed., Oxford University Press, (2006).
96. F. Calleja, S. Fakirov, H. Zachmannm, Ed: S. Fakirov, "Transreactions in Condensation Polymers", Wiley-VCH, 429-473, (2008).
97. C. Mangun, Personal Communication, (2014).
98. F. Shi and J. Economy, "Aliphatic/aromatic copolyester thermoset adhesives: Synthesis and characterization", *Polym. Eng. and Sci.*, 37, 549-558, (1997).
99. M. Guo, "Design of aromatic thermosetting polyester composites for thermally stable devices", University of Illinois, (2014).
100. F. Shi, J. Economy, "Thermomechanical studies on newly developed copolyester thin films. Part I: Thermal expansion coefficients", *Polym. Eng. and Sci.*, 38, 499-504, (1998).

101. F. Shi, J. Economy, "Thermomechanical studies on newly developed copolyester thin films. Part II: Thermal and intrinsic stress", *Polym. Eng. and Sci.*, 38, 971-975, (1998).
102. J. Selby, M. Shannon, K. Xu, J. Economy, "Sub-micrometer solid-state adhesive bonding with aromatic thermosetting copolyesters for the assembly of polyimide membranes in silicon-based devices, J. Micromech. And Microeng., 11, 672-685, (2001).
103. K. Xu, J. Selby, M. Shannon, J. Economy, "Adhesion mechanisms in the solid-state bonding technique using submicrometer aromatic thermosetting copolyester adhesive", *J. App. Polym. Sci.*, 92, 3843-3856, (2004).
104. Y. Huang, J. McCormick, J. Economy, "Adhesion of an aromatic thermosetting copolyester with copper foils", *Polym. for Adv. Tech.*, 16, 1-5, (2005).
105. J. Zhang, A. Polycarpou, J. Economy, "An Improved Tribological Polymer Coating System for Metal Surfaces", *Tribol. Lett.*, 38, 355-365, (2010).
106. K. Xu, J. Economy, "Hyperbranched Thermosetting Poly(imide-esters): Synthesis and Properties", *Macromolecules*, 37, 4146-4155, 2004.
107. Y. Huang, J. Economy, "Wear properties of UHMWPE/aromatic thermosetting copolyester blends in unlubricated sliding", *Wear*, 262, 943-948, (2007).
108. F. Shi, L. Schneggenburder, J. Economy, "New photoimageable dielectric insulating copolyester thin films: Synthesis and characterization", *J. App. Polym. Sci.*, 63, 1199-1211, (1997).
109. S. Ebnesajjad and R. Morgan, "Fluoropolymer additives", Elsevier, (2012).
110. L. Carlsson, D. Adams, R. Pipes, "Experimental Characterization of Advanced Composite Materials, 4th Ed.", CRC Press, (2014).
111. L. McKeen, "Fluorinated Coatings and Finishes Handbook: The Definitive User's Guide", Elsevier, (2006).
112. M. Capelot , D. Montarnal , F. Tournilhac , and L. Leibler, "Metal-Catalyzed Transesterification for Healing and Assembling of Thermosets", *J. Am. Chem. Soc.*, 134, 7664–7667, (2012).
113. W. MacDonald, A. McLenaghan, G. McLean, R. Richards, S. King, "A neutron scattering investigation of the transesterification of a main-chain aromatic polyester", *Macromolecules*, 24, 6164-6167, (1991).
114. A. Padias and H. Hall, "Mechanism Studies of LCP Synthesis", *Polymers*, 3, 833-845, (2011).
115. X. Han, A. Padias, H. Hall, H. Sung, "Synthesis of thermotropic LCPs usingp-methoxycarbonyloxy aromatic acids", *J. of Polym. Sci. Part A: Polym. Chem.*, 37, 1703-1707, (1999).
116. M. Barikani, H. Saidpour, M. Sezen, "Mode-I Interlaminar Fracture Toughness in Unidirectional Carbon-fibre/Epoxy Composites", *Iranian Polym. J.*, 11, 413-424, (2002).
117. K. Holmberg, A. Matthews: "Coatings Tribology: Properties, Mechanisms, Techniques and Applications in Surface Engineering", Elsevier Science, (2009).
118. S. Yeo, A. Polycarpou, "Fretting experiments of advanced polymeric coatings and the effect of transfer films on their tribological behavior", *Tribol. Int*. 79, 16-25 (2014)
119. A. D'Amore, A. Pompo, L. Nicolais, "Viscoelastic effects in poly(ether ether ketone) (PEEK) and PEEK-based composites" *Compos. Sci. and Tech.*, 41, 303-325 (1991).
120. S. Shankar, D. Karthikeyan, L. Dokos, K. Kannan, "Global Powder Coatings Market: Demand for High Performance and Sustainable Products Steers Growth", Frost & Sullivan, (2014).

121. K. Almara, S. Saber-Samandari, C. Berndt, "Splat taxonomy of polymeric thermal spray coating", *Surf. & Coat. Tech.*, 205, 5028-5034, (2011).
122. F. Sciance, "The Transition from HFC-134a to a Low-GWP Refrigerant in Mobile Air Conditioners", General Motors Public Policy Center, (2013).
123. B. Minor, D. Spatz, "HFO-1234yf Low GWP Refrigerant Update", *International Refrigeration and Air Conditioning Conference*, (2008).
124. I. Gibson, B. Stucker, D. Rosen, "Additive Manufacturing Technologies: 3D Printing, Rapid Prototyping, and Direct Digital Manufacturing, 2nd Ed.", Springer, (2015).
125. D. Thomas, S. Gilbert, "Costs and Cost Effectiveness of Additive Manufacturing", *NIST Special Publication 1176*, (2014).
126. A. Lovatt, D. Shercliff, "Material selection and processing", http://www-materials.eng.cam.ac.uk/mpsite/, (2002).
127. J. Bauer, S. Hengsbach, I. Tesari, R. Schwaiger, O. Kraft, "High-strength cellular ceramic composites with 3D microarchitecture", *Proceedings of the National Academy of Sciences*, 111, 2453-2458, (2014).
128. M. Ashby, "The properties of foams and lattices", Phil. Trans. R. Soc. A, 364, 15-30, (2006).
129. "Dupont Vespel SF Polyimide Foam Parts", E. I. du Pont de Nemours and Company, (2010).
130. ASTM Standard D3039, "Standard Test Method for Tensile Properties of Polymer Matrix Composite Materials", ASTM Internation, (2014).
131. A. Brooks, "NASA & Boeing Team up to Construct Composite Fuel Tank", *Composites Today*, http://www.compositestoday.com/2014/03/nasa-boeing-team-construct-composite-fuel-tank/ , (2014).
132. J. Zhang, "Design of polymer composites with improved adhesion and wear properties", University of Illinois, 2008.
133. B. Piascik, "Materials, Structures, Mechanical Systems, and Manufacturing Roadmap, Technology Area 12", NASA, (2012).
134. J. Johnston, F. Li, F. Harris, T. Takekoshi, "Synthesis and characterization of imide oligomers end-capped with 4-(phenylethynyl)phthalic anhydrides", 35, 4865-4873, (1994).
135. J. Moll, S. White, N. Sottos, "A self-sealing fiber-reinforced composite" *J. of Compos. Mater.*, 44, 2573-2585 (2010).
136. U. Gaur, B. Miller, "Effects of environmental exposure on fiber/epoxy interfacial shear strength", *Polym. Compos.*, 11, 217-222, (2004).
137. B. Blaiszik, M. Baginska, S. White, N. Sottos, "Autonomic Recovery of Fiber/Matrix Interfacial Bond Strength in a Model Composite" *Adv. Funct. Mater.*, 20, 3547–355, (2010).
138. R. Heydenreich, "Cryotanks in future vehicles", *Cryogenics*, 38, 125-130, (1998).
139. B. Briscoe, S. Sinha, "Wear of polymers", *Proc. Inst. Mech. Eng., Part J: J. Eng. Tribol.* 216, 401-413, (2002).
140. J. Hay, G. Pharr, "Instrumented Indentation Testing, ASM Handbook Volume 8: Mechanical Testing and Evaluation, 10th ed.", 231-243, (2000).
141. "Victrex PEEK 450G", Victrex PLC, (2015)
142. "Dupont Vespel SP-1 Polyimide Isostatic Shapes", E. I. du Pont de Nemours and Company, (2014).

143. H. Brown, A. Yang, T. Russell, W. Volksen, E. Kramer, T. Russel, "Diffusion and Self-Adhesion of the Polyimide PMDA-ODA" *Polymer,* 29, 1807 (1988).
144. A. Yamamoto, T. Hamada, I. Hisaki, M. Miyata, N. Tohnai, "Dynamically Deformable Cube-like Hydrogen-Bonding Networks in Water-Responsive Diamondoid Porous Organic Salts", *Angewandte Chemie International Edition,* 52, 1709-1712, (2013).